Measurement of Neutrino Induced, Charged Current, Charged Pion Production

by

Michael Joseph Wilking

B.Ch.E., University of Minnesota, 2001

M.S., University of Colorado, 2007

A thesis submitted to the

Faculty of the Graduate School of the

University of Colorado in partial fulfillment

of the requirements for the degree of

Doctor of Philosophy

Department of Physics

2009

This thesis entitled:
Measurement of Neutrino Induced, Charged Current, Charged Pion Production
written by Michael Joseph Wilking
has been approved for the Department of Physics

Prof. Eric Zimmerman

Prof. John Cumalat

Prof. Kevin Stenson

Prof. Senarath De Alwis

Prof. Andrew Hamilton

Date

The final copy of this thesis has been examined by the signatories, and we find that both the content and the form meet acceptable presentation standards of scholarly work in the above mentioned discipline.

Wilking, Michael Joseph (Ph.D., Physics)

Measurement of Neutrino Induced, Charged Current, Charged Pion Production

Thesis directed by Prof. Eric Zimmerman

Neutrinos are among the least understood particles in the standard model of particle physics. At neutrino energies in the 1 GeV range, neutrino properties are typically determined by observing the outgoing charged lepton produced in a charged current quasi-elastic interactions. The largest charged current background to these measurements comes from charged current pion production interactions, for which there is very little available data.

This document presents a measurement of neutrino induced, charged current, charged pion production at neutrino energies directly relevant to many of the next generation of oscillation experiments. The interaction cross section has been measured as a function of several kinematic quantities, such as the kinetic energies and directions of the muons and pions produced in these processes, as well as the incident neutrino energy. The cross section measured on a $CH_{2.06}$ target has been found to steadily increase from $(0.62 \pm 0.08) \times 10^{-38}$ cm^2 at a neutrino energy of 0.5 GeV, to a value of $(10.7 \pm 2.1) \times 10^{-38}$ cm^2 at the highest measured neutrino energy of 2 GeV.

Dedication

To my wife, Jen. Despite the sacrifices we have made for science, you have always been my top priority.

Acknowledgements

My path to graduation has been a bit more circuitous than most. I have had the benefit (or misfortune?) of working on three different experiments as a graduate student: KTeV, CKM, and MiniBooNE. Throughout my time on each of these experiments, I've received support from more people than I can possibly hope to list here, so let me simply say thank you to all of my colleagues. With so many intelligent, creative, interesting, and kind people throughout the experiments on which I have worked, it is very easy to enjoy what I do.

In 2001, I began working on the KTeV experiment under the direction of Tony Barker. Tony had an intensity about the research that, I think it is safe to say, was unmatched by anyone else I have ever met. At times, this resulted in heated arguments that were often difficult to navigate. However, these interactions taught me quite a bit about thinking efficiently, maintaining academic rigor, and gaining a complete understanding of a problem before making a judgment. I firmly believe that I grew more as a physicist in those initial, somewhat turbulent years than would have otherwise been possible. When Tony passed away in the spring of 2004, I was left without an advisor, but much more importantly, I lost a good friend.

My KTeV days were spent working with the Colorado kaon group. Jason Ladue was the first person I met when I arrived at CU. As the first group member to graduate during my tenure, Jason provided the earliest exposure I had to the frenetic pace of the Ph.D. endgame. Despite his misguided love for the Chicago Bears, Jason was very

good-natured and was always willing to devote some time to help out the new guy. I had quite a bit more overlap with the other senior graduate student in our group, Pat Toale. Pat became the de facto postdoc of the group, helping the rest of us through our analyses. Discussions with Pat greatly contributed to my understanding of what it meant to study physics, and playing tackle football games with Pat greatly contributed to my understanding of physical pain. Rune Niclasen and I began graduate school the same year. I will greatly miss wandering into Rune's office to discuss the latest quantum mechanical paradox that I had spent way too much time thinking about. If you ever find yourself in a Rubik's cube competition, you may want to avoid a match-up with the fragile Dane. The last person to join the Colorado kaon group was Jim Hirschaur. Jim and I were already friends long before his return from ski-batical. Our conversations would range from intense discussions about wave-function collapse, to which album was Ween's best, to whether Joe Borowski was even qualified to close for the Kane County Cougars. Just don't tell him that you can throw a screwball.

After spending the better part of three years working on flavor physics, I transitioned to neutrinos and the MiniBooNE experiment with a new advisor, Eric Zimmerman. Eric's managerial style was about as different as I could have imagined. He had a very laissez faire approach to his graduate students, emphasizing the importance of working through an issue rather than of simply being provided with an answer. This was a perfect fit for me at this stage in my education, as it allowed me to formulate my own methodologies from scratch and take more on responsibility for, and ownership of, my analysis. Whenever I did run into problems, however, he always provided excellent advice. Eric had a unique ability to immediately ascertain the important issues at the core of any given problem. Through these conversations, I gained a much finer appreciation for the distinction between working hard and working effectively. I have learned an incredible amount from Eric, and I am grateful for having had the opportunity to work with him.

The majority of my time on MiniBooNE was spent with the Colorado neutrino group. On my first neutrino trip to Fermilab, I was introduced to MiniBooNE by our first postdoc, Terry Hart. Terry took the time to explain many of the design and analysis concepts of the experiment, as well as guiding me through the details of living at the lab. He also taught me that if you fit historical data to a particular combination of hyperbolic tangent functions, you can do an extremely good job of filling out an NCAA tournament bracket. Many thanks are in order for my fellow graduate student and office mate, Bob Nelson. A significant fraction of our time was spent proposing ideas to each other and working them out on the blackboard. They didn't always pan out, but I always enjoyed the discussions. Much has already been said about Bob's ability to find a good time in even the most unlikely situations, but I will always know him as a resourceful problem solver, an inquisitive mind, and a loyal friend. During the spring and summer I spent at Fermilab in 2005, my desk was occupied by Josh Spitz. One of our more enjoyable rituals was the daily hike to the engineering building with Jim and Rune to get a coffee from Lindsey at Celestial Seasonings. Josh liked it so much that he married her. While his fantasy football skills may be questionable, there was never any doubt that he was on his way to graduate school, and I was glad I had the opportunity to get to know him. Martin Tzanov didn't move to Boulder until the last couple of years of my time there, but we wasted no time ramping up to full blown physics debates. During our review of the Princeton analysis, countless hours were spent arguing about the details error evaluation and data unfolding. I'm fully aware of how that last sentence sounds, but it was one of the most enjoyable months that I spent on the experiment. Martin's understanding of statistical techniques and his grounding in advanced mathematics meant that he was terrific resource throughout those last few years, and he was always willing to spend as much time as required to discuss any issues I might encounter.

I'd like to thank all of my MiniBooNE collaborators for contributing so much

great work to such a well executed experiment. To my fellow graduate students, whose talent and dedication established such lofty standards of achievement, it has been a privilege to work with you, and I have very much enjoyed our time together (even the 2 mile walks through Tampa, FL at 1am). Special thanks are in order for Ryan Patterson who, after leaving the experiment for a postdoc at Caltech, spent a week of his time in Pasadena guiding me through the details of his reconstruction package, and, perhaps more importantly, for introducing me to the double double, animal style. I would also like to thank both of my analysis coordinators: Steve Brice for the oscillation analysis and Sam Zeller for cross sections. To all the young physicists out there, I strongly suggest you get yourself a Steve. I still fail to understand how someone with Steve's time constraints was able to set aside 3 hours at a moment's notice to discuss unfolding bias, or flux systematics, or multisim weights, or anything else I might be curious about that particular day. For lack of a better phrase, Sam Zeller is the anchor for all MiniBooNE cross section analysis. Her enthusiasm for the physics is unmistakable. It was always comforting to know that any new insight or result that one might produce, no matter how seemingly unimportant, wouldn't go unnoticed. I very much admire the care with which she examines each new physics result to ensure that the collaboration is always well represented.

To my parents, Joe and Sue Wilking, thank you for your steady support through the full duration of my education. From a very young age I was always encouraged to question the world around me, which is perhaps the trait that I now value most. Despite discarding my undergraduate studies and making the somewhat unconventional switch from engineering to physics, you always supported my decisions, and for that I am grateful. To my sisters, Melissa and Jenny, thanks for always making an effort to keep in touch even after I decided to move a thousand miles away. I've appreciated the phone calls and the trips to Colorado; they've always been a lot of fun.

Finally, I'd like to thank my wife, Jen, for all of her support throughout this very

long journey. The field of high energy physics demands long periods of separation that can be trying for even the most self-sufficient people. You have always been there for me during the rough and even tumultuous periods along the way, and that means more to me than you may ever know.

Contents

Chapter

Tables

Table

Figures

Figure

Chapter 1

Introduction

Neutrinos are unique among all matter particles in that they participate in only two of the four fundamental interactions. In addition to gravity, which is very weak and affects all particles, neutrinos interact only through the weak nuclear force. Since neutrino interactions are free of interfering electromagnetic and strong contributions, they are very clean probes of the structure of atomic nuclei. In addition, neutrinos are uniquely able to probe both the vector and axial-vector character of interactions with target nuclei due to the parity violating nature of the weak force.

Weak interactions can proceed via charged current (CC) or neutral current (NC) channels. In charged current interactions, a $W^{\pm}$ boson is emitted as the neutrino converts into its charged lepton partner. Neutral current interactions are facilitated by the exchange of a Z^0 boson that leaves the neutrino flavor unchanged. The specific type of charged or neutral current interaction is classified by the composition of the hadronic final state.

This introductory chapter describes the properties of charged current neutrino scattering on baryon targets. The theory of these interactions is introduced, in addition to complications that arise when these processes take place in a nuclear medium. The main topic of this document is discussed, a measurement of charged current π^+ production, as well as the experiment in which the measurement is made: MiniBooNE.

1.1 Charged Current Interactions

At neutrino energies below a few GeV, the most common neutrino interactions are those that minimally affect the interaction target. For charged current interactions with baryon targets, the baryon must, at a minimum, undergo a change in its electric charge to accommodate the exchange of the charged W boson; these are called charged current quasi-elastic interactions. If, instead of simply altering the charge of the target baryon, the $W^{\pm}$ transfers enough momentum to promote the target into a low-mass resonance state, the decay of the resonance will typically produce a nucleon and a pion. Such processes are referred to as charged current pion production.

1.1.1 Charged Current Quasi-Elastic Interactions

The simplest type of charged current interaction occurs when the neutrino interacts with a nucleon and produces the requisite charged lepton along with a single nucleon in the final state. These are referred to as charged current quasi-elastic (CCQE) interactions. Since a W^{+} is exchanged, the hadronic current must convert from a neutron to a proton as shown in Fig. 1.1.

CCQE interactions are the dominant reaction channel for neutrino energies below $\sim$1.5 GeV. Due to its clean experimental signature, and because the neutrino type is provided by the flavor of the outgoing lepton, the CCQE channel is the preferred signal mode in neutrino oscillation searches.

1.1.2 Charged Current Pion Production

When a neutrino interacts with a target nucleon, the hadronic current can be excited into a resonance state. At low neutrino energies, these resonance states are composed of isospin 1/2 (N^{*}) and 3/2 (Δ) states, which generally decay into a nucleon and a pion as shown in Fig. 1.2 [1]. In charged current interactions, the most common

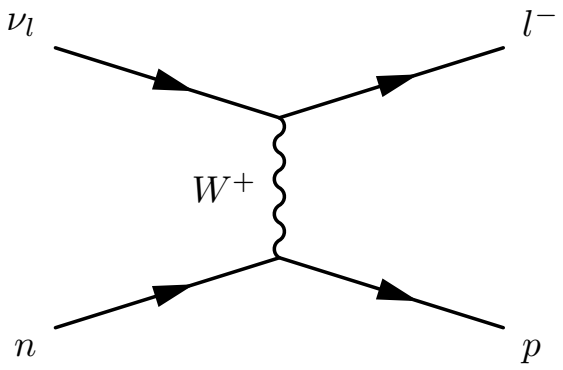

Figure 1.1: A Feynman diagram is shown for CCQE interactions. There is a lepton and a nucleon in both the initial and final states, which accounts for the (quasi) elastic character of the interaction.

of these processes produces a π^+ particle and the original target nucleon type. This channel, $\nu_\mu N \rightarrow \mu^- \pi^+ N$, is referred to as charged current π^+ production (CCπ^+).

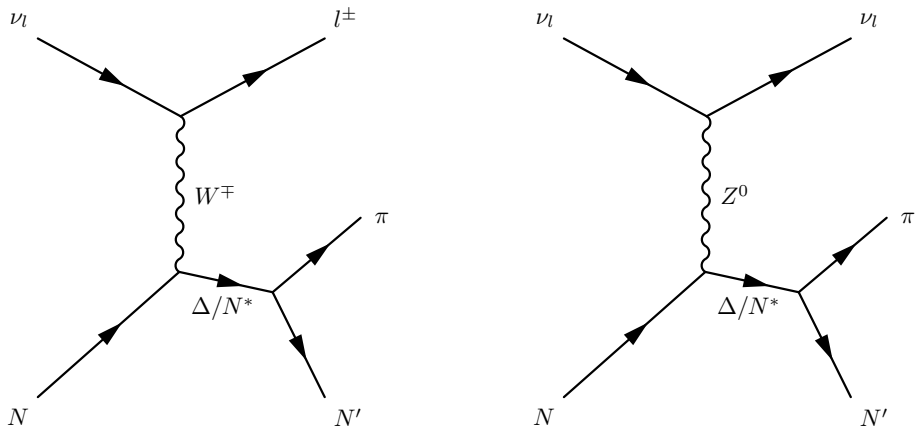

(a) Charged current resonant interaction (b) Neutral current resonant interaction

Figure 1.2: Charged current and Neutral current Feynman diagrams are shown for the resonant νN interactions considered by the Rein-Sehgal model.

1.1.2.1 Rein-Sehgal Model of ν-induced Pion Production

The Rein-Sehgal (RS) model describes all neutrino- and anti-neutrino-induced pion production processes using one uniform framework [2]. All non-strange resonances below 2 GeV are combined, including all interference terms, to produce the amplitudes of the 14 neutrino induced pion production channels. In addition, a small amount of isospin 1/2 non-resonant background is added incoherently to improve the agreement with data.

Using the weak interaction Feynman rules and leaving the hadronic current in a general form for now, the invariant amplitude is written in the following way,

$$T_{CC}(\nu N \to l N^*) = \frac{g^2 \cos\theta_C}{8} \left[\bar{u}_l \gamma^\mu \left(1-\gamma^5\right) u_\nu\right] \left(\frac{g_{\mu\nu} - \frac{q_\mu q_\nu}{M_W^2}}{q^2 - M_W^2}\right) \langle N^* \left|J^\mu\right| N\rangle \qquad (1.1)$$

$$T_{NC}(\nu N \to \nu N^*) = \frac{g^2 \cos\theta_C}{8\cos^2\theta_W} \left[\bar{u}_l \gamma^\mu \left(1-\gamma^5\right) u_\nu\right] \left(\frac{g_{\mu\nu} - \frac{q_\mu q_\nu}{M_Z^2}}{q^2 - M_Z^2}\right) \langle N^* \left|J^\mu\right| N\rangle \qquad (1.2)$$

where θ_W is the weak mixing angle, and θ_C is the Cabibbo angle. The W and Z 4-momenta are given by $q = (E_q, \mathbf{q})$, with on-shell masses of M_Z and M_W, respectively. Since the model is concerned with $\left|q^2\right| < 2$ GeV, all terms proportional to $\left|q^2\right|/M_{W,Z}$ can be neglected. By making the identifications

$$\frac{G_F}{\sqrt{2}} = \frac{g^2}{8M_W^2}, \quad G = G_F \cos\theta_C \approx G_F, \quad \frac{M_W^2}{M_Z^2 \cos^2\theta_W} \approx 1,$$

the expressions in Equations 1.1 and 1.2 can be combined in a single form,

$$T\left(\nu N \to l N^*\right) = \frac{G}{\sqrt{2}} \left[\bar{u}_l \gamma^\mu \left(1-\gamma_5\right) u_\nu\right] \langle N^* \left|J_\mu\right| N\rangle \,. \qquad (1.3)$$

The leptonic current matrix element gives the polarization of the exchanged W or Z boson in the interaction, and can be expressed in terms of its right-handed, left-

handed, and scalar components, which are defined by the following unit vectors.

$$e_L^\mu = \frac{1}{\sqrt{2}}(0, 1, -i, 0) \tag{1.4}$$

$$e_R^\mu = \frac{1}{\sqrt{2}}(0, -1, -i, 0) \tag{1.5}$$

$$e_0^\mu = (1, 0, 0, 0) \tag{1.6}$$

The leptonic matrix element is most easily evaluated in the lepton Breit frame (LBF) where the neutrino momentum is pointed along the z-axis, and is equal and opposite to the outgoing lepton momentum. Neglecting lepton masses,

$$\bar{u}_l \gamma^\mu (1 - \gamma_5) u_\nu|_{LBF} = -2\sqrt{-2q^2} e_L^\mu. \tag{1.7}$$

The hadronic current matrix element, however, is most conveniently expressed in the resonance rest frame (RRF) with the incoming nucleon traveling along the -z-axis. This can be accomplished by two Lorentz transformations. The first connects the lepton Breit frame with the nucleon Breit frame (NBF) in which the incoming nucleon and outgoing resonance momenta are equal and opposite. This transformation yields

$$\bar{u}_l \gamma^\mu (1 - \gamma_5) u_\nu|_{NBF} = -\sqrt{-2q^2}\left[(1 - \cosh\xi) e_L^\mu + (1 - \cosh\xi) e_R^\mu + 2\sinh\xi e_0^\mu\right], \tag{1.8}$$

where $\cosh\xi = (E_\nu^{lab} + E_l^{lab})/\left|\mathbf{q}^{lab}\right|$. To reach the RRF, an additional boost is needed along the z-axis to bring the resonance momentum to zero. Both e_L^μ and e_R^μ are unaffected by this transformation, while the scalar component can be transformed by replacing e_0^μ with e_s^μ, which is defined as

$$e_s^\mu = \frac{1}{\sqrt{-q^2}}\left(\left|\mathbf{q}^{RRF}\right|, 0, 0, E_q^{RRF}\right). \tag{1.9}$$

To simply the notation, define

$$u = \frac{E_\nu^{lab} + E_l^{lab} + \left|\mathbf{q}^{lab}\right|}{2E_\nu}, \quad v = \frac{E_\nu^{lab} + E_l^{lab} - \left|\mathbf{q}^{lab}\right|}{2E_\nu}, \quad Q^2 = -q^2. \tag{1.10}$$

The final expression for the leptonic matrix element in the RRS is then

$$\bar{u}_l \gamma^\mu \left(1-\gamma_5\right) u_\nu|_{RRF} = -2E_\nu^{lab}\sqrt{\frac{-2q^2}{|\mathbf{q}^{lab}|^2}}\left[ue_L^\mu - ve_R^\mu + \sqrt{2uv}e_s^\mu\right]. \tag{1.11}$$

The energy dimension of the hadronic current, J_μ, is removed by factoring out the resonance mass,

$$F_\mu = J_\mu/2M. \tag{1.12}$$

The components of the remaining portion of the current are extracted in the same basis as the leptonic current using the same polarization unit vectors.

$$F_+ = \qquad e_R^\mu F_\mu = \frac{-1}{\sqrt{2}}\left(F_x + iF_y\right) \tag{1.13}$$

$$F_- = \qquad e_L^\mu F_\mu = \frac{1}{\sqrt{2}}\left(F_x - iF_y\right) \tag{1.14}$$

$$F_0 = \sqrt{\frac{Q^2}{|\mathbf{q}^{RRF}|^2}}\; e_s^\mu F_\mu = F_t + \frac{E_q}{|\mathbf{q}^{RRF}|}F_z \tag{1.15}$$

Combining the appropriate terms of the hadronic and leptonic currents according to helicities gives

$$T\left(\nu N \to lN^*\right) = -4GME\left[\sqrt{\frac{Q^2}{|\mathbf{q}|^2}}\left\langle N^*\left|uF_- - vF_+\right|N\right\rangle + \frac{m_N}{M}\sqrt{2uv}\left\langle N^*\left|F_0\right|N\right\rangle\right] \tag{1.16}$$

The invariant amplitude can be combined with the usual phase space and flux factors to produce a cross section,

$$\frac{\partial\sigma}{\partial Q^2 \partial E_q} = \frac{1}{64\pi m_N E_\nu^2}\sum_{spins}\left|T\left(\nu N \to lN^*\right)\right|^2 \frac{1}{2\pi}\cdot\frac{\Gamma}{(W-M)^2+\Gamma^2/4}. \tag{1.17}$$

The last factor in Equation 1.17 is the Breit-Wigner function for a resonance of mass M, width Γ, and observed mass W.

To properly determine each cross section, all resonances that contribute to the interaction process must be included in the calculation. The relevant resonances for each process are determined by isospin conservation. CCπ^+ events occur with two different final states, (μ^-, π^+,neutron) and (μ^-, π^+,proton), depending on the target nucleon

with which the neutrino interacts. The Clebsch-Gordan coefficients for each final state, $|I, I_3\rangle$, give

$$\left|\pi^+ p\right\rangle = |1,1\rangle \otimes \left|\frac{1}{2},\frac{1}{2}\right\rangle \quad = \quad \left|\frac{3}{2},\frac{3}{2}\right\rangle \tag{1.18}$$

$$\left|\pi^+ n\right\rangle = |1,1\rangle \otimes \left|\frac{1}{2},-\frac{1}{2}\right\rangle = \sqrt{\frac{1}{3}}\left|\frac{3}{2},\frac{1}{2}\right\rangle + \sqrt{\frac{2}{3}}\left|\frac{1}{2},\frac{1}{2}\right\rangle \tag{1.19}$$

Isospin 3/2 states are referred to as Δ resonances, whereas isospin 1/2 states, having the same isospin as protons and neutrons, are simply referred to as N resonances.

The final ingredient needed to determine the cross sections are the helicity amplitudes from Equation 1.16,

$$f_\pm = \langle N, j_z \pm 1 \ |F_\pm|\, N^*, j_z\rangle \tag{1.20}$$

$$f_0 = \quad \langle N, j_z \ |F_0|\, N^*, j_z\rangle \tag{1.21}$$

These are provided by the Feynman-Kislinger-Ravndal (FKR) relativistic quark model of hadronic states [3]. The FKR model represents hadrons as relativistic harmonic oscillators of their component quarks. For baryons, the Hamiltonian is given by

$$\mathcal{H} = 3\left(p_a^2 + p_b^2 + p_c^2\right) + \frac{\Omega^2}{36}\left((u_a - u_b)^2 + (u_b - u_c)^2 + (u_c - u_a)^2\right) + C, \tag{1.22}$$

where p_a and u_a are the 4-momentum and 4-position of quark a. Using only 3 adjustable constants (the spacing of energy levels per unit angular momentum, Ω, the pseudoscalar-meson coupling to hadrons, and a scaling factor as a function of energy) and the particle masses, 75 different transition amplitudes have been calculated.

The FKR model has been extended by Ravndal to calculate production cross sections for all nuclear resonances below 1.75 GeV [4]. This formulation makes use of separate vector and axial vector form factors, each with its own free mass parameter, m_V and m_A, respectively.

$$G^V(Q^2) = \left(1 + \frac{Q^2}{4m_N^2}\right)^{1/2-n}\left(\frac{1}{1 + Q^2/m_V^2}\right)^2 \tag{1.23}$$

$$G^A(Q^2) = \left(1 + \frac{Q^2}{4m_N^2}\right)^{1/2-n}\left(\frac{1}{1 + Q^2/m_A^2}\right)^2 \tag{1.24}$$

where n is the number of oscillator quanta present in the final resonance. The vector mass, m_V, is well measured in electron scattering experiments to be 0.84 GeV, under the conserved vector current hypothesis [5]. The only remaining uncertain quantity in the determination of the CCπ^+ cross section is the axial mass, m_A, which can only be measured in neutrino interactions.

1.1.2.2 Corrections to the Rein-Sehgal Model

The RS model, in its original form, is insufficient to fully describe the kinematics of CCπ^+ interactions. There exist experimental data that significantly disagree with the model, especially at low Q^2 [6]. The data show a significant deficit of events with forward going muons relative to the prediction. Several modifications have been proposed in an attempt to explain this discrepancy [7].

In the calculation presented in the previous section, the muon mass has been neglected. Several methods for reinstating the muon mass have been proposed [8, 9, 10, 11]. The size of the correction varies depending on the method, but each method has the effect of reducing the low Q^2 prediction [7].

Alternatives to the vector and axial vector form factors used in the RS model have also been suggested. As a common example, several of these new models employ the Rarita-Schwinger formalism, in which a spin-3/2 field is introduced to describe the Δ^{++} resonance [12, 13, 14]. Instead of incorporating the results of the FKR model, the vector and axial vector components of the Δ transition amplitude are written more generally in terms of several form factors, $C_i^{V,A}$,

$$\left\langle \Delta^{++}(p') \left| J^V_\mu \right| N(p) \right\rangle = \sqrt{3}\Psi_\lambda(p') \left[g^\lambda_\mu T_\nu q^\nu - q^\lambda T_\mu + g^\lambda_\mu C^V_6 \right] \gamma_5 u(p) \times \frac{1}{(2\pi)^3} \sqrt{\frac{M m_N}{E_p E_{p'}}} \tag{1.25}$$

$$\left\langle \Delta^{++}(p') \left| J^A_\mu \right| N(p) \right\rangle = \sqrt{3}\Psi_\lambda(p') \left[g^\lambda_\mu B_\nu q^\nu - q^\lambda B_\mu + g^\lambda_\mu C^A_5 + \frac{q^\lambda q_\mu}{M^2} C^A_6 \right] \gamma_5 u(p) \times \frac{1}{(2\pi)^3} \sqrt{\frac{M m_N}{E_p E_{p'}}} \tag{1.26}$$

where Ψ_A is the Rarita-Schwinger field, and

$$T_\mu = \frac{C^V_3}{m_N}\gamma_\mu + \frac{C^V_4}{m^2_N} p'_\mu + \frac{C^V_5}{m^2_N} p_\mu, \tag{1.27}$$

$$B_\mu = \frac{C^A_3}{m_N}\gamma_\mu + \frac{C^A_4}{m^2_N} p'_\mu. \tag{1.28}$$

1.1.2.3 Coherent CCπ^+ Interactions

In addition to the resonant interactions just described, neutrinos can interact with the entire target nucleus coherently. These coherent processes can occur in both neutral current interactions, $\nu + A \rightarrow \nu + \pi^0 + A$, and charged current interactions, $\nu + A \rightarrow l^- \pi^+ A$. In either case, the target nucleus is unchanged.

Despite the relative simplicity of the final states they produce, coherent interactions are not well understood when compared to the analogous resonant processes. Several models exist that describe coherent pion production [15, 16, 17], but the absolute cross sections predicted by these models can vary by an order of magnitude. In addition, both the K2K and SciBooNE experiments have measured an absence of coherent CCπ^+ events, well below predicted levels [18, 19], while similar deficits are not observed in neutral current coherent π^0 production [20].

1.2 Nuclear Effects

Neutrino scattering experiments are often conducted in nuclear media. The properties of the free nucleon interactions considered by the RS model are modified by sev-

eral multi-nucleon effects, such as nuclear binding, particle motion, and the screening of internal nucleons by particles on the surface of the nucleus. In addition, once an interaction takes place, the final state particles must traverse the nuclear medium before they can be detected, which can alter the meaning of a measured cross section.

Most neutrino interaction simulations model the dynamics of the protons and neutrons in the nucleus as a relativistic Fermi gas. The nucleons are treated with a uniform momentum density below the cutoff Fermi momentum, p_F. This indeterminate contribution to the target momentum produces an irreducible reduction in the precision with which the kinematics of the event can be determined. Further, since all energy levels in the Fermi gas are filled, only interactions in which the outgoing nucleon has a momentum higher than p_F are allowed. Forbidden interactions below this threshold are said to be Pauli blocked. Finally, as the target nucleons are in a bound state, some energy is consumed in liberating the interacting nucleon. Both Pauli blocking and nuclear binding have the effect of reducing the number of interactions at low Q^2.

When neutrino interactions take place in the nucleus, the particles that are produced can interact with the nuclear medium, thus modifying the observed characteristics of the interaction. Pions are particularly susceptible to the effects of the nuclear medium, since they interact via the strong nuclear force. Charged pions can either be absorbed or converted into neutral pions via $n\pi^+ \rightarrow p\pi^0$. The nuclear medium can also influence whether a pion is even created. When a nucleon is excited into a $\Delta(1232)$ resonance, the Δ travels on the order of 1 fm before it decays, which is a significant fraction of the size of the nucleus. The Δ can then interact via $\Delta N \rightarrow NN$, which reduces the number of observed pions. The sizes of these effects are discussed in Section 4.2.2.

Finally, the validity of the Rein-Sehgal model predictions for interactions with bound nucleons is unclear. The FKR predictions for transitions to higher resonances are not obviously valid for protons and neutrons bound in a nucleus, which can be significantly off-shell. Additionally, the modification to the masses and widths of the

resonances due to the nuclear medium are not accounted for in the model.

1.3 The CCπ^+ Measurement

In addition to furthering the theoretical understanding of neutrino-nuclear interactions, there exist more pragmatic reasons for measuring the CCπ^+ cross section. Two of the largest next generation neutrino experiments, T2K and NOνA, will search for neutrino oscillations at peak energies of ~ 0.7 GeV and ~ 2 GeV, respectively [21, 22]. The oscillation parameters are measured via CCQE interactions and, at these energies, the largest charged current neutrino background is from CCπ^+ events. In addition, the T2K and NOνA detectors employ nuclear targets, whereas most previous cross section measurements were on hydrogen and deuterium targets, and therefore do not probe the nuclear effects described in section 1.2.

Any measurement of the CCπ^+ cross section on a nuclear target will contain contributions from many weakly constrained physical effects. Several different models attempt to describe the nucleon form factors of these interactions, and none of them are particularly well constrained. Off shell effects of the nuclear medium have not been accounted for, there are large uncertainties in the final state interactions that occur in the nucleus, and finally, as recently described by one group of theorists, "There is a general consensus among the theorists that a simple Fermi Gas (FG) model, widely used in the analysis of neutrino oscillation experiments, fails to provide a satisfactory description of the measured cross sections, and inclusion of further nuclear effects is needed." [23].

There is a clear demand for more data to provide a means by which the current theoretical picture can be improved. The current levels of theoretical uncertainty suggest that a model-independent accounting of the observed, post-nucleus cross section would be the most fruitful result to report, rather than a measurement of the parameters of a small subset of available models. The results presented in subsequent chapters are

guided by this philosophy.

1.4 MiniBooNE

MiniBooNE (Mini Booster Neutrino Experiment; E898) is a neutrino oscillation experiment located at the Fermi National Accelerator Laboratory in Batavia, Illinois. Neutrinos produced by the Booster neutrino beam travel half a kilometer before reaching the 807 ton MiniBooNE detector. The Cherenkov and scintillation light from the particles produced in a neutrino interaction is used to reconstruct the kinematics of each event.

Although originally designed to search for the appearance of ν_e in a high purity ν_μ beam, MiniBooNE is well suited to measure neutrino cross sections. The experiment has collected the world's largest sample of accelerator-based ν_μ events below 2 GeV, with very little contamination from ν_e and $\bar{\nu}$ interactions. MiniBooNE has a unique opportunity to provide high statistics measurements of weakly constrained neutrino cross sections on a nuclear target, and at neutrino energies that are directly applicable to the next generation of accelerator based neutrino oscillation experiments. The remainder of this document describes a measurement of the largest charged current background to these oscillation searches: CCπ^+interactions.

Chapter 2

The Booster Neutrino Beam

The purpose of the Booster neutrino beam (BNB) is to produce a high purity ν_μ beam with very little intrinsic ν_e contamination as required by the oscillation analysis. The main source of ν_μ's are charged pions, which decay via $\pi^+ \to \mu^+\nu_\mu$ 99.9870(4)% of the time [1]. To maximize the π^+ flux, the Booster proton beam is focused onto a very long, thin beryllium target to ensure a high beam reaction rate, while minimizing the absorption of the resulting large-angle pions. The target is placed inside of a magnetic horn that produces a toroidal field to reduce the transverse component of the π^+ particles and create a forward-focused neutrino beam. A cartoon of the entire process is shown in Figure 2.1.

2.1 Booster Proton Beam

The Booster is the third in a series of five accelerator stages at Fermilab. Protons emerging from the Linear Accelerator with a kinetic energy of 400 MeV are accelerated to 8 GeV after $\sim 20,000$ laps around the 472 m accelerator ring. The beam is then sent along the Main Injector 8 GeV beam line before being diverted toward the MI-12 enclosure (as shown in Fig. 2.2), which houses the MiniBooNE target and horn assembly.

Beam spills to MiniBooNE delivered $\sim 4 \times 10^{12}$ protons at 3-5 Hz. Each spill was composed of 84 buckets arriving at a rate of 53 MHz, which corresponded to a total spill duration of 1.6 μs. The weekly accumulation of protons on target (POT) over

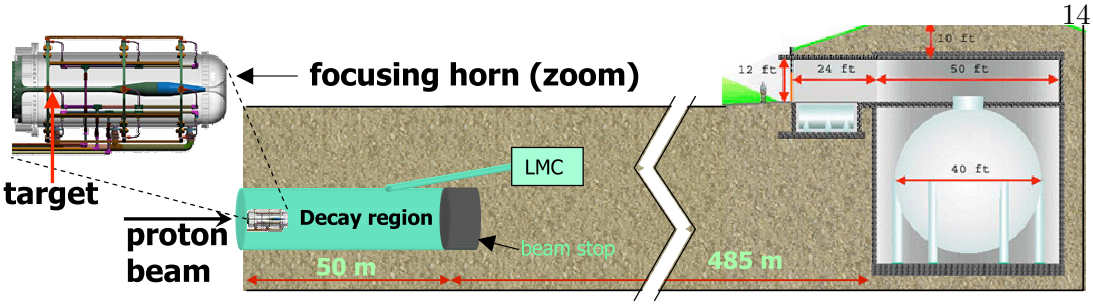

Figure 2.1: A cartoon of the neutrino flux production is shown. Protons from the Booster interact in the target, which is located inside the horn. The secondary particles created in the interactions are focused by the horn and decay within the decay region. The resulting neutrinos then travel through half a kilometer of earth before reaching the MiniBooNE Detector.

the duration of the run is shown in Fig. 2.3. The POT was measured by two toroids placed 5 and 50 m upstream of the target, and provided a measurement uncertainty of $\sim 1\%$ [24]. The results in this thesis are based on the entire MiniBooNE neutrino dataset of 6.461×10^{20} POT.

The 8 GeV Booster proton beam was directed toward the center of the MiniBooNE target. Just upstream of the target, the root mean square (RMS) beam size was 1.51 mm horizontally and 0.75 mm vertically. The beam was focused such that the horizontal and vertical angular distributions (RMS values of 0.66 mrad and 0.40 mrad, respectively) were highly anti-correlated with the corresponding position distributions, which produced a beam waist at the center of the target.

2.2 Target and Horn

The target was composed of 7 cylindrical beryllium slugs, each 4 inches long and 3/8 inches in diameter. The target was attached to a cylindrical beryllium sleeve by 21 thin beryllium fins spaced at regular intervals around the target. The beam deposited a significant amount of heat, which was removed using a stream of forced air.

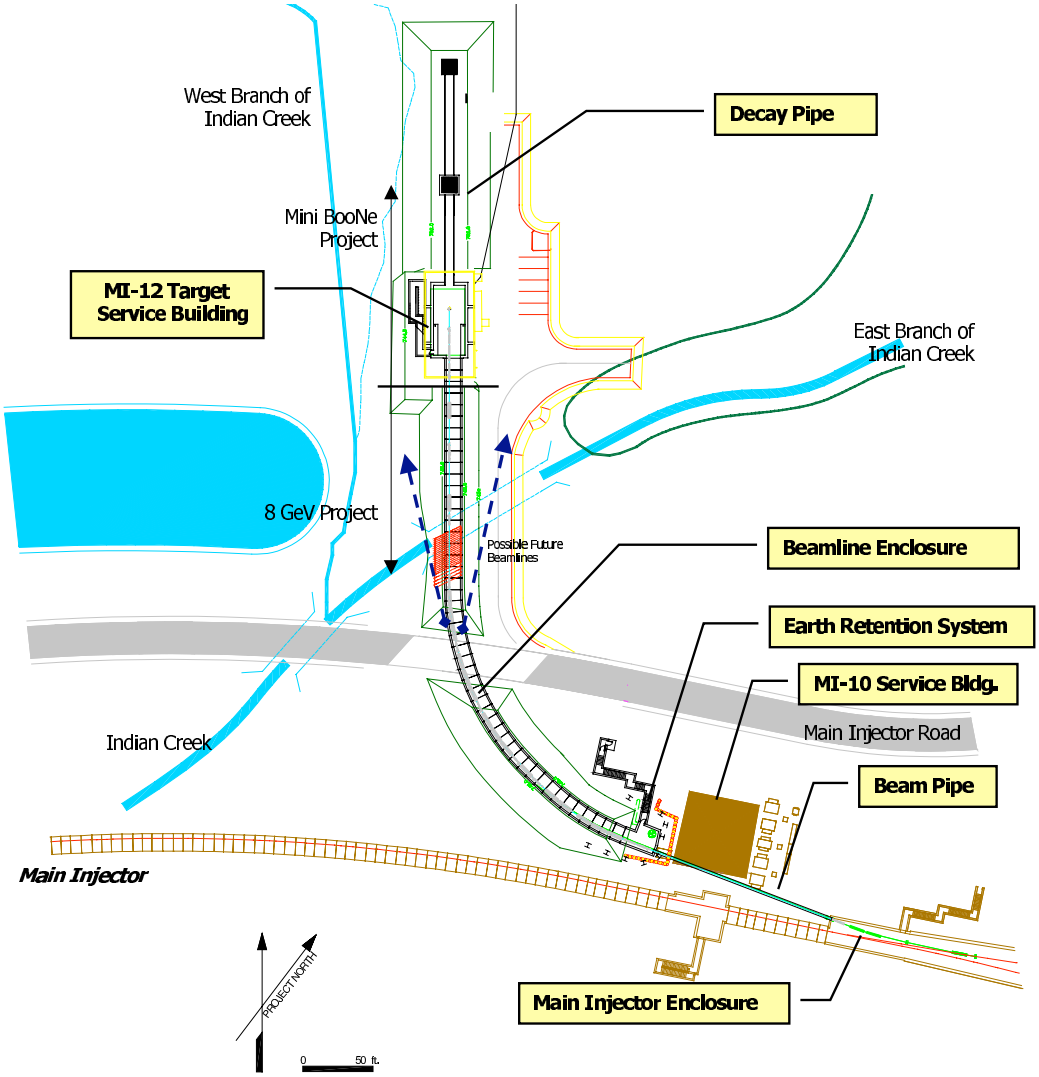

Figure 2.2: The layout of the Booster Neutrino Beam [25] is shown. The extraction point from the Main Injector 8 GeV transfer line is shown in the bottom right. The beam then passes to the MI-12 service building, which houses the target and horn. The secondary beam created in MI-12 passes through the 50 m decay pipe before reaching the steel beam stop.

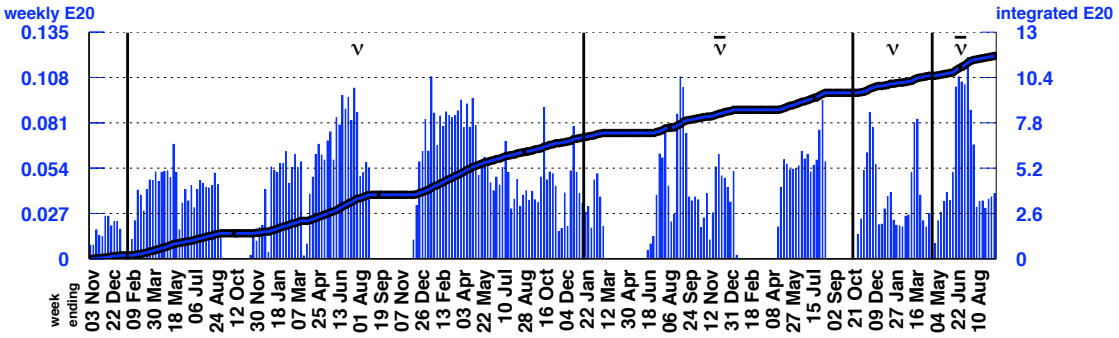

Figure 2.3: The weekly and integrated protons on target delivered to MiniBooNE are given from November 2002 through August 2008. The periods of neutrino (ν) and anti-neutrino ($\bar{\nu}$) horn configurations have been separated for clarity. Only the neutrino configuration is used for the present analysis.

The target was positioned in the center of the two coaxial aluminum cylinders that constituted the horn. The horn was 185.4 cm in length with a diameter of 60 cm. The inner conductor radius varied between 2.2 cm and 6.54 cm. An electric current was run along the outer conductor toward the interface with the inner conductor at the downstream end of the horn. The current then traveled back up the inner conductor, producing an azimuthal magnetic field between the conductors and a negligible field elsewhere. The azimuthal symmetry of the horn produced an easily understood magnetic field given by Ampere's Law,

$$B = \frac{\mu_0 I}{2\pi r}, \tag{2.1}$$

where I is the current and r is the distance from the horn axis. The current was sinusoidally ramped to a peak current of 174 kA and lowered back to zero over a period of 143 μs. The peak of the current pulse was timed to correspond with the arrival of each beam spill.

Several nozzles were inset along the outer conductor to spray cooling water into the horn. The nozzles were designed to direct most of the water toward the outer surface of the inner conductor. A schematic drawing of the horn and water cooling system is

shown in figure 2.4.

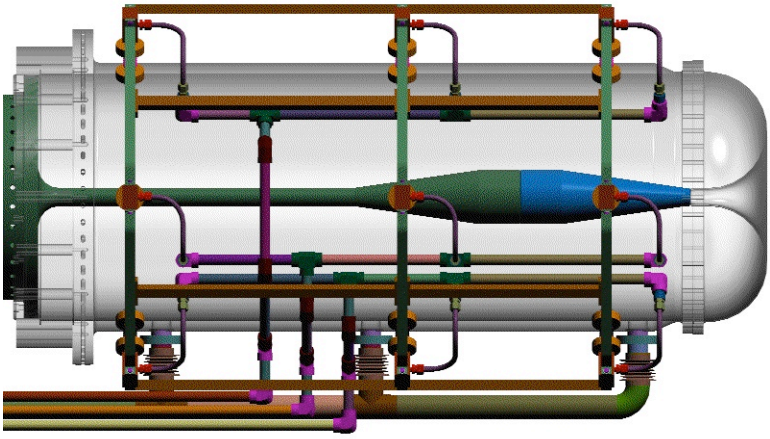

Figure 2.4: An elevation view of the horn and water cooling system [26]. The outer conductor is transparent to show the inner horn structure.

The target and horn were placed inside a small cavity, which was separated from the accessible portion of the target hall by nearly 2000 tons of concrete. Just downstream of the horn was a steel collimator that shaped the secondary beam before it entered the meson decay region. The collimator began 259 cm downstream of the target and extended for 214 cm; the upstream radius was 30 cm and expanded linearly to 35.5 cm.

2.3 Meson Decay Region

Mesons that passed through the collimator entered the 50 m decay pipe. The pipe was 6 ft in diameter and surrounded by dolomite pebbles. The remaining neutrinos not created upstream of the collimator were produced by decays of mesons and muons inside the air volume contained in the pipe.

The content of the neutrino beam produced by BNB could be discretely varied by changing the direction of the horn current. In "$\nu-$mode" running, the current (in the positive sense) traveled from the outer conductor to the inner conductor, which produced a counter-clockwise pointing magnetic field along the direction of the beam.

This caused positively charged particles with momentum components transverse to the beam direction to deflect forward toward the detector, while negatively charged particles were bent radially outward and removed from the secondary beam. By reversing the current direction, the horn could also be run in "$\bar{\nu}-$mode", which focused negatively charged particles to produce a $\bar{\nu}$ beam via $\pi^- \rightarrow \mu^- \bar{\nu}_\mu$ decay.

At the end of the pipe was a beam stop composed of 10 ft of steel and 3 ft of concrete. The beam stop terminated the portion of the decay pipe in which particles could decay in flight, however a significant number of neutrinos were produced from particle decays at rest. All decay-at-rest neutrino energies are too low to contribute to CCπ^+ production. In the center of the pipe, about 25 m downstream of the target, a duplicate beam stop was suspended above the decay region and could be lowered to shorten the effective length of the pipe. The 25 m absorber was not implemented for the data used in this analysis.

2.4 Neutrino Flux

The properties of the neutrino flux produced by the Booster Neutrino Beam (BNB) must be known in order to extract useful information from the data. The center of the MiniBooNE detector is located 541 meters downstream of the center of the target and only 1.896 meters above the center of the neutrino beam. Neutrinos that intersect the detector, therefore, are almost uniformly traveling in the same direction. This means that the flux can be characterized almost completely by the neutrino energy distributions for each neutrino type.

The neutrino energy spectrum is not measured at the point of production. As such, MiniBooNE relies on a detailed simulation of the aforementioned components of the BNB to predict the properties of the flux. The results of this simulation are described in Section 4.1.

Chapter 3

The MiniBooNE Detector

The MiniBooNE detector is a 610.6 cm radius, spherical tank filled with 818 tons of mineral oil. Inside the tank is an additional 574.6 cm radius concentric sphere that divides the volume into an inner "main" region and an outer "veto" region. The design of the detector was driven by the $\nu_\mu \rightarrow \nu_e$ oscillation search, which required that ν_μ and ν_e events be distinguishable with sufficiently well determined energies. In a charged current interaction, the species and energy of a neutrino are derived from the kinematics of the outgoing charged lepton (described in Section 5.3.2.1). As charged particles propagate through the oil, a large amount of Cherenkov radiation is produced along with some additional scintillation light. An array of 1280 photomultiplier tubes is mounted on the inside surface of the inner volume region to detect the generated light. The properties of each charged particle can then be deduced from the distribution of light in the event, and, in particular, from the rings produced by the cone shaped emission of Cherenkov light. The inner surface of the main tank volume is painted black to reduce reflections that can degrade the performance of event reconstruction algorithms.

The outer veto region of the tank is a spherical shell with a 35 cm thickness that surrounds the inner fiducial volume. The purpose of the veto is to detect particles entering or exiting the tank. The neutrino interactions of interest occur inside the main tank volume, and do not produce particles that exit the tank. Conversely, background events from cosmic rays and neutrino interactions just outside the tank can be rejected

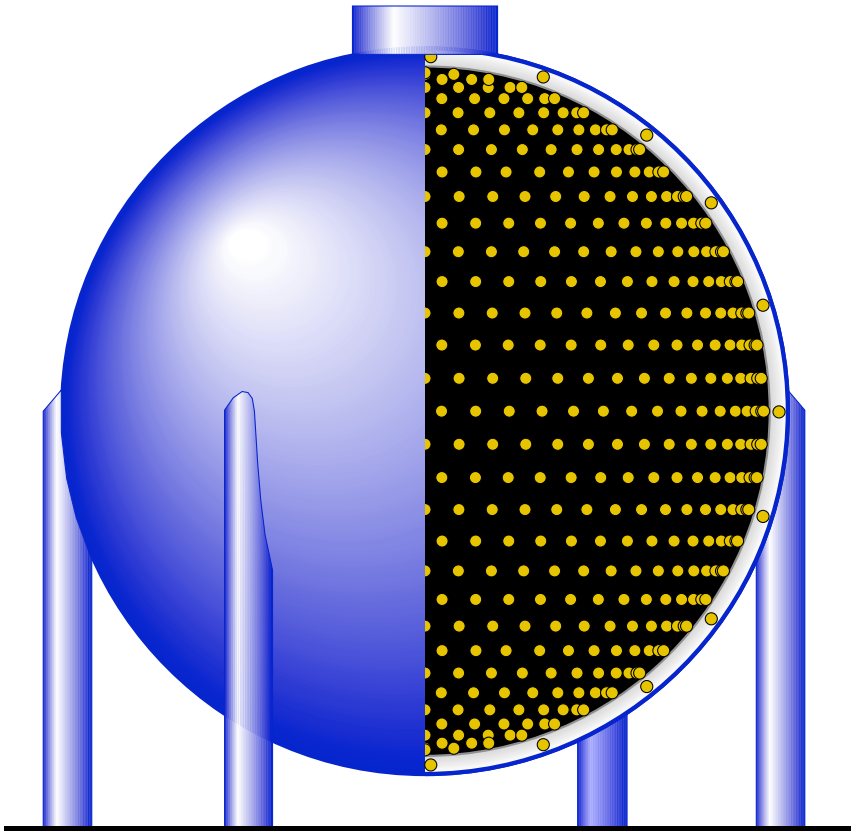

Figure 3.1: A schematic of the MiniBooNE detector. Half of the front face has been removed to reveal the internal structure. The tank photomultiplier tubes are shown along the inside surface of the main fiducial region. The white outer shell houses the veto tubes [27].

based on the presence of light in the outer veto region. The veto is instrumented with 240 photomultiplier tubes, and the walls are painted white to maximize the chances of photon detection.

The tank is located in a 1.5 foot thick, concrete cylindrical vault. The vault is 43 feet high with a 45 foot diameter, the bulk of which lies below ground level. Directly above the vault is the MiniBooNE surface building, which houses most of the detector electronics. The surface building is covered with an earth overburden rising to a maximum of 24 feet above the ground that provides a minimum of 3 m earth

equivalent that reduces the rate of cosmic rays entering the detector.

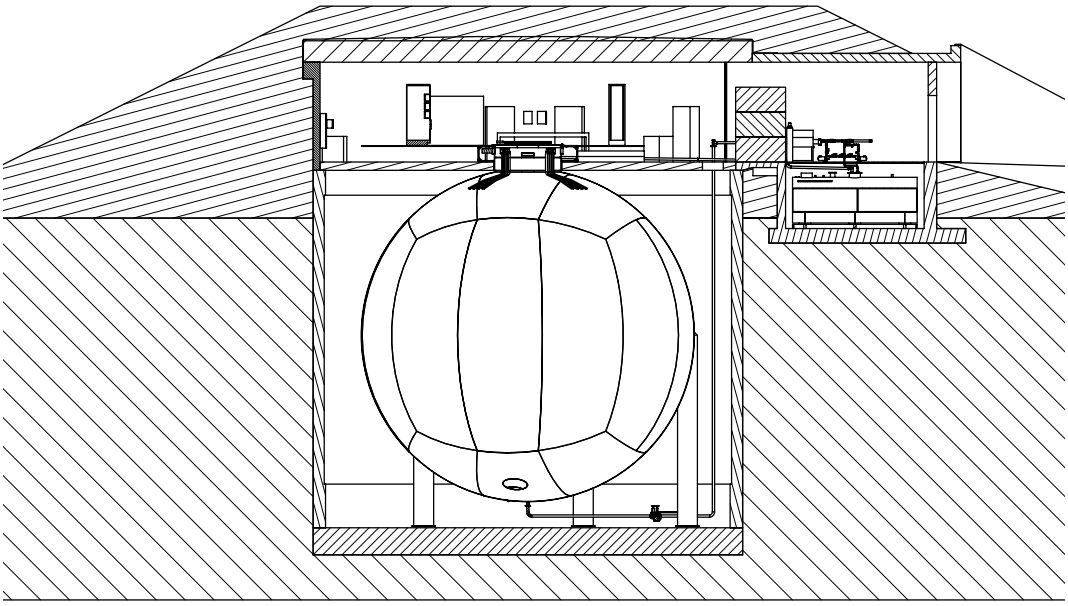

Figure 3.2: An illustration of the vault and surface building that house the MiniBooNE detector. The earth overburden is shown covering the enclosure [27].

3.1 Mineral Oil

The oil used in MiniBooNE was Exxon/Mobile Marcol 7 Light Mineral Oil. It was chosen among 10 oils tested based on its superior optical properties. Since the faces of the photo-tubes are ∼550 cm from the center of the tank, photons often must travel a substantial distance before they are detected. An extinction length > 20 m for 420 nm light was required to ensure that no more than 25% of the light would be lost in a neutrino interaction at the center of the tank [28]. Other desirable properties of the oil, such as a high refraction index, low dispersion, and low levels of scintillation light, also contributed to the selection process.

Despite providing fewer nuclear targets due to its somewhat lower density of 0.845(1) g/cm^3, mineral oil provides several advantages over water. Light travels slower in mineral oil, which results in more Cherenkov light and improved particle recon-

struction. In addition, a lower energy Cherenkov threshold extends the reach of the MiniBooNE detector to lower neutrino energies. One of the most important event identification tools in MiniBooNE is the presence of delayed light from stopped particle decays (see Section 6.3), and mineral oil has a muon capture rate of only 8% compared to 20% in water [28]. Further details on the optical properties of the oil can be found in the detector simulation discussion in Section 4.4.

3.2 Photomultiplier Tubes

The MiniBooNE detector was instrumented with 1,520 eight inch diameter photomultiplier tubes (PMTs). Of these, 1,198 were Hamamatsu R1480 PMTs reused from the LSND experiment, and 322 Hamamatsu R5912 tubes ordered specifically for MiniBooNE. Because of their superior detection capabilities, the "new" (R5912) PMTs were all deployed inside the main tank to be used in event reconstruction. From the 1,198 "old" (R1480) PMTs, the 240 with the lowest measured dark rates were selected for the veto region to minimize the number of false vetoes. The remaining 958 old tubes were randomly distributed in the main tank volume. Figure 3.3 shows a map of old and new photo-tube placement throughout the tank.

The PMTs were distributed over the inside surface of the tank as uniformly as practical. For logistical purposes, the PMTs were separated into evenly-spaced horizontal rows. The reduction in the circumference of each latitudinal slice from equator to pole makes a full staggering of adjacent PMT rows impossible, however each row was clocked by half a PMT spacing relative to the PMT start point of the previous row. The final tube positions were surveyed by the Fermilab Alignment Group. The veto PMTs were mounted back-to-back, facing perpendicular to the center of the tank to view as much of the veto shell as possible. A schematic of the main and veto tube mounting is shown in Figure 3.4.

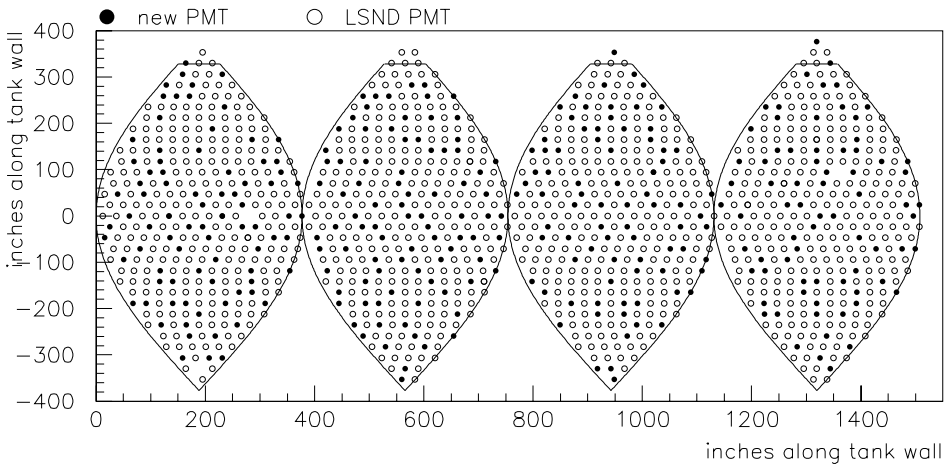

Figure 3.3: The distribution of "old" Hamamatsu R1480 (clear) and "new" Hamamatsu R5912 (solid) photomultiplier tubes over the inside surface of the tank is shown.

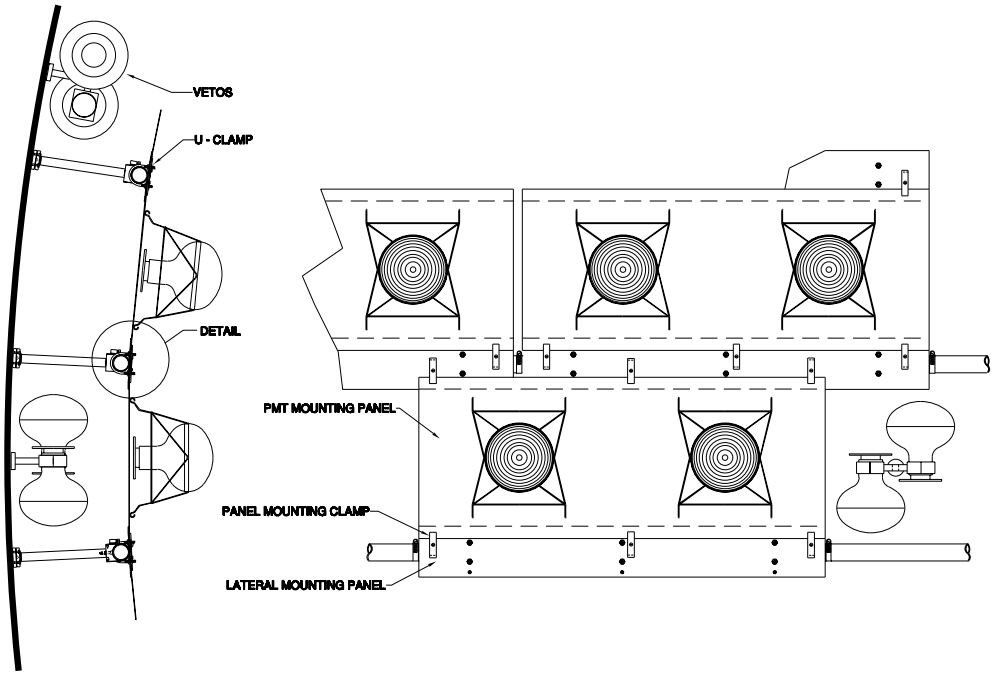

Figure 3.4: The PMT configurations for both the main tank and veto region are shown. The tank PMTs face the center of the fiducial volume, while the veto PMTs are arranged to view the directions perpendicular to the tank wall.

3.3 Electronics

The measurable quantities recorded by the PMTs are the number of photo-electrons that hit the tube, given by the measured charge, and the time of the hit. The determination of these values is illustrated in Figure 3.5. Charge and time information is recorded at intervals determined by the 10 MHz clock. When a tube is hit, the resulting pulse, V_{pmt}, is integrated and convolved with a slowly decaying exponential with a time constant of $\sim$1.2 μs. This integrated charge signal, V_q, is sampled at four consecutive clock times, beginning with the time immediately preceding the hit. Using the empirically measured shapes of the integrated charge bleed-off curves, the charged deposited by the hit can be extracted. If the initial pulse, V_{pmt}, crosses a threshold of roughly 0.25 photo-electrons, the asynchronous discriminator is fired, which triggers a voltage ramp, V_t, at the time of the crossing. The ramp voltage is sampled at the same 4 clock ticks during which V_q is recorded to determine the initial hit time.

3.4 Calibration Systems

Cosmic muons, which enter the tank at a rate of 10 kHz, are used to understand the detector energy reconstruction. A muon hodoscope composed of four planes of Bicron BC-408 plastic scintillator is positioned directly above the detector to measure the transverse position of entering muon tracks at two vertical locations separated by one meter. Inside the detector are six 5 cm scintillator cubes deployed at various depths ranging from 30 to 400 cm (the deepest cube is 7.6 cm on a side). Muons that are detected by the tracker and stop in a cube have a well defined initial energy given by the muon range in mineral oil. With these data, a variety of detector properties can be studied such as the time offsets, gains, and time slewing of the PMTs, as well as the light attenuation properties of the oil. The direction and energy also allow for tests of higher level reconstructed quantities. Figure 3.6 shows a comparison between the muon

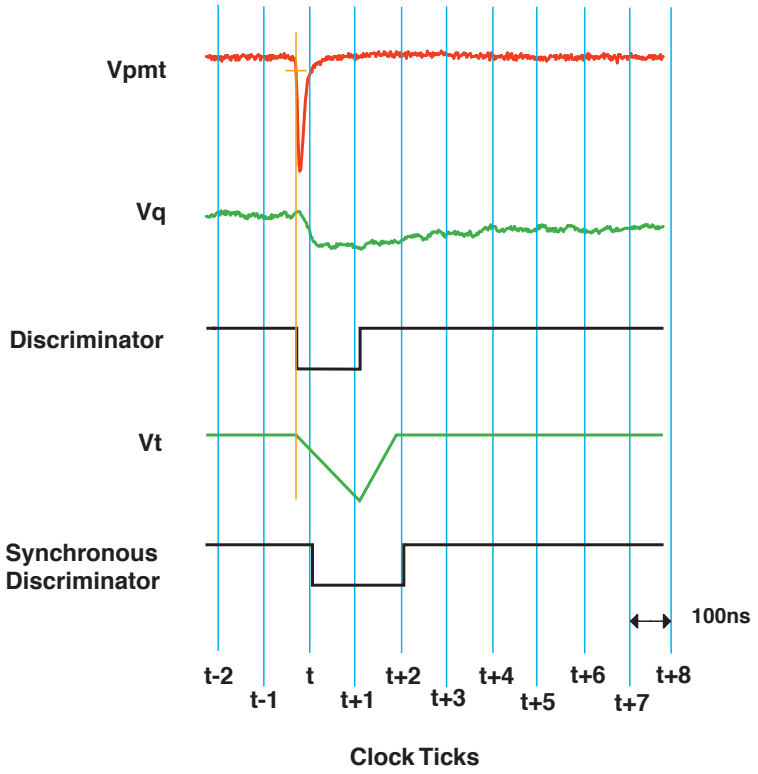

Figure 3.5: A cartoon of the PMT electronic is shown. A PMT hit triggers the asynchronous discriminator, which triggers a voltage ramp, V_t. The integrated charge, V_q, and V_t are recorded at the 4 times labeled (t-1) through (t+2) from which the charge and time is deduced.

range energy and the measured tank energy.

To produce controlled bursts of light of known intensity and wavelength, four calibration laser sources are deployed throughout the tank. Each source is a 10 cm glass bulb filled with LUDOX to disperse the light isotropically. Under normal running conditions, a laser flask at the center of the tank produces 100 ps pulses of 397 nm light at a rate of 3.33 Hz. The laser data are used to calibrate the PMT gains, as well as tube-to-tube time measurement discrepancies.

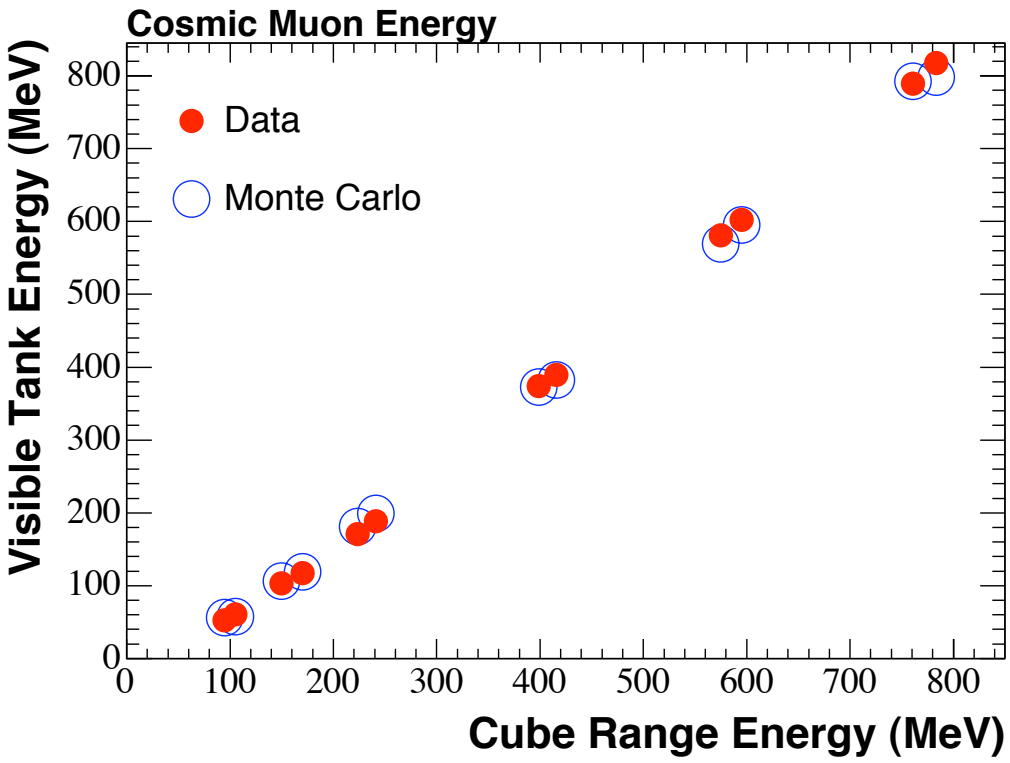

Figure 3.6: The energy determined by the muon range in the tracker/cube system is compared with the visible energy in the tank. The data show the expected linear correlation and agree well with the Monte Carlo simulation.

3.5 Data Acquisition

The data collection triggers are based on PMT hit multiplicity information, as well as external signals from the accelerator and calibration systems. The primitive PMT signals formed by the trigger logic indicate tank activity exceeding 10, 24, 60, 100, and 200 hits, as well as the presence of at least 4 or 6 veto PMT hits. The presence of beam is determined from the accelerator clock signals.

The main physics trigger for the experiment was satisfied whenever beam was present, regardless of the activity in the tank. The data stream was initialized 5 μs prior to the arrival of the beam spill and remained active for a total of 19.2 μs. The presence of beam prohibited the firing of any of the other triggers.

Additional triggers were defined to perform a variety of other functions. Calibration triggers for the laser and cube data were used for the aforementioned detector studies. A random trigger was implemented to collect beam off data to provide a sample of cosmic activity that could be overlayed on simulated events to better reproduce the features of the data. Events were also recorded during beam spills to the adjacent NuMI beam line. Other triggers based on PMT multiplicities were implemented to collect samples of events with ≥ 60 tank and ≥ 6 veto hits for detector monitoring, cosmic muon decays (i.e. "Michel" events; ≤ 200 tank hits and ≤ 6 veto hits), and to search for cosmic and supernova neutrinos. A list of MiniBooNE triggers with average rates is given in Table 3.1.

Table 3.1: The optical parameters of the beam are listed just upstream of the target.

Trigger	Rate (Hz)	Prescale	Time Window (μs)
Booster Beam	2-5	1	19.2
NuMI Beam	0.5	1	19.2
random	2	1	19.2
cosmic μ	0.66	1	19.2
Michel	1.2	600	19.2
supernova	9.9	1	3.2
tank	0.4	90000	19.2
veto	0.4	5000	19.2
laser	3.33	1	9.6
cube	1.1	1	12.8
tracker	0.7	170	12.8
total	$\sim$26		

Chapter 4

Event Simulation

To produce a cross section measurement, the entire data production process must be simulated, including the booster proton beam, the properties of the neutrino flux, neutrino interaction processes, and the propagation of final state particles through the detector. To accomplish this, several different software packages are run in succession. In this chapter, each element of the simulation chain is described along with any associated systematic uncertainties.

4.1 Neutrino Flux Simulation

Protons that interact inelastically produce a variety of secondary particles. At the proton energy produced by the Booster, 8 GeV, the dominant particle species produced in the target is π^+, which is primarily responsible for the < 2 GeV neutrino flux. The goal of the flux simulation is to predict the number of neutrinos that hit the detector per proton on target, and to determine the neutrino energy spectrum.

4.1.1 Beam Monte Carlo

The majority of the flux prediction is produced in the GEANT4-based [29] beam Monte Carlo simulation. Beam protons are generated 4.5 cm upstream of the front face of the target with an initial position and direction randomly selected according to the beam parameters given in Table 4.1. The protons then interact with the target to

produce a variety of secondary particles. Many of these particles enter the horn where their trajectories are modified by the magnetic field. Any neutrino produced in the decay of a secondary particle is recorded in the beam Monte Carlo output steam.

Table 4.1: The beam optics parameters are listed just upstream of the target.

mean x	0
mean y	0
σ_x	1.51 mm
σ_y	0.75 mm
mean θ_x	0
mean θ_y	0
σ_{θ_x}	0.66 mr
σ_{θ_y}	0.40 mr

4.1.1.1 Geometry

The full geometry of the Booster neutrino beam, described in Chapter 2, is modeled in the simulation. The most critical elements of the geometry are the target and the inner conductor of the horn. The target is composed of pure beryllium with a length of 28 in and a diameter of 3/8 in. The target is attached to a thin cylinder of beryllium (inner radius of 13.7779 mm, outer radius of 14.6177 mm) via twenty-one beryllium fins, three for each slug, positioned at intervals of 120 degrees around the target. Each flange had a cross sectional area of 2.1545 mm and a length of 3.5 inches.

The horn is defined by 14 vertices in length and radius. A plot of the length versus radius is compared to the horn engineering drawing in Figure 4.1. The aluminum inner conductor has a thickness of 3 mm and is cylindrically symmetric. Between the inner and outer conductor the magnetic field is given by Ampere's law, and inside the inner conductor the field is zero. The field within the inner conductor aluminum is determined by the "skin depth" of the horn current, and is approximated as an exponential function of the radius.

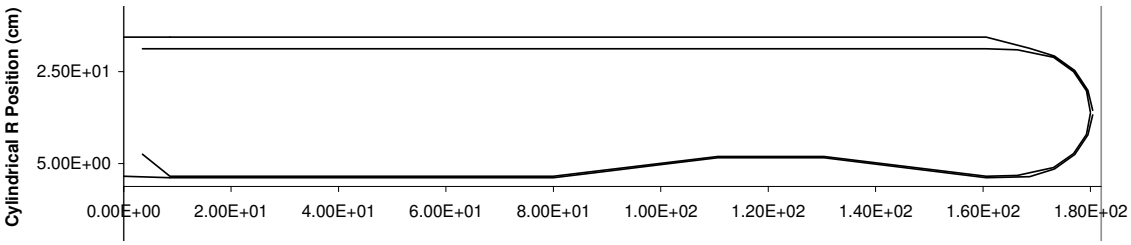

(a) The radial cross section of the horn as modeled in the beam Monte Carlo simulation

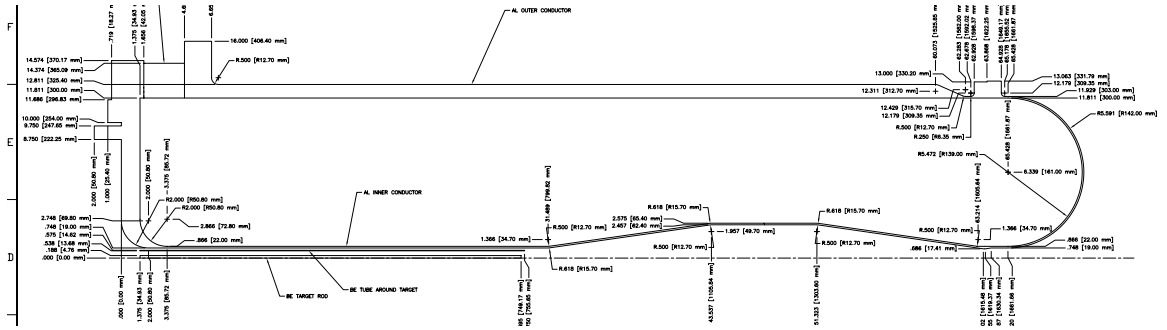

(b) The engineering drawing of the horn radial cross section

Figure 4.1: The horn geometry in the beam Monte Carlo simulation (top) is compared with the engineering draw (bottom). The critical feature is the shape of the inner (low R) conductor, which is well modeled.

The target and horn assembly are located within a 1.3 m thick box of 1030 steel, which is positioned inside a 60 cm thick concrete enclosure. The beam line enters the horn enclosure through a 14 cm diameter steel tube, and the steel collimator through which the secondary beam exits has a 60 cm diameter that grows to 71 cm at the terminal end, 7 ft downstream.

The 50 m decay region is composed of two 6 ft inner-diameter concrete tubes that surround the 25 m absorber enclosure. At the end of the decay region is the steel and concrete beam stop. The entire beam Monte Carlo structure is surrounded by dolomite, which is simulated with a density of 2.28 g/cm^3 to account for the actual dolomite density of 2.84 g/cm^3 and a packing fraction of 0.79.

4.1.1.2 Interaction Cross Sections

The beam Monte Carlo simulation employs a custom model for proton, neutron, and pion interactions with both beryllium and aluminum [30]. The total cross section is divided into (coherent) elastic and inelastic components. Interactions between the incident hadron and individual nucleons that do not produce or absorb initial state particles are referred to as quasi-elastic interactions, and are separated from the remaining "reaction" portion of the inelastic cross section. Each of these cross sections are related by the following expression,

$$\sigma_{TOT} = \sigma_{ELA} + \sigma_{INE} = \sigma_{ELA} + \sigma_{QE} + \sigma_{REA}. \tag{4.1}$$

Theoretical models are used to parametrize many of the cross sections in Equation 4.1. Wherever possible, these parametrizations are fit to the existing data. The forward elastic cross section amplitude is calculated using the Glauber model [31], which combines known hadron-nucleon scattering amplitudes into one coherent target. From the elastic scattering amplitude, the total cross section can be derived using the optical theorem. The quasi-elastic interactions are mostly described by the corresponding hadron-nucleon cross sections with an additional correction for the attenuation of the hadron wave function as it penetrates the nucleus. This effect is treated using the shadowed multiple scattering expansion [31].

The inelastic cross sections are well measured, and parametrizations are used to fit the existing data. The proton-Be/Al interactions have been measured over the entire momentum range of interest [32, 33]. Data exist for nearly all of the $\pi^{\pm}$ momentum range as well, except at low momentum where the data are extrapolated from higher nuclei [32, 33, 34, 35]. These parametrizations of the total, quasi-elastic, and inelastic cross sections fully specify the relation given in Equation 4.1. Plots of the pion and nucleon total, inelastic, and quasi-elastic parametrizations are given in Figures 4.2 and 4.3. Additional details can be found in Refs. [36, 37].

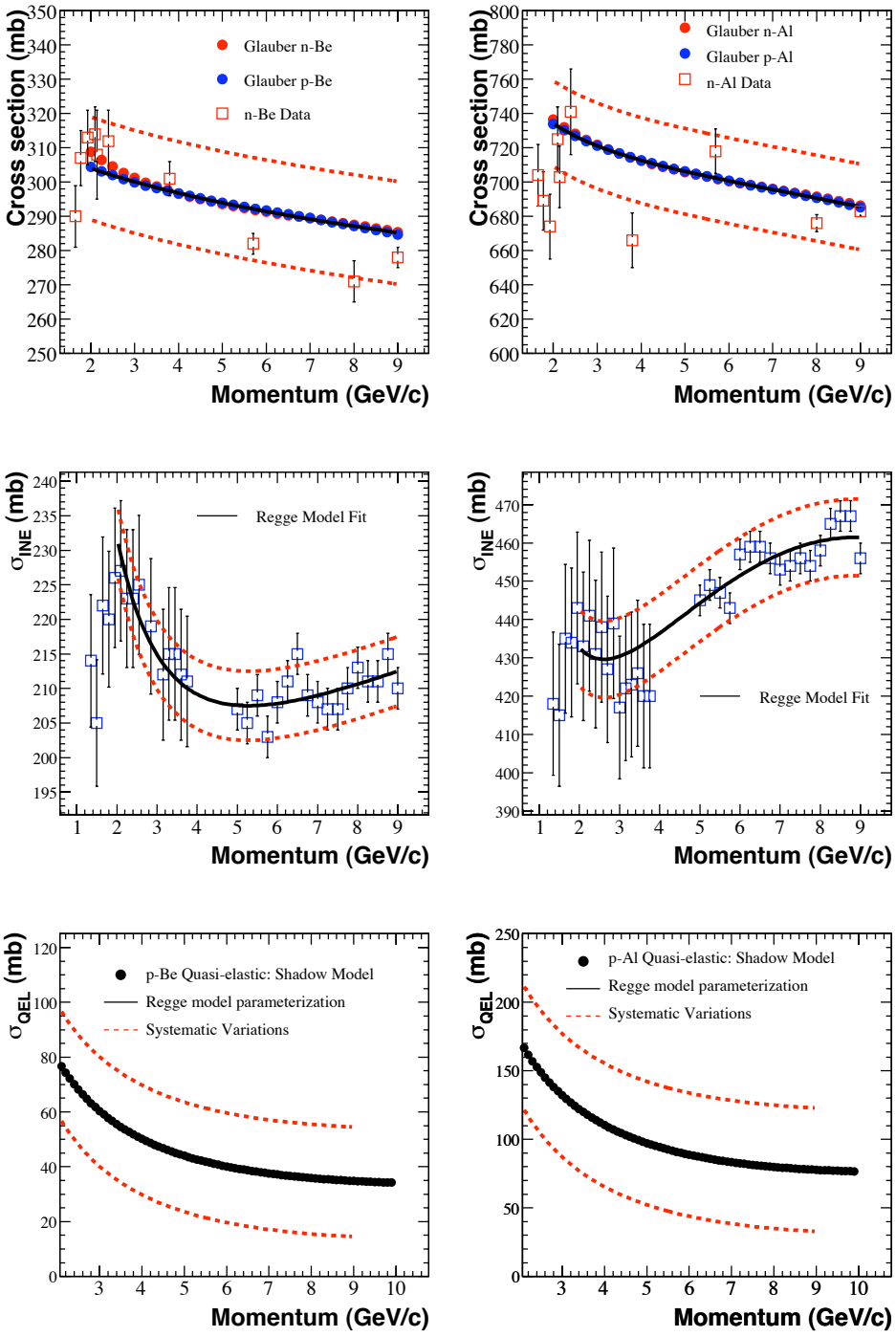

Figure 4.2: The nucleon total (top), inelastic (middle), and quasi-elastic (bottom) parametrizations for interactions with beryllium (left) and aluminum (right) are shown. The systematic errors assumed for each are also given and compared with data where possible [36].

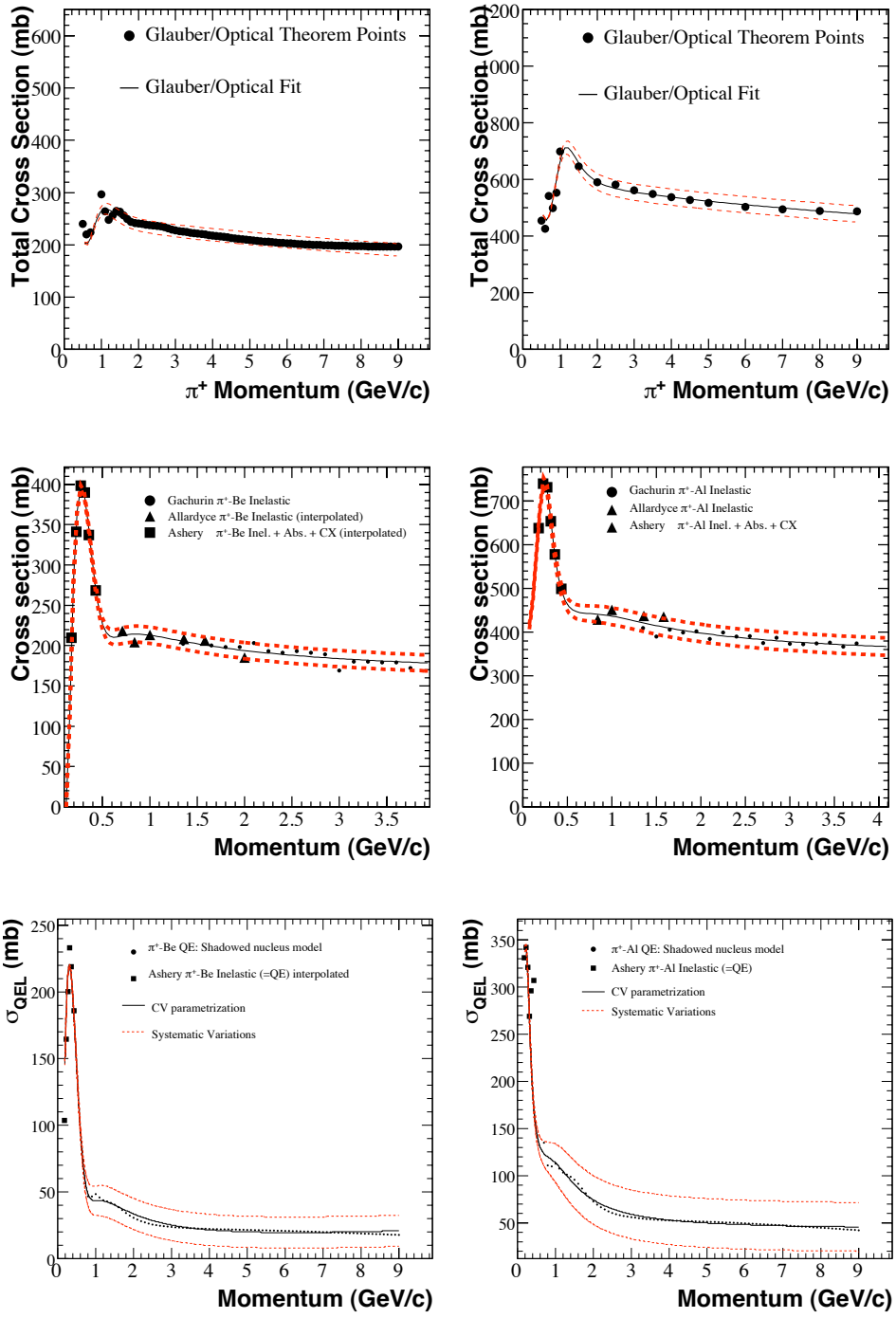

Figure 4.3: The pion total (top), inelastic (middle), and quasi-elastic (bottom) parametrizations for interactions with beryllium (left) and aluminum (right) are shown. The systematic errors assumed for each are also given and compared with data where possible [36].

4.1.1.3 Particle Production Cross Sections

For each inelastic proton-beryllium interaction that takes place, a collection of secondary particles are produced. Interactions between 8 GeV kinetic energy protons and nucleons at rest can produce any flavorless or strange hadron. The center of momentum energy for such collisions is 4.2 GeV, which is insufficient to create a J/ψ,N,N final state (E_{min} = 3.10+0.94+0.94 = 4.98 GeV), or for the reaction $p + N \rightarrow N + D + \Lambda_c^+$ to occur (E_{min} = 0.94+1.86+2.29 = 5.09 GeV); therefore, the booster neutrino beam contains no charm decay products.

The kinematics and multiplicity of each secondary particle species are determined from double differential production cross sections, $\partial^2\sigma/\partial p\partial\Omega$. Since the simulation is only concerned with generating the proper secondary particle spectra on average, no attempt is made to conserve energy or momentum in individual proton-beryllium interactions. Instead, the multiplicity of each secondary particle type is drawn from a Poisson distribution with a mean given by the ratio of the integrated production cross section to the total inelastic cross section. To determine the momentum and angle of a given secondary particle, the double differential cross section is normalized to unity, and the particle kinematics are drawn from the resulting probability distribution function. For the secondaries most important to the neutrino flux, pions and kaons, the double differential cross sections are determined from fits to external data [38, 39]. Production cross sections for π^+, π^-, and K_L particles are parametrized by Sanford-Wang function [40]. For K^+ particles, a Feynman scaling parametrization is used [39]. The remaining simulated secondary particles, p, n, and K^-, have very little impact on the neutrino flux, and are generated according to the MARS14 hadron production program [41].

The Sanford-Wang parametrization of double differential production cross sec-

tions takes the following form,

$$\frac{\partial^2\sigma}{\partial p\partial\Omega} = c_1\left(1-\frac{p}{p_B-c_9}\right)\exp\left(-c_3\frac{p^{c_4}}{p_B^{c_5}}-c_6\theta\left(p-c_7p_B\cos^{c_8}\theta\right)\right), \tag{4.2}$$

where p and θ are the direction and angle of the outgoing pion, and p_B is the momentum of the incident beam protons. The parameter c_9 is set to 1 GeV in fits to pion data [38]. The HARP experiment at CERN was run at the same 8 GeV proton beam energy produced by the Fermilab booster, and measures a range in the pion phase space (0.75 GeV/c $< p_\pi <$ 6.5 GeV/c; 30 mr $< \theta_\pi <$ 210 mr) that covers more than 80% of the pion phase space that produces neutrinos that reach the MiniBooNE detector [42]. Data from the E910 experiment at the Brookhaven National Laboratory also constrain a large portion of the pion phase space (0.4 GeV/c $< p_\pi <$ 5.6 GeV/c; 18 mr $< \theta_\pi <$ 400 mr) at beam energies of 6.4, 12.3, and 17.5 GeV/c, and has been extrapolated to 8 GeV to be included in the fit as well.

The simultaneous fit to HARP and E910 data minimizes the following χ^2,

$$\chi^2 = \sum_{i,j,k}\left(D_{ik}-N_kT_{ik}\right)V_{ijk}^{-1}\left(D_{jk}-N_kT_{jk}\right)+\sum_k\frac{\left(N_k-1\right)^2}{\sigma_k^2}, \tag{4.3}$$

where V_{ijk} is the covariance matrix for experiment k over measured bins i and j, D_{ik} and T_{ik} are the measured and SW function values in bin i of experiment k, and N_k is the normalization of experiment k, which is constrained by the reported normalization uncertainty, σ_k. The fit produces a minimum χ^2/N_{dof} value of 1.8, indicating that the fit uncertainty does not sufficiently cover the spread of the data. To compensate for this deficiency, the error on each data point is scaled by $\sqrt{1.8}$ and the fit is performed again. The final fit result gives normalization values of 0.973 and 1.039 for HARP and E910, respectively, which are slightly smaller than the 4% and 5% normalization uncertainties reported by each experiment. The best fit Sanford-Wang function is compared to the HARP data in Figure 4.4.

The Sanford-Wang parametrization is used to fit the π^- and K_L production cross sections as well. Data from both HARP and E910 are once again used to fit the π^-

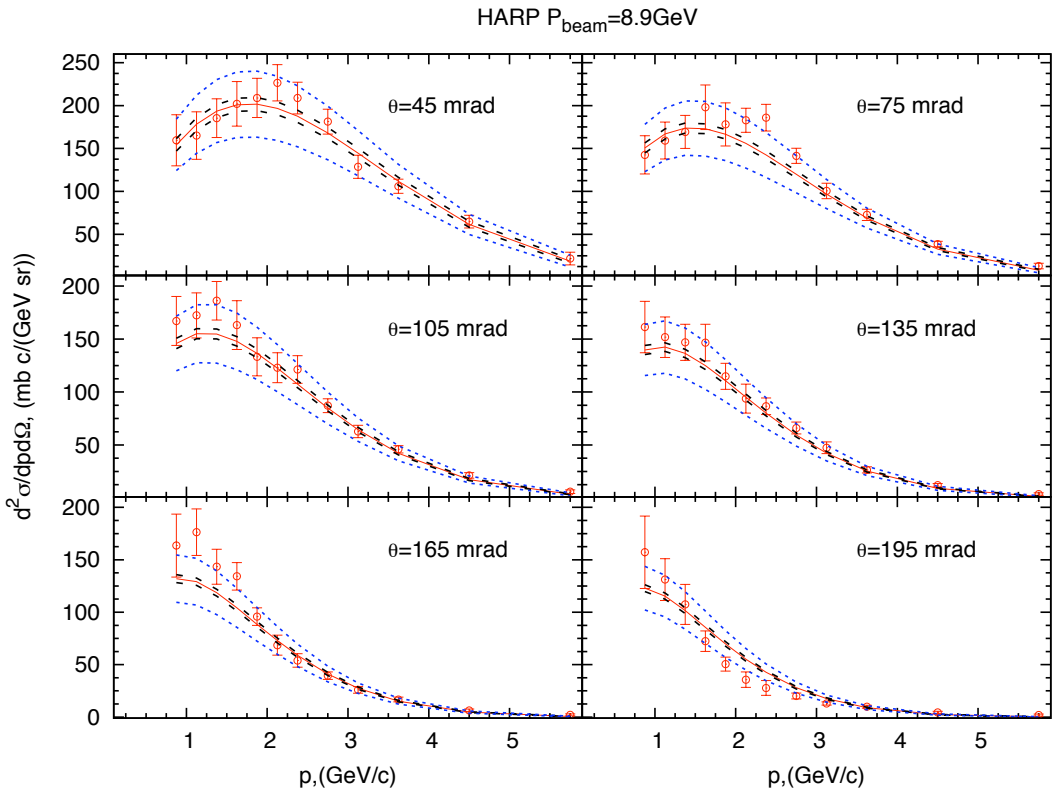

Figure 4.4: The result of the π^+ Sanford-Wang fit to HARP and E910 data is shown with the HARP data (red points) overlayed. The uncertainties from both the initial fit (dashed line) and the fit with scaled data errors (dotted line) are given.

cross section. The K_L fit is performed on data from E910 and Abe et. al. [43]. Unlike the pion fits, the K_L fit allows c_9 to float [44]. The results from each fit are given in Table 4.2.

Table 4.2: A list of Sanford-Wang parameters for the π^+, π^-, and K_L, fits is shown.

Fit	c_1	c_2	c_3	c_4	c_5	c_6	c_7	c_8	c_9
π^+	220.7	1.080	1.000	1.978	1.32	5.572	0.08678	9.686	1
π^-	213.66	0.93785	5.4537	1.2096	1.2836	4.7807	0.073383	8.3294	1
K_L	15.13	1.975	4.084	0.9277	0.7306	4.362	0.04789	13.3	1.278

The K^+ production cross section is fit using a Feynman scaling parametriza-

tion [39]. The cross section is written in terms of the transverse momentum of the secondary, p_t, and a scaling factor, $x_F = p_{\parallel}^{cm}/p_{\parallel\,\max}^{cm}$, where $p_{\parallel}^{cm}$ is the longitudinal momentum in the center of momentum frame of the proton-beryllium interaction. The cross section is given by

$$\frac{\partial^2\sigma}{\partial p\partial\Omega} = \left(\frac{p}{E}\right) c_1 \left(1 - |x_F|\right)^{c_8} \exp\left[-c_3 |x_F|^{c_4} - c_7 |p_t x_F|^{c_6} - c^2 p_t - c_5 p_t^2\right]. \qquad (4.4)$$

The parametrization is fit to seven different data sets [45, 46, 47, 48, 49, 50, 51]. In the fit minimization, c_8 takes on negative values with large uncertainties, so for the final fit it has been fixed to zero. Just as in the pion fit, the minimum $\sqrt{\chi^2/N_{dof}}$ of $\sqrt{2.28}$ is used to scale the size of the data errors. The result of the fit is given in Table 4.3.

Table 4.3: The result for each of the Feynman scaling parameters in the K^+ fit is given.

Fit	c_1	c_2	c_3	c_4	c_5	c_6	c_7	c_8
K^+	11.70	0.88	4.77	1.51	2.21	2.17	1.51	0.0

4.1.2 Meson Decays

The decay branching fractions for kaons and pions were last updated to correspond to the 2006 Particle Data Group averages [52], the values of which have not changed significantly to date. Of particular importance were the decay channels in which neutrinos are produced. Each such decay mode was faithfully reproduced in the simulation, and the sum of modes was set to unity by adjusting the branching fraction of the smallest neutrino-less process. The effect of CP violation has been accounted for in neutral kaon decays using the measured charge asymmetries [52]. The values used in the simulation are given in Table 4.4.

The default GEANT4 routines are used to conduct all particle decays. In the case of muon decays, the `G4MuonDecayChannelWithSpin.cc` class properly simulates the V-A coupling with first order radiative corrections, however the neutrino energy

Table 4.4: The branching fractions used in the beam Monte Carlo simulation are given for $\pi^{\pm}$, $K^{\pm}$, and K_L. The values that have been modified from their Particle Data Group values are labeled as "mod." For the negatively charged mesons, the same values are used for the charge conjugate processes.

Decay Mode	Branching Fraction (measured uncertainty)
$\pi^+ \to \mu^+\nu_\mu$	0.9998770(4)
$\pi^+ \to e^+\nu_e$	0.0001230(4)
$K^+ \to \mu^+\nu_\mu$	0.6344(14)
$K^+ \to \pi^+\pi^0$	0.2092(12)
$K^+ \to \pi^+\pi^+\pi^-$	0.05590(31)
$K^+ \to \pi^0 e^+\nu_e$	0.0498(7)
$K^+ \to \pi^0\mu^+\nu_\mu$	0.0332(6)
(mod) $K^+ \to \pi^+\pi^0\pi^0$	0.0175
(PDG) $K^+ \to \pi^+\pi^0\pi^0$	0.01757(24)
$K_L \to \pi^0\pi^0\pi^0$	0.1956(14)
$K_L \to \pi^+\pi^-\pi^0$	0.1256(5)
$K_L \to \pi^- e^+\nu_e$	0.20333(75)
$K_L \to \pi^+ e^-\bar{\nu}_e$	0.20197(75)
$K_L \to \pi^-\mu^+\nu_\mu$	0.13551(35)
$K_L \to \pi^+\mu^-\bar{\nu}_\mu$	0.13469(35)
$K_L \to \pi^+\pi^-$	0.001976(8)
$K_L \to \pi^0\pi^0$	0.000869(4)
(mod) $K_L \to \gamma\gamma$	0.000455
(PDG) $K_L \to \gamma\gamma$	0.000548(5)

spectra are not generated correctly. This deficiency is corrected in the following stage of the Monte Carlo generation process described next.

4.1.3 Statistics Amplification

Most neutrinos produced in meson decays in the beam Monte Carlo simulation do not intersect the detector. To increase the number of usable neutrinos per generated proton on target, the beam Monte Carlo output is passed to a Fortran program that, for each neutrino produced, simulates the decay of the parent meson (or muon) multiple times (typically 1000), and records the neutrinos that hit the detector. This technique effectively boosts the number of protons on target of the simulation. In addi-

tion, since the particle decay final states produced by the beam Monte Carlo simulation are discarded, any deficiencies in the GEANT4 decay generators are corrected at this stage.

For most events, this parent "re-decay" process works quite well; however, for certain regions of neutrino parent phase space, the additional neutrinos become problematic. In particular, parents with a large longitudinal momentum component, p_z, tend to produce neutrinos that hit the tank at a very high frequency. These events contribute a large number of mono-energetic neutrinos at high energies where the neutrino energy spectrum is already sparsely populated. The result is a collection of non-statistical bumps in the high energy tail of the distribution.

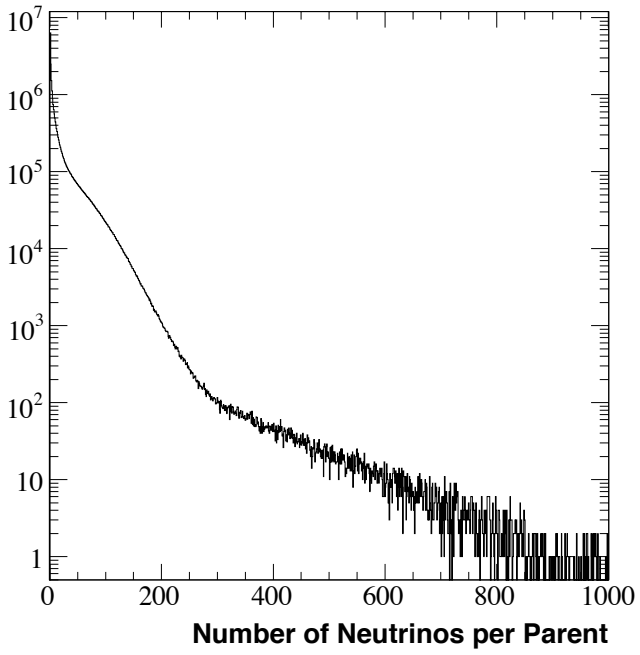

Figure 4.5: The number of neutrinos that hit the detector is plotted for each neutrino parent. Note that this plot has been made after beam Monte Carlo cross section weighting has been implemented, which exponentially increases the high multiplicity events. Even with this amplification, 75% of neutrino parents put less than 10 neutrinos in the detector.

To mitigate the effect of these high-p_z neutrino parents, the double differential particle production cross sections are weighted by an exponential function of p_z,

$$w(p_z) = c_1 \exp(c_2 * p_z). \tag{4.5}$$

Each event that is produced is given a weight of $1/w$ so that the shape of the neutrino energy spectrum is restored. The effect of this weighting procedure is shown in Figure 4.6. Since the cross section weighted distributions are shifted to higher neutrino energies, the reduced the statistical uncertainty in the high energy neutrino tail occurs in the regions of phase space that are relatively more important for the simulated event rate. The values of the weighting function parameters for each modified neutrino parent species is given in Table 4.5.

Table 4.5: The parameters for the exponential weighting function in Equation 4.5 are given for each modified particle species.

Secondary Particle	c_1	c_2	$w(p_z = 10$ GeV)
π^+	1	0.852	5000
π^-	1	0.852	5000
K^+	1.1	0.801	3300
K^-	1.1	0.801	3300
K_L	3	0.801	9000

For the oscillation analysis, one additional weighting technique is needed to reliably produce the neutrino spectrum from muon decays. Muons are produced through the $\pi^+ \rightarrow \mu^+\nu_\mu$ decay channel responsible for the majority of the neutrino flux. Since the muon lifetime is two orders of magnitude larger than the pion lifetime, μ^+ particles rarely decay in flight in a typical Monte Carlo run. To estimate this important contribution to the ν_e flux, for each muon that is produced, nineteen identical copies are created to improve the probability of observing a decay in flight; the corresponding events are weighted by a factor of 1/20.

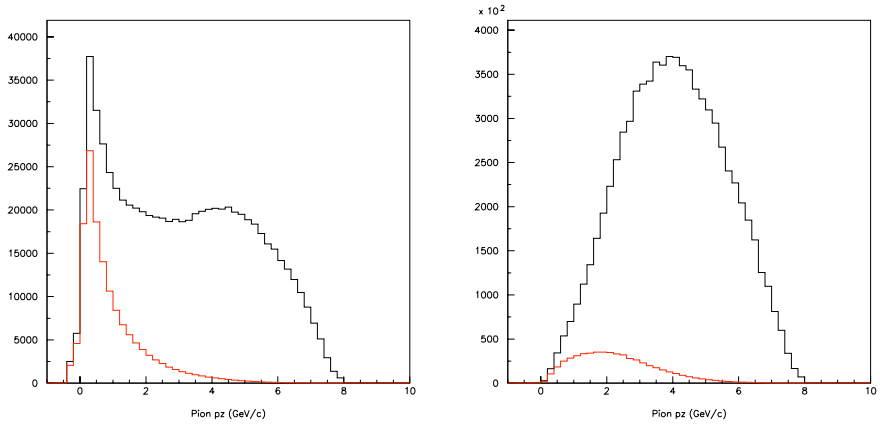

(a) The generated (black) and actual (red) π^+ p_z in the beam Monte Carlo simulation (in GeV/c)

(b) The generated (black) and actual (red) π^+ p_z after the re-decaying of the neutrino parents (in GeV/c)

Figure 4.6: The effect of the exponential weighting function of Equation 4.5 is shown on the π^+ p_z distribution after the beam Monte Carlo (left) and the parent re-decay simulation stages. The increased statistics at high p_z improve the precision of the high energy neutrino spectrum.

4.1.4 Flux Predictions

The energy spectra for neutrinos that hit the detector are given in Figures 4.7 and 4.8. Figure 4.7 gives the flux for each of the four neutrino species produced by the Booster neutrino beam. In Figure 4.8, the ν_μ-only flux, needed to perform the CCπ^+ cross section measurement, is plotted for each of the contributing neutrino parent species.

The neutrino flux is dominated by ν_μ, especially at energies greater than 0.3 GeV where the CCπ^+ cross section turns on. At low neutrino energies, the ν_μ flux comes mostly from $\pi^+ \rightarrow \mu^+\nu_\mu$ decays. At ~2.3 GeV, kaon decays become the dominant component of the ν_μ flux, however the neutrino population at that point is only ~1% of the peak value.

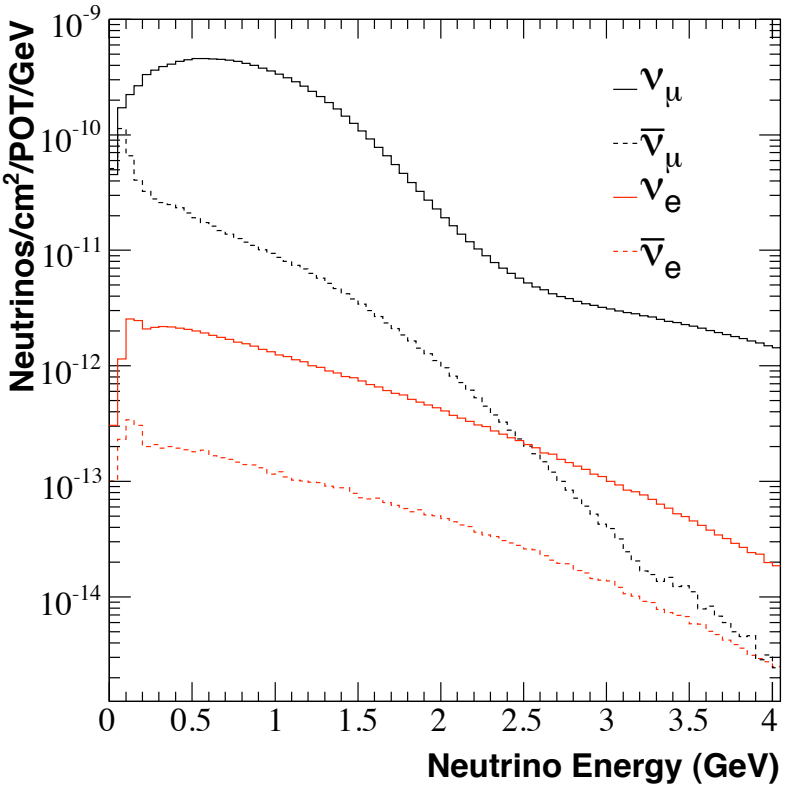

Figure 4.7: The neutrino energy spectrum for each of the four neutrino species is shown for neutrinos that hit the MiniBooNE detector.

4.1.5 Systematic Uncertainties

As described in Section 4.1.1.3, the π^+ Sanford-Wang parametrization produces a poor fit to the HARP and E910 data. To account for the disagreement, the errors on the data are increased until they become compatible with the shape dictated by the parametrization. The resulting covariance matrix from such a fit is dominated by the normalization uncertainty. The failure of the parametrization to fit the data is due to its inability to reproduce the data shape for any choice of parameters. The cross section measurement data have reached a level of precision such that it can no longer be described by the model.

The systematic uncertainties in the knowledge of the neutrino flux need not absorb

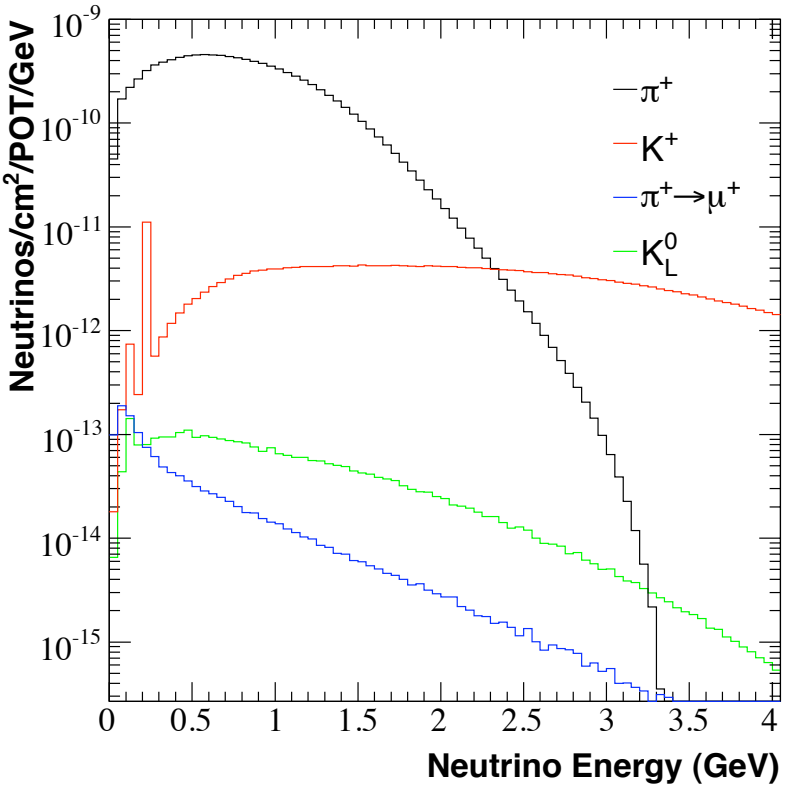

Figure 4.8: The neutrino energy spectrum for ν_μ particles that hit the MiniBooNE detector. The contributions from each of the neutrino parent particle types are shown separately.

this additional contribution from the failure of the model. Instead, the data have been fit with a spline function to faithfully capture all the features of the data [53]. The spline function is a collection of 3rd-order polynomials, each fit over a small interval of data, that are required to have common first and second derivatives at the interval boundaries. The results of the spline fit are compared with the HARP data in Figure 4.9.

Rather than abandon the Sanford-Wang shape completely the systematic error is calculated from the variation of the spline covariance matrix about the Sanford-Wang central value. In this way, the uncertainty acquires an additional component in regions where the parametrization has trouble accommodating the data. Further details are

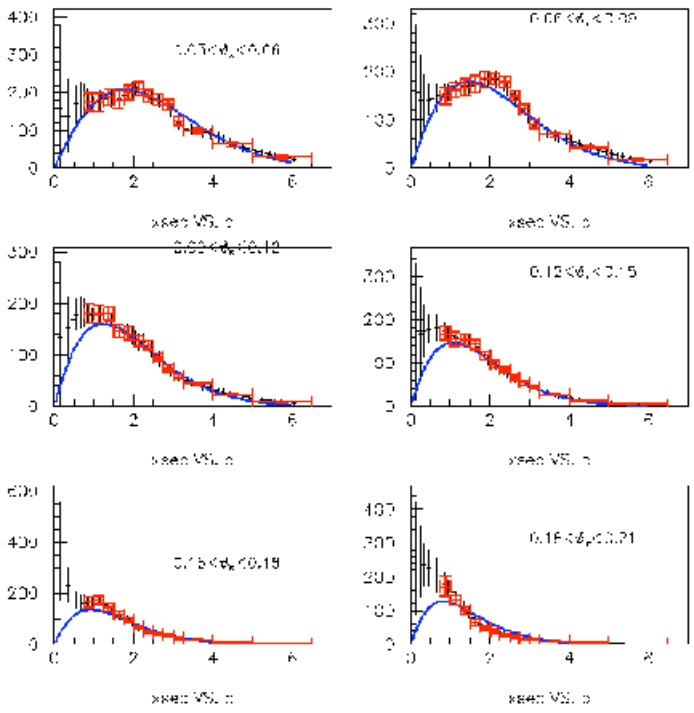

Figure 4.9: The result of the spline fit (black points) is compared to the HARP data (red points) and the Sanford Wang function (blue line) as a function of pion momentum in six different pion angle bins. The uncertainties on the spline fit, shown as black error bars, grow as expected as the function moves further from the data (figure taken from Ref. [53]).

given in Section 6.4.7.1. The flux contributions from the other neutrino parent particles are small enough that the full uncertainty from fits to either Sanford-Wang or Feynman scaling are used with little impact on the total error.

The remaining uncertainties in the neutrino flux are calculated from additional Monte Carlo simulations in which the uncertain parameters are varied by their uncertainties. Each of these altered Monte Carlo sets is referred to as a "unisim." The uncertainties in the nucleon and pion interaction cross sections are shown in Figures 4.2 and 4.3. Without data to which it can be compared, the quasi-elastic cross section uncertainties have been estimated to be very large and dominate the uncertainties from hadron production.

The remaining beam unisims vary the properties of the horn. The horn current has been varied by 1 kA, significantly outside of its measured variation. The uncertainty in the extent to which the current penetrates the inner conductor (i.e. the skin depth) has been estimated by removing the effect completely and treating the result as a variation of one standard deviation. The effect of the largest beam unisim excursions is shown in Figure 4.10.

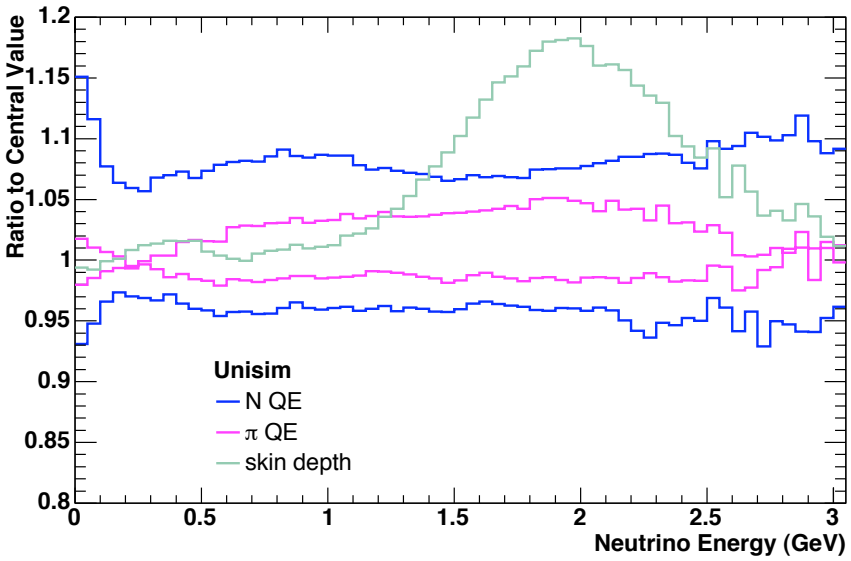

Figure 4.10: The effect of the largest beam unisim excursions are shown. Any unisim that did not vary more than 2% from the central value has been excluded for clarity. The largest integrated effects are from the nucleon and pion quasi-elastic scattering uncertainties. Along the high energy tail of the neutrino flux, the skin depth variation causes changes of almost 20%.

4.2 Nuance

MiniBooNE uses the Nuance event generator to simulate neutrino interactions [54]. Nuance is a Fortran-based software package that takes as input the generated fluxes for each neutrino species and produces a cross section weighted spectrum for each type of neutrino interaction. These event rate distributions are then used to simulate neutrino

interactions and propagate the particles created in the interaction through the nuclear medium. Each event is then written out as a list of particle types and momenta emerging from the nucleus.

Nuance simulates essentially all neutrino interaction processes relevant at MiniBooNE energies. Ninety-nine charged and neutral current processes for both neutrinos and anti-neutrinos are simulated. A summary of the relevant charged current processes as a function of neutrino energy is given in Figure 4.11. At MiniBooNE flux energies (< 2 GeV), neutrino interactions are dominated by CCQE and CCπ^+ interactions.

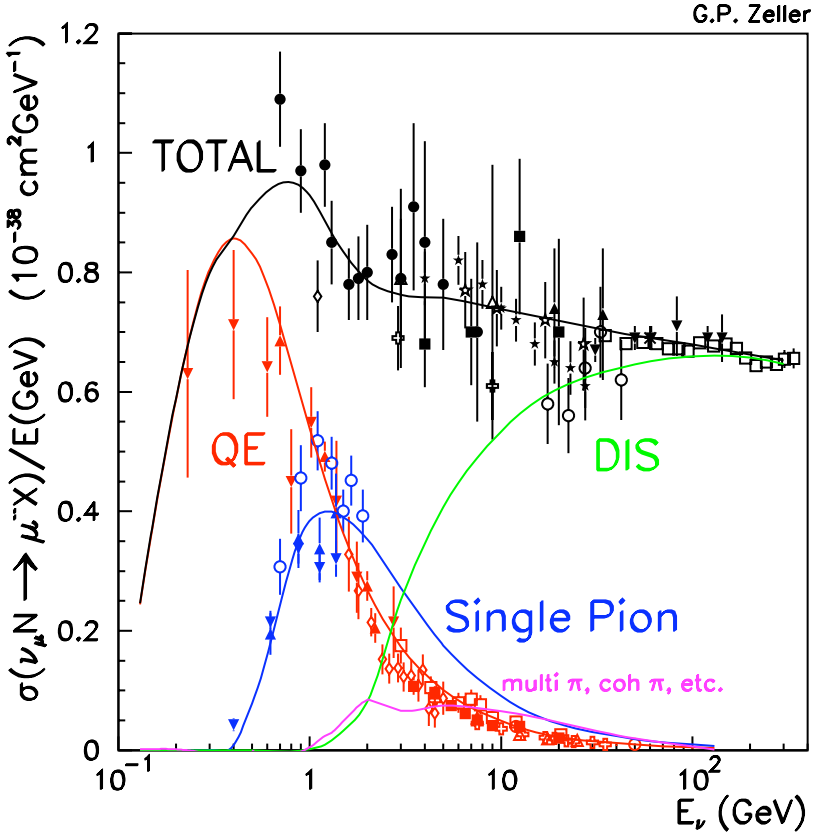

Figure 4.11: The charged current interaction processes are shown as a function of neutrino energy. The peak neutrino energy at MiniBooNE is ~700 MeV. This region is dominated by CCQE and CCπ^+.

Nuance classifies each cross section based on the particles produced in the initial interaction, before they traverse the nucleus. The event rates derived from the MiniBooNE flux are given in Table 4.6.

Table 4.6: Event rate fractions produced by Nuance using the MiniBooNE flux from Figure 4.8. The CCπ^+ and NCπ^0 fractions include coherent scattering off of the entire nucleus.

Name	Interaction Process	Rate Fraction
CCQE	$\nu_\mu n \rightarrow \mu^- p$	0.400
CCπ^+	$\nu_\mu N \rightarrow \mu^- N \pi^+$	0.237
NCEL	$\nu_\mu N \rightarrow \nu_\mu N$	0.170
NCπ^0	$\nu_\mu N \rightarrow \nu_\mu N \pi^0$	0.066
CCπ^0	$\nu_\mu n \rightarrow \mu^- p \pi^0$	0.040
NCπ^+	$\nu_\mu p \rightarrow \nu_\mu n \pi^+$	0.021
CCmultiπ	$\nu_\mu N \rightarrow \mu^- \Delta \pi$	0.015
NCπ^-	$\nu_\mu n \rightarrow \nu_\mu p \pi^-$	0.016
CCDIS	$\nu_\mu N \rightarrow \mu^-$+hadrons	0.010
CCmeson$B$	$\nu_\mu N \rightarrow \mu^- + (\rho, K, \eta)$+baryon	0.006
$\bar{\nu}$	$\bar{\nu} N \rightarrow$anything	0.004
other	each < 0.01	0.015

4.2.1 CCQE

Charged current quasi-elastic interactions (CCQE) are simulated according to the model of Llewellyn Smith [55]. Just as in the derivation of CCπ^+ interactions described in Section 1.1.2.1, the leptonic current is easily calculated, and the crux of the model lies in the parametrization of the hadronic current. The cross section for neutrino scattering is given by

$$\frac{\partial \sigma}{\partial Q^2} = \frac{G_F^2 m_N^2 V_{ud}^2}{8\pi E_\nu^2} \left[A(Q^2) + B(Q^2)\frac{s-u}{m_N^2} + C(Q^2)\frac{(s-u)^2}{m_N^4} \right], \tag{4.6}$$

where s and u are the Mandelstam variables such that $(s-u) = 4m_N E_\nu - Q^2 - m_l^2$, and

$$A(Q^2) = \frac{m_l^2+Q^2}{m_N^2}\left[(1+\tau)F_A^2 - (1-\tau)F_1^2 + \tau(1+\tau)F_2^2 + 4\tau F_1 F_2 \right. \quad (4.7)$$

$$\left. -\frac{m_l^2}{4m_N^2}[F_1^2 + (F_A + 2F_P - 4(1+\tau)F_P^2]\right], \quad (4.8)$$

$$B(Q^2) = 4\tau F_A(F_1+F_2), \quad (4.9)$$

$$C(Q^2) = \frac{1}{4}(F_A^2 + F_1^2 + \tau F_2^2), \quad (4.10)$$

for $\tau = \frac{Q^2}{4m_N^2}$. The hadronic form factors, (F_1, F_2, F_P, F_A), are once again parametrized with a dipole form given by,

$$F_1(Q^2) = \frac{1+\tau(1+\mu_p-\mu_n)}{(1+\tau)\left(1+\frac{Q^2}{m_V^2}\right)^2}, \quad (4.11)$$

$$F_2(Q^2) = \frac{(\mu_p-\mu_n)}{(1+\tau)\left(1+\frac{Q^2}{m_V^2}\right)}, \quad (4.12)$$

$$F_A(Q^2) = \frac{F_A(0)}{\left(1+\frac{Q^2}{m_A^2}\right)^2}, \quad (4.13)$$

$$F_P(Q^2) = \frac{2m_N^2}{m_\pi^2+Q^2}, \quad (4.14)$$

where m_V and m_A are the vector and axial masses described in Section 1.1.2.1, and μ_p and μ_n are the proton and neutron magnetic moments. The parameter $F_A(0) = -1.27$ is determined from neutron beta decay [55].

4.2.2 Nuclear Effects

The motion of the protons and neutrons in the nucleus are described by the Fermi gas model of Smith and Moniz [56]. The observed cross sections are modified by the motion of the nucleons as well as the strength to which they are bound to the rest of the nucleus. The binding energy of 34 MeV and cutoff momentum of 220 MeV/c are determined using electron scattering data [57].

Once a neutrino interaction occurs, the final state particles must traverse the nucleus before they can be observed. This effect is particularly important for final state pions, as they interact strongly with the nucleons. Events created with π^+ will not be observed if the pion is either absorbed or takes part in a charge exchange interaction, $\pi^+ + n \rightarrow \pi^0 + p$. The cross section for both of these processes is given as a function of pion energy in Figure 4.12.

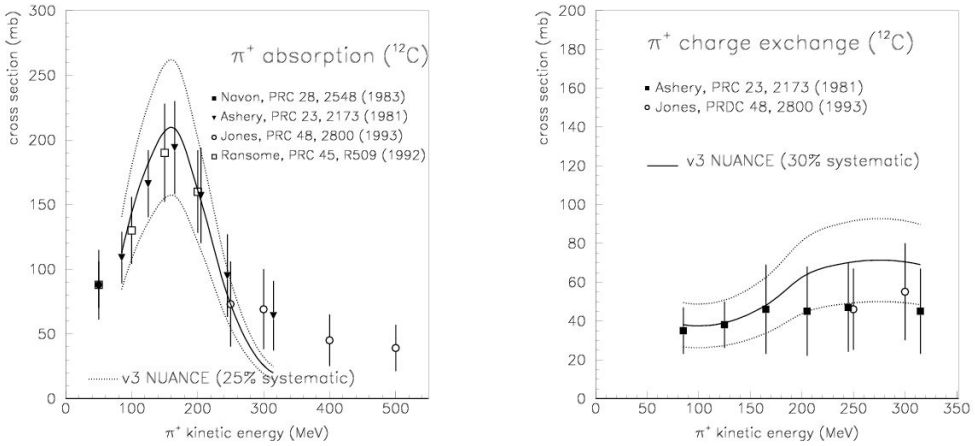

(a) pion absorption vs pion kinetic energy

(b) pion charge exchange vs pion kinetic energy

Figure 4.12: The pion absorption and charge exchange cross sections are shown as a function of pion kinetic energy. The absorption systematic uncertainty is 25%, and the charge exchange cross section is assigned a 30% uncertainty.

4.2.3 Systematic Uncertainties

The common feature of all exclusive charged current interactions is that the axial-vector portion of each interaction is parametrized as a dipole with an axial mass, m_A. The two background processes most relevant to the CCπ^+ cross section measurement described in Chapter 6 are CCQE and CCmultiπ. The main uncertainty in each of these processes is the value of the axial mass, and the variations for each are given in

Table 4.7. The CCDIS cross section normalization is varied by 25%.

Table 4.7: The axial mass values for CCQE and CCmultiπ interactions are listed with associated systematic uncertainties.

parameter	central value	systematic uncertainty
m_A(CCQE)	1.234 GeV	0.077 GeV
m_A(CCmultiπ)	1.30 GeV	0.52 GeV

The pion absorption and charge exchange uncertainties are given in Figure 4.12. Pions can also be effectively absorbed if the Δ resonance interacts with a nucleon via $\Delta N \rightarrow NN$. The effect of eliminating this process completely is taken as a one sigma variation. For historical reasons, the pion interaction uncertainties in the nucleus are included in the detector optical model uncertainties, while the pion interaction uncertainties for processes that occur outside the nucleus (discussed in Section 4.2.3) are included here as part of the cross section model uncertainties.

Finally, systematic uncertainties are assigned to the properties of the Fermi gas model. The binding energy is varied by 9 MeV (26%) and the Fermi momentum is assigned an uncertainty of 30 MeV/c (14%).

4.3 BooNEGlob

Nuance can generate neutrino events only from a neutrino energy histogram for each neutrino species. All other information from the beam Monte Carlo simulation is discarded. In particular, the particle type and generation kinematics of the neutrino parent is lost. Additionally, several intra-event correlations are not preserved, such as the neutrino angle and interaction vertex, the event time and neutrino parent type, and the neutrino parent type and the neutrino interaction process.

To reinstate these correlations, each Nuance event is paired with a beam event in a Fortran-based program known as "BooNEGlob." In any given Nuance event, the only variables that are shared with the incident beam neutrino are the neutrino energy

and species. BooNEGlob loops over the beam Monte Carlo output used to generate the neutrino flux and tabulates the events with the same neutrino type that are within a small energy window surrounding the Nuance event. For ν_μ events, this energy tolerance is set to 1 MeV. An event is then randomly selected from the list of pairing candidates according to its beam Monte Carlo event weight.

Once a Nuance event is paired, the event can be manipulated in a variety of useful ways. Most importantly, the directions of the Nuance final state particles are all rotated to correspond to the direction of the incident neutrino. The Nuance events can also be weighted and filtered to amplify interesting regions of phase space. Finally, the beam Monte Carlo also assigns a neutrino parent type to each event so that it can be reweighted according to its parent production cross section function (Sanford-Wang, Feynman scaling, or the spline fit) when evaluating the systematic errors due to uncertainties in the fit parameters.

4.4 Detector Simulation

After Nuance produces a list of final state particles that exit the nucleus, the remainder of the particle propagation is handled by the detector Monte Carlo simulation. The detector Monte Carlo is GEANT3-based simulation package [58] that tracks each particle through the oil, including each optical photon produced via Cherenkov or scintillation radiation. As these photons constitute all of the data recorded by the detector, a detailed optical model has been developed that simulates effects such as absorption, scattering, and reflections. This section presents an overview of the features of the simulation. A detailed description of each component can be found elsewhere [59].

Several modifications have been made to the default GEANT3 algorithms. Additional processes have been added to model π^0 Dalitz decays ($\pi^0 \rightarrow e^+e^-\gamma$) and muon decay ($\mu \rightarrow e\nu\nu$). The observed stopped μ^- capture rate on carbon of 7.77simulated [60].

The default GEANT3 hadronic interaction model, GFLUKA, has been replaced with GCALOR [61]. This switch was motivated by the handling of the pion absorption and charge exchange interactions that occur in the tank, analogous to the nuclear interactions described in Section 4.2.2. The cross sections predicted by each model as a function of pion kinetic energy are compared with data from Ashery et. al. in Figure 4.13 [34]. The FLUKA model over-predicts the charge exchange and under-predicts absorption by significant margins, whereas the GCALOR model mostly agrees with the data.

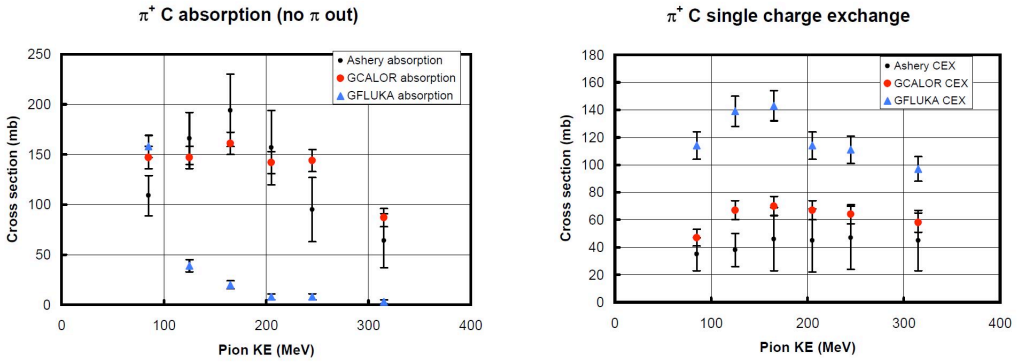

(a) pion absorption vs pion kinetic energy

(b) pion charge exchange vs pion kinetic energy

Figure 4.13: The GFLUKA and GCALOR predictions for pion absorption and charge exchange cross sections in oil are compared with data as a function of pion kinetic energy. The GCALOR model is used for hadronic interactions in the detector Monte Carlo simulation.

4.4.1 Optical Model

The creation, propagation, and detection of optical photons produced in neutrino interactions are handled by the optical model. Photons are propagated until they are either absorbed or detected by a PMT. The photons are created through Cherenkov and scintillation emission from charged particle tracks, or through fluorescence from the

molecules in the mineral oil. After the photons are created, they can undergo Rayleigh or Raman scattering, which has also been incorporated into the model.

Cherenkov radiation is created when a charged particle moves through a medium faster than light can propagate in the medium. The angular emission profile relative to the path of the particle is given by the ratio of these velocities,

$$\cos\theta_{Cher} = \frac{v_{light}}{v_{particle}}, \tag{4.15}$$

where v_{light} and $v_{particle}$ are the velocities of the light and the charged particle, respectively. Cherenkov light is produced instantaneously, and as the particle slows down due to energy losses in the medium, the Cherenkov "cone" is reduced until the particle drops below Cherenkov threshold as its velocity slows below v_{light}.

As charged particles travel through the oil, carbon and hydrogen atoms are ionized. The subsequent de-excitation of these states produces scintillation light. The flux of scintillation light produced per unit of energy deposited is given by Birks law [62],

$$\frac{dN_{sci}}{dE} = \frac{31.64\ \text{MeV}^{-1}}{1 + B_1\left(\frac{1}{\rho_{oil}}\frac{dE}{dx}\right) + B_2\left(\frac{1}{\rho_{oil}}\frac{dE}{dx}\right)^2}. \tag{4.16}$$

Unlike Cherenkov radiation, scintillation light is delayed exponentially relative to the track from which it is produced with a time constant of 34 ns.

Molecules in the mineral oil can also become excited through interactions with higher energy photons and decay to produce optical photons in a process known as fluorescence. The characteristics of the fluoresced light depend on the properties of the medium. An analysis of the mineral oil has identified 4 independent fluors, each with its own time constant and emission profile, all of which are included in the simulation.

As optical photons propagate through the detector, Figure 4.14 shows the extinction rates for various processes that can affect the photon propagation path. The absorption used in the simulation is determined by the difference of total extinction rate and the sum of the exclusively measured components. A comparison of hit time

distributions between laser calibration data and the simulation is shown in Figure 4.15. The modeling of photon reflections and scattering account for a significant portion of the timing structure, especially at late times.

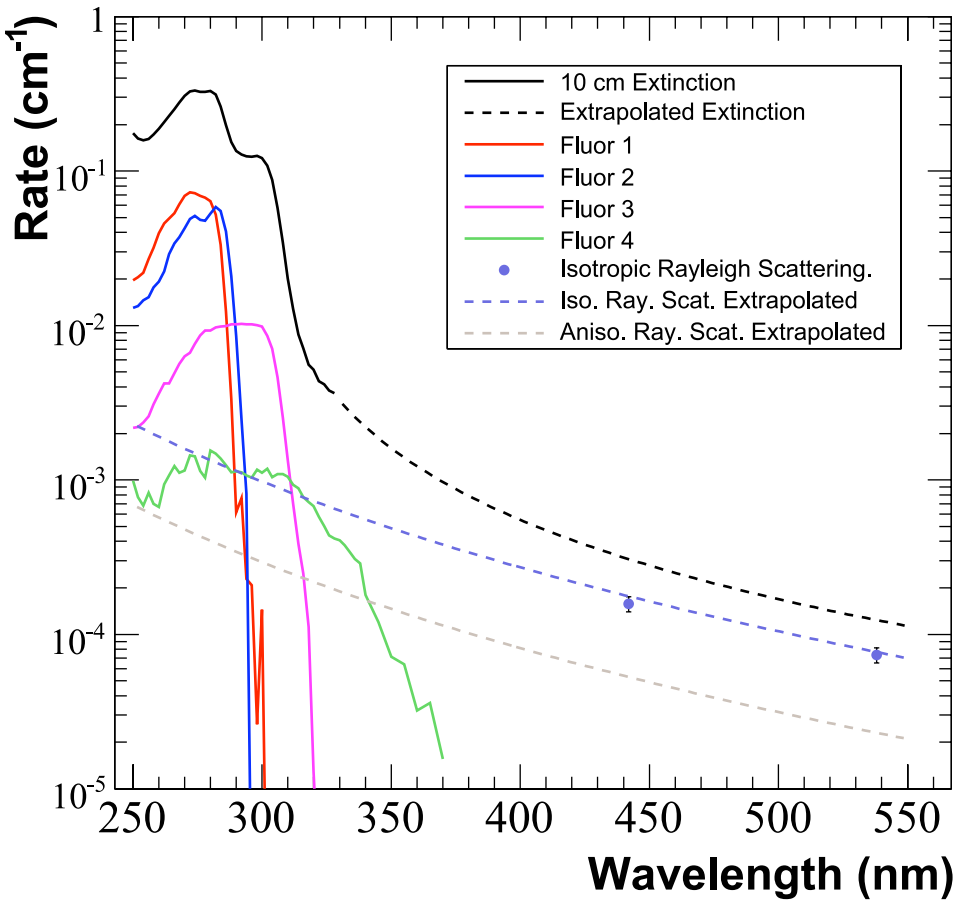

Figure 4.14: The extinction rates are given for several light sources as a function of wavelength. The total extinction curve (black) was measured using a 10 cm cell at Fermilab. The rates due to the 4 fluors and the effect of Rayleigh scattering are also shown.

4.4.2 Systematic Uncertainties

The optical model is a conglomeration of several physical quantities used to describe the production and propagation of optical photons. Of these quantities, 35 parameters describing phenomena such as the light yield from each of the sources, the

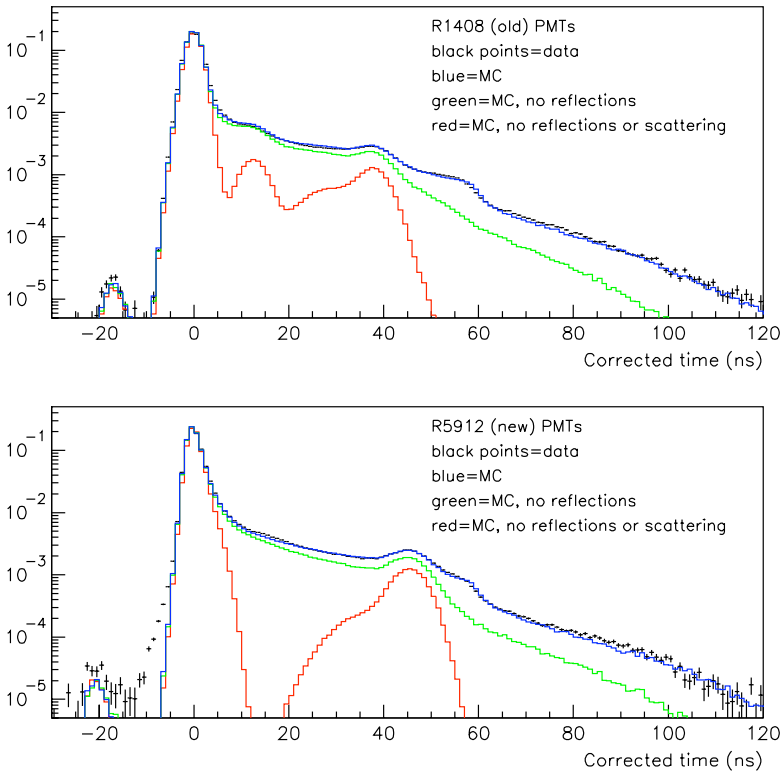

Figure 4.15: The detector Monte Carlo simulation of new and old PMTs is compared with data taken by the 397 nm laser. The importance of modeling scattering and reflections is evident.

Birks law coefficients, the extinction length, scattering, reflections, and the quantum efficiency of the PMTs have been varied to determine the systematic uncertainties of the model. Several thousand random draws from this parameter set were used in an attempt to quantify, not only the uncertainties in the parameters, but some amount of the correlation between them. The resulting covariance matrix is used to produce systematic variations to assess the uncertainties in the measured distributions (see Section 6.4.7.1).

The uncertainties in the pion absorption and charge exchange cross sections in the tank are slightly higher than their nuclear analogs. The discrepancy between the GCALOR description and the data requires a 35% variation in pion absorption and a 50% uncertainty in the charge exchange cross section. As mentioned in Section 4.2.3,

the uncertainties on pion interactions in the tank are counter-intuitively included in the cross section errors, while the analogous nuclear processes are included in the optical model uncertainties.

Chapter 5

Event Reconstruction

The MiniBooNE data acquisition system records charge and time information from each photomultiplier tube (PMT) over a 20 μs time window surrounding the arrival of the beam pulse. When a neutrino interaction occurs, the particles produced in the interaction propagate through the tank for tens of centimeters and come to rest on the order of 10 ns after the interaction takes place. Any promptly produced photons in the interaction can take up to 40 ns to reach a PMT if they traverse the entire tank, and some amount of delayed light is produced with an exponential decay constant of about 30 ns. Since the discriminator for each PMT can fire only once every 200 ns, each neutrino interaction produces no more than one charge and one time in each PMT from which the event must be reconstructed. Only the PMTs inside the main tank can be used for event reconstruction, so the kinematics of all particles in the event must be deduced from, at most, 2,560 pieces of information.

The initial state of a particle track is fully specified by the particle type and the following seven parameters:

- energy (E_0)
- direction (θ_0 and ϕ_0)
- 4-vertex (X_0, Y_0, Z_0, and T_0)

To reconstruct a track, an operator must be produced that converts a given set of track

parameters, $\mathbf{x}$, into probability distribution functions (PDFs) of the charge, q, and time, t, for each hit PMT in the event. The PDFs from each hit tube can then be combined with the measured information from each tube to form a likelihood function,

$$\mathcal{L}(\mathbf{x}) = \prod_{i=1}^{N_{unhit}} \mathcal{P}_i(\text{unhit};\mathbf{x}) \prod_{j=1}^{N_{hit}} \mathcal{P}_j(\text{hit};\mathbf{x}) f(q_j;\mathbf{x}) f(t_j;\mathbf{x}), \tag{5.1}$$

where $N_{hit}(N_{unhit})$ is the number of hit(unhit) PMTs in the event and $\mathcal{P}_i(\text{hit};\mathbf{x})(\mathcal{P}_i(\text{unhit};\mathbf{x}))$ is the probability that PMT i will be hit(unhit) for a track specified by $\mathbf{x}$. The charge and time PDFs for $\mathbf{x}$ ($f(q_j;\mathbf{x})$ and $f(t_j;\mathbf{x})$, respectively) are evaluated at the measured charge, q_j, and time, t_j, in PMT j. The task, then, is to find the set of parameters, $\mathbf{x}$, that maximize the likelihood.

Rather than work with $\mathcal{L}$ directly, it is often more convenient to use $-\log(\mathcal{L})$. This transforms the product in Equation 5.1 into a sum over each PMT. The charge and time components become additive and can be treated independently,

$$-\log(\mathcal{L})(\mathbf{x}) = F_q(\mathbf{x}) + F_t(\mathbf{x}), \tag{5.2}$$

where

$$F_q(\mathbf{x}) = -\sum_{i=1}^{N_{unhit}} \log(\mathcal{P}_i(\text{unhit};\mathbf{x})) - \sum_{j=1}^{N_{hit}} \log(\mathcal{P}_j(\text{hit};\mathbf{x}) f(q_j;\mathbf{x})), \tag{5.3}$$

$$F_t(\mathbf{x}) = -\sum_{j=1}^{N_{hit}} \log(f(t_j;\mathbf{x})). \tag{5.4}$$

The hit probabilities are naturally grouped with the charge PDFs, since an unhit PMT is just a measurement of zero charge. The functions $F_q(\mathbf{x})$ and $F_t(\mathbf{x})$ are referred to as the charge and time likelihoods despite technically being the negative logarithm of their respective likelihoods. To determine the track parameters, $\mathbf{x}$, that best fit the event, the sum $F_q(\mathbf{x}) + F_t(\mathbf{x})$ must be minimized.

MiniBooNE employs a detailed description of the light production along an extended track to derive the time and charge likelihoods in Equation 5.2. A complete description of this process in terms of the muon and electron track hypotheses can be

found in Ref. [59]. The next section will present the important features of the likelihood calculation in terms of the new pion particle hypothesis.

5.1 Straight Pion Tracks

As particles propagate through the tank, they experience a variety of processes including elastic scattering, inelastic nuclear interactions, and decay. To convert a set of track parameters into a likelihood function, one must decide which features of the particle track to attempt to measure, and which features to average over. For charged leptons, the reconstruction assumes that the particle travels in a straight line. Typical trajectories for a muon and a pion are illustrated in Figures 5.1 and 5.2, respectively. The straight line hypothesis is quite accurate for muons, which propagate in long, smooth paths with very little scattering. Electrons, on the other hand, travel relatively short distances and produce energetic photons that convert into e^+/e^- pairs some time later. The charge and time likelihoods for electrons are averages over all of these interactions.

In building the pion likelihood functions, the π^+ trajectories are characterized by the same straight track characterization of the particle propagation as was used for the charged leptons. However, for reasons that will be explained in Section 5.2, the likelihoods are calculated for pions that do not decay or interact hadronically.

5.1.1 Charge Likelihood

The charge recorded by a PMT is only a function of the number of photoelectrons produced in the tube. If an average number of photoelectrons (called the predicted charge, μ) can be found for each PMT as a function of the track parameters, $\mathbf{x}$, the probability for a tube to be hit is given by the Poisson distribution,

$$\mathcal{P}(\text{hit}; \mu(\mathbf{x})) = 1 - \mathcal{P}(\text{unhit}; \mu(\mathbf{x})) = 1 - e^{-\mu}. \tag{5.5}$$

The task, then, is to calculate the predicted charge on each tube.

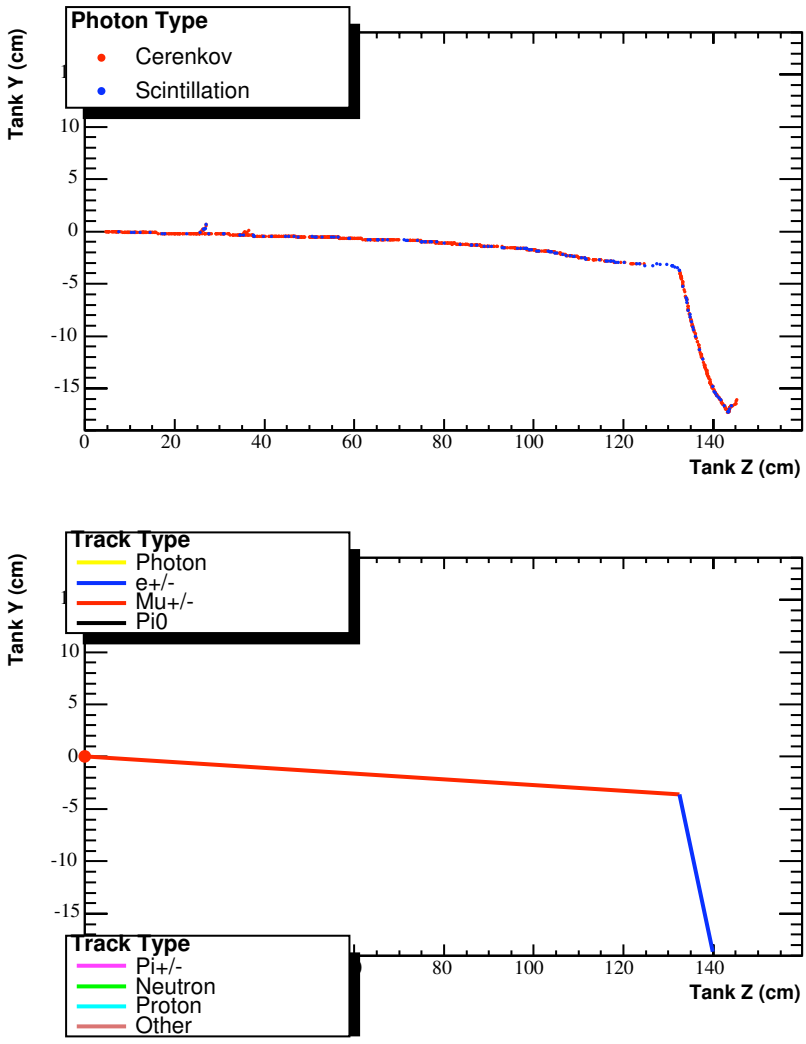

Figure 5.1: An event display of a typical 300 MeV muon track is shown (for a full description of the "event displays" that are shown throughout this chapter, see Appendix A). The top plot shows the Monte Carlo emission point of every optical photon created in the event, and the bottom plot gives the identity of each particle. The display is cumulative over the entire duration of the event, including the muon propagation, muon stop point, and the electron produced from the muon decay at rest.

The predicted charge depends on the amount of light produced by the track, Φ, the transmission of the light through the oil, T, the solid angle of the PMT as seen by the track, and the angular acceptance of the PMTs, ϵ. Each of these properties are functions of the position along the track, s. If the light produced by the track is

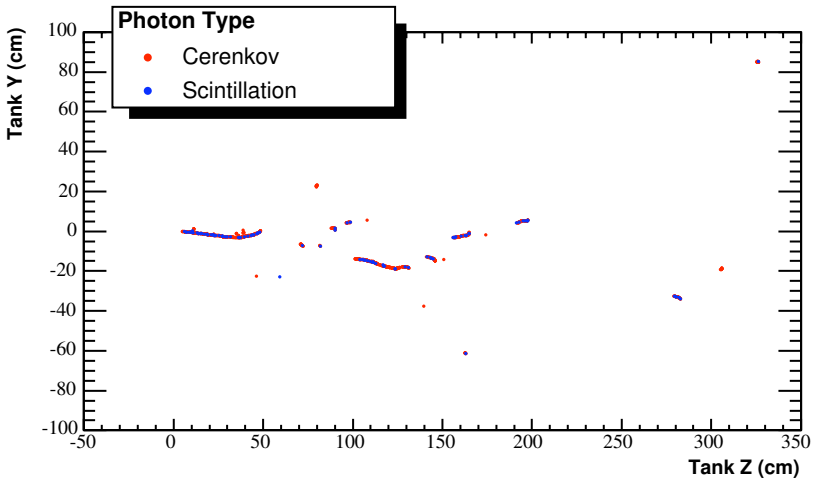

Figure 5.2: An event display of a typical 300 MeV electron track is shown. The Monte Carlo emission point is given for every optical photon created in the event. The initial track produces photons (which produce no light) that create e^+/e^- pairs further downstream.

isotropic (i.e. scintillation light), the predicted charge is given by

$$\mu_{sci} = \Phi(E_0) \int_s \rho(E_0, s)\Omega(s)T(s)\epsilon(s)ds, \tag{5.6}$$

where $\Phi(E_0, s)$ has been separated into the total light produced, $\Phi(E_0)$, and the light emission probability along the track, $\rho(E_0, s)$. An example of $\rho(E_0, s)$ for scintillation light is given in Figure 5.3.

Cherenkov light is a bit more complicated since it is not emitted isotropically. In addition to integrating over the probability for light emission along the track path, a new factor, $g(\cos\theta, s)$, must be introduced that gives the angular distribution of the emitted light as a function of s and satisfies

$$\int_\theta g(\cos\theta, s)d(\cos\theta) = 1 \tag{5.7}$$

for all s. The predicted charge for Cherenkov emission can then be written as

$$\mu_{Cher} = \Phi(E_0) \int_s \rho(E_0, s)g(\cos\theta, s)\Omega(s)T(s)\epsilon(s)ds. \tag{5.8}$$

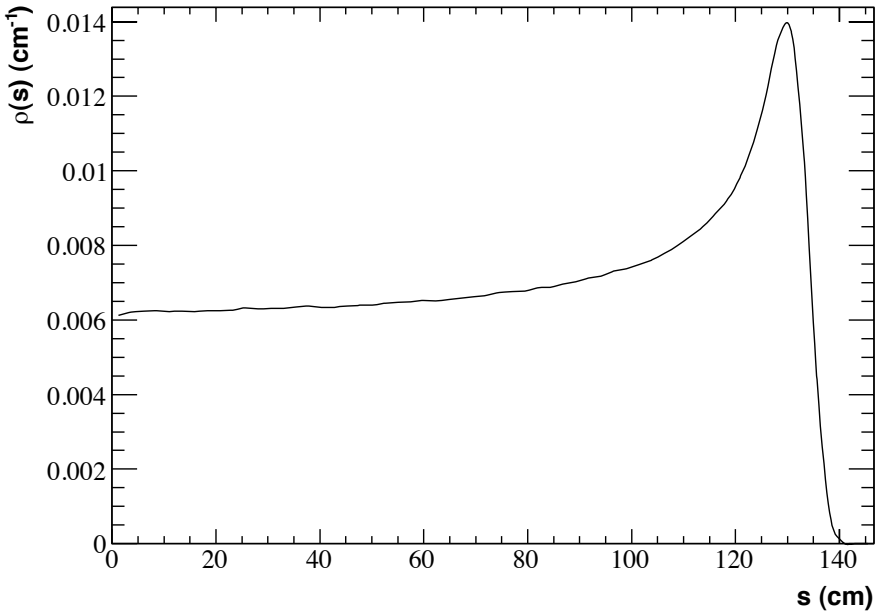

Figure 5.3: The scintillation light emission PDF, $\rho(E_0, s)$, is shown for 300 MeV "non-hadronic" pions.

The $\rho(E_0, s)$ and $g(\cos\theta, s)$ PDFs for 300 MeV pions are given in Figures 5.4 and 5.5, respectively.

The remaining contribution to the predicted charge comes from photon scattering. Much of the generated light will experience Rayleigh and Raman scattering before reaching a PMT. To account for this effect, the detector Monte Carlo is used to generate scattering tables that map out the scintillation and Cherenkov photons that reach a PMT after scattering out of their initial trajectories. The scattering tables are a function of the position and direction of each track segment, ds, and are included in the scintillation and Cherenkov integrals given in Equations 5.6 and 5.8.

The final piece of Equation 5.3 needed to calculate the charge likelihood is the charge PDF for a hit tube as a function of the predicted charge. All of the details of the track geometry, optical model properties, and photo-tube acceptance have been folded into the predicted charge. Hence, the charge PDF is only meant to characterize effects

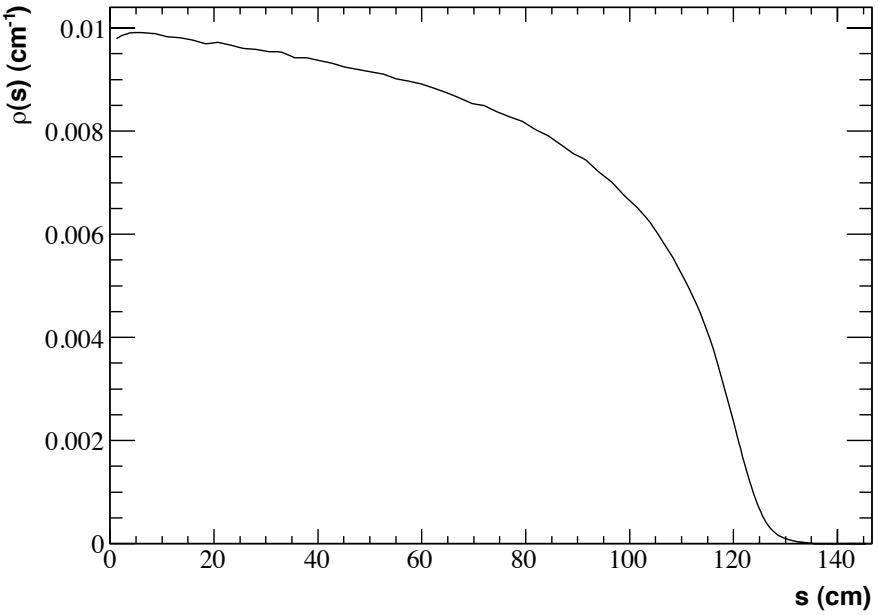

Figure 5.4: The Cherenkov light emission PDF, $\rho(E_0, s)$, is shown for 300 MeV "non-hadronic" pions.

downstream of the light propagation, such as the PMT efficiencies, the electronics, the data readout, etc., for the number of photoelectrons given by μ. Such PDFs can be empirically determined, and have been measured using the laser data [63].

5.1.2 Time Likelihood

Unlike the charge likelihood, the time likelihood cannot be simplified in terms of a "predicted time." The reason is that the charge measured by a PMT is an integrated quantity whereas the time is an instantaneous quantity. For example, if a PMT lies near the edge of a Cherenkov ring, the flux of photons it sees as a function of time might have an early peak from the prompt Cherenkov light and a later peak from a coherent contribution of scintillation light along the particle track. The predicted charge for such a configuration is just the integral of this bimodal photon arrival distribution. To determine the time PDF, the detailed shape of the bimodal distribution is

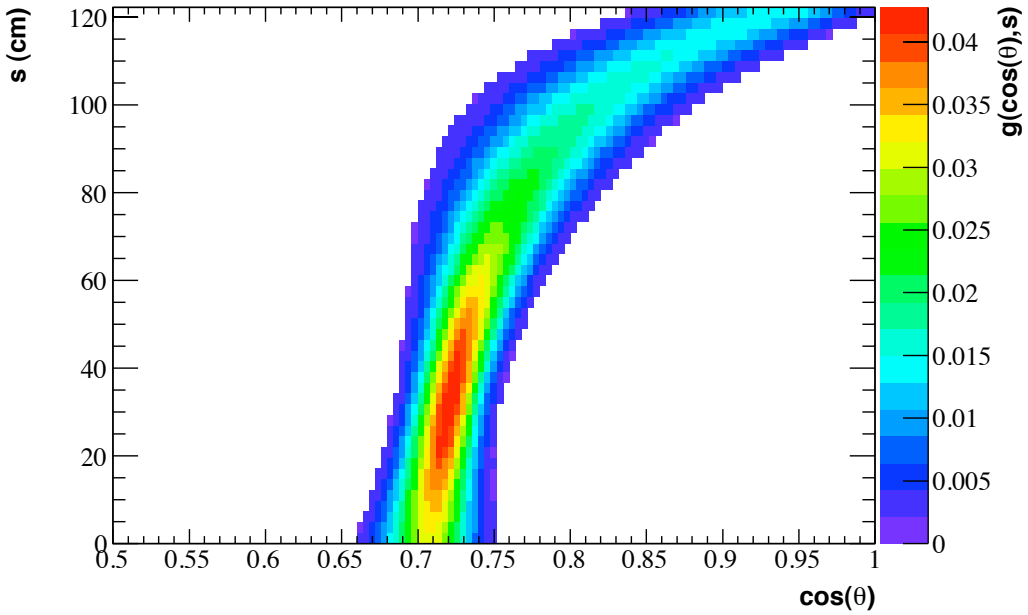

Figure 5.5: The angular light emission PDF, $g(\cos\theta, s)$, for Cherenkov light along the particle path length is shown for 300 MeV "non-hadronic" pions.

required. Therefore, a rigorously correct treatment of the time likelihood would require a tabulation of time PDFs as a function of the full seven dimensional input parameter space (defined relative to the PMT). The generation, implementation, and use of such a tabulation is beyond the capabilities of our computing resources.

In order to calculate the time PDFs, several approximations are made. Both the event time and the PMT/track distance can be removed from the problem by defining the corrected time,

$$t^c = t - T_0 - \frac{r(\Delta s_{mid}(E_0))}{c_n} - \frac{\Delta s_{mid}(E_0)}{c}, \tag{5.9}$$

where t is the measured hit time, T_0 is the event time (i.e. when the neutrino interaction took place), $\Delta s_{mid}(E_0)$ is the mean of the Cherenkov emission PDF, $r(\Delta s_{mid}(E_0))$ is the distance from the mean emission point to the PMT, and c_n and c are the speed of light in the tank and in vacuum, respectively. The corrected time is the elapsed time

between the earliest moment a photon from the mean emission point could reach the PMT, and the actual recorded hit. This reduces the time PDF tabulation to a five dimensional input space.

The remaining parameters that affect the time PDF are the energy and direction of the track, and the angular position of the track with respect to the PMT. The most important feature characterized by the relative values of these four angles is the location of the PMT with respect to the Cherenkov ring. Fortunately, this information is already well characterized by the Cherenkov-only predicted charge. The critical observation to be made is that the time PDF for either Cherenkov or scintillation light can be characterized almost completely by the Cherenkov and scintillation predicted charge in the PMT. In addition, this simplification also partially takes into account several other minor effects, such as photon attenuation and the variation of the Cherenkov flux with the photon emission angle.

To determine the primitive Cherenkov and scintillation time PDFs, $G_{Cher}(t^c; E_0, \mu_{Cher})$ and $G_{sci}(t^c; E_0, \mu_{sci})$, the detector Monte Carlo is run at several pion energies ranging from 100 to 2000 MeV, allowing only the production of either direct Cherenkov light or direct scintillation light. In each simulation, pions are generated isotropically and uniformly distributed throughout the tank (with hadronic interactions and particle decays turned off). The corrected times for each PMT hit are recorded in bins of the logarithm of the corresponding predicted charge. Each histogram is then fit to a selected parametrization based on the characteristics of the light source being considered. The direct Cherenkov corrected times are well approximated by Gaussian distributions, and the scintillation light is parametrized by the sum of two exponential functions, with fixed decay constants of 5 and 30 ns, and a Gaussian smearing width.

To perform track fits, the likelihood function must be smoothly varying to avoid the presence of false local minima; therefore, the Gaussian and exponential fits of the corrected times must be extrapolated across both predicted charge and energy in a

non-discrete fashion. To accomplish this, the fit parameters from the corrected time fits are, themselves, fit to a 6th order polynomial function of the predicted charges for each energy. An example of these fits is given in Figure 5.6. At this point, the time primitives are smooth functions of time and predicted charge at discrete energies. The same procedure is used again to smooth over energies. Each of the 7 parameters of the 6th order polynomial predicted charged fits are, themselves, fit to 4th order polynomial functions of energy, as shown in Figure 5.7.

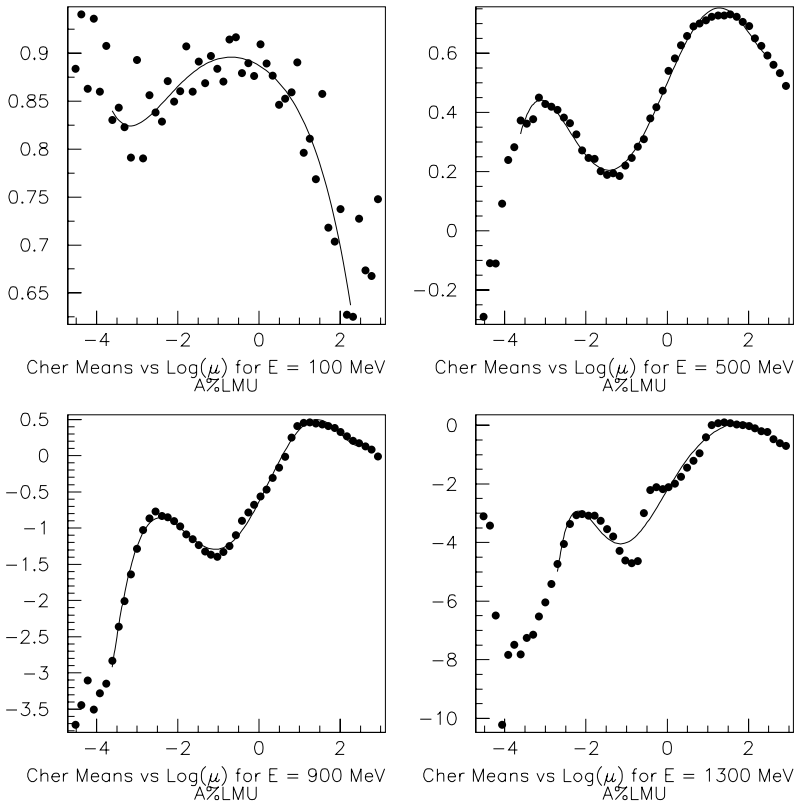

Figure 5.6: The means from the Gaussian fits to the corrected time distributions (performed in bins of predicted charge and energy) have been fit to a 6th order polynomial function of $\log(\mu)$ (still in bins of energy). The fits in four such energy bins are shown.

In order to use the primitive time PDFs to describe all the light in the event, the predicted charge is divided into two classes: prompt and late. The prompt charge is

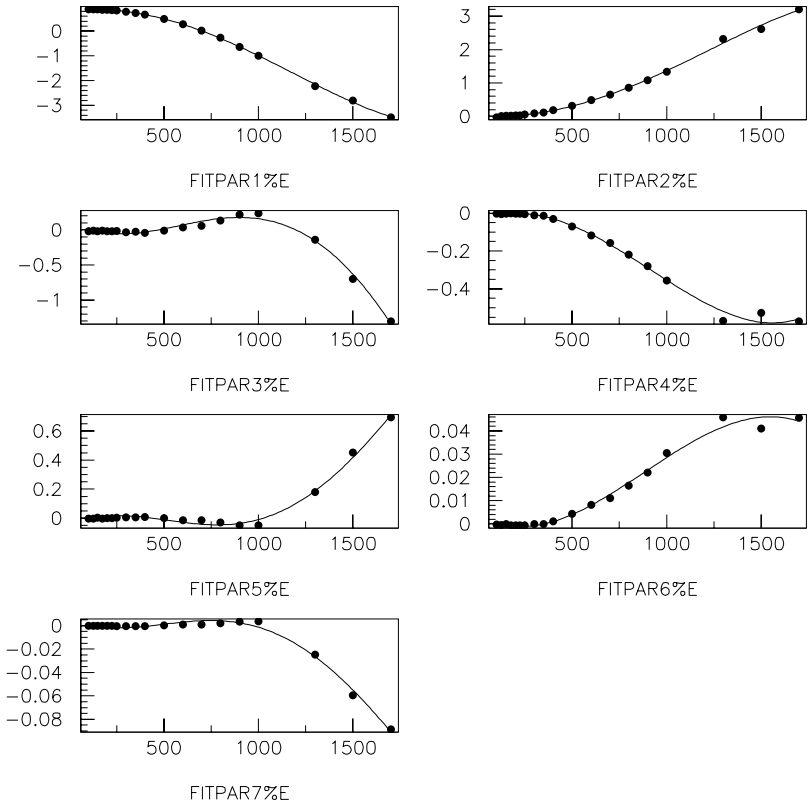

Figure 5.7: The 7 parameters that describe the 6th order polynomials produced in the fits shown in Figure 5.6 are, themselves, fit as a function of energy. The fit to each of these 7 parameters is shown.

just (most of) the direct Cherenkov predicted charge. The late charge is everything else with 5% of the Cherenkov charge included to account for PMT late pulsing.

$$\mu_{prompt} = 0.95\mu_{Cher}^{direct} \tag{5.10}$$

$$\mu_{late} = 0.05\mu_{Cher}^{direct} + \mu_{sci}^{direct} + \mu_{Cher}^{indirect} + \mu_{sci}^{indirect} \tag{5.11}$$

Since all light sources other than direct Cherenkov light have been combined into one predicted charge, the shape derived from the scintillation only distribution is implicitly used for all late light. This is a reasonable approximation since the dominant source of late light is UV florescence, which shares the same time structure as scintillation light.

To calculate the time PDF for a given set of track parameters, the following

prescription is used.

- Evaluate all 14 of the 6th order polynomials at the given track energy.
- Build the five 4th order polynomials (Cherenkov means, Cherenkov sigmas, scintillation start time, scintillation relative exponential weights, and scintillation Gaussian smearing) from the parameters extracted in the previous step, and evaluate them at the appropriate (prompt or late) predicted charge.
- Use the parameters extracted in the previous step to produce the prompt and late primitive time PDFs
- Combine the Cherenkov and scintillation PDFs to form the full corrected time PDF.

The prompt and late primitive PDFs are combined using the probabilities that the PMT was hit by at least one prompt or late photon, both of which are given by the Poisson distribution,

$$\mathcal{P}(\text{no prompt hit}; \mu_{prompt}) = \quad 1 - \mathcal{P}(\text{prompt hit}; \mu_{prompt}) \quad = e^{-\mu_{prompt}} \tag{5.12}$$

$$\mathcal{P}(\text{no late hit}; \mu_{late}) = \qquad 1 - \mathcal{P}(\text{late hit}; \mu_{late}) \qquad = e^{-\mu_{late}} \tag{5.13}$$

Any PMT that was hit by at least one prompt photon follows the prompt primitive PDF since the measured time is given by the earliest detected photon; therefore, the probability for one prompt hit sets the weight, w_p, for the prompt time PDF, and its complement sets the weight, w_l, for the late time PDF. Since the time PDF has already been multiplied by the probability that the PMT was hit by any photon (prompt or late) in Equation 5.1, only the additional probability of a prompt hit given the presence

of any hit is needed to set the weights, w_p and w_l,

$$\begin{aligned} w_p &= \mathcal{P}(\text{prompt hit} \mid \text{hit}; \mu_{prompt}(\mathbf{x})) \\ &= \frac{1 - \mathcal{P}(\text{no prompt hit}; \mu_{prompt}(\mathbf{x}))}{1 - \mathcal{P}(\text{no prompt hit}; \mu_{prompt}(\mathbf{x}))\mathcal{P}(\text{no late hit}; \mu_{late}(\mathbf{x}))} \\ &= \frac{1 - e^{-\mu_{prompt}}}{1 - e^{-\mu_{prompt}} e^{-\mu_{late}}}, \\ w_l &= 1 - w_p. \end{aligned} \tag{5.14}$$

These weights, together with the Cherenkov and scintillation primitive distributions, G_{Cher} and G_{sci}, give the full expression for the time PDF,

$$f(t; \mathbf{x}) = w_p G_{Cher}(t^c; E_0, \mu_{prompt}) + w_l G_{sci}(t^c; E_0, \mu_{late}). \tag{5.15}$$

To verify that reasonable results are produced by this method of "parametrizing the parametrization of the fit parameters," the resulting PDFs can be compared with the raw corrected time distributions from which they were produced. These comparisons are shown for a variety of energies and predicted charges in Figures 5.8 and 5.9.

5.1.3 Likelihood Maximization

The maximization of the likelihood is accomplished by minimizing Equation 5.2. The minimization is performed by MINUIT [64]. MINUIT takes as input any multi-dimensional function, and returns a set of best fit parameters. MINUIT is typically run using the "MIGRAD" minimization method, which uses derivatives of the input function with respect to the parameters to find the minimum. Unfortunately, the discrete nature of the PMTs causes the derivatives of the likelihood function to behave unreliably, and often traps the fit in false minima. Instead, the "SIMPLEX" sampling method is used, which provides much more robust results.

Before MINUIT can begin the fit minimization, an initial set of track parameters must be provided about which the fit will explore the parameter space. The values chosen for these seeding parameters can be very important for the more complicated

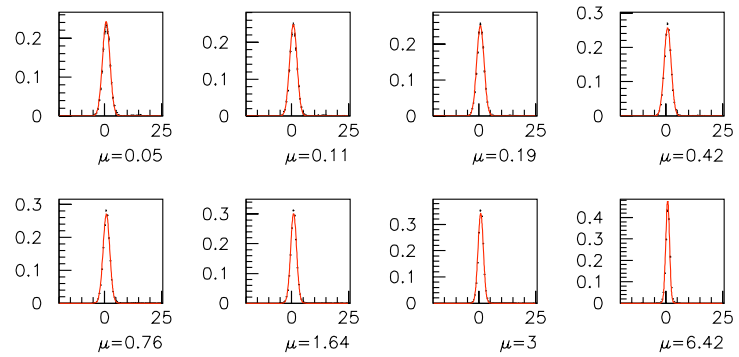

(a) Corrected time (ns) for 250 MeV "non-hadronic" pions.

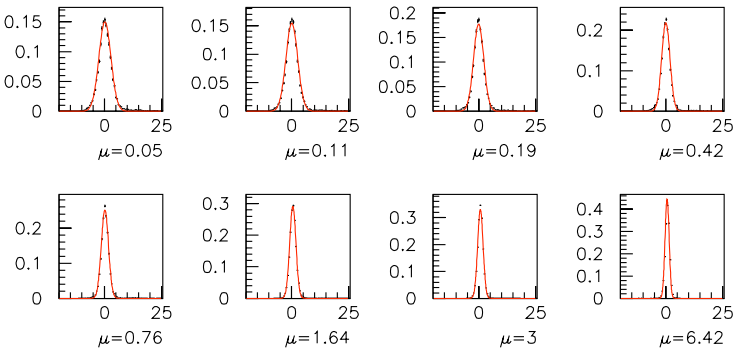

(b) Corrected time (ns) for 600 MeV "non-hadronic" pions.

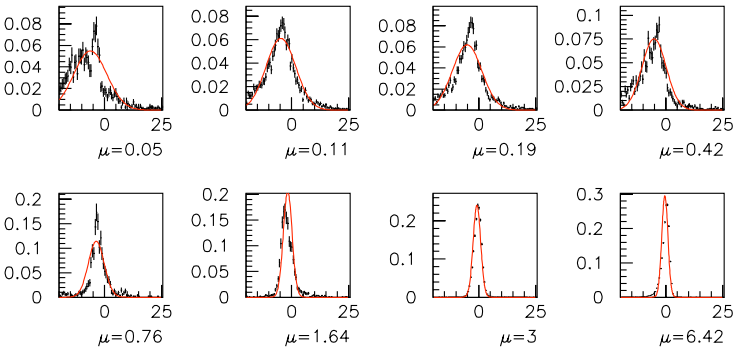

(c) Corrected time (ns) for 1500 MeV "non-hadronic" pions.

Figure 5.8: The Cherenkov corrected time distributions are compared with the primitive Cherenkov time parametrization for a variety of energies and predicted charges.

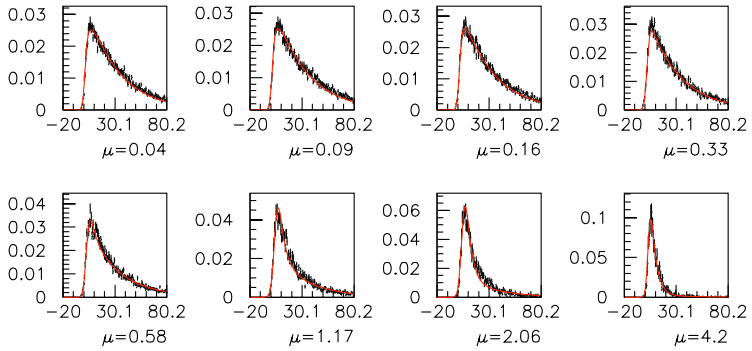

(a) Corrected time (ns) for 250 MeV "non-hadronic" pions.

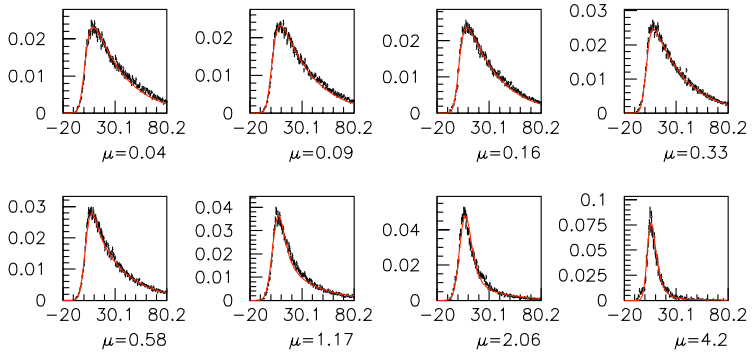

(b) Corrected time (ns) for 600 MeV "non-hadronic" pions.

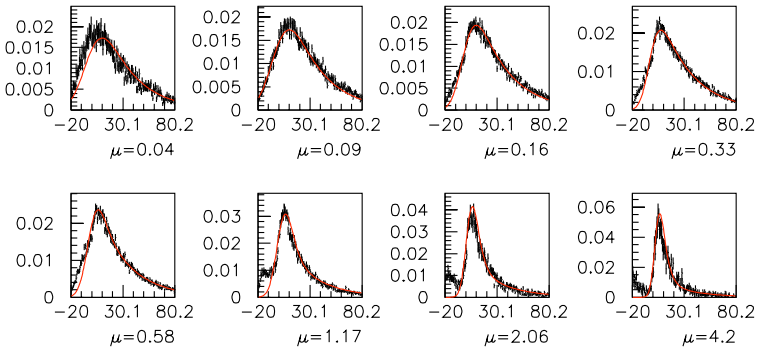

(c) Corrected time (ns) for 1500 MeV "non-hadronic" pions.

Figure 5.9: The scintillation corrected time distributions are compared with the primitive scintillation time parametrization for a variety of energies and predicted charges.

fitters discussed throughout the remainder of this chapter, but for single track events, a fit seed that generally points in the direction of the Cherenkov cone is sufficient. Fortunately, there exists a fast fitter that interprets the observed light as though it were generated by a point source. The fast fitter provides a reasonable estimate of the track parameters and is used to seed the fit [63].

5.1.4 Comparison With the Muon Fitter

The charge and time likelihood components have been calculated for muons and electrons as well [59]. To reconstruct an event, one of the three particle hypotheses must be chosen. The fitter will interpret the measured light distribution as having been produced by the hypothesized particle and return corresponding fit parameters.

With hadronic interactions removed, which is how the likelihood tables were calculated, muons and pions propagate in a similar manner. As such, the muon and pion hypothesis fits produce very similar results. The most notable exception is the kinetic energy reconstruction. Figure 5.10 shows 600 MeV muons and pions reconstructed with the muon and straight pion hypothesis fits. For either set of particles, the reconstructed muon hypothesis energy is shifted 30 MeV, or 5%, lower than the pion hypothesis energy. For each event, the energy derived from the same tank light distribution varies by 30 MeV when interpreted as either the result of a muon or a pion. Since the size of this variation is the same as the change in the reconstructed energy of both fitters when the generated particles are switched from pions to muons, the relative energy reconstruction from the two fit hypotheses exhibits the correct behavior.

Perhaps the most important reason for creating different fit hypotheses is to provide a method for particle identification. This is accomplished by fitting each event with two (or more) different particle hypotheses and comparing the likelihoods (i.e. the goodness of fit) returned by each fitter. In fits to electrons and muons, the likelihoods from the electron and muon fit hypotheses differ significantly due to the differences in

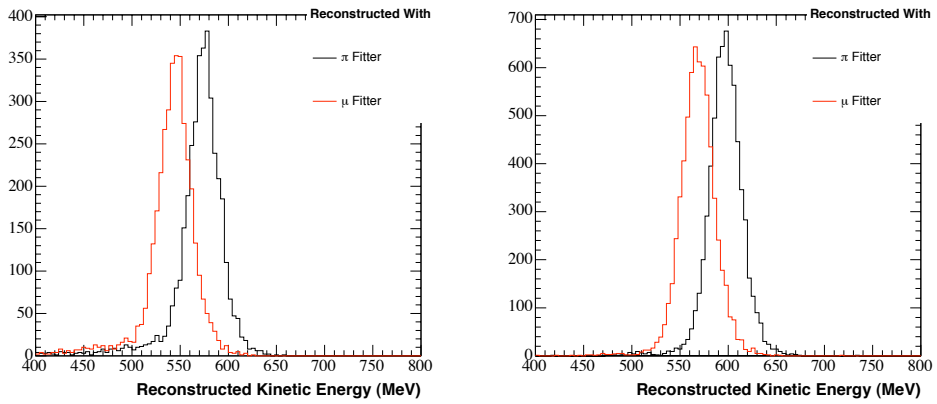

(a) 600 MeV pions with hadronic interactions and decays turned off

(b) 600 MeV muons with hadronic interactions and decays turned off

Figure 5.10: The reconstructed kinetic energies from both the muon and straight pion hypothesis fits are shown for 600 MeV pions (left) and 600 MeV muons (right). Hadronic interactions and decays have been turned off to correspond with conditions used to create the likelihoods. The 30 MeV gap in the reconstructed energies of the two fit hypotheses corresponds to the 30 MeV shift in both peaks when the generated pions are replaced by muons. (Note: All tracks in these plots have been produced at the center of the tank and point along the z-axis; track energies in this particular configuration reconstruct about 5% low overall.)

the manner in which each track propagates through the detector as shown in Figures 5.1 and 5.12 [59]. Conversely, pions without hadronic interactions and muons produce very similar trajectories through the tank. Figure 5.11 shows the logarithm of the likelihood ratio for fits to muons and non-hadronic pions. The average likelihood ratio for fits to non-hadronic pions is shifted relative to the ratio for muons, but the size of the shift is too small to provide any meaningful particle separation. The improvement in particle identification is the topic of the next section.

5.2 Pion Reconstruction

In the absence of hadronic interactions, pions and muons are nearly indistinguishable, as demonstrated in Figure 5.11. Fortunately, pions do interact hadronically, and

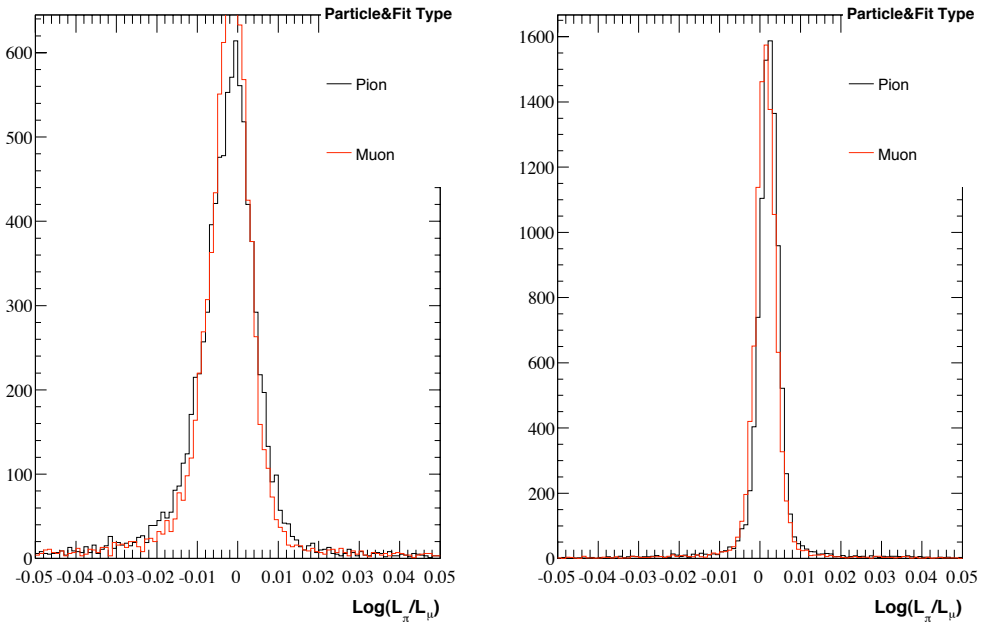

(a) 300 MeV muons and pions

(b) 600 MeV muons and pions

Figure 5.11: A comparison of the muon and straight pion hypothesis fit likelihoods is shown. The plotted variable is the logarithm of the muon/pion hypothesis fit likelihood ratio. Muons (red) and pions (black) without hadronic interactions were generated at 300 (left) and 600 MeV (right). For 300 MeV pions, which are more indicative of a typical CCπ^+ pion energy, there is no muon/pion separation. At 600 MeV, the fits to pions are shifted slightly higher than the fits to muons.

when such an interaction occurs, it produces a very distinct signature. The characteristic straight pion trajectory experiences a sharp change in direction at the interaction point. These "kinked" particle tracks offer a measurable characteristic of pion propagation to exploit with the appropriate particle identification algorithm. The hadronic debris produced in the interaction is almost always below Cherenkov threshold, and thus contributes only a slight increase to the late time charge distribution. An example of a typical pion trajectory is given in Figure 5.12.

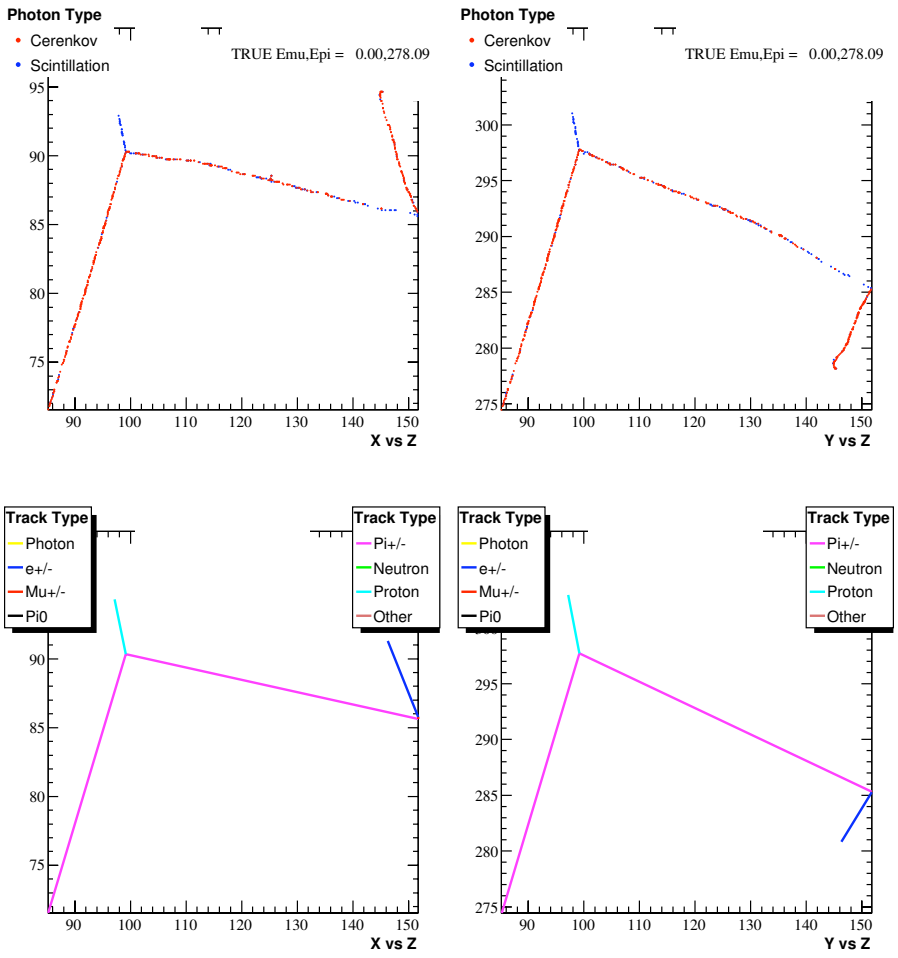

Figure 5.12: An event display for a typical pion track is shown. The top plots show the emission point of every optical photon in the event. The bottom plots give the identity of each particle emerging from a hadronic interaction or decay. A hadronic interaction occurs (at z = 100 cm) that emits a sub-Cherenkov proton and causes a sharp "kink" in the pion trajectory.

5.2.1 Fitting Kinked Tracks

To properly reconstruct pions, the likelihood method described in Section 5.1.1 must be slightly altered. One way to account for the hadronic interactions would be to regenerate the charge and time likelihood tables with hadronic interactions turned on. This method, however, would essentially average over the entire space of kinked trajectories and force the resulting light distributions into a straight line track hypoth-

esis, thus worsening the resolution on the track energy and direction. Instead, the track hypothesis is altered to allow for the reconstruction of a kinked track trajectory.

To fit a kinked track trajectory, the initial set of seven track parameters must be expanded to include four new parameters.

- ΔE_{up} is the amount of energy lost in the track from the moment it is created until the hadronic interaction takes place. This quantity characterizes the length of the upstream portion of the kinked track.

- ΔE_{kink} is the amount of energy lost by the pion in the hadronic interaction. This parameter allows the fitter to start the downstream portion of the track at an energy lower than $E_0 - \Delta E_{up}$.

- θ_{down} and ϕ_{down} specify the direction of the downstream (i.e. post-kink) portion of the track in tank coordinates.

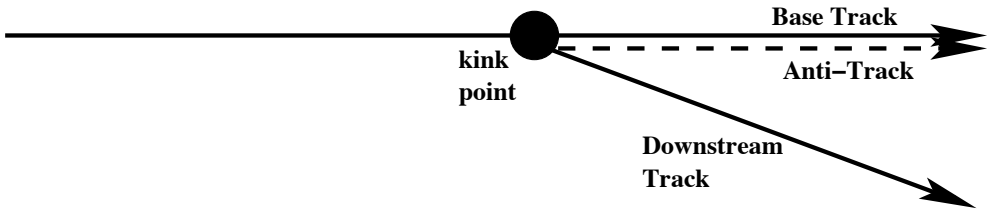

Figure 5.13: The composition of a kinked track is shown. The base track provides the charge prediction for the upstream portion of the track. The anti-track charge prediction is subtracted from each PMT to remove the downstream portion of the base track. A third track that begins at the kink point provides the charge prediction for the downstream portion of the track.

A kinked track is built from a set of three standard straight tracks as shown in Figure 5.13. The "base track" is created at the event vertex, (X_0, Y_0, Z_0, T_0), with an energy and direction given by E_0, θ_0, and ϕ_0. Above Cherenkov threshold, the distance traveled as a function of kinetic energy lost is well approximated as a linear relationship.[1]

The value of ΔE_{up}, therefore, gives the distance along the base track between the event vertex and the kink point. The time difference is found by integrating the inverse of the velocity from the kink point to the vertex,

$$\Delta t = \frac{1}{c}\int_{x_1}^{x_2} \frac{dx}{\beta(x)} = \frac{1}{c}\int_{x_1}^{x_2} \frac{dx}{\sqrt{1-1/\gamma(x)^2}}. \tag{5.16}$$

Assuming, once again, a linear relationship between the change in kinetic energy and the distance traveled, $x(K) = sK + x_0$, the integral over distance can be shifted to an integral over kinetic energy,

$$\Delta t = \frac{1}{c}\int_{K_1}^{K_2} \frac{s \cdot dK}{\sqrt{1-\frac{m^2}{(K+m)^2}}} = \frac{sm}{c}\left[\sqrt{\left(\frac{K+m}{m}\right)^2 - 1}\right]_{K_1}^{K_2}. \tag{5.17}$$

At the kink point, a second track, known as the "anti-track," is created with a direction given by θ_0 and ϕ_0, and an energy of $E_0 - \Delta E_{up}$. The predicted charges calculated from the anti-track are subtracted from the base track predicted charges to remove contributions to the light distribution from the downstream portion of the base track. Finally, the downstream track is produced at the kink point 4-vertex with an energy given by, $E_0 - \Delta E_{up} - \Delta E_{kink}$, and a direction determined by the fit parameters, θ_{down} and ϕ_{down}.

The primitive time distributions for the upstream and downstream portions of the track are combined in a similar manner to the method used for prompt and late distributions in the straight track fitter. Each light source (prompt and late from both tracks) must again be prioritized according to the time of flight of its parent track to a given PMT. In this case, there are two prompt sources of light, one from each track segment. Priority is given to the segment with the shortest time of flight to the PMT. For the downstream track, the time of flight is calculated with respect to its center, as is done in a standard straight track fit. The upstream segment time of flight is calculated

[1] To determine the linear relationship between kinetic energy and propagation distance, $x(K) = sK + x_0$, a Monte Carlo sample of pions without hadronic interactions was produced, and the scatter plot of stopping distance versus kinetic energy was fit to a straight line between 100 and 800 MeV.

from the kink point.[2] In this way, the downstream prompt time distribution is given priority in all PMTs located in the half sphere pointed to by the downstream track. The late time light sources for both tracks are always prioritized last, and are combined by averaging the respective PDFs.

Using these criteria to define the "near" (n), "far" (f), and "late" (l) no-hit probabilities,

$$\bar{\mathcal{P}}_n \equiv \mathcal{P}_n(\text{no hit}; \mu_{prompt,n}(\mathbf{x})) = e^{-\mu_{prompt,n}} \tag{5.18}$$

$$\bar{\mathcal{P}}_f \equiv \mathcal{P}_f(\text{no hit}; \mu_{prompt,f}(\mathbf{x})) = e^{-\mu_{prompt,f}} \tag{5.19}$$

$$\bar{\mathcal{P}}_l \equiv \mathcal{P}_l(\text{no hit}; \mu_{late}(\mathbf{x})) = e^{-\mu_{late}}, \tag{5.20}$$

the weights for each of the PDFs are given by

$$w_n = \frac{1-\bar{\mathcal{P}}_n}{1-\bar{\mathcal{P}}_n\bar{\mathcal{P}}_f\bar{\mathcal{P}}_l} \tag{5.21}$$

$$w_f = \frac{1-\bar{\mathcal{P}}_f}{1-\bar{\mathcal{P}}_f\bar{\mathcal{P}}_l}(1-w_n) \tag{5.22}$$

$$w_l = 1 - w_n - w_f, \tag{5.23}$$

and the full expression for the time PDF is

$$f(t;\mathbf{x}) = w_n G_{Cher}(t_n^c; E_n, \mu_{prompt,n}) + w_f G_{Cher}(t_f^c; E_f, \mu_{prompt,f}) + w_l \hat{G}_{sci}(\hat{t}^c; E_0, \mu_{late,tot}). \tag{5.24}$$

5.2.2 Fit Seeding

The seeding of the kinked fitter begins with a straight track fit. The result of the straight fit is assumed to point at either the filled-in ring of the downstream track or the open ring formed by the upstream track segment. To determine the direction

[2] The corrected time for the upstream track is still calculated with respect to the center of the base track. The predicted prompt charge on a PMT depends only on the portion of the track from which it was created, so although the predicted charge contributions from the post-kink section of the base track have been removed in the anti-track subtraction, the time PDFs calculated in the non-subtracted PMTs still require the same definition of corrected time used to build the charge dependent time likelihood tables.

of the other ring, a downstream track segment is attached to the straight track fit result, and a scan of the downstream directions is performed over 100 equally spaced directions. At each point in the scan, the likelihood function is evaluated at several energies, ranging from one to two times the one track fit energy, and each energy is divided between the upstream and downstream portions of the track in several different fractions. This process is repeated under the assumption that the straight track fit instead found the downstream track segment. The best likelihood returned by both the upstream and downstream scans determines the seed point for the fit. A sample fit is shown in Figure 5.14.

A scan of the angular phase space is conducted to avoid starting the fit near a local, but not global, minimum. The shape of the likelihood surface gets significantly altered in the presence of another ring, so there is much more potential for the fitter to get trapped in the wrong part of phase space. A scan coarsely surveys the phase space in its entirety, and provides the fitter with the best opportunity to correctly reconstruct the event.

5.2.3 Particle Identification

The separation ability of the kinked pion fitter is displayed in Figure 5.15. The reconstructed pion peak is shifted relative to the reconstructed muons. More significantly, the pion distribution has a much larger tail of events that extend away from the muon portion of the likelihood ratio. These are events where kinked trajectories occurred and were successfully found by the fitter. The peak region is mostly composed of lower energy pions that may not have developed a kink, or produced downstream portions that are near or below the Cherenkov energy threshold. A small population of muon events extend into the pion region as well. Although muons do not interact hadronically, it is possible to produce kink-like trajectories over small distances via hard Coulomb scattering. The kinked hypothesis will fit these events much better as well.

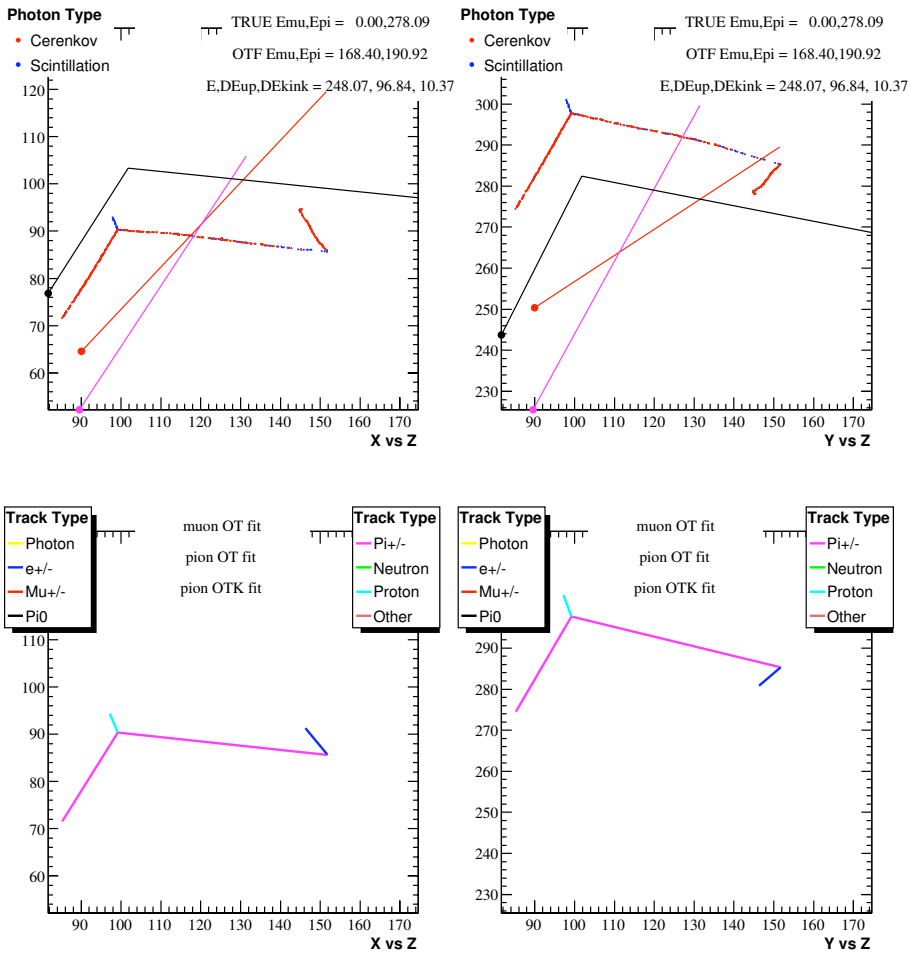

Figure 5.14: The event in Figure 5.12 has been fit with a muon hypothesis (red line), a straight pion hypothesis (magenta line), and a kinked pion hypothesis (black line). The straight fitters underestimate the track energy by more than 30%. The kinked fitter provides an energy estimate that is about 10% low, which is near the edge of the energy resolution.

The μ/π separation provided by the kinked pion fitter is not perfect. There is no ideal location to place a cut that would reject a large population of muons while retaining a significant fraction of pions. The goal of this analysis, however, is to reconstruct events with both a muon and a pion present, and to determine the identity of each track. In that case, the separation power indicated by Figure 5.15 is doubled, and the probability that at least one track travels a significant distance, and thus increases the discriminating power of the fitters, is increased.

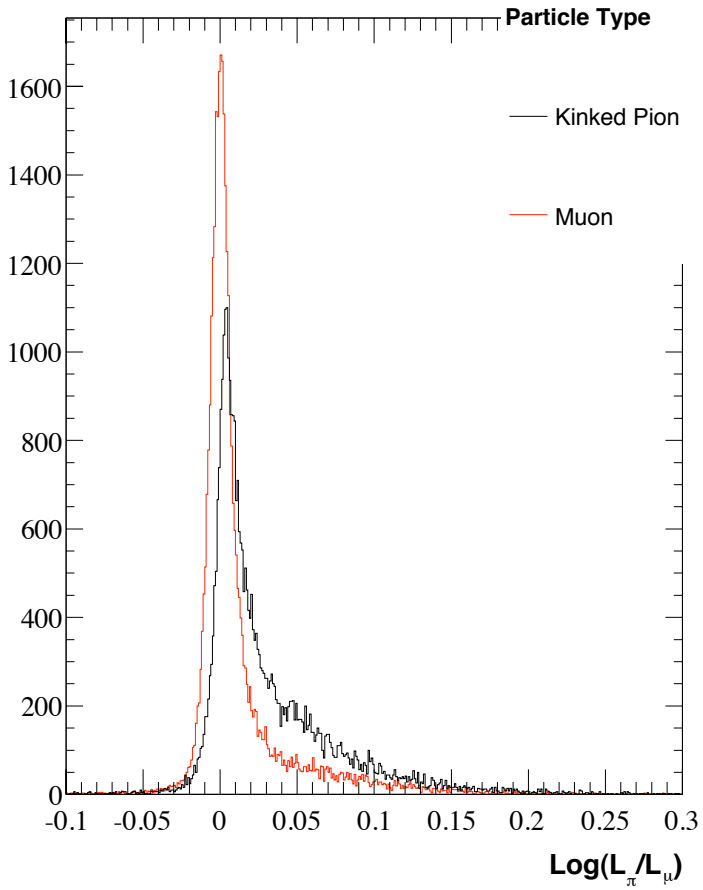

Figure 5.15: The straight muon and kinked pion likelihood ratios are shown for muons (red) and pions (black) with full hadronic interactions and decays. The particles were generated from a flat kinetic energy distribution ranging from 50 to 450 MeV to more closely represent the true pion energy spectrum of CCπ^+ events. Unlike the 300 MeV straight fitter comparison in Figure 5.11, there is now clear separation in the muon and pion peaks, and a large excess of pion events is seen along the high side tail.

5.2.4 Fit Resolution

Although the main motivation for developing a kinked track fitter was to provide a means for separating muons from pions, the improved modeling of pion trajectories results in superior event reconstruction. The energy resolutions from both the straight and kinked pion fitters are shown in Figure 5.16(a). The straight pion fitter recon-

structs pion energies 10% low, whereas the kinked fitter resolution function peaks at zero. In addition, the "shoulder" feature just below the peak of the resolution function, where the reconstructed energy underestimates the true pion energy, is reduced by the kinked pion fitter. The two-dimensional plot of the resolution versus the true energy in Figure 5.16(b) shows that the shoulder comes from higher energy pions that can produce multi-kink events and cause larger pion energy losses at each kink. The pion direction reconstruction is also significantly improved with the kinked fitter, as shown in Figure 5.17. The event populations in each of the first few bins of the angle between the reconstructed and true directions are nearly doubled in the kinked fitter relative to the straight fitter.

5.3 The CCπ^+ Fitter

With the ability to reconstruct charged pions, a full CCπ^+ fitter is formed by simultaneously fitting for a straight muon and a kinked pion. A CCπ^+ fit has 14 parameters:

- (X_0, Y_0, Z_0, T_0): the event 4-vertex
- E_μ: the initial energy of the muon track
- (θ_μ, ϕ_μ): the initial direction of the muon track
- E_π: the initial energy of the pion track
- (θ_π, ϕ_μ): the initial direction of the pion track
- ΔE_{up}: the energy lost by the pion track before the kink
- ΔE_{kink}: the energy lost by the pion track in the kink
- $(\theta_{down}, \phi_{down})$: the direction of the downstream segment of the pion track

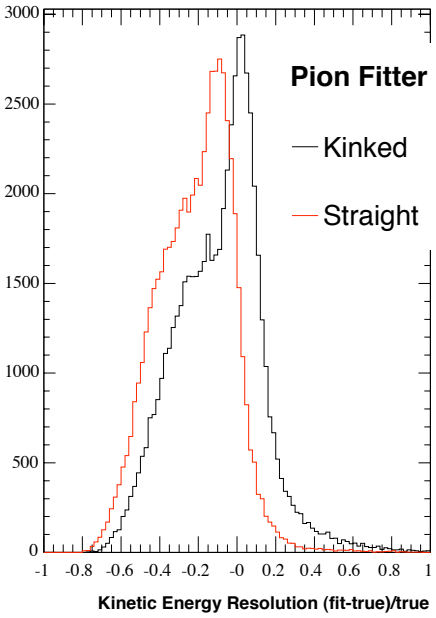

(a) Pion kinetic energy resolution from the straight and kinked pion fits

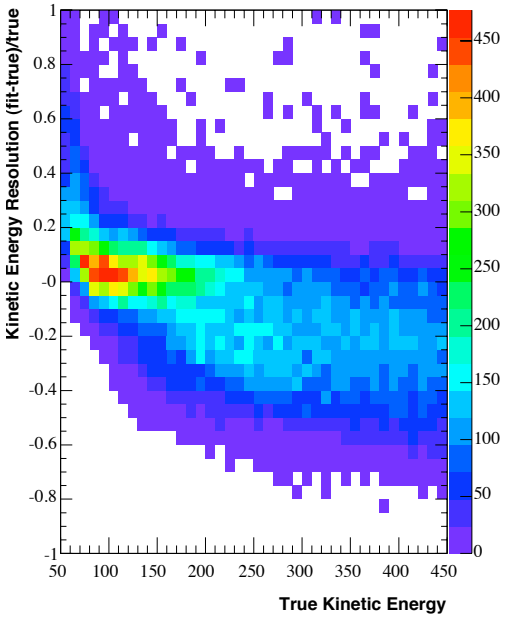

(b) The pion kinetic energy resolution as a function of true pion kinetic energy from the kinked pion fit

Figure 5.16: The reconstructed pion energy resolution is shown for both the straight and kinked pion fitters (left). The kinked fitter resolution is also plotted versus the true pion energy (right). The two-dimensional plots indicate that the low fit energy "shoulder" is caused by higher energy pions. The low energy shoulder is significantly reduced in the kinked fitter, and rather than being 10% low, as is the case with the straight fitter, the peak of the kinked fitter resolution function is centered at zero.

Just as in the kinked pion fitter, the predicted charges from all track segments (upstream pion, downstream pion, and muon) are summed to get the total predicted charge for each PMT. The time PDF follows the same prescription given in Equations 5.21-5.24, with an additional prompt source from the muon that is prioritized according to the photon time of flight from the center of the track to the PMT.

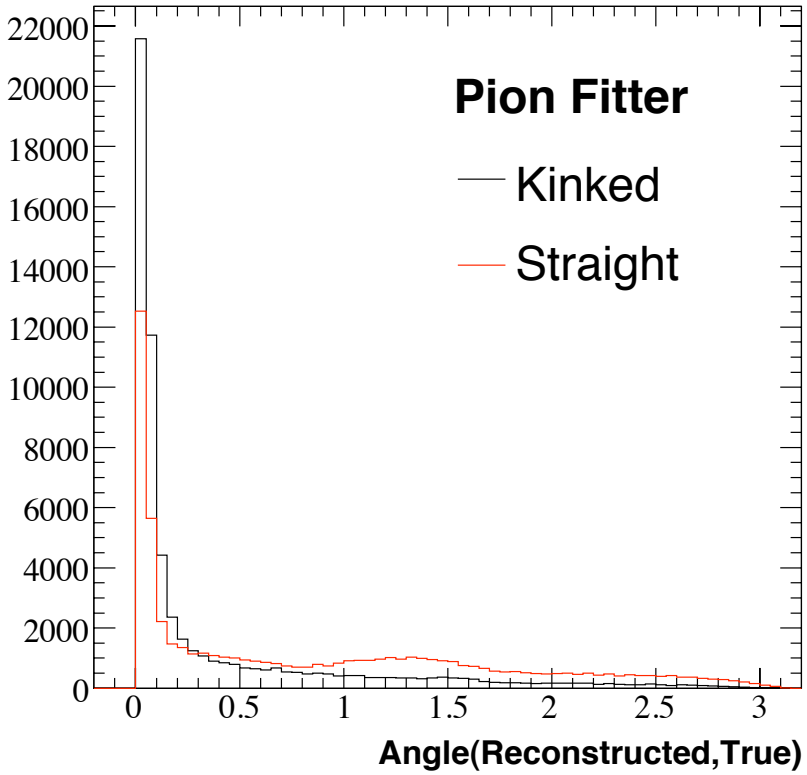

Figure 5.17: The angle between the reconstructed and true pion directions is shown for both the straight and kinked pion fitters. The population in the lowest few bins where the properly reconstructed events lie is nearly twice as large for the kinked fitter.

5.3.1 Fit Seeding

Each CCπ^+ event is assumed to have three Cherenkov rings from the three track segments in the event: the upstream pion segment, the downstream pion segment, and the muon track. Each ring is found in succession using intermediate two and three track likelihood functions. The three tracks are then pieced together in several different pairings to create the kinked pion track and the straight muon track. The pairing that produces the best likelihood is used to seed the CCπ^+ fitter.

The first of the three rings is found by performing a one track fit. The results of the fit are frozen in place, and a scan for a second track is performed over 100 equally

spaced directions. At each scan point, a two track likelihood function is evaluated, and the configuration that gives the best likelihood value sets the direction of the second track. The one track fit result is held in place during the likelihood scan to effectively cancel out the prompt predicted charge from the first Cherenkov ring. This minimizes the effect of the first ring on the shape of the likelihood surface during the scan for the second ring. The two track scan point that returns the best likelihood value is used to seed a full two track fit. The two track fit adjusts both directions and redistributes the amount of energy in each track. This process is repeated by freezing the result of the two track fit and scanning for a third track using a three track likelihood function. The result of the scan seeds a full three track fit.

The likelihood scans are not very sensitive to the energy chosen for the new track. The energy mainly just sets the prediction for the diameter of the Cherenkov ring, so the scan will usually locate a ring even if the predicted diameter is incorrect. The excess light generated by an energy overestimate, for example, results in a worse likelihood than the proper energy would have produced, but this extra energy is present at all scan points so the relative likelihoods are mostly unaffected. For the two track scan, an energy of 200 MeV has been chosen, which is near the average pion energy in CCπ^+ events. In the three track scan, the remaining unidentified track typically has a lower energy than the tracks returned by the two track fit, so the scan energy placed midway between the lower of the two found tracks and 60 MeV, which is slightly above the pion Cherenkov energy threshold.

Although the choice of the scan track energy has little effect on the ability of the scans to find the proper track directions, it can affect the energy reconstruction. At each intermediate fit stage, the seed track directions and event vertex have been determined much more precisely than the track energies. The energies from previous fits are usually overestimates of the true ring energies to account for some of the additional unfit light in the event, and the scan energy is an ad hoc choice. Since there is no convenient

way to specify to MINUIT which variables have better seed values than others, a fit is performed where only the track energies are varied before the full two or three track fit is performed. The final muon resolution from the full CCπ^+ fitter is shown with and without an extra energy fit stage in Figure 5.18. The extra energy fits improve the correlation between fit and true energies, and the peak is shifted closer to zero.

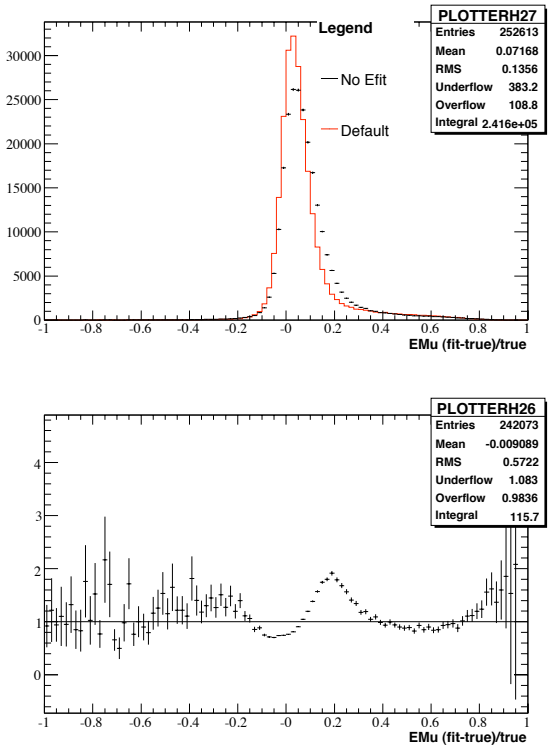

Figure 5.18: The muon energy resolution is shown for the default Monte Carlo, and the Monte Carlo absent the extra energy fit (EFit) stages of the fit seeding process. The lower plot shows the ratio of the two distributions. The EFit Monte Carlo has a smaller width, and the peak is shifted closer to zero.

Once three tracks are found that characterize the Cherenkov rings in the event, they are combined to form a straight muon and a kinked pion. In a CCπ^+ event, two of the tracks found in the three track fit point to rings that are properly characterized by the likelihood tables, the muon ring and the downstream pion ring. The other track points to the upstream pion ring, which is the result of a track segment, and

therefore not a filled in ring. Since the reconstructed track energy is mostly driven by the outer diameter of the ring, the straight track approximation of this ring only slightly underestimates the total pion energy to compensate for the missing charge at the center of the ring. Therefore, as the three tracks are combined, only pairings where the downstream pion track has a lower energy than the upstream pion track are allowed. This reduces the number of possible groupings to three. Each of these three seeds is passed to the full CCπ^+ fitter, and the fit that produces the best likelihood is chosen. A series of event displays for each step of the seeding and fit procedure are shown in Appendix A.

5.3.2 Fit Results

The kinetic energy resolutions for the muon and pion tracks are given in Figure 5.19. The muon kinetic energy has a small tail at low reconstructed energy due to μ/π mispairing.[3] The reconstructed pion kinetic energy has the same low energy shoulder from high energy particles seen in the pion-only fit in Figure 5.16(a). In addition, the fitter tends to place about 5% too much energy in the muon track at the expense of the pion track.

Although the pion energy fit is more accurate at low track energies, the opposite is true for the reconstructed pion direction. The track direction reconstruction relies on the existence of a well defined Cherenkov ring from the upstream pion track segment. 20% of the generated pion kinetic energy spectrum lies below 70 MeV. This corresponds to an above-Cherenkov propagation distance of less than 10 cm, which is typically insufficient to determine the direction. For comparison, only 1% of muons are generated below 70 MeV. In addition, the pion interaction length in mineral oil is approximately 1 m [1], which means 10% of all pions will have upstream segments shorter than 10 cm. The

[3] The pairing is determined by forming the angle between reconstructed and true track directions for all four such pairings (μ_{rec}/μ_{true}, π_{rec}/π_{true}, μ_{rec}/π_{true}, and π_{rec}/μ_{true}). If the smallest angle is between like particles (μ_{rec}/μ_{true} or π_{rec}/π_{true}), then the event is said to be paired correctly.

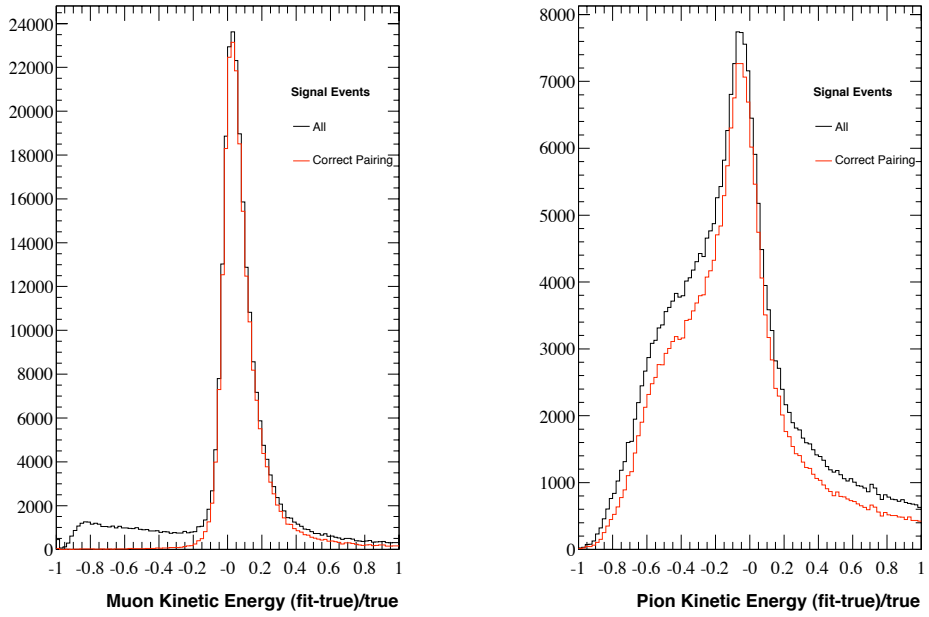

(a) Muon kinetic energy resolution

(b) Pion kinetic energy resolution

Figure 5.19: The kinetic energy resolution is shown for muons (left) and pions (right) for all signal events and correctly paired signal events. Most of the low fit energy muon tail is due to mispaired events. The pion distribution shows the same reconstructed low energy shoulder seen in the pion-only fit in Figure 5.16(a).

fitter reconstructs pions to within 300 mr of the true direction 50% of the time, and the μ/π misidentification rate is 20%.

The ability of the fitter to correctly reconstruct both the muon and the pion directions is shown in Figure 5.20. The reconstructed angle between the muon and pion is plotted against the larger of the two reconstructed/true angles. A perfect fitter would place all events in the lowest column where both reconstructed/true angles are zero, which has the largest population of events in Figure 5.20. The other significant event population is along the diagonal of the plot. These are events where the fitter has misidentified the muon as a pion and vice versa. In such cases, the angle between both the true and reconstructed muon and the true and reconstructed pion will be roughly

equivalent to the reconstructed μ/π angle.

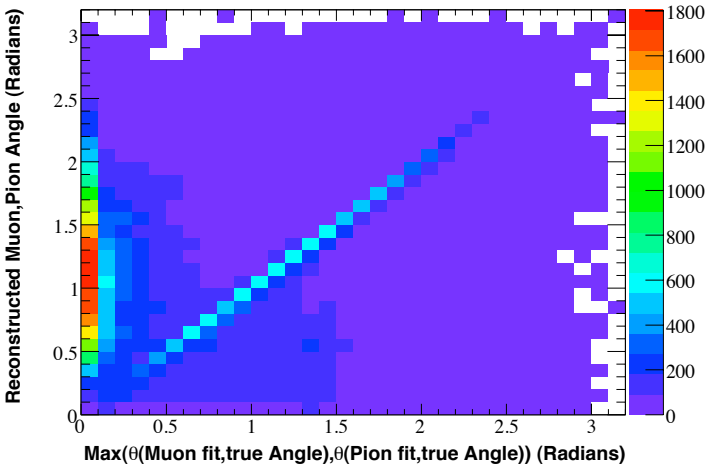

Figure 5.20: The reconstructed angle between the muon and pion directions is shown versus the larger (i.e. worse reconstructed) of the two reconstructed/true angles, $\theta(\mu_{rec}, \mu_{true})$ and $\theta(\pi_{rec}, \pi_{true})$. The events in the left-most columns represent events where both tracks have been properly reconstructed. The events where the tracks have been misidentified appear along the diagonal.

5.3.2.1 Neutrino Energy

With reconstructed energies and directions for the both the muon and the pion, the energy of the incident neutrino can be determined. Assuming the target nucleon is at rest and the remaining, unmeasured final state particle is a nucleon, the neutrino energy is specified by 4-momentum conservation,

$$E_\nu = \frac{m_\mu^2 + m_\pi^2 - 2m_N(E_\mu + E_\pi) + 2p_\mu \cdot p_\pi}{2\left(E_\mu + E_\pi - |\mathbf{p}_\mu|\cos\theta_{\nu,\mu} - |\mathbf{p}_\pi|\cos\theta_{\nu,\pi} - m_N\right)}, \tag{5.25}$$

where m_p, E_p, p_p, and $|\mathbf{p}_p|$ are the mass, energy, 4-momentum, and 3-momentum magnitude of particle p in the detector frame, and $\theta_{\nu,\mu}(\theta_{\nu,\pi})$ is the angle between the directions of the muon(pion) and the neutrino. The neutrino direction is determined by the event vertex location and the mean neutrino emission point from the beam Monte Carlo prediction, although the large distance between the beam and the detector means this

angle is never larger than one degree. The comparison between reconstructed and true neutrino energy is given in Figure 5.21. The resolution is 15% over most of the sensitive range, with a slight increase at the highest energies.

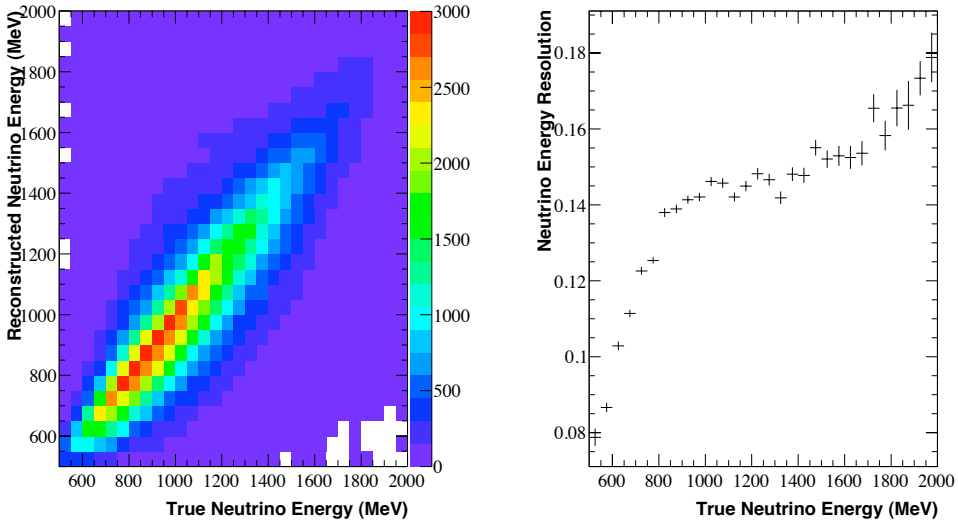

(a) Reconstructed versus true neutrino energy

(b) Neutrino energy resolution versus true neutrino energy

Figure 5.21: The comparison of reconstructed and true neutrino energy is shown (left) along with the Gaussian widths of the energy resolution distribution as a function of true neutrino energy (right). The resolution is about 15% over most of the energy range to which the analysis is sensitive.

The inability of the fitter to properly reconstruct all pion directions has little impact on the neutrino energy reconstruction. These misreconstructed events are dominated by low energy pions and events where the muon and pion tracks were misidentifed. The neutrino energy calculation becomes less sensitive to the reconstructed pion direction as the pion energy is reduced. Events with misidentified tracks that are otherwise well reconstructed will produce nearly the same neutrino energy, since muons and pions have similar masses.

5.3.2.2 Δ Mass

By making the aforementioned assumptions required to calculate the neutrino energy, the kinematics of the interaction are fully specified. Previous attempts to measure CCπ^+ interactions by reconstructing only the muon required the additional assumption that the recoiling nucleon was an on-shell Δ baryon [65]. Since the width of the Δ resonance is about 10% of its mass, this assumption results an irreducible contribution neutrino energy resolution. By measuring the pion as well, the Δ mass constraint has been removed in the present analysis.

The absence of a Δ mass constraint means that the $\pi^+ + N$ invariant mass, which is dominated by the Δ resonance mass, can be measured. Figure 5.22 shows the reconstructed $\pi^+ + N$ mass, as well as a breakdown of the background composition. The fact that the CCQE background events peak sharply near threshold lends credence to the quality of the reconstruction since those events typically do not produce a pion. A comparison of reconstructed data and Monte Carlo with full systematic errors is given in Figure B.19.

5.3.2.3 Q^2

The final variable measured in this analysis is the 4-momentum transfer, q, from the leptonic current to the hadronic portion of the decay, which is characterized by its relativistic invariant, $Q^2 = -q^2$. Since Q^2 is a property of the exchanged W boson, it is completely specified by the change in the leptonic current. However, this also means that, unlike the neutrino energy calculation, the reconstructed Q^2 distribution is quite sensitive to μ/π misidentification. Figure 5.23(a) shows the fractional error in the reconstructed Q^2 distribution, normalized in columns of true Q^2. Most of the columns peak near zero, but at high Q^2, a second population of events appears in which the fit underestimates the true Q^2. These are events that are dominated by a high

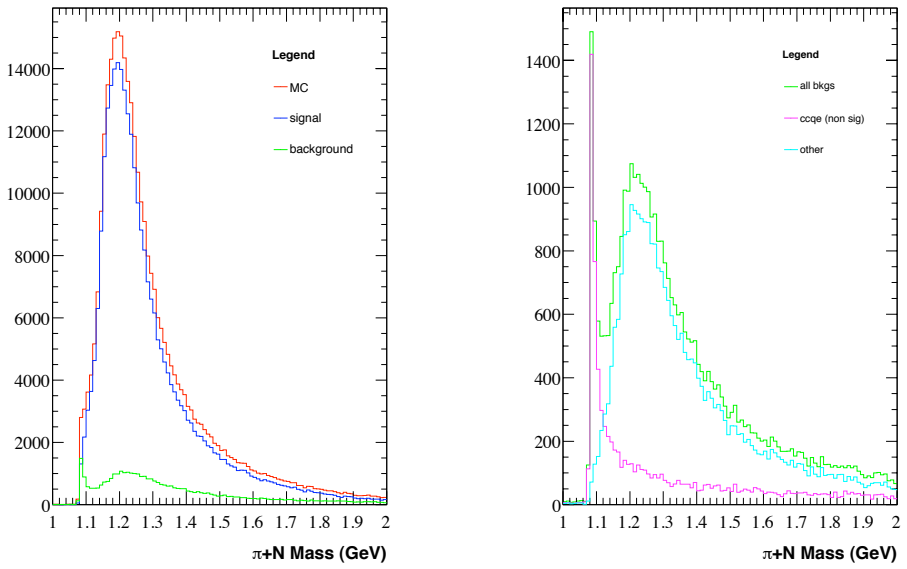

(a) The total Monte Carlo prediction (red) is divided into signal (blue) and background (green) components.

(b) The background distribution (green) is divided into contributions from CCQE (magenta) and all other backgrounds (cyan).

Figure 5.22: The reconstructed Monte Carlo $\pi^+ + N$ distribution is shown in the left plot for signal and background events. On the right, the background distribution is divided into CCQE background events, and all other backgrounds. Since the CCQE events do not contain a pion, they are peaked near threshold ($m_\pi + m_N$). The definition of signal events is given in Section 6.2.

energy muon that has been misidentified as a pion, giving the impression that most of the neutrino momentum was transferred to the hadronic system. The resolution for correctly identified events is given as a function of true Q^2 in Figure 5.23(b).

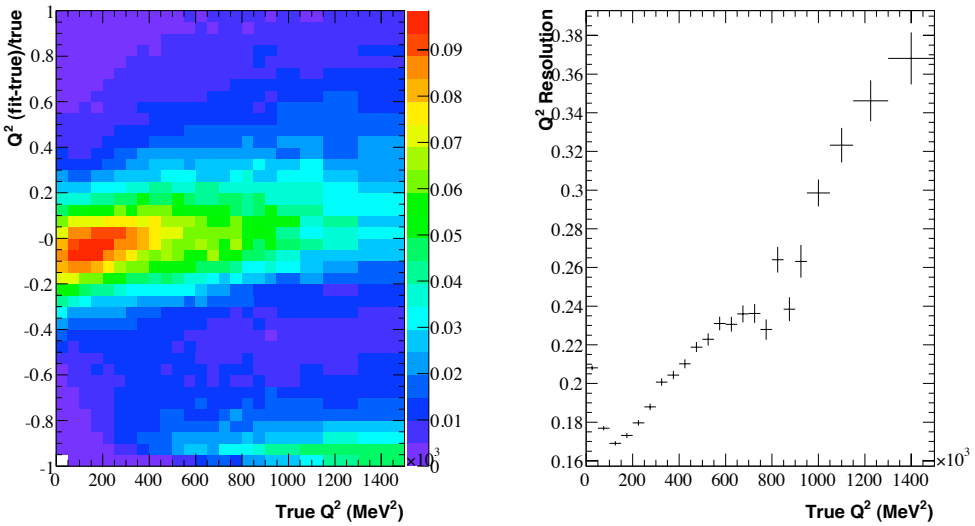

(a) Q^2 resolution versus true Q^2 (column normalized)

(b) Q^2 resolution versus true Q^2

Figure 5.23: The fractional error is plotted versus true Q^2 (left) where each true column has been normalized to one to highlight the population of misidentified events at high true Q^2, and low fit Q^2. The Gaussian width of the resolution distribution for events with correctly identified tracks is also shown (right).

Chapter 6

CCπ^+ Cross Section Analysis

The most fundamental quantities that can be measured in a particle interaction are the frequency with which the interaction takes place and the kinematics of the initial and final state particles. The results of these measurements are most conveniently expressed as cross sections. The cross section, σ, is defined as the ratio of the number of interactions, N^{int}, to the product of the number of interaction targets, N_{targ}, and the flux, Φ, which is the number of incident neutrinos per unit area,

$$\sigma = \frac{N^{int}}{N_{targ}\Phi}. \tag{6.1}$$

6.1 Cross Section Definitions

A cross section can be measured as a function of any variable in the interaction. There is, however, an important distinction to be made between initial and final state variables. A cross section measured in terms of an initial state variable, such as neutrino energy, still gives the probability that an interaction takes place; it just expresses that probability separately for each value of the initial state variable. A cross section measured as a function of a final state variable, such as muon kinetic energy, is a fundamentally different quantity that encapsulates not only the probability that the interaction takes place, but also the additional probability that the resulting muon has a particular energy. By definition, the integral over all possible muon energies restores

the original interaction probability, and, therefore, cross sections expressed in terms of a final state variable, v, are derivatives with respect to v: $\partial\sigma/\partial v$.

To perform a cross section measurement, the initial and final state dependencies of the other quantities in Equation 6.1 must be taken into account as well. The flux cannot be meaningfully expressed in terms of final state variables. For example, it is not possible to separate the number of incident neutrinos per unit area into bins of outgoing muon direction. With respect to initial state variables, the flux is an aggregate quantity (that is, the flux over an infinitesimal interval, du, of an initial state variable, u, is half as large as the flux over twice the interval, $2du$), and so, to recover the flux, the differential flux must be integrated over the desired interval,

$$\Phi\left(u_{min}; u_{max}\right) = \int_{u_{min}}^{u_{max}} \frac{\partial\Phi}{\partial u} du. \tag{6.2}$$

The number of interactions is an aggregate quantity with respect to both initial and final state variables. Put another way, the fraction of events in, for example, a given range of both neutrino energy and muon kinetic energy is well defined, and all such fractions must sum to the total number of interactions. After implementing these dependencies, Equation 6.1 can be written in its most general form in terms of M initial state variables, $u_1 \ldots u_M$, and N final state variables, $v_1 \ldots v_N$,

$$\begin{aligned} N^{int} &= N_{targ} \int_{u_1} \cdots \int_{u_M} \int_{v_1} \cdots \int_{v_N} \frac{\partial\sigma(u_1, \ldots, u_M)}{\partial v_1 \ldots \partial v_N} dv_1 \ldots dv_N \frac{\partial\Phi}{\partial u_1 \ldots \partial u_M} du_1 \ldots du_M \\ &= \int_{u_1} \cdots \int_{u_M} \int_{v_1} \cdots \int_{v_N} \frac{\partial N^{int}}{\partial v_1 \ldots \partial v_N \partial u_1 \ldots \partial u_M} dv_1 \ldots dv_N du_1 \ldots du_M. \end{aligned} \tag{6.3}$$

Cross section measurements are, by necessity, performed over finite intervals of the initial and final state variables. In order to measure a cross section in a bin, i, of an initial state variable, u, all integrals other than the integral over u in Equation 6.3 must first be performed. The final state variable integrations are straightforward. They simply return the initial state N^{int} derivatives on the second line of Equation 6.3, and

the total cross section on the first line, since the flux dependence can be factored out of all final state integrals. The initial state integrals must be treated more carefully, since both the cross section and the flux must be integrated together. This results in a cross section that is averaged over the flux shape in the initial state variables, as will be described momentarily via Equation 6.5. The remaining integral over u is performed over each bin. The number of events in bin i, N_i^{int}, can then be expressed as

$$N_i^{int} = N_{targ} \int_{u_{i,min}}^{u_{i,max}} \sigma(u) \frac{\partial \Phi}{\partial u} du = N_{targ} \left\langle \sigma \frac{\partial \Phi}{\partial u} \right\rangle_i \Delta u_i, \tag{6.4}$$

where $\left\langle \sigma \frac{\partial \Phi}{\partial u} \right\rangle_i$ is the average value of the integrand over bin i, and Δu_i is the bin width (i.e. $u_{i,max} - u_{i,min}$). The average value of the differential flux within the bin my be factored out of $\left\langle \sigma \frac{\partial \Phi}{\partial u} \right\rangle_i$, leaving only the flux shape in the average,

$$\left\langle \sigma \frac{\partial \Phi}{\partial u} \right\rangle_i \Delta u_i = \left(\left\langle \frac{\partial \Phi}{\partial u} \right\rangle_i \Delta u_i \right) \left\langle \sigma \frac{\partial \Phi}{\partial u} \Big/ \left\langle \frac{\partial \Phi}{\partial u} \right\rangle_i \right\rangle_i \equiv \Phi_i \left\langle \sigma \right\rangle_{\Phi_i}. \tag{6.5}$$

Φ_i is the integrated flux over bin i, and $\langle \sigma \rangle_{\Phi_i}$ is called the "flux averaged" cross section in bin i. Any cross section measurement is necessarily averaged over the shape of the flux in each measured bin; therefore, in the following sections we will drop the cumbersome notation $\langle \sigma \rangle_{\Phi_i}$, and instead use $\sigma(u_i)$. Substituting Equation 6.5 into Equation 6.4 gives the final expression for the flux averaged cross section in bin i of an initial state variable,

$$\sigma(u_i) \equiv \langle \sigma \rangle_{\Phi_i} = \frac{N_i^{int}}{N_{targ} \Phi_i}. \tag{6.6}$$

As mentioned previously, $\sigma(u_i)$ is also implicitly flux averaged over the full range of all other initial state variables.

To perform a cross section measurement in a bin, i, of a final state variable, v, all integrals in Equation 6.3 are performed except for the integral over v, which is performed separately in each bin,

$$N_i^{int} = N_{targ} \Phi \int_{v_{i,min}}^{v_{i,max}} \left\langle \frac{\partial \sigma}{\partial v} \right\rangle_\Phi dv = N_{targ} \Phi \left\langle \frac{\partial \sigma}{\partial v} \right\rangle_{i,\Phi} \Delta v_i. \tag{6.7}$$

Once again, the integrals over the initial state variables yield a flux averaged cross section times the integrated flux, and the right side has been rewritten in terms of the average integrand over the bin. The final expression for the differential cross section is then

$$\frac{\partial\sigma}{\partial v}(v_i) \equiv \left\langle \frac{\partial\sigma}{\partial v} \right\rangle_{i,\Phi} = \frac{N_i^{int}}{\Delta v_i N_{targ} \Phi}, \tag{6.8}$$

where the explicit flux and bin averaging notation has been dropped, as was done in Equation 6.6.

In general, the cross section can be measured in bins of any number of initial and final state variables. The generalization of the expressions in Equations 6.6 and 6.8 to multidimensional cross section measurements is achieved by separating one additional integral in Equation 6.3 into bins. The explicit form for each of the three two-dimensional cases are as follows:

$$\frac{\partial^2\sigma}{\partial v_1 \partial v_2}(v_{1i}, v_{2j}) = \frac{N_{ij}^{int}}{\Delta v_i \Delta v_j N_{targ} \Phi} \tag{6.9}$$

$$\frac{\partial\sigma}{\partial v}(u_i, v_j) = \frac{N_{ij}^{int}}{\Delta v_j N_{targ} \Phi_i} \tag{6.10}$$

$$\sigma(u_{1i}, u_{2j}) = \frac{N_{ij}^{int}}{N_{targ} \Phi_{ij}} \tag{6.11}$$

6.2 Defining the Signal: "Effective" CCπ^+ Events

In nuclear media, interaction processes must be carefully defined. A neutrino can interact with a quark, a nucleon, or a collection of several nucleons. In addition, as the particles created in the initial interaction travel through the nucleus, other types of interactions can take place such as pion absorption and charge exchange ($\pi^+ n \to \pi^0 p$). Regardless of the details of the goings on inside the nucleus, only the characteristics of particles that exit the nucleus are accessible to experiment. Of course, it is possible to use a simulation of the various types of targets and nuclear effects to attempt to extrapolate the measured quantities back to the initial interaction, but such a result

would fold in quite a bit of model dependence, and an experimental measurement is typically not the place for such an extrapolation.

In the results that follow, an "effective" CCπ^+ event is defined as any ν_μ interaction that produces a set of particles exiting the nucleus with the following composition:

- one and only one μ^-
- one and only one π^+
- any number of protons and neutrons (including zero)
- any number of multi-nucleon states (including zero)
- any number of photons (including zero)

The presence of both the μ^- and π^+ particles is a necessary requirement for CCπ^+ interactions. In coherent interactions, it is possible for the final state to contain no additional particles. Resonant interactions eject either a proton or neutron from the nucleus, and in some cases the remainder of the nucleus may be broken apart as well, which can produce other multi-nucleon fragments in the final state. Photons were allowed in the final state to avoid setting an arbitrary energy cut-off to differentiate between radiative and non-radiative events, and because radiative corrections were not implemented in the Monte Carlo simulation.

6.3 Event Selection

To perform cross section measurements, a sample of CCπ^+ events must be isolated from the data. As described in section 3.5, data from the photomultiplier tubes (PMTs) are collected in a 19.2 μs time window, which begins 4.6 μs prior to the arrival of the 1.6 μs beam pulse. These data contain two main sources of background: cosmic rays and electrons from stopped muon decays (called "Michel" electrons). By requiring less than 6 hits from PMTs in the veto region, 99.987% of cosmic rays that enter the detector in

the beam time window are rejected [28]. The Michel electron contamination comes from cosmic ray muons that enter the tank before the beginning of the beam time window and decay while data are being recorded. The maximum energy for an electron from a stopped muon decay is 52.8 MeV, which results in many less PMT hits than are created in a typical neutrino interaction. Requiring more than 175 tank hits mostly removes the Michel background. Figure 6.1 shows that after imposing the veto hits and tanks hits cuts, essentially all non-beam-related background is eliminated.

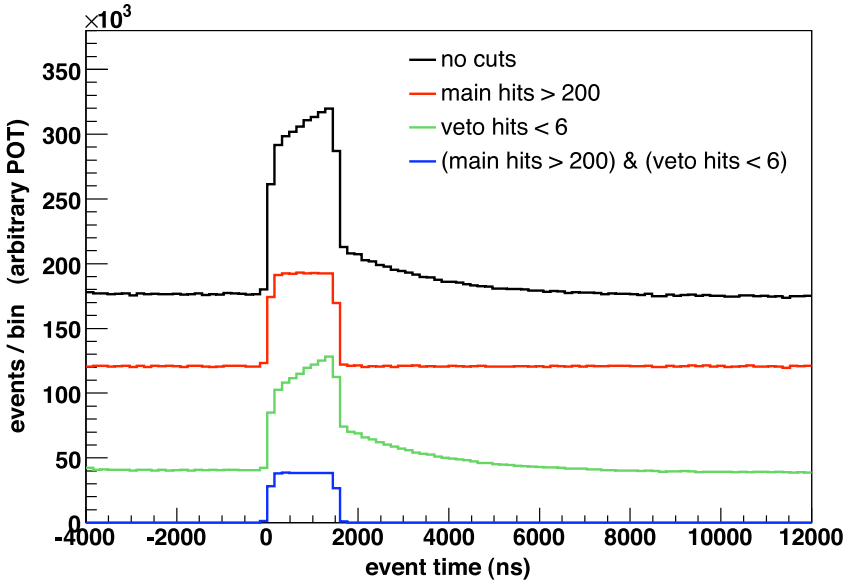

Figure 6.1: The plot shows the average hit time distribution for the first subevent (i.e. the first arrival of PMT hits) with no cuts (black), after requiring more than 200 hits in the tank region (red), after requiring less than 6 hits from PMTs in the veto region (green), and with both the tank and veto hits applied simultaneously (blue). The veto hits cut removes all events that contain particles entering or exiting the tank, and the tank hits cut removes the exponentially falling background due to decays of stopped cosmic muons that entered the tank prior to the event time window. These two cuts remove essentially all of the beam-unrelated background. Note that in the present analysis, very few Michels satisfy the three subevent cut, so the tank hits cut has been relaxed to 175.

Isolating effective CCπ^+ events from other neutrino induced backgrounds can also be accomplished simply and effectively. The PMT hits in each event are separated into time slices called subevents. A subevent is created for any group of 10 or more hits

that have no more than two 20 ns gaps between them, and spacings no larger than 10 ns otherwise. The effective CCπ^+ analysis requires exactly three subevents: one for the simultaneous muon and pion created in the initial neutrino interaction, one for the Michel electron from the decay of the stopped muon, and one for the Michel electron from the $\pi^+ \rightarrow \mu^+ \rightarrow e^+$ decay chain. Muons created in stopped pion decays have a kinetic energy of only 4.1 MeV and therefore rarely produce any light.

Most event types with comparable event rates to CCπ^+, as described in Table 4.6, are greatly reduced by the three subevents requirement. The vast majority of CCQE events are eliminated, since they typically produce only one Michel electron, which corresponds to two subevents. NCEL events produce one subevent, CCπ^0 events produce two subevents, and high multiplicity interactions such as CCmultiπ and CCDIS usually produce more than three subevents. The efficiencies for signal and background events for various combinations of cuts are given in Tables 6.1 and 6.2, respectively.

In addition to the aforementioned tank and veto hits cuts used for the initial neutrino interaction, cuts are imposed on the number of tank and veto hits in the second and third subevents as well. The same veto hits cut imposed in the first subevent is used for subevents 2 and 3 to ensure that neither subevent was caused by a cosmic ray. In effective CCπ^+ events, both subsequent subevents are from Michel electrons, so each is required to have less than 200 tank hits. The effect of these cuts on the second subevent is shown in Figure 6.2.

The final set of cuts are designed to eliminate events that occur too close to the edge of the detector. Rather than define a fixed fiducial volume, events are cut based on the distance between the tank wall and the event vertex along the trajectory of either of the two reconstructed particles. Particles that are pointed at the tank wall are poorly reconstructed. They deposit Cherenkov light in very few tubes, which allows the fitter to freely vary the energy without incurring much of a penalty in the likelihood function. Conversely, events that occur very close to the tank wall with inward pointing

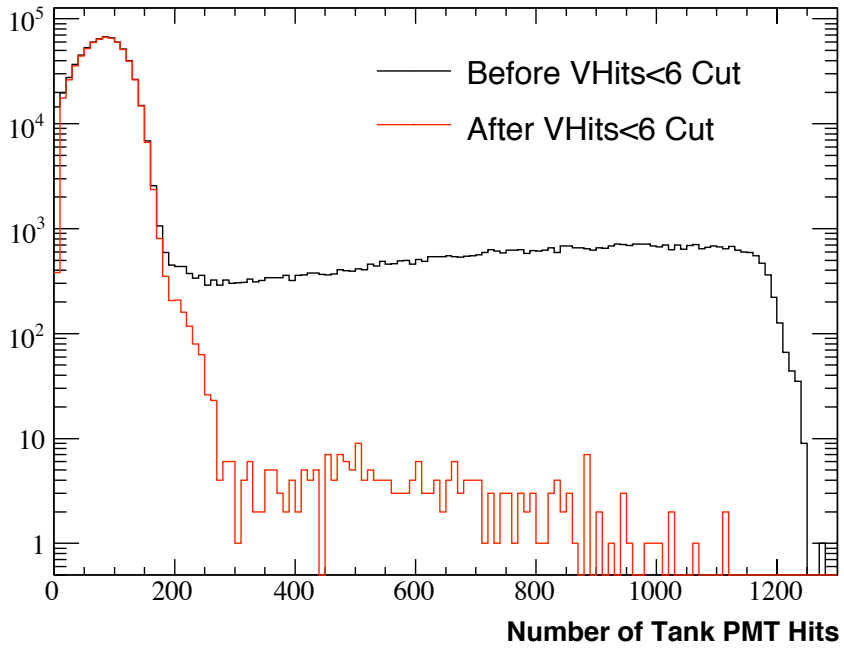

Figure 6.2: The tank hits distribution is shown for the second subevent before and after requiring less than 6 hits in the veto. The Michel electron peak is mostly unaffected, while the large tail from entering comic rays is mostly removed.

particles can be reconstructed quite well since light in the backward direction is not very important in determining particle energies and directions. The distance between the event vertex and tank wall is required to be at least 150 cm along both the muon and pion trajectories. The effect of this cut is shown in Figure 6.3.

After all cuts, 67,318 events are seen in the data with a signal efficiency of 16.9%. The sample has a purity of 87.2%, and the largest backgrounds (listed by percentage of the total sample) are from Nuance CCmultiπ events (4.0%), Nuance CCQE events (3.3%), and Nuance CCπ^+ events (1.7%). The complete list of signal and background compositions by Nuance process are given in Tables 6.1 and 6.2, respectively.

Table 6.1: The signal efficiency and purity are shown after each successive analysis cut. The additional rows give the distribution of signal events according to generated Nuance process (see Section 4.2). The final three rows list the three components of the CCπ^+ population separately. Note that Nuance CCπ^+ events are not equivalent to effective CCπ^+ events as defined in the cross section measurement. The cuts below are defined as follows: veto hits < 6 and tank hits > 175 in the first subevent (H1), exactly 3 subevents (S3), veto hits < 6 and tank hits < 200 in the second and third subevents (H23), and vertex/wall distance along the muon and pion trajectories > 150 cm (WD).

	No Cuts	H1	H1+S3	H1+S3+H23	H1+S3+H23+WD
Signal Efficiency	1.000	0.475	0.232	0.196	0.169
Signal Purity	0.187	0.236	0.605	0.863	0.872
Signal Composition	No Cuts	H1	H1+S3	H1+S3+H23	H1+S3+H23+WD
CCπ^+	0.959	0.962	0.959	0.959	0.961
CCQE	0.019	0.020	0.023	0.023	0.023
CCπ^0	0.008	0.009	0.009	0.009	0.009
CCmultiπ	0.004	0.004	0.004	0.004	0.004
CCDIS	0.009	0.005	0.004	0.004	0.003
other	0.001	0.000	0.001	0.001	0.000
CCπ^+ Components	No Cuts	H1	H1+S3	H1+S3+H23	H1+S3+H23+WD
$\nu p \rightarrow \mu^- p \pi^+$	0.750	0.761	0.766	0.767	0.764
$\nu n \rightarrow \mu^- n \pi^+$	0.136	0.134	0.126	0.124	0.124
$\nu A \rightarrow \mu^- A \pi^+$	0.073	0.066	0.068	0.068	0.072

6.4 Cross Section Measurements

The effective CCπ^+ analysis includes measurements of the cross section in terms of several variables. Since the incident neutrino flux can be almost completely characterized by its energy spectrum, the cross section has been measured as a function of neutrino energy. The other one dimensional measurements are differential cross sections as a function of various final state variables that describe the muon and pion energies and directions and Q^2. Since these one dimensional measurements are necessarily averaged over the full neutrino energy spectrum, a corresponding two dimensional measurement of each variable is made in bins of neutrino energy. Finally, the energy and direction are measured together for both the muon and pion in two double differential cross section measurements. The full list of measured cross sections is as follows:

Table 6.2: The background acceptance and the level of background contamination of the signal sample are given after each successive analysis cut. The additional rows give the distribution of background events according to generated Nuance process (see Section 4.2). Note that Nuance CCπ^+ events are not equivalent to effective CCπ^+ events as defined in the cross section measurement. The cuts below are defined as follows: veto hits < 6 and tank hits > 175 in the first subevent (H1), exactly 3 subevents (S3), veto hits < 6 and tank hits < 200 in the second and third subevents (H23), and vertex/wall distance along the muon and pion trajectories > 150 cm (WD).

	No Cuts	H1	H1+S3	H1+S3+H23	H1+S3+H23+WD
Background Acceptance	1.000	0.354	0.035	0.007	0.006
Background Contamination	0.813	0.764	0.395	0.137	0.128
Background Composition	No Cuts	H1	H1+S3	H1+S3+H23	H1+S3+H23+WD
CCmultiπ	0.017	0.020	0.076	0.295	0.309
CCQE	0.488	0.611	0.597	0.244	0.254
CCπ^+	0.071	0.094	0.110	0.128	0.131
CCmeson$B$	0.008	0.007	0.025	0.089	0.090
CCDIS	0.010	0.007	0.027	0.106	0.080
CCπ^0	0.048	0.059	0.066	0.059	0.061
$\bar{\nu}$	0.005	0.006	0.006	0.009	0.010
other	0.353	0.196	0.093	0.070	0.065

- the average cross section in bins of neutrino energy, $\sigma(E_\nu)$
- the differential cross section in Q^2, $\partial\sigma/\partial(Q^2)$
- the differential cross section in muon kinetic energy, $\partial\sigma/\partial(KE_\mu)$
- the differential cross section in the cosine of the muon-neutrino angle, $\partial\sigma/\partial(cos(\theta_{\mu,\nu}))$
- the differential cross section in pion kinetic energy, $\partial\sigma/\partial(KE_\pi)$
- the differential cross section in the cosine of the pion-neutrino angle, $\partial\sigma/\partial(cos(\theta_{\pi,\nu}))$
- the differential cross section in Q^2, measured in bins of neutrino energy, $\partial\sigma(E_\nu)/\partial(Q^2)$
- the differential cross section in muon kinetic energy, measured in bins of neutrino energy, $\partial\sigma(E_\nu)/\partial(KE_\mu)$

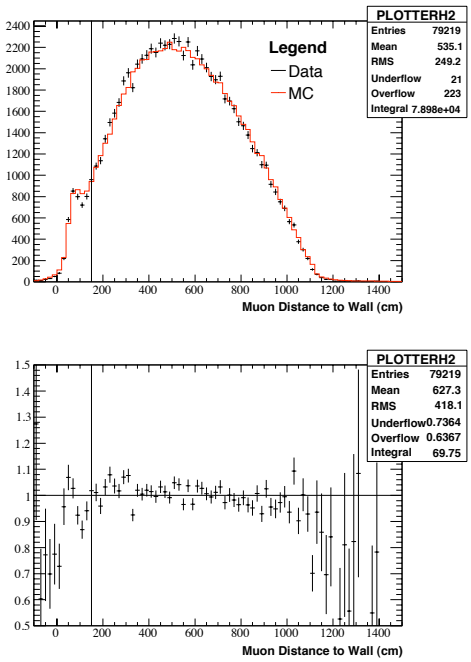

(a) Distance between the tank wall and event vertex along the muon trajectory.

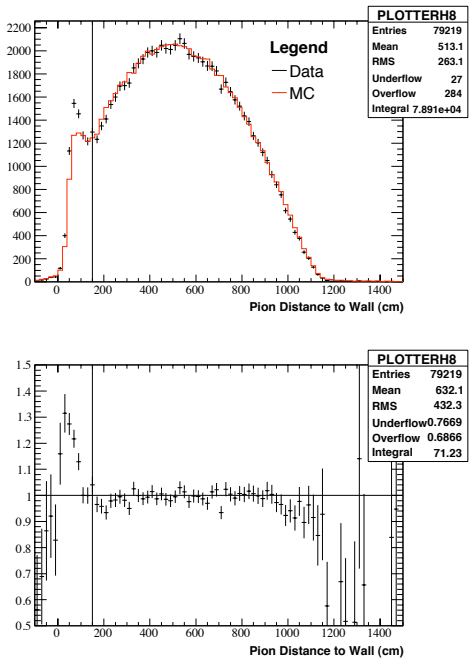

(b) Distance between the tank wall and event vertex along the pion trajectory.

Figure 6.3: The data/Monte Carlo comparisons of the muon and pion trajectory tank wall distances are presented. The bottom panels show the data/Monte Carlo ratio. A cut is placed on both distributions to remove events below 150 cm.

- the differential cross section in the cosine of the muon-neutrino angle, measured in bins of neutrino energy, $\partial\sigma(E_\nu)/\partial(cos(\theta_{\mu,\nu}))$
- the differential cross section in pion kinetic energy, measured in bins of neutrino energy, $\partial\sigma(E_\nu)/\partial(KE_\pi)$
- the differential cross section in the cosine of the pion-neutrino angle, measured in bins of neutrino energy, $\partial\sigma(E_\nu)/\partial(cos(\theta_{\pi,\nu}))$
- the double differential cross section in the cosine of the muon-neutrino angle and the muon kinetic energy, $\partial^2\sigma/\partial(cos(\theta_{\mu,\nu}))\partial(KE_\mu)$
- the double differential cross section in the cosine of the pion-neutrino angle and

the pion kinetic energy, $\partial^2\sigma/\partial(cos(\theta_{\pi,\nu}))\partial(KE_\pi)$

The following discussion will present the measurement technique used for all cross section measurements in terms of the muon kinetic energy measurement. In certain sections, the treatment of the bivariate cross section measurements may require additional discussion, and the $cos(\theta_{\mu,\nu})$ versus KE_μ distributions will be used to illuminate the discussion as required. For the sake of brevity and to clearly describe the analysis procedure, the full details of all measurements are relegated to the appendices.

6.4.1 Event Rate Corrections

The expression for the differential cross section in Equation 6.8 is written in terms of the number of interactions in a final state bin, i. In practice, the true number of interactions is not directly accessible to experiment. The histogram measured in the data, D_i, will typically contain backgrounds, as well as inefficiencies due to detector performance and analysis cuts. The signal efficiency, ϵ_i, and the background distribution, B_i, are both estimated from the Monte Carlo simulation. Assuming perfect detector resolution, the number of observed interactions, N_i^{int}, can be replaced by these experimental quantities,

$$\frac{\partial\sigma}{\partial v}(v_i)^{\text{perfect resolution}} = \frac{(D_i - B_i)/\epsilon_i}{\Delta v_i N_{targ}\Phi}. \tag{6.12}$$

Of course, the detector does not actually have perfect resolution. The complete expression for the differential cross section requires one additional ingredient: data unfolding.

6.4.2 Data Unfolding

Due to biases and imperfect resolution in the event reconstruction, the event distributions measured in the data do not accurately represent the underlying "true" distributions. For example, as shown in Figure 5.16(b), the pion energy reconstructed by the CCπ^+ fitter is systematically high at low true energy, and falls below the true

energy as the energy increases. Since these biases are modeled in the Monte Carlo, it is possible to "unfold" any bin migration effects.

The Monte Carlo bin migration matrix for a given variable, v, is constructed by forming a two dimensional histogram of the reconstructed value of v versus the true value, and normalizing each true column to unity as illustrated in Figure 6.4. Each element, B_{ij}, in the bin migration matrix represents the probability that an event generated with a value of v in bin j will be reconstructed in bin i. By definition,

$$N_j^{int} = \sum_i B_{ji} T_i, \tag{6.13}$$

where N_i^{int} is the reconstructed distribution and T_j is the true distribution.

The goal of unfolding is to perform the opposite task of Equation 6.13. An operator, M_{ij}, must be obtained that transforms the background subtracted data distribution into the inferred true distribution (I_i),

$$I_i = \sum_j M_{ij}(D_j - B_j). \tag{6.14}$$

The most obvious choice for the unfolding matrix is the inverse of the bin migration matrix. Unfortunately, this unfolding technique is highly unstable, because the bin migration matrix is not very well behaved, and is often singular. In addition, large statistical fluctuations in the off-diagonal elements of B_{ij} get incorporated in the diagonal elements of B_{ij}^{-1}, which produce large fluctuations in the results [66].

To avoid these issues, the unfolding matrix is formed from the same reconstructed versus true histogram used to construct the bin migration matrix, except that instead of normalizing the true columns of the histogram, each reconstructed row is normalized to unity. The result is a matrix, M_{ij}, where each element gives the probability that an event in reconstructed bin j was produced in true bin i, which satisfies the condition of Equation 6.14. An example of the unfolding, bin migration, and reconstructed versus true matrices used in the muon kinetic energy measurement are shown together in Figure 6.4.

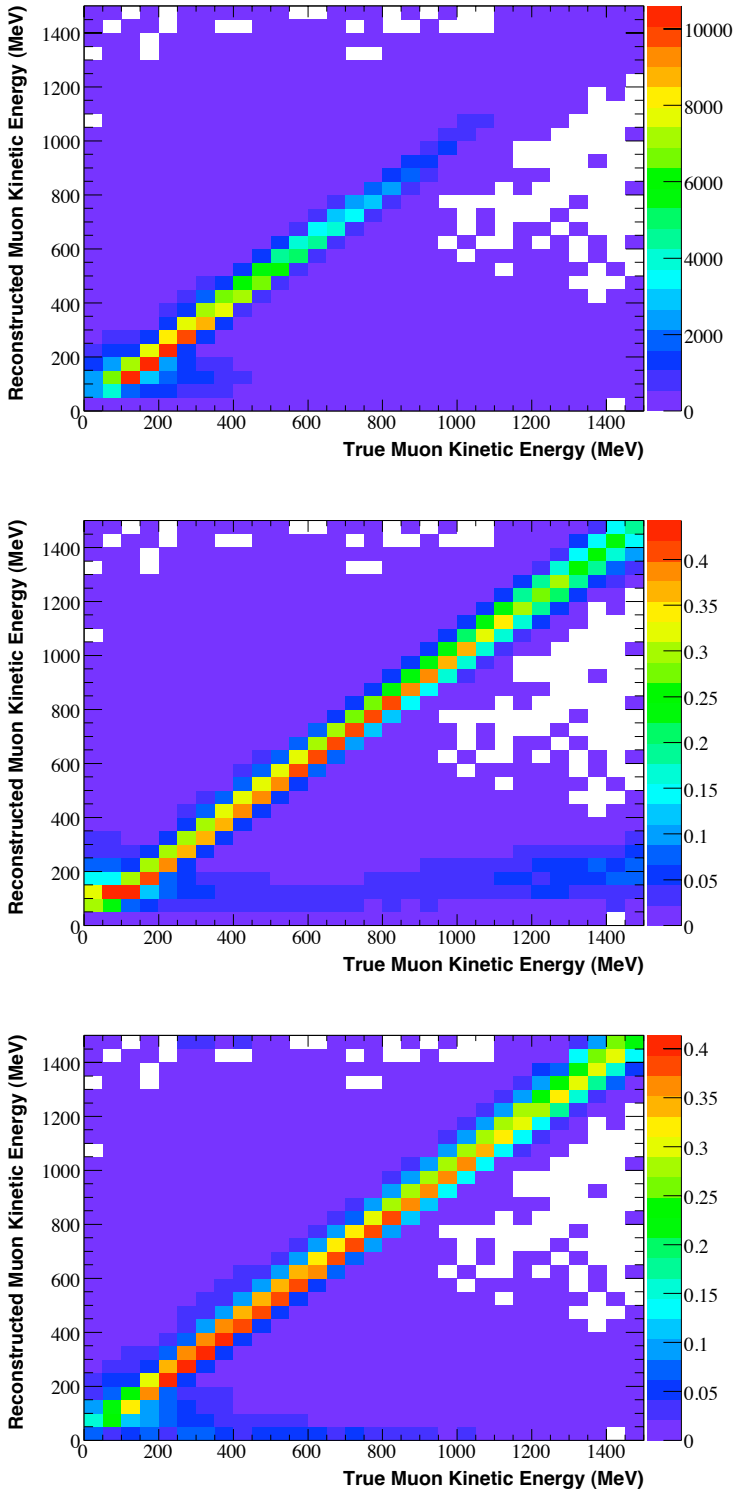

Figure 6.4: The reconstructed versus true (top), bin migration (middle), and unfolding (bottom) matrices are shown for muon kinetic energy. The bin migration matrix is formed by normalizing the true columns of the reconstructed vs true matrix to unity, while the unfolding matrix is formed by normalizing the reconstructed rows.

Unlike B_{ij}^{-1}, which satisfies the unfolding condition of Equation 6.14 by definition (the product $\sum_j B_{ij}^{-1} B_{jk}$ gives the identity matrix) the matrix M_{ij} is designed such that the true distribution, T_i, is an eigenvector of the product $\sum_j M_{ij} B_{jk}$ with a corresponding eigenvalue of one,

$$T_i = \sum_j \sum_k M_{ij} B_{jk} T_k. \tag{6.15}$$

Introducing the unfolding matrix into Equation 6.12 gives the most complete expression for the differential cross section,

$$\frac{\partial \sigma}{\partial v}(v_i) = \frac{\sum_j M_{ij}(D_j - B_j)}{\epsilon_i \Delta v_i N_{targ} \Phi}. \tag{6.16}$$

In order to apply the same unfolding formula in Equation 6.14 to the bivariate measurements, each two-dimensional bin is arbitrarily assigned one universal bin number according to the following prescription,

$$bin = bin_x + bin_y \cdot Nbins_x, \tag{6.17}$$

where bin is the universal bin number and $Nbins_x$ is the number of x bins in the measurement. A reconstructed versus true histogram can then be created, and an unfolding matrix can be calculated using the same row normalization procedure. The central value reconstructed versus true histogram is given in Figure 6.5.

6.4.3 Unfolding Bias

Although the use of M_{ij} rather than B_{ij}^{-1} avoids the variance issues involved with matrix inversion, it does introduce some bias. In general, unfolding procedures often require the introduction of some amount of bias in order to reduce the statistical variances associated with matrix inversion such that the overall uncertainty is reduced [67]. Since the bin migration matrix, B_{ij}, is normalized in columns of the true distribution, B_{ij} and B_{ij}^{-1} are fully independent of the true Monte Carlo distribution, and are therefore unbiased transformations. The M_{ij} matrix is normalized in reconstructed rows, which

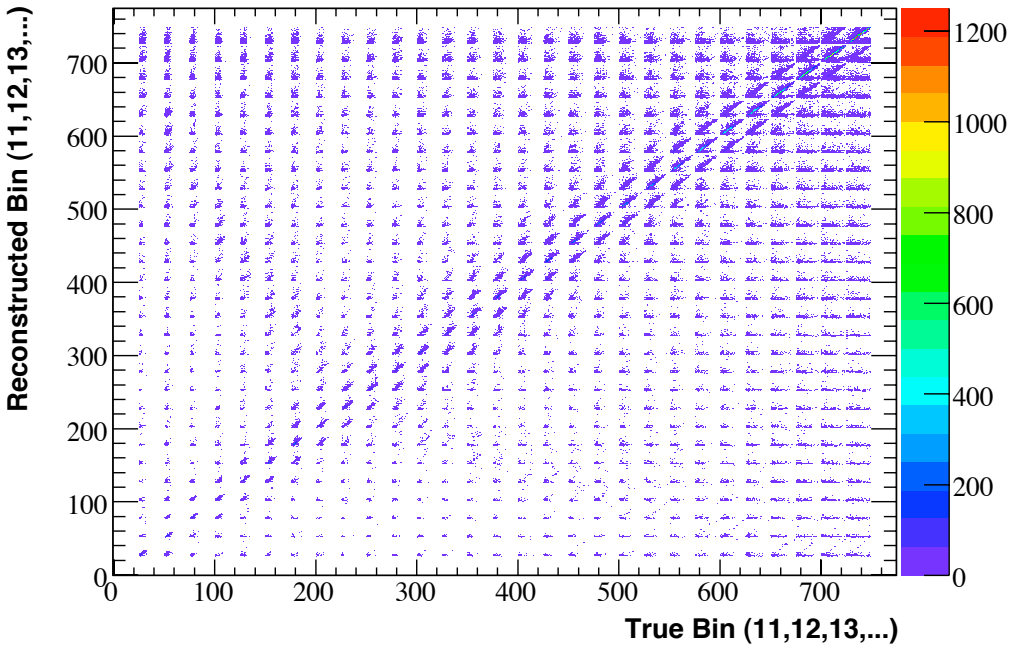

Figure 6.5: The reconstructed versus true distribution for the two-dimensional muon kinetic energy versus cos(muon-neutrino angle) histogram is shown. Each bin of the histogram has been assigned a number between 1 and 775 and plotted in the appropriate 2D bin of the 775×775 reconstructed versus true histogram.

means any change to the shape of the true distribution slice within a reconstructed bin will result in the reconstructed events in that bin being assigned to the true bins in different proportions.

It is important to note that changes to the true Monte Carlo distribution do not necessarily result in an increase in unfolding bias. The normalization of each true slice may be arbitrarily varied, and as long as the shape is unchanged, the unfolding result is also unchanged, despite any changes to the total true distribution. For example, if each Monte Carlo event were reweighted (according to its reconstructed value) by an arbitrary histogram that shares the same binning as the reconstructed histogram, the unfolding result is unchanged.

In this way, the size of the unfolding bias is closely linked with the precision (but not necessarily the accuracy) of the event reconstruction. If events could be reconstructed with perfect resolution, the unfolding bias would be zero by definition, independent of any inaccuracies in the true Monte Carlo distribution. More generally, if the Monte Carlo inaccurately models the true distribution, the unfolding bias will be small as long as that inaccuracy does not change how the event reconstruction places events from true bins into reconstructed bins, even if it places them into the wrong reconstructed bins.

To quantify the size of the unfolding bias, an iterative technique is used. The background subtracted, unfolded data provide an inferred true distribution as described in Section 6.4.2. Each Monte Carlo event is then assigned a weight given by the binned ratio of inferred true data to the true Monte Carlo. Using these weights, a new reconstructed versus true histogram is created from which a new M_{ij} unfolding matrix is formed. The data distribution is unfolded again using the new unfolding matrix and the processes is repeated. The result of the first 9 iterations is given in Figure 6.6. Figure 6.7 shows a two-dimensional iterative example.

Successive iterations of the inferred data distribution have two distinct features.

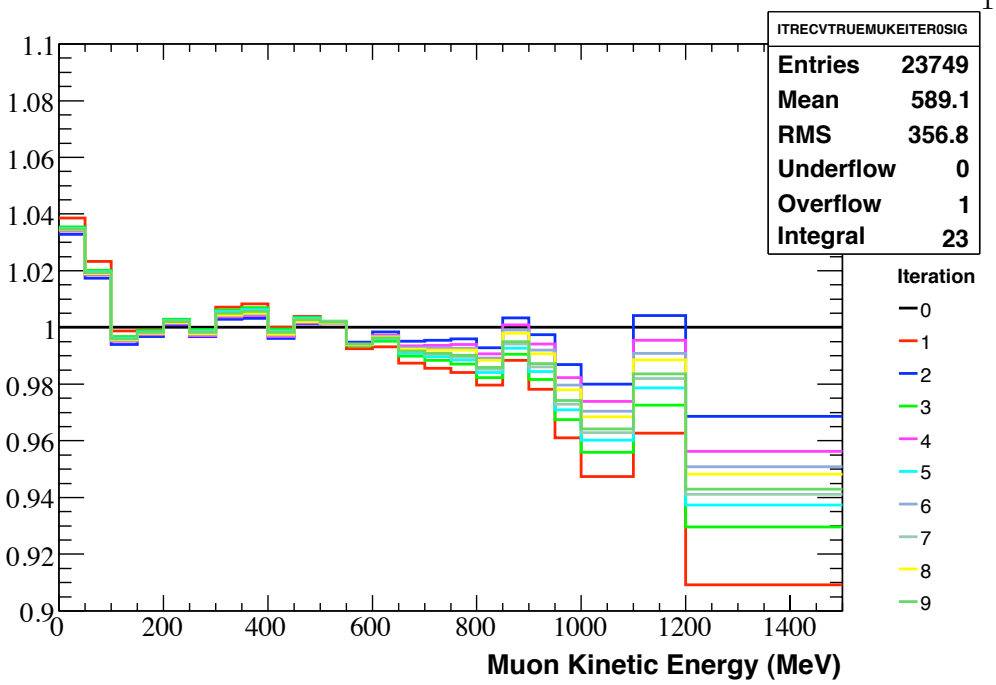

Figure 6.6: The ratios of the iterated inferred true data distributions (i.e. $\sum_j M_{ij}^{iter,n}(D_j - B_j)$) to the uniterated distribution are shown. The number of iterations for the numerator of each ratio are given in the legend. Note the oscillatory behavior of successive iterations, and that the largest excursion from the uniterated distribution occurs in the first iteration.

The first is that the largest excursion relative to the uniterated inferred distribution is in the first iteration. The other is that each successive iteration oscillates about an intermediate preferred value, and the amplitude of those oscillations decreases as the number of iterations increases.

It is tempting to continue iterating the result until the answer converges; however, the correction to the true Monte Carlo distribution that is taking place at each step is a convolution of the desired data informed corrections, and the inadequacies of the Monte Carlo bin migration matrix. Of the infinite possible ways to transform a reconstructed distribution into true distribution, it is unlikely that iterating the unfolding procedure along one particular dimension gives the correct true distribution. Instead, the strategy

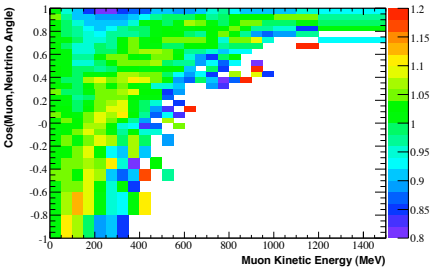

(a) The ratio of the first iteration to the uniterated distribution.

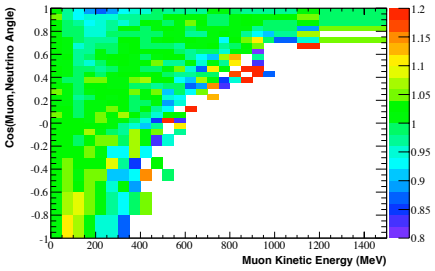

(b) The ratio of the second iteration to the uniterated distribution.

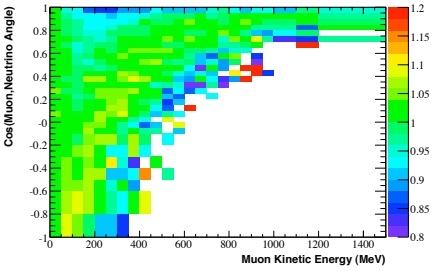

(c) The ratio of the third iteration to the uniterated distribution.

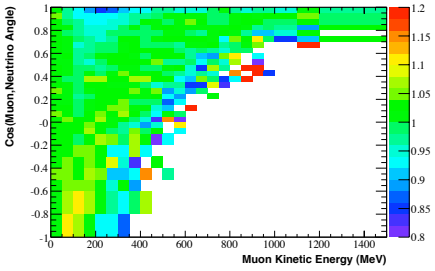

(d) The ratio of the fourth iteration to the uniterated distribution.

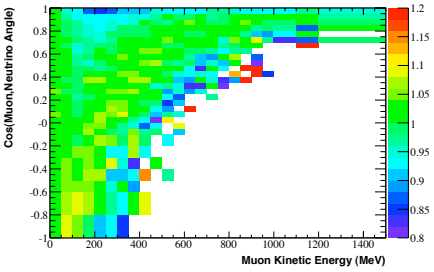

(e) The ratio of the fifth iteration to the uniterated distribution.

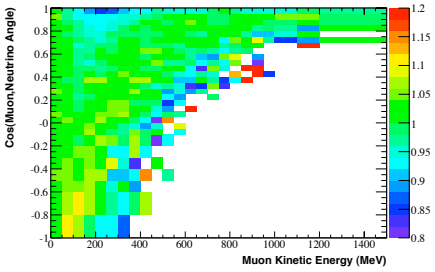

(f) The ratio of the sixth iteration to the uniterated distribution.

Figure 6.7: The ratios of the iterated inferred true data distributions (i.e. $\sum_j M_{ij}^{iter,n}(D_j - B_j)$) to the uniterated distribution are shown for the two-dimensional case. Note the oscillatory behavior of successive iterations, and that the largest excursion from the uniterated distribution occurs in the first iteration.

is to take the most conservative variation in each distribution as the systematic error, and show that it is not the dominant error in almost all regions of phase space. The

uniterated inferred data distribution is taken to be the central value, and the most conservative estimate of the unfolding bias, the excursion in first iteration, is taken as a two-sided systematic uncertainty.

6.4.4 Efficiency Correction

After the data are unfolded, the inferred true data distribution is corrected for events lost due to data selection cuts and detector inefficiency. The numerator of the efficiency correction is the true distribution of all Monte Carlo events that pass the cuts. The denominator is the "generated" Monte Carlo distribution, formed before any cuts are imposed. The ratio of these two distributions gives the fraction of events in a particular bin that survive the analysis cuts,

$$\epsilon_i = \frac{N_i^{true\ after\ cuts}}{N_i^{generated}}. \tag{6.18}$$

The efficiency should be fairly insensitive to changes in the underlying physical parameters used to produce the generated distribution. If any portion of the generated distribution is incorrectly enhanced, a proportional effect should be seen in the true distribution, and thus cancel in the efficiency.

Monte Carlo events are generated out to a radius of 610.6 cm to include all neutrino interactions in the main tank, the veto region, and the tank wall. Since the measurement being performed is a neutrino cross section in mineral oil, all other materials must be excluded in forming the generated Monte Carlo distribution. To avoid the PMTs and, in particular, the material voids inside the PMTs, the efficiency denominator is formed from a subset of these events generated within a radius of 550 cm.

Nearly all of the events generated outside of 575 cm are removed by the veto hits cut; however, there will be a population of events generated between 550 cm and 575 cm that pass all cuts, particularly in the upstream portion of the tank. This means that ϵ_i is not technically an efficiency in the strict definition of the term. However, since the

properties of the incident neutrinos and the oil in the 550-575 cm shell are the same as the properties within 550 cm, this definition of the efficiency should have no effect on the result. Any extra contributions from events in the 550-575 cm shell should be present in both the inferred true data and the true Monte Carlo distributions. The signal efficiency in bins of muon kinetic energy is given in Figure 6.8.

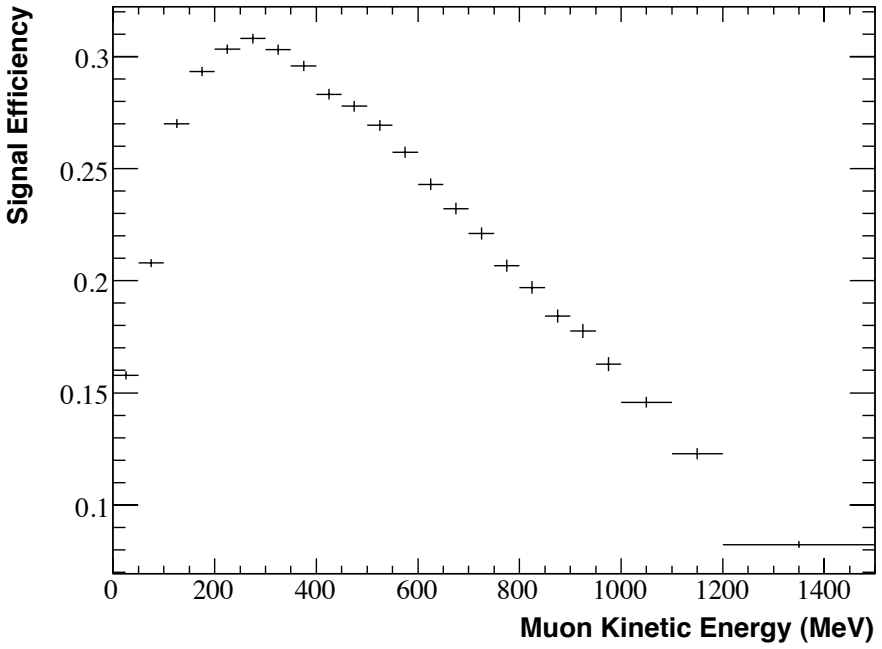

Figure 6.8: The signal efficiency is shown in bins of muon kinetic energy with Monte Carlo statistical errors. Low energy events pass the tank hits cut less frequently, and high energy tracks tend to exit the tank and trigger the veto.

6.4.5 Interaction Targets

To measure a cross section, an interaction target must be well defined. Mineral oil is composed of long, single-bonded chains of carbon atoms. In its atomic form, carbon possesses electrons in four of its eight outer shell states. Molecular carbon, therefore, forms four covariant bonds. Within a long chain, carbon atoms form two bonds with neighboring carbon atoms, which leaves two bonding sites available for hydrogen atom

bonds. The exceptions are carbon atoms located at the end of a chain, which are bonded to three hydrogen atoms. The molecular formula for a mineral oil molecule is, therefore, C_nH_{2n+2}, where n is the length of the carbon chain. On average, the carbon chains in the mineral oil have a length of ~ 33, so the molecular formula can be rewritten as $n\,(CH_{2.06})$. Since the cross section will only depend on the relative amount of each atomic species, the interaction is chosen to be an "average" single unit on the hydrocarbon chain, $CH_{2.06}$.

The number of interaction targets in the cross section formula, N_{targ}, must correspond with the definition of the generated volume used in the efficiency calculation. To extract the number of targets from the volume, the only experiment dependent quantity needed is the oil density, which has been measured to be 0.841 ± 0.001 g/cm^3 [28]. The full expression for the number of interaction targets is

$$N_{targ} = \frac{4}{3}\pi R_{gen}^3 \cdot \rho_{oil} \cdot \frac{N_A}{W(\mathrm{CH_{2.06}})}, \tag{6.19}$$

where R_{gen} is the radius of generated events used in the efficiency denominator (550 cm), ρ_{oil} is the density of the oil, N_A is Avogadro's number (number of targets per mol), and $W(\mathrm{CH_{2.06}})$ is the molecular weight of $\mathrm{CH_{2.06}}$ (g/mol).

6.4.6 Flux Factor

The implementation of the flux factor varies significantly depending on the type of cross section measurement being performed. For the measurements binned in the lone initial state variable, $\sigma(E_\nu)$, the flux factor a binned quantity used normalized each measured bin to the rate per incident neutrino. While the measured cross section is still flux averaged, the averaging only takes place over the width of each bin.

In the differential and double differential cross section measurements, the flux factor is the fully integrated neutrino flux, and the cross section is flux averaged over the entire neutrino energy spectrum. Such a measurement is certainly experiment depen-

dent in that the particular incident neutrino flux shape is folded into the cross section. However, the fundamental physics of the interaction are fully characterized if the neutrino flux prediction is reported along with the measured cross sections. The reason for providing each of the differential cross sections in bins of neutrino energy was to remove this dependence on the experiment-dependent flux shape. This topic is revisited in Chapter 7.

6.4.7 Systematic Uncertainties

All systematic uncertainties are from one of seven possible error sources. Each source is a set of correlated uncertainties from a particular stage of the simulation. The following is a complete list of error sources applicable to effective CCπ^+ production, including the sections in which they are described:

- "π^+": Beam π^+ production cross section uncertainties in proton-beryllium interactions (Section 4.1.5).
- "K^+": Beam K^+ production cross section uncertainties in proton-beryllium interactions (Section 4.1.5).
- "Beam": includes each of the following (Section 4.1.5):
  - total, inelastic, and quasi-elastic cross section uncertainties for proton and pion interactions with beryllium and aluminum
  - horn current uncertainties
  - horn current skin depth uncertainties
- "XSec": Nuance cross section model uncertainties (Section 4.2.3).
- "OM": optical model uncertainties (Section 4.4.2).
- "ITER": iteration uncertainty to assess unfolding bias (Section 6.4.3)

- "DISC": discriminator threshold uncertainty (Section 3.3).
- "QTCORR": a conservatively chosen variation in the correlation between the integrated charged and the recorded hit time in each PMT (Section 3.3).

A handful of other uncorrelated uncertainties have been excluded due to their negligible size, such as the number of protons on target ($\sim 1\%$) and the oil density ($< 0.1\%$).

6.4.7.1 Multisims

The effect of each error source on any particular measured distribution is determined by producing several systematically varied distributions called "multisims." The parameters of each error source are related by an error matrix from which a set of correlated, Gaussian distributed parameter values can be drawn. Each new set of parameters produces a systematically varied version of any reconstructed distribution. The spread in the normalization and shapes of the multisims are used to calculate the total systematic uncertainty as described in the next section.

There are two distinct types of systematic variations. Some systematics, such as the flux and cross section uncertainties, only affect the probability with which an event will occur. For this type of uncertainty, a systematically varied distribution can be produced by reweighting the central value Monte Carlo distribution. Each event is multiplied by the ratio of the event probability calculated with the systematically varied set of parameters to the central value event probability.

The other type of systematic variation affects the measured properties of the event after it is produced, such as the amount of light generated as a function of wavelength and the propagation of the light through the oil. In general, these variations cannot be accomplished via reweighting. Instead, these errors were determined using 67 data-sized Monte Carlo simulations that were generated using parameter draws from the optical model error matrix. A plot of the optical model multisims is shown in Figure 6.9.

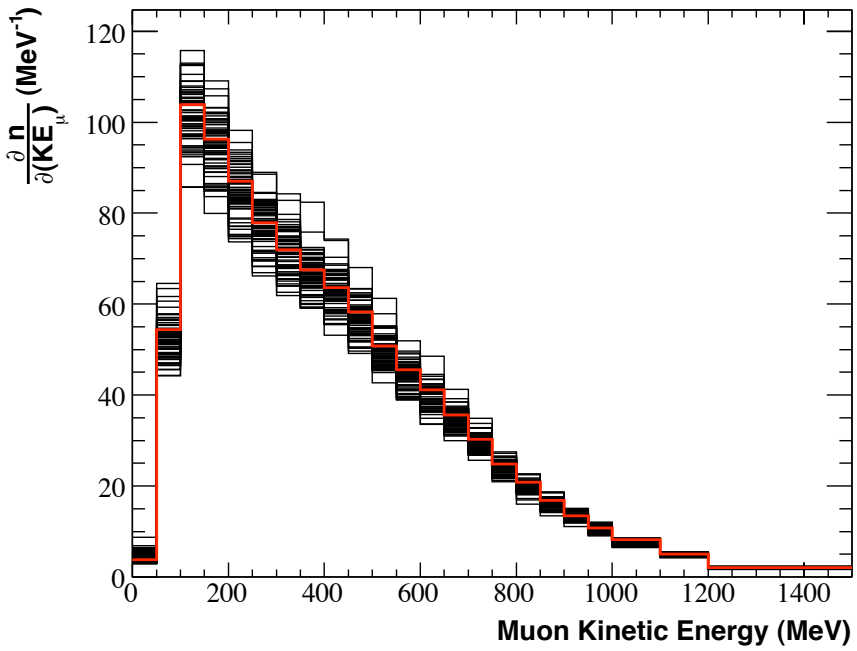

Figure 6.9: The reconstructed muon kinetic energy is plotted in each of the 67 optical model multisims. The central value Monte Carlo distribution (red) is overlayed for comparison.

.

6.4.7.2 Error Matrices

Just as each systematic error source was described by an error matrix that characterized the correlated uncertainties in the source parameters, the uncertainties in the measured cross sections are described by an error matrix that characterizes the correlated uncertainties in the measured values in each bin. For each error source, an error matrix is calculated from the bin population differences in the multisims compared to the central value,

$$M_{ij}^{source} = \frac{1}{N} \sum_{m=1}^{N} \left(n_{m,i} - n_{CV,i}\right) \left(n_{m,j} - n_{CV,j}\right), \tag{6.20}$$

where N is the number of multisims, $n_{m,i}$ is the number of events in bin i of multisim m, and $n_{CV,i}$ is the number of events in bin i in the central value Monte Carlo simulation.

Once an error matrix has been calculated for each source, the total error matrix is given by summing each component matrix. For the two-dimensional measurements, the bins are ordered according to Equation 6.17 in order to calculate the full error matrix.

Since the statistical fluctuations in a particular bin are unrelated to the fluctuations in any other bin, statistical error matrices are always diagonal. By design, these uncertainties are built into the optical model error matrix since each optical model multisim was constructed to have the same number of events as the data. Unfortunately, this also has the effect of adding statistical fluctuations to the off-diagonal terms as well. As more optical model multisims are incorporated into the calculation of the error matrix, the size of these spurious fluctuations is decreased. The fluctuations are also smaller for bins with significant event populations. For this reason, cross section results will only be reported for bins with at least 25 unfolded data events. In the one-dimensional cross section measurements, the event populations are large enough that this effect is negligible. The reweighting multisims do not suffer from this effect.

To evaluate the systematic uncertainties in the cross section, the full cross section calculation procedure outlined in Equation 6.16 is performed in each multisim. The multisim distributions replace the corresponding central value distributions in the calculation. The reconstructed data distribution remains the same, but multisim distributions are used for the unfolding matrix, the background prediction, and the signal efficiency. The formula for the differential cross section with multisim dependent quantities explicitly identified is

$$\frac{\partial \sigma^m}{\partial v}(v_i) = \frac{\sum_j M_{ij}^m (D_j - B_j^m)}{\epsilon_i^m \Delta v_i N_{targ} \Phi^m}, \tag{6.21}$$

where m is the multisim index.

The results presented throughout the remainder of this document will only list the diagonal errors on each bin. The full error matrices for each distribution are quite large, and in the case of the two-dimensional measurements, they can contain over one million

elements. The main uses for the full error matrix are hypothesis testing and fitting models. These matrices will be made available to the community via the MiniBooNE website [68].

6.4.7.3 Flux Uncertainties

In addition to producing separate cross section weighted distributions, the flux must also be modified to correspond to the systematically varied parameters in each multisim. Only three of the seven systematic sources affect the flux. The diagonal uncertainties of the flux variations are shown in Figure 6.10.

The largest of the flux errors is the uncertainty in the beam π^+ production in proton-beryllium interactions. The portion of the flux relevant to effective CCπ^+ interactions occurs at neutrino energies larger than about 400 MeV. For the peak neutrino energies in this range (<1 GeV), the beam π^+ flux uncertainties are around 8%. At higher neutrino energies, the beam π^+ uncertainty grows to as large as 25%. The beam π^+ fluctuations also exhibit very distinct features in shape. The residual effect of the wiggling behavior of the spline fits to the HARP data, discussed in Section 4.1.5, are apparent. In particular, the low energy flux exhibits very large systematic excursions since there are no HARP data to constrain the fits in that region.

The other two flux related error sources have a smaller effect on the total uncertainty. The beam unisim uncertainties are generally around the 5% level below 1 GeV and then expand at higher neutrino energies. The main contributor at high energies is the skin depth excursion, which causes a ∼15% effect between 1.5 and 2.5 GeV. The K^+ uncertainties are mostly irrelevant for this analysis. K^+ mesons become the dominant source of ν_μ production at 2.3 GeV, and the uncertainties become dominant at neutrino energies greater than 2.5 GeV, where the flux is very small.

For the measurements not involving neutrino energy, the cross section calculation is only affected by the uncertainty in the integrated flux. The size of these variations

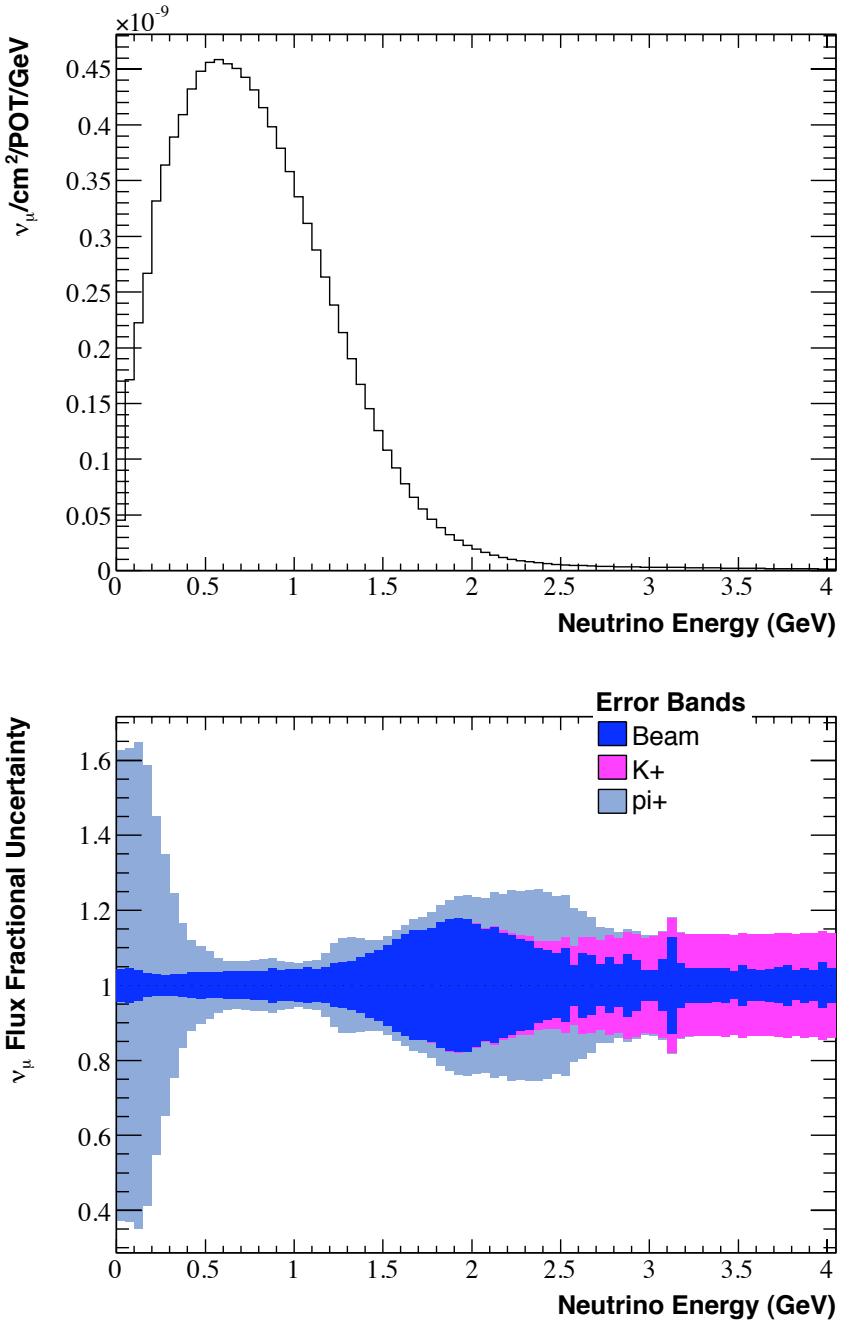

Figure 6.10: The ν_μ flux is shown (top) along with the fractional diagonal flux errors (bottom).

for each of the flux error sources is given in Table 6.3.

Table 6.3: The uncertainties in the integrated flux are given for each of the flux error sources.

Error Source	Integrated Flux Uncertainty
π^+	10.4%
Beam	4.1%
K^+	0.4%

6.4.8 Results

The results of each of the cross section measurements are presented here.

- $\sigma(E_\nu)$: Figure 6.11
- $\frac{\partial\sigma}{\partial(Q^2)}$: Figure 6.12
- $\frac{\partial\sigma}{\partial(KE_\mu)}$: Figure 6.13
- $\frac{\partial\sigma}{\partial(\cos(\theta_{\mu,\nu}))}$: Figure 6.14
- $\frac{\partial\sigma}{\partial(KE_\pi)}$: Figure 6.15
- $\frac{\partial\sigma}{\partial(\cos(\theta_{\pi,\nu}))}$: Figure 6.16
- $\frac{\partial^2\sigma}{\partial(KE_\mu)\partial(\cos(\theta_{\mu,\nu}))}$: Figure 6.32 (uncertainty components are given in Figures 6.33 and 6.34)
- $\frac{\partial^2\sigma}{\partial(KE_\pi)\partial(\cos(\theta_{\pi,\nu}))}$: Figure 6.35 (uncertainty components are given in Figures 6.36 and 6.37)
- $\frac{\partial\sigma(E_\nu)}{\partial(Q^2)}$: Figure 6.17 (uncertainty components are given in Figures 6.18 and 6.19)

Additional details for each measurement, including tables of the central values and uncertainties in each bin, are given in the appendices. The uncertainties in the one-dimensional measurements are shown in a stacked format such that each successive error band shows the additional contribution of that error source when combined with all

smaller error bands. The outer-most error band is the total systematic error. The two-dimensional histograms are presented with their total uncertainties, and the contribution from each error source is plotted separately in subsequent figures.

The binning for each of the one dimensional distributions has been chosen such that the true Monte Carlo prediction in each bin exceeds 300 events after all cuts. The one dimensional bin sizes are used for the two dimensional measurements as well to retain sufficient precision in the most interesting regions of phase space. This also creates several bins with very small numbers of predicted events. As described in Section 6.4.7.1, the data-sized optical model multisims produce unreliable uncertainties in bins with small event populations. Hence, results will only be reported for bins that contain at least 25 inferred true data events.

In each of the one-dimensional differential cross section measurements, the two largest sources of uncertainty are the π^+ production and the cross sections. The 12-15% π^+ uncertainty is dominated by the variation in the integrated flux, which uniformly accounts for 10.4% of the variation across all bins. The remaining few percent variation is mostly due to changes in the background prediction. Any systematic change in a flux bin results in a proportional change to the observed Monte Carlo distribution, which directly affects the size and shape of the background subtraction. In addition, variations in the background subtraction is almost completely correlated with variations in the flux, since both an increased flux prediction and an increased background prediction result in a lower measured cross section and vice versa. Finally, any bias in the unfolding procedure that is sensitive to the flux shape can also give a small contribution to the overall π^+ uncertainty.

The largest effect in the cross section multisims is the variation in pion absorption and charge exchange interactions in the oil. If the pion is absorbed, it will not produce a Michel electron and the event will fail the three subevent requirement; therefore, pion absorption and charge exchange will directly affect the cut efficiencies. As described

in Section 4.4.2, a 50% uncertainty is assigned to pion charge exchange and a 35% uncertainty is assigned to pion absorption, which is the dominant source of cross section error. The remainder of the cross section uncertainty is due to variations in the form factors of each background process.

Since the neutrino energy cross section measurement uses the flux prediction in each measured bin rather than the integrated flux factor, the π^+ uncertainty is significantly lower, and generally remains below 10% except at the highest neutrino energies. The cross section uncertainty is roughly the same size as seen in the differential cross section measurements.

For most of the measured phase space, the unfolding iteration uncertainty is negligible; however, it becomes significant at low Q^2 in both the one- and two-dimensional measurements. This particular region has two features that generally make unfolding difficult. The first is that the shape is rapidly changing, which strongly affects bin migration. Also, this is a region where the data and Monte Carlo shapes significantly disagree, which increases the probability that the shape of the true slices in each reconstructed bin are incorrect. Despite these features, the unfolding uncertainty is still not the dominant systematic effect in most bins, and is of comparable size in the few bins susceptible to these effects.

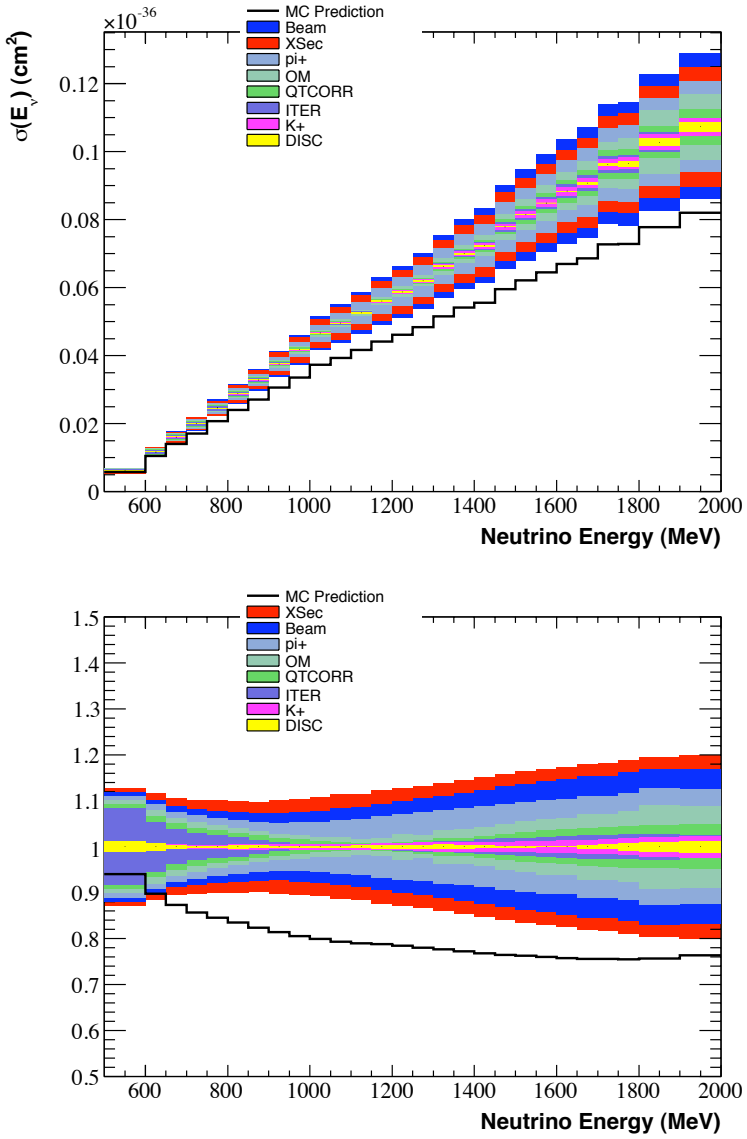

Figure 6.11: The $\sigma(E_\nu)$ measurement is shown with cumulative systematic errors. The absolutely normalized Monte Carlo prediction is shown for comparison. The bottom plot shows the fractional uncertainties and the ratio to the Monte Carlo prediction.

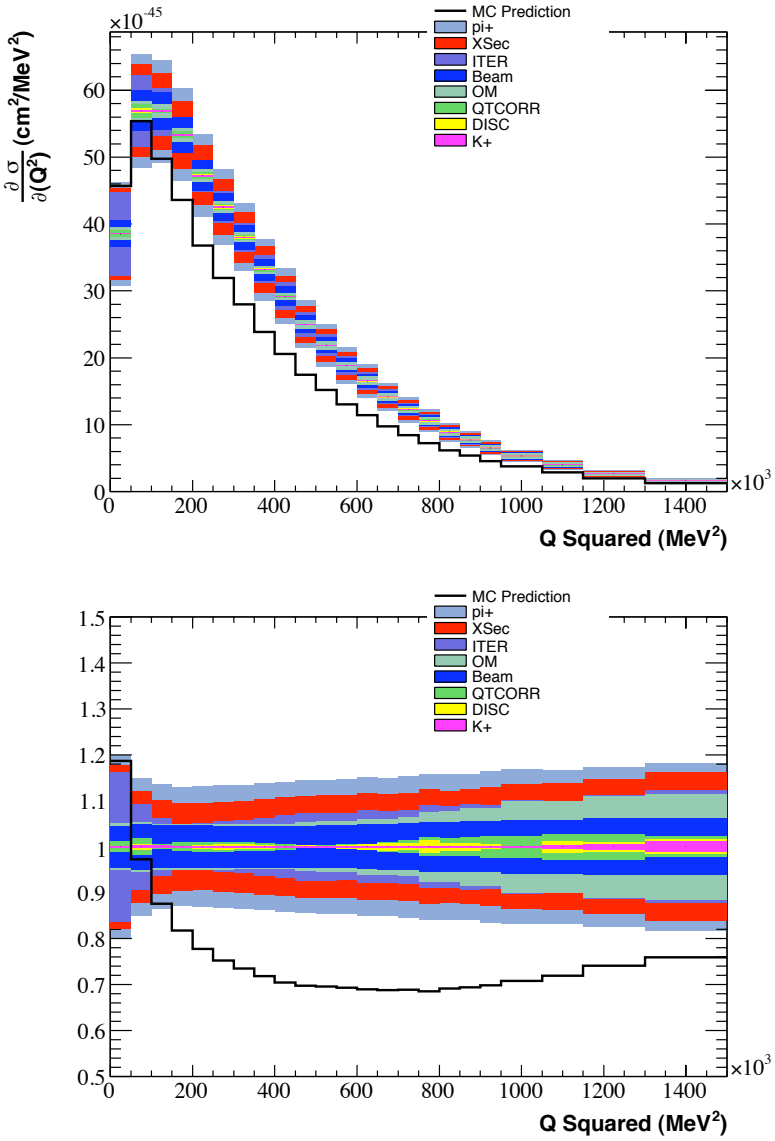

Figure 6.12: The $\partial\sigma/\partial(Q^2)$ measurement is shown with cumulative systematic errors. The absolutely normalized Monte Carlo prediction is shown for comparison. The bottom plot shows the fractional uncertainties and the ratio to the Monte Carlo prediction.

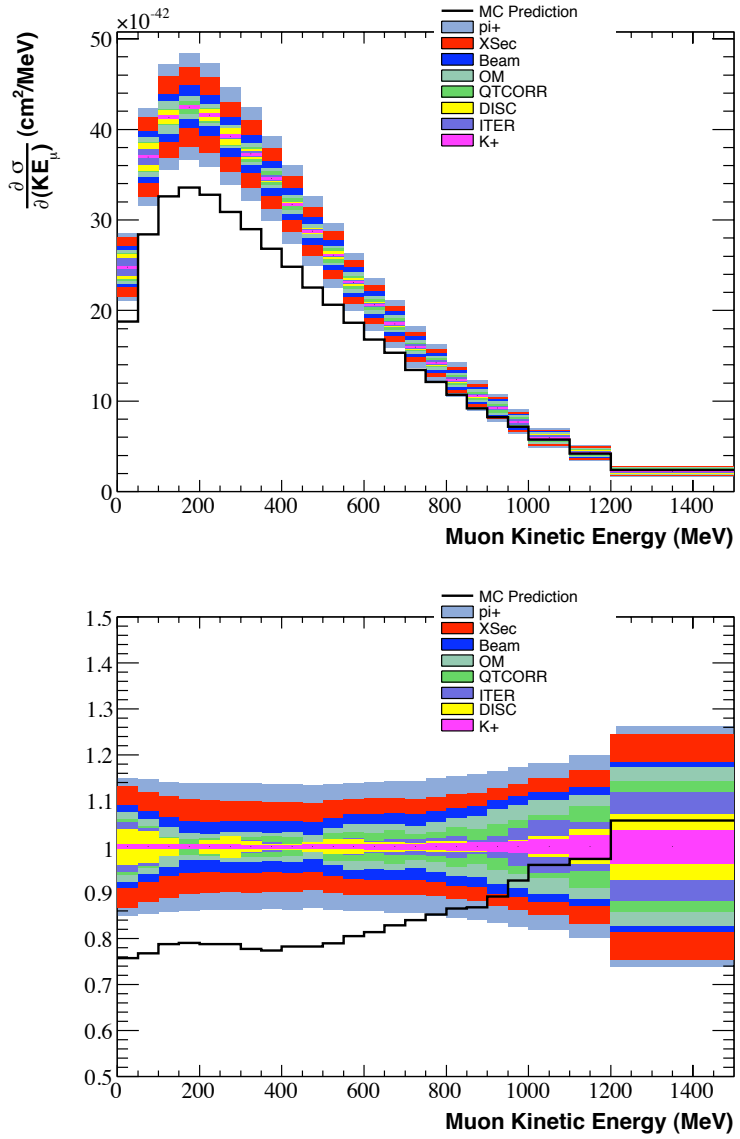

Figure 6.13: The $\partial\sigma/\partial(KE_\mu)$ measurement is shown with cumulative systematic errors. The absolutely normalized Monte Carlo prediction is shown for comparison. The bottom plot shows the fractional uncertainties and the ratio to the Monte Carlo prediction.

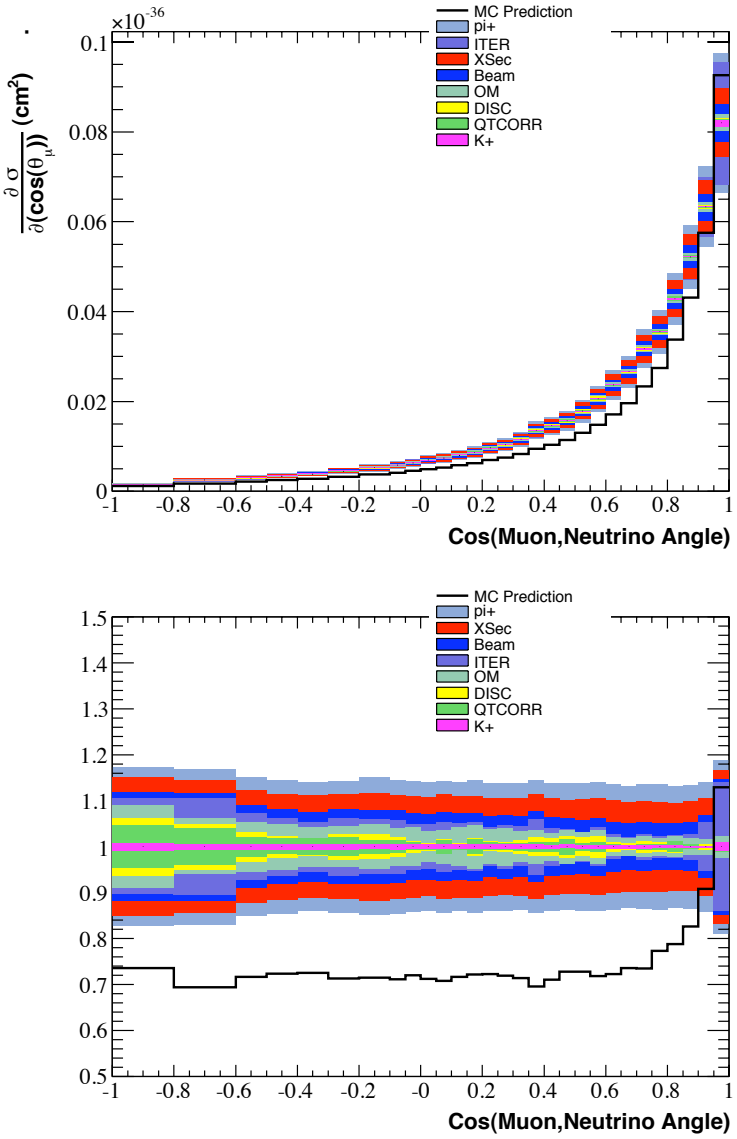

Figure 6.14: The $\partial\sigma/\partial cos(\theta_{\mu,\nu})$ measurement is shown with cumulative systematic errors. The absolutely normalized Monte Carlo prediction is shown for comparison. The bottom plot shows the fractional uncertainties and the ratio to the Monte Carlo prediction.

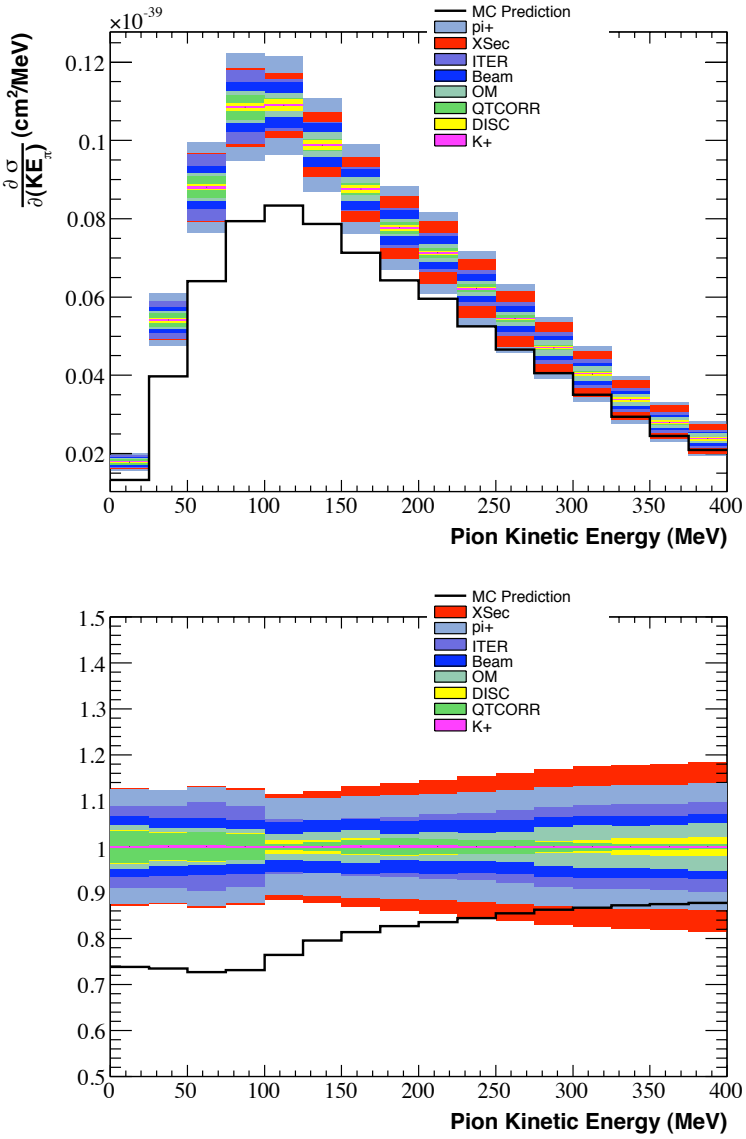

Figure 6.15: The $\partial\sigma/\partial(KE_\pi)$ measurement is shown with cumulative systematic errors. The absolutely normalized Monte Carlo prediction is shown for comparison. The bottom plot shows the fractional uncertainties and the ratio to the Monte Carlo prediction.

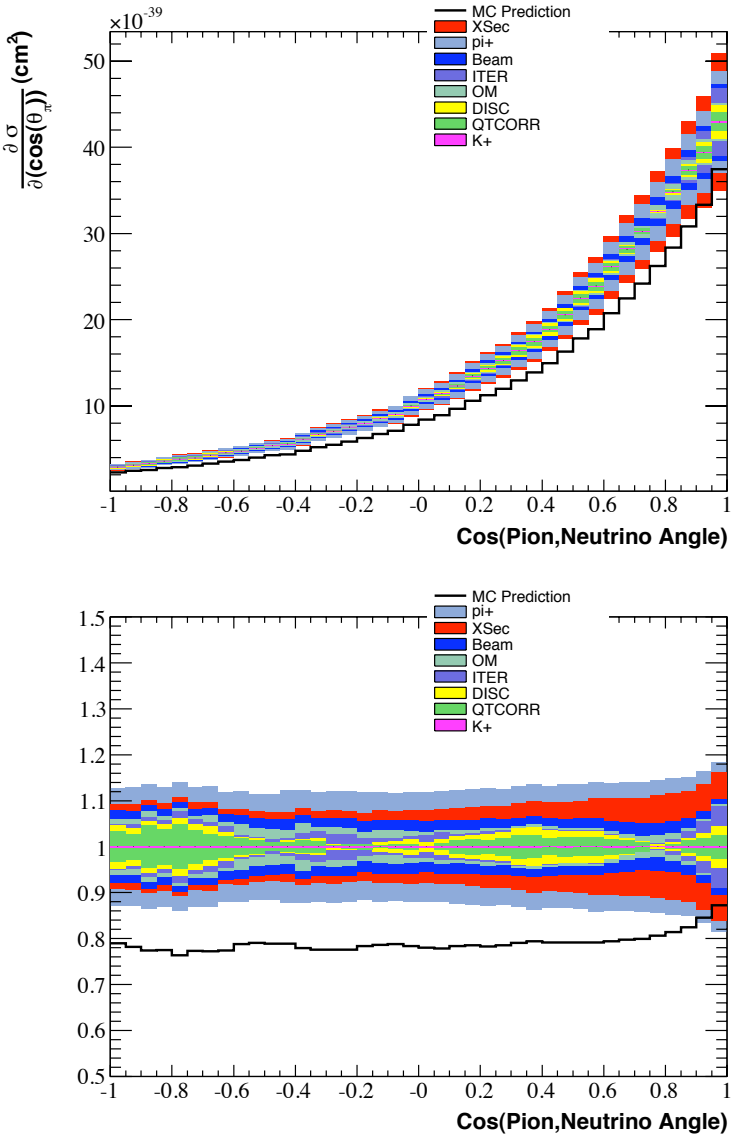

Figure 6.16: The $\partial\sigma/\partial cos(\theta_{\pi,\nu})$ measurement is shown with cumulative systematic errors. The absolutely normalized Monte Carlo prediction is shown for comparison. The bottom plot shows the fractional uncertainties and the ratio to the Monte Carlo prediction.

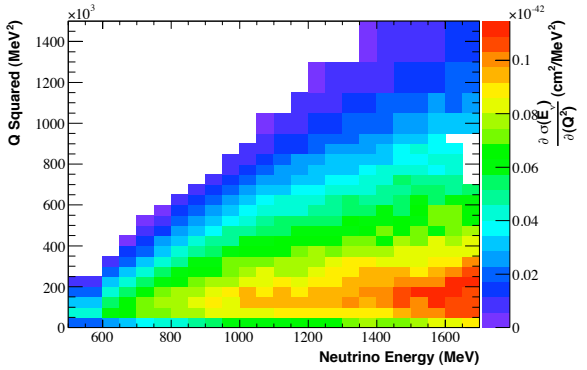

(a) Measured cross section

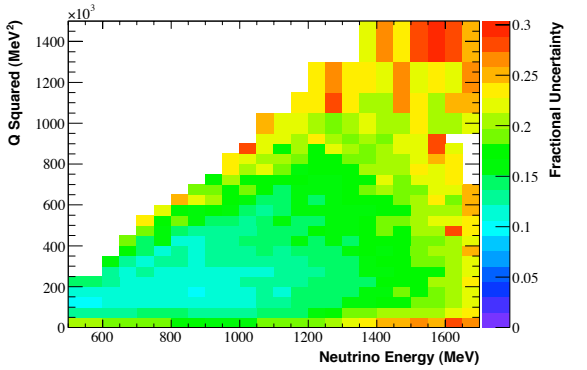

(b) Total fractional error on the measured cross section

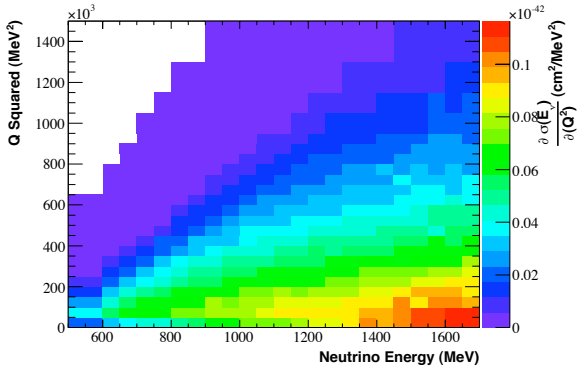

(c) Monte Carlo predicted cross section

Figure 6.17: The measured $\partial\sigma(E_\nu)/\partial(Q^2)$ values are shown along with the total fractional uncertainties. The Monte Carlo predicted cross section is shown for comparison.

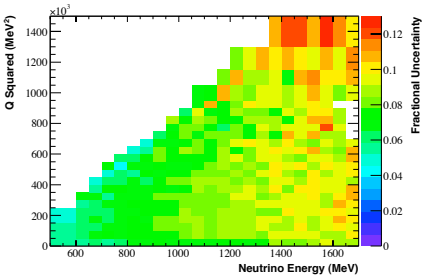

(a) The fractional systematic uncertainty from the "XSec" error source.

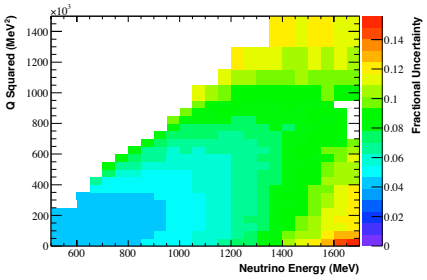

(b) The fractional systematic uncertainty from the "Beam" error source.

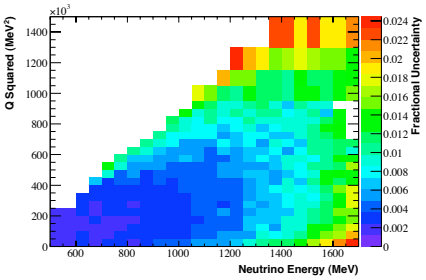

(c) The fractional systematic uncertainty from the "K^+" error source.

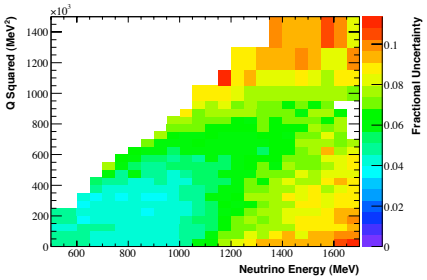

(d) The fractional systematic uncertainty from the "π^+" error source.

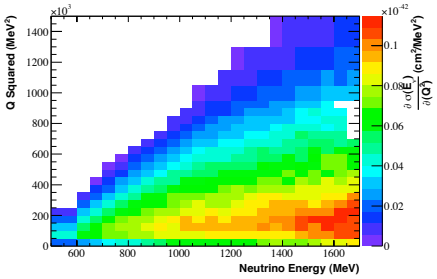

(e) Central value $\partial\sigma(E_\nu)/\partial(Q^2)$ measurement.

Figure 6.18: The fractional systematic uncertainties on the measured $\partial\sigma(E_\nu)/\partial(Q^2)$ values are shown for four of the error sources. The central value measurement is shown for reference. Note that the color scales differ for each systematic error source. An explanation of each error is given in Section 6.4.7.

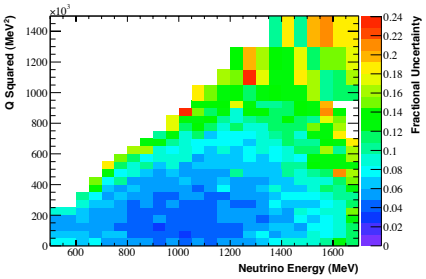

(a) The fractional systematic uncertainty from the "OM" error source.

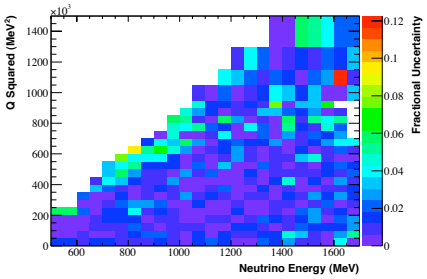

(b) The fractional systematic uncertainty from the "DISC" error source.

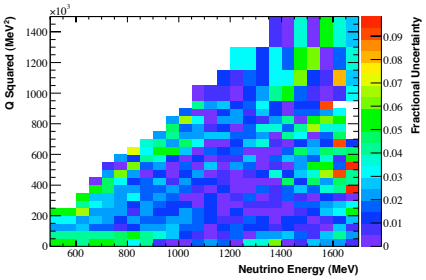

(c) The fractional systematic uncertainty from the "QTCORR" error source.

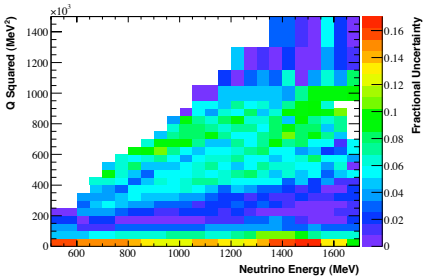

(d) The fractional systematic uncertainty from the "ITER" error source.

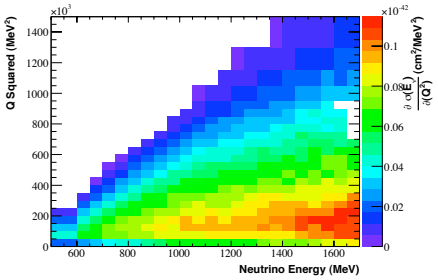

(e) Central value $\partial\sigma(E_\nu)/\partial(Q^2)$ measurement.

Figure 6.19: The fractional systematic uncertainties on the measured $\partial\sigma(E_\nu)/\partial(Q^2)$ values are shown for four of the error sources. The central value measurement is shown for reference. Note that the color scales differ for each systematic error source. An explanation of each error is given in Section 6.4.7.

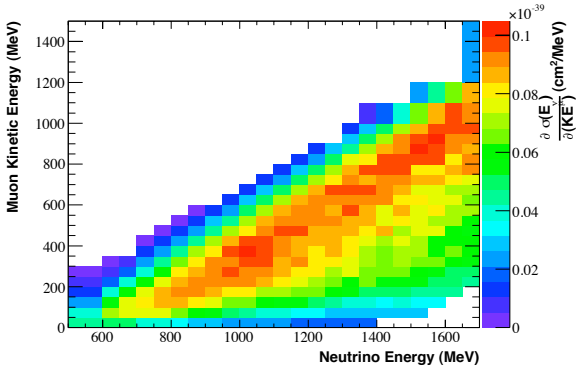

(a) Measured cross section

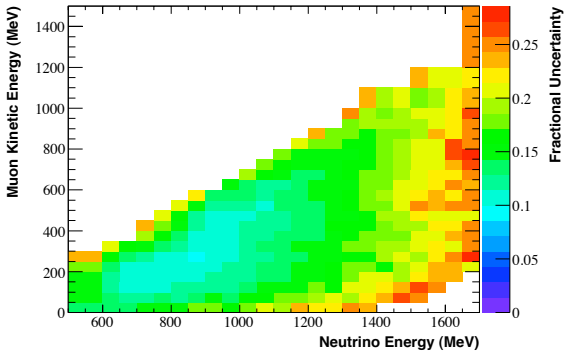

(b) Total fractional error on the measured cross section

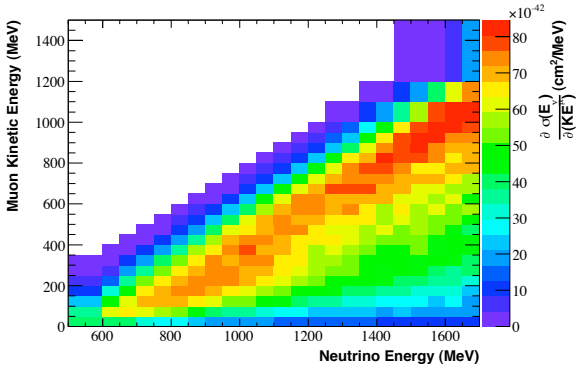

(c) Monte Carlo predicted cross section

Figure 6.20: The measured $\partial\sigma(E_\nu)/\partial(KE_\mu)$ values are shown along with the total fractional uncertainties. The Monte Carlo predicted cross section is shown for comparison.

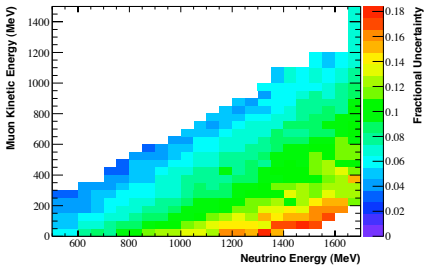

(a) The fractional systematic uncertainty from the "XSec" error source.

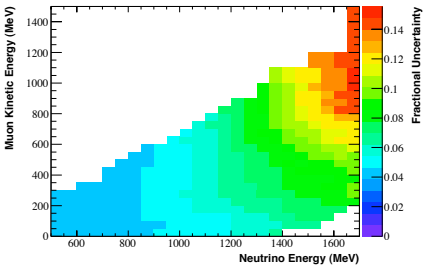

(b) The fractional systematic uncertainty from the "Beam" error source.

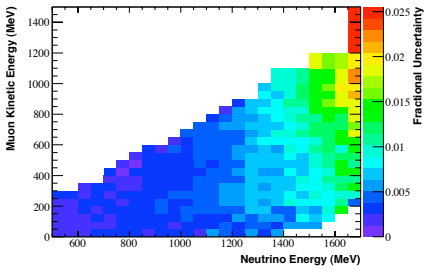

(c) The fractional systematic uncertainty from the "K^+" error source.

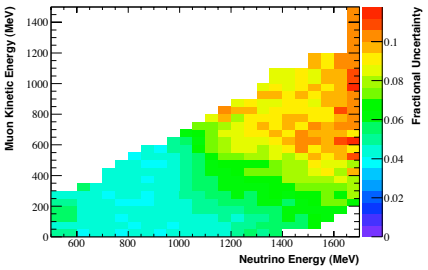

(d) The fractional systematic uncertainty from the "π^+" error source.

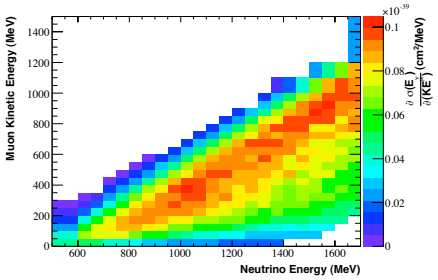

(e) Central value $\partial\sigma(E_\nu)/\partial(KE_\mu)$ measurement.

Figure 6.21: The fractional systematic uncertainties on the measured $\partial\sigma(E_\nu)/\partial(KE_\mu)$ values are shown for four of the error sources. The central value measurement is shown for reference. Note that the color scales differ for each systematic error source. An explanation of each error is given in Section 6.4.7.

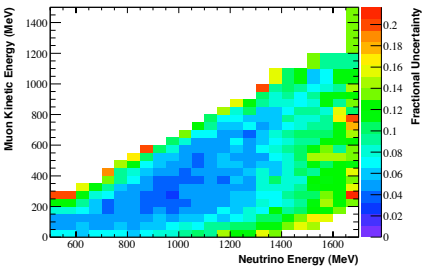

(a) The fractional systematic uncertainty from the "OM" error source.

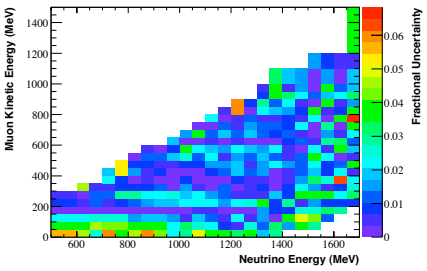

(b) The fractional systematic uncertainty from the "DISC" error source.

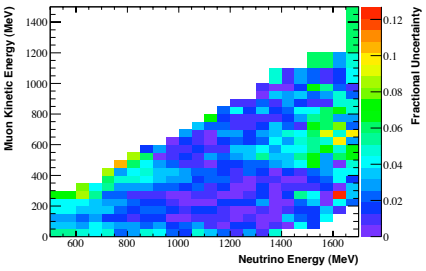

(c) The fractional systematic uncertainty from the "QTCORR" error source.

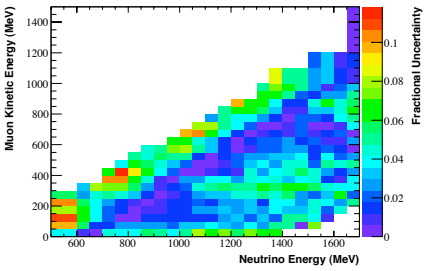

(d) The fractional systematic uncertainty from the "ITER" error source.

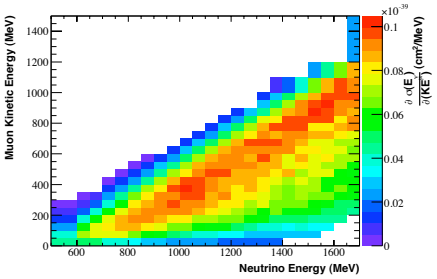

(e) Central value $\partial\sigma(E_\nu)/\partial(KE_\mu)$ measurement.

Figure 6.22: The fractional systematic uncertainties on the measured $\partial\sigma(E_\nu)/\partial(KE_\mu)$ values are shown for four of the error sources. The central value measurement is shown for reference. Note that the color scales differ for each systematic error source. An explanation of each error is given in Section 6.4.7.

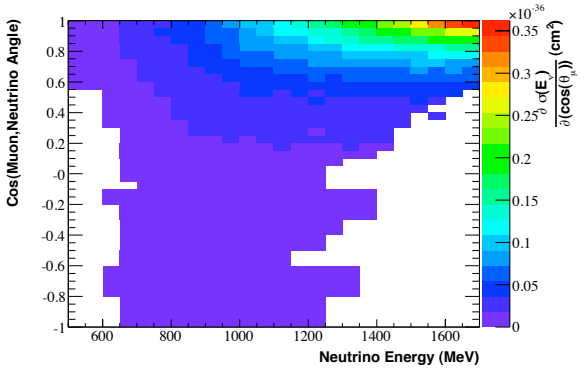

(a) Measured cross section

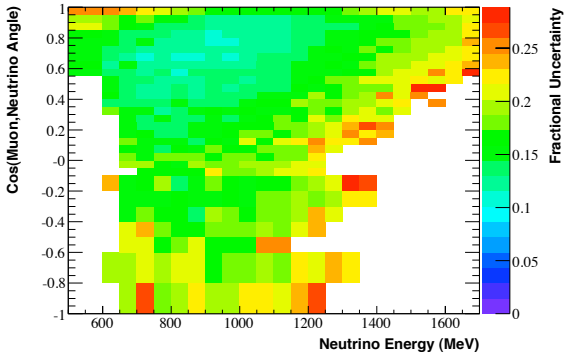

(b) Total fractional error on the measured cross section

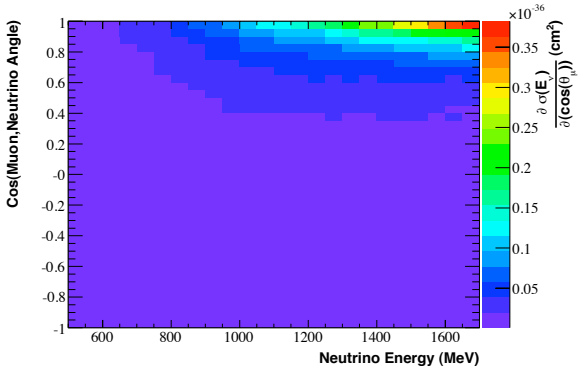

(c) Monte Carlo predicted cross section

Figure 6.23: The measured $\partial\sigma(E_\nu)/\partial(cos(\theta_{\mu,\nu}))$ values are shown along with the total fractional uncertainties. The Monte Carlo predicted cross section is shown for comparison.

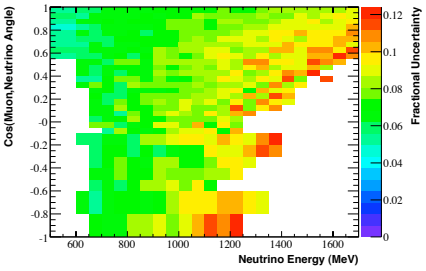

(a) The fractional systematic uncertainty from the "XSec" error source.

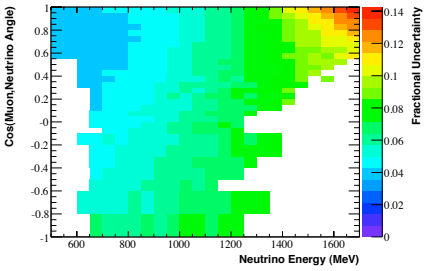

(b) The fractional systematic uncertainty from the "Beam" error source.

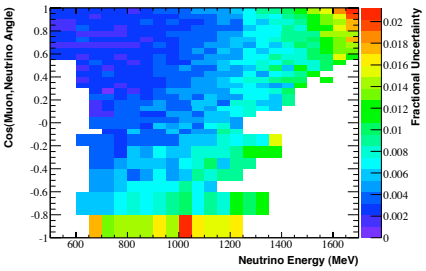

(c) The fractional systematic uncertainty from the "K^+" error source.

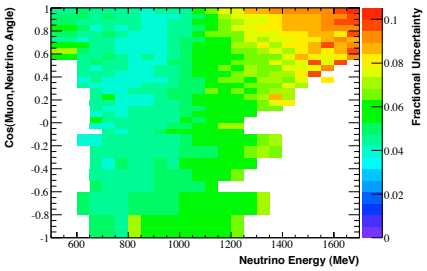

(d) The fractional systematic uncertainty from the "π^+" error source.

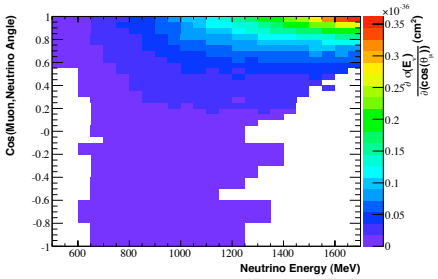

(e) Central value $\partial\sigma(E_\nu)/\partial(cos(\theta_{\mu,\nu}))$ measurement.

Figure 6.24: The fractional systematic uncertainties on the measured $\partial\sigma(E_\nu)/\partial(cos(\theta_{\mu,\nu}))$ values are shown for four of the error sources. The central value measurement is shown for reference. Note that the color scales differ for each systematic error source. An explanation of each error is given in Section 6.4.7.

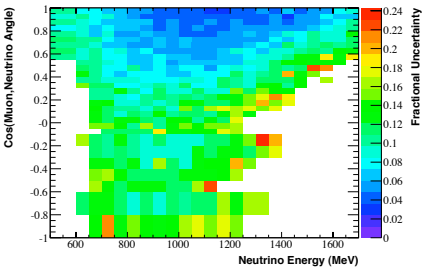

(a) The fractional systematic uncertainty from the "OM" error source.

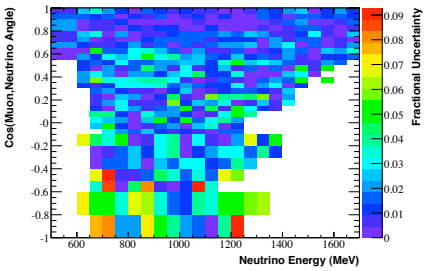

(b) The fractional systematic uncertainty from the "DISC" error source.

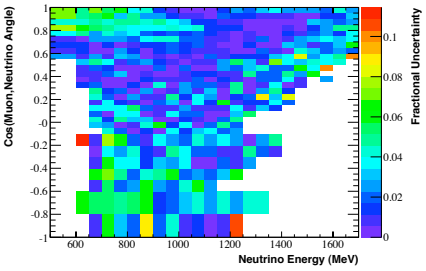

(c) The fractional systematic uncertainty from the "QTCORR" error source.

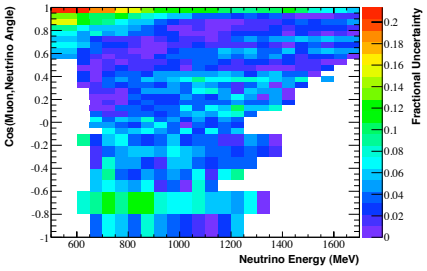

(d) The fractional systematic uncertainty from the "ITER" error source.

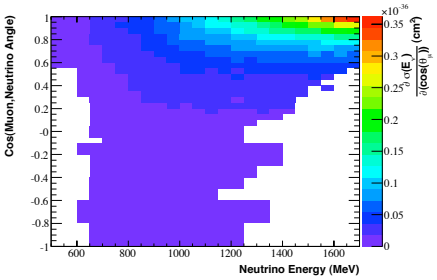

(e) Central value $\partial\sigma(E_\nu)/\partial(cos(\theta_{\mu,\nu}))$ measurement.

Figure 6.25: The fractional systematic uncertainties on the measured $\partial\sigma(E_\nu)/\partial(cos(\theta_{\mu,\nu}))$ values are shown for four of the error sources. The central value measurement is shown for reference. Note that the color scales differ for each systematic error source. An explanation of each error is given in Section 6.4.7.

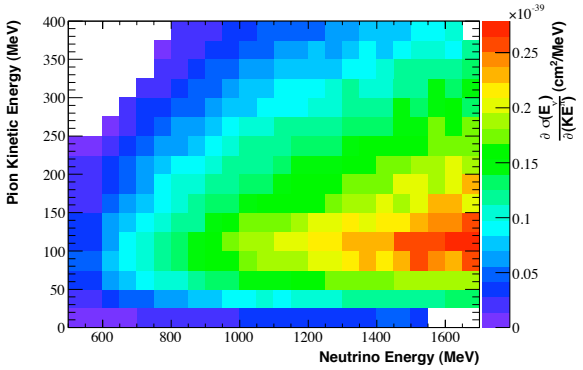

(a) Measured cross section

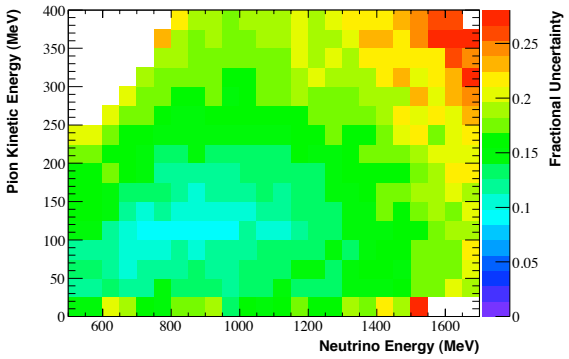

(b) Total fractional error on the measured cross section

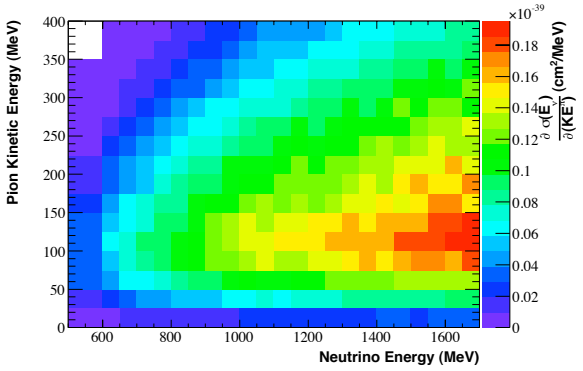

(c) Monte Carlo predicted cross section

Figure 6.26: The measured $\partial\sigma(E_\nu)/\partial(KE_\pi)$ values are shown along with the total fractional uncertainties. The Monte Carlo predicted cross section is shown for comparison.

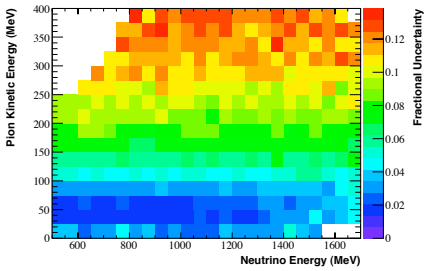

(a) The fractional systematic uncertainty from the "XSec" error source.

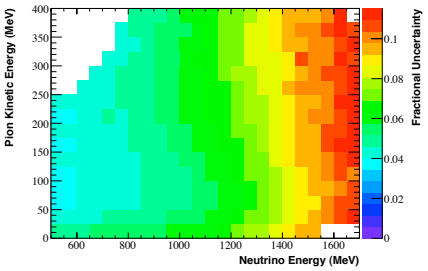

(b) The fractional systematic uncertainty from the "Beam" error source.

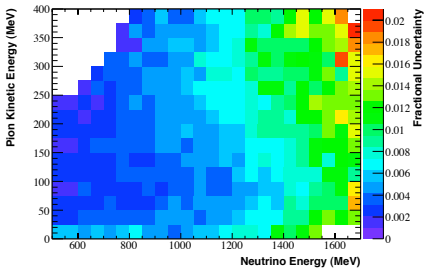

(c) The fractional systematic uncertainty from the "K^+" error source.

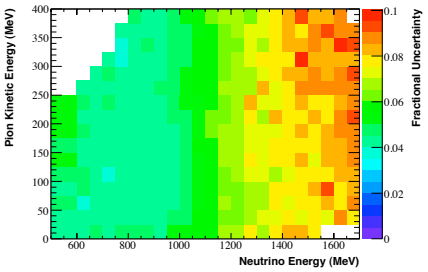

(d) The fractional systematic uncertainty from the "π^+" error source.

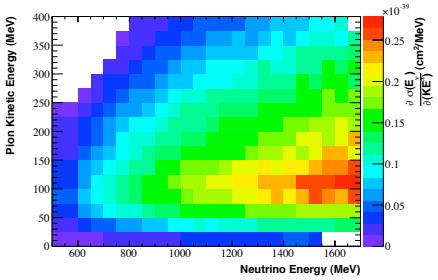

(e) Central value $\partial\sigma(E_\nu)/\partial(KE_\pi)$ measurement.

Figure 6.27: The fractional systematic uncertainties on the measured $\partial\sigma(E_\nu)/\partial(KE_\pi)$ values are shown for four of the error sources. The central value measurement is shown for reference. Note that the color scales differ for each systematic error source. An explanation of each error is given in Section 6.4.7.

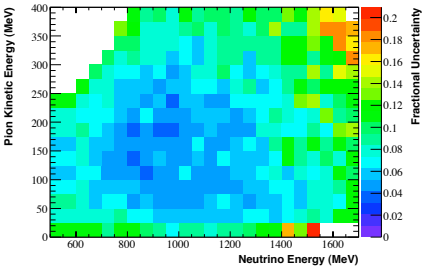

(a) The fractional systematic uncertainty from the "OM" error source.

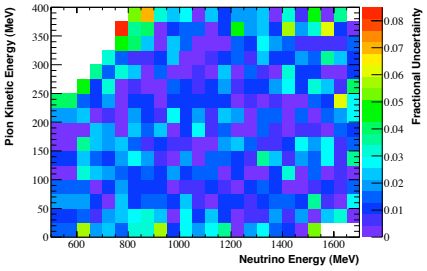

(b) The fractional systematic uncertainty from the "DISC" error source.

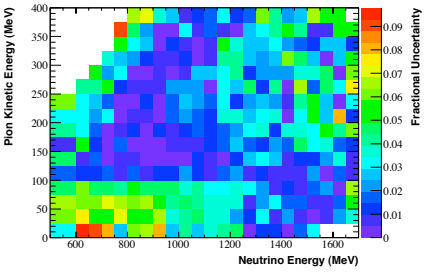

(c) The fractional systematic uncertainty from the "QTCORR" error source.

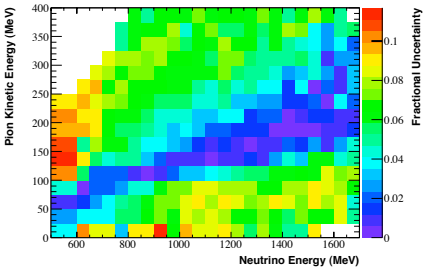

(d) The fractional systematic uncertainty from the "ITER" error source.

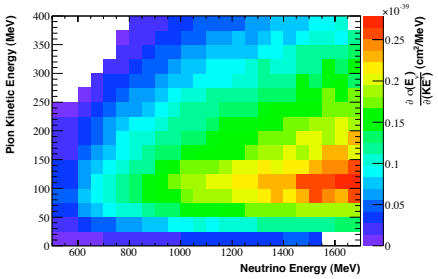

(e) Central value $\partial\sigma(E_\nu)/\partial(KE_\pi)$ measurement.

Figure 6.28: The fractional systematic uncertainties on the measured $\partial\sigma(E_\nu)/\partial(KE_\pi)$ values are shown for four of the error sources. The central value measurement is shown for reference. Note that the color scales differ for each systematic error source. An explanation of each error is given in Section 6.4.7.

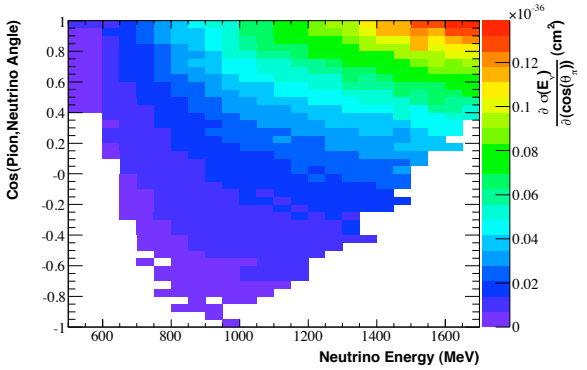

(a) Measured cross section

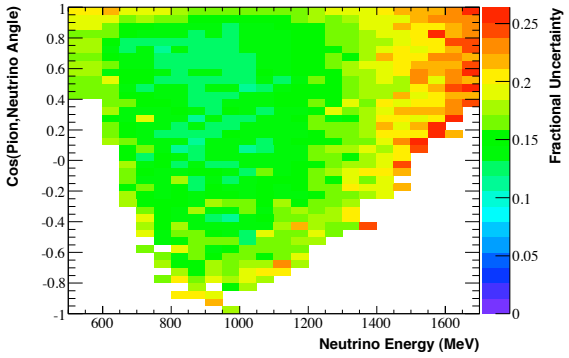

(b) Total fractional error on the measured cross section

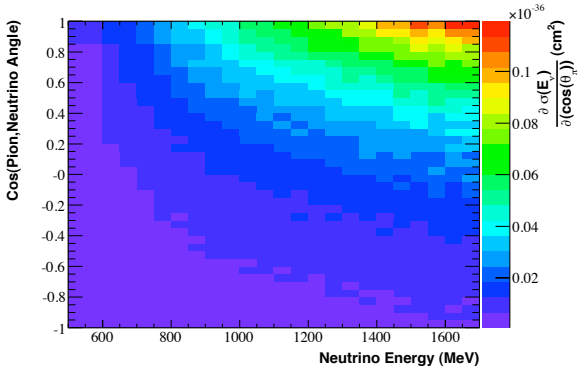

(c) Monte Carlo predicted cross section

Figure 6.29: The measured $\partial\sigma(E_\nu)/\partial(cos(\theta_{\pi,\nu}))$ values are shown along with the total fractional uncertainties. The Monte Carlo predicted cross section is shown for comparison.

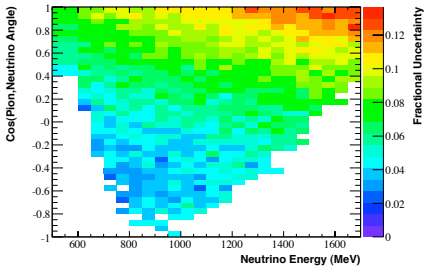

(a) The fractional systematic uncertainty from the "XSec" error source.

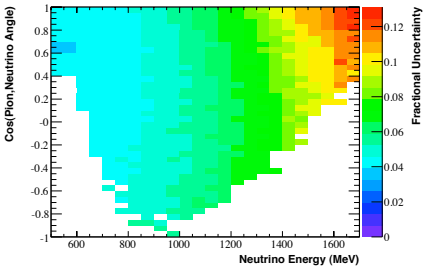

(b) The fractional systematic uncertainty from the "Beam" error source.

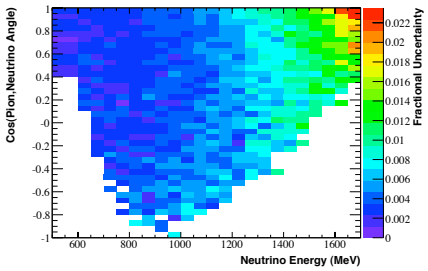

(c) The fractional systematic uncertainty from the "K^+" error source.

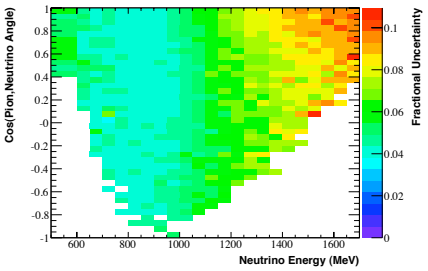

(d) The fractional systematic uncertainty from the "π^+" error source.

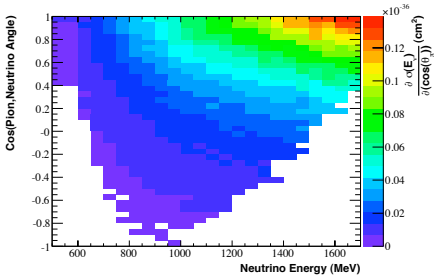

(e) Central value $\partial\sigma(E_\nu)/\partial(cos(\theta_{\pi,\nu}))$ measurement.

Figure 6.30: The fractional systematic uncertainties on the measured $\partial\sigma(E_\nu)/\partial(cos(\theta_{\pi,\nu}))$ values are shown for four of the error sources. The central value measurement is shown for reference. Note that the color scales differ for each systematic error source. An explanation of each error is given in Section 6.4.7.

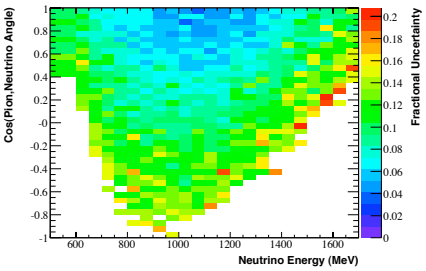

(a) The fractional systematic uncertainty from the "OM" error source.

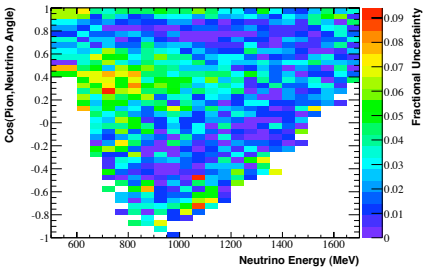

(b) The fractional systematic uncertainty from the "DISC" error source.

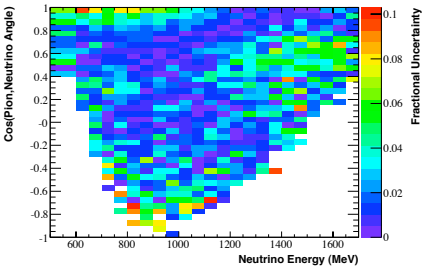

(c) The fractional systematic uncertainty from the "QTCORR" error source.

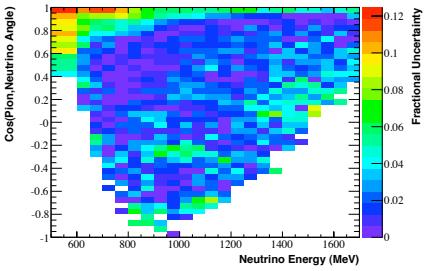

(d) The fractional systematic uncertainty from the "ITER" error source.

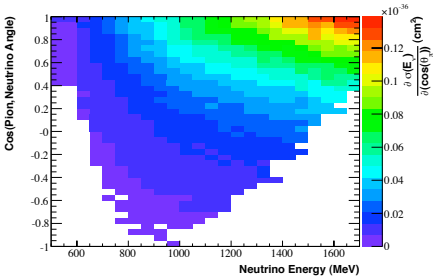

(e) Central value $\partial\sigma(E_\nu)/\partial(cos(\theta_{\pi,\nu}))$ measurement.

Figure 6.31: The fractional systematic uncertainties on the measured $\partial\sigma(E_\nu)/\partial(cos(\theta_{\pi,\nu}))$ values are shown for four of the error sources. The central value measurement is shown for reference. Note that the color scales differ for each systematic error source. An explanation of each error is given in Section 6.4.7.

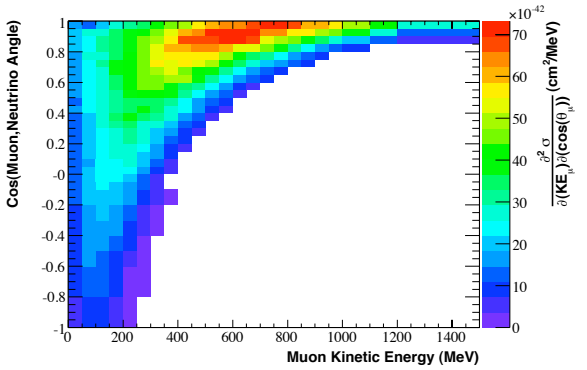

(a) Measured cross section

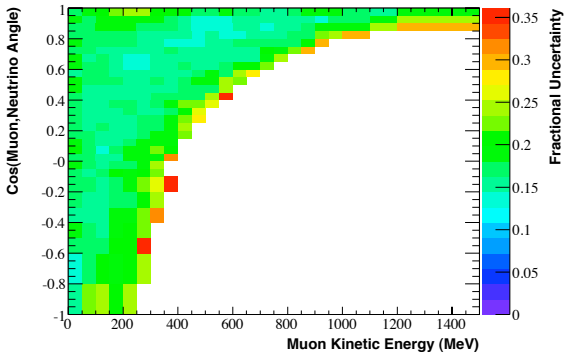

(b) Total fractional error on the measured cross section

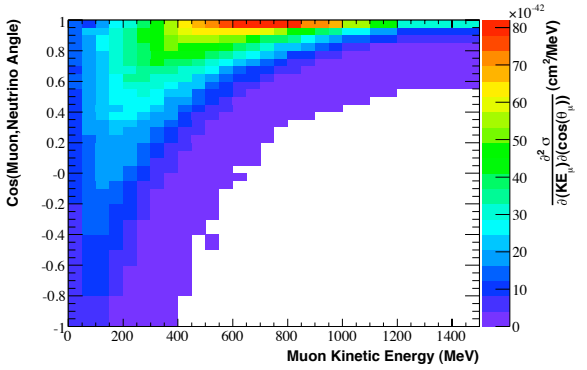

(c) Monte Carlo predicted cross section

Figure 6.32: The measured $\partial^2\sigma/\partial(cos(\theta_{\mu,\nu}))\partial(KE_\mu)$ values are shown along with the total fractional uncertainties. The Monte Carlo predicted cross section is shown for comparison.

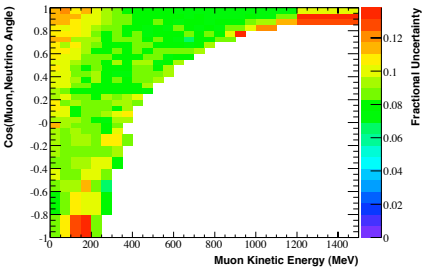

(a) The fractional systematic uncertainty from the "XSec" error source.

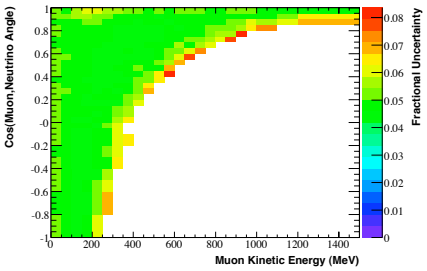

(b) The fractional systematic uncertainty from the "Beam" error source.

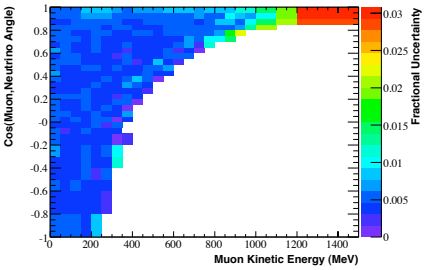

(c) The fractional systematic uncertainty from the "K^+" error source.

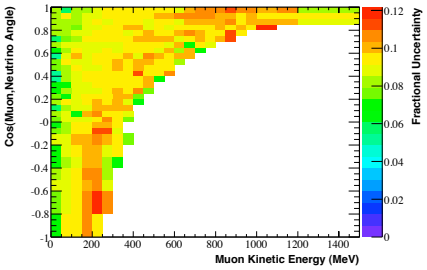

(d) The fractional systematic uncertainty from the "π^+" error source.

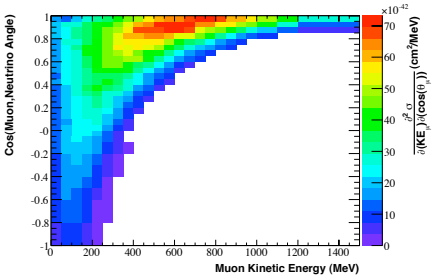

(e) Central value $\partial^2\sigma/\partial(cos(\theta_{\mu,\nu}))\partial(KE_\mu)$ measurement.

Figure 6.33: The fractional systematic uncertainties on the measured $\partial^2\sigma/\partial(cos(\theta_{\mu,\nu}))\partial(KE_\mu)$ values are shown for four of the error sources. The central value measurement is shown for reference. Note that the color scales differ for each systematic error source. An explanation of each error is given in Section 6.4.7.

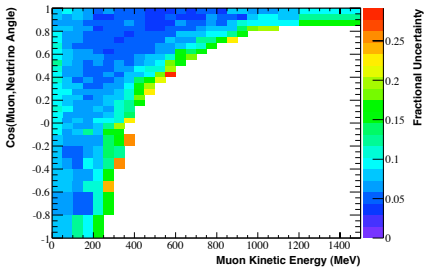

(a) The fractional systematic uncertainty from the "OM" error source.

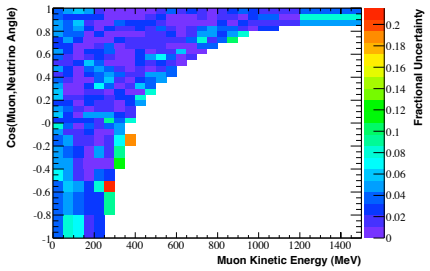

(b) The fractional systematic uncertainty from the "DISC" error source.

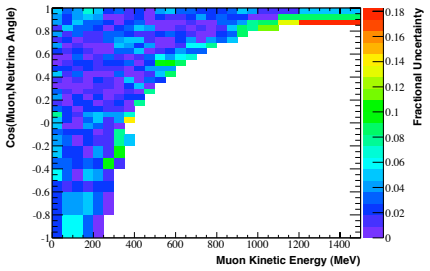

(c) The fractional systematic uncertainty from the "QTCORR" error source.

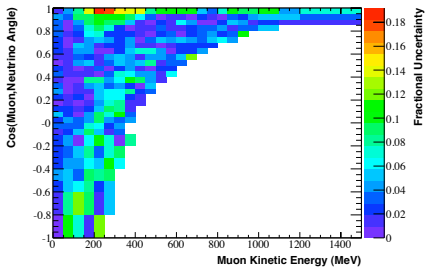

(d) The fractional systematic uncertainty from the "ITER" error source.

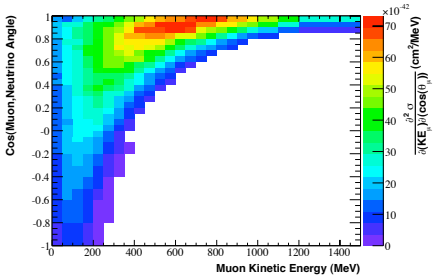

(e) Central value $\partial^2\sigma/\partial(cos(\theta_{\mu,\nu}))\partial(KE_\mu)$ measurement.

Figure 6.34: The fractional systematic uncertainties on the measured $\partial^2\sigma/\partial(cos(\theta_{\mu,\nu}))\partial(KE_\mu)$ values are shown for four of the error sources. The central value measurement is shown for reference. Note that the color scales differ for each systematic error source. An explanation of each error is given in Section 6.4.7.

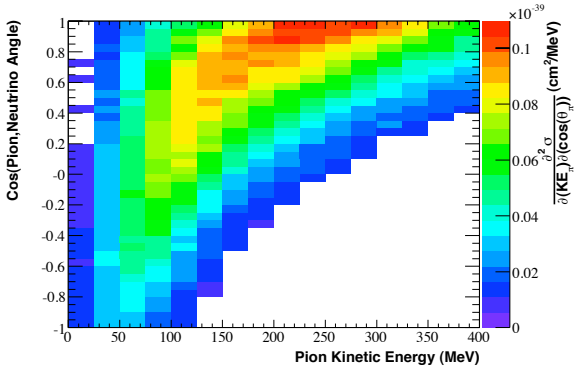

(a) Measured cross section

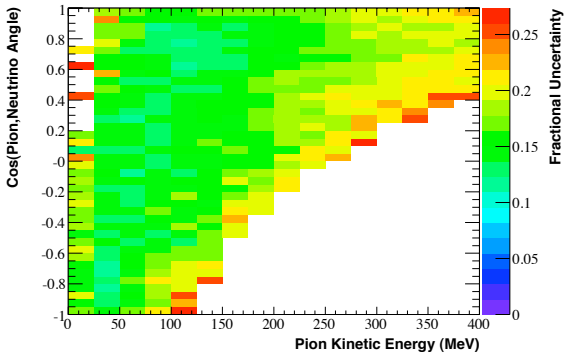

(b) Total fractional error on the measured cross section

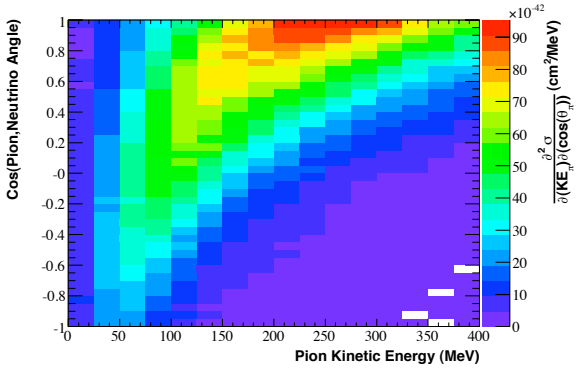

(c) Monte Carlo predicted cross section

Figure 6.35: The measured $\partial^2\sigma/\partial(cos(\theta_{\pi,\nu}))\partial(KE_\pi)$ values are shown along with the total fractional uncertainties. The Monte Carlo predicted cross section is shown for comparison.

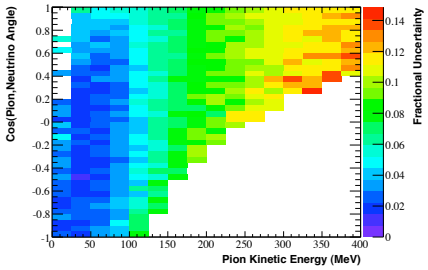

(a) The fractional systematic uncertainty from the "XSec" error source.

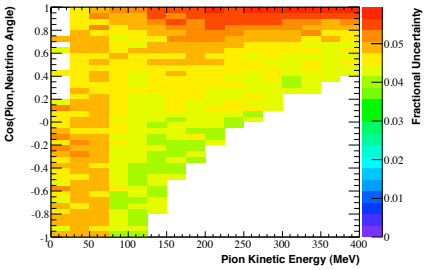

(b) The fractional systematic uncertainty from the "Beam" error source.

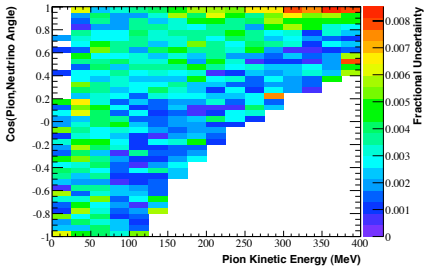

(c) The fractional systematic uncertainty from the "K^+" error source.

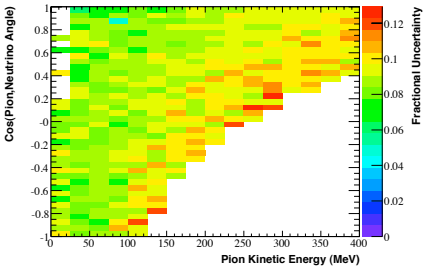

(d) The fractional systematic uncertainty from the "π^+" error source.

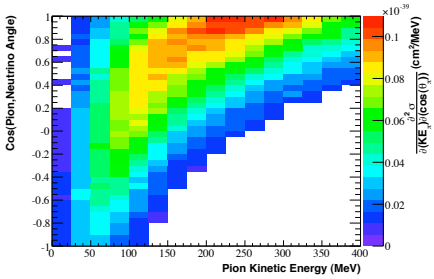

(e) Central value $\partial^2\sigma/\partial(cos(\theta_{\pi,\nu}))\partial(KE_\pi)$ Measurement

Figure 6.36: The fractional systematic uncertainties on the measured $\partial^2\sigma/\partial(cos(\theta_{\pi,\nu}))\partial(KE_\pi)$ values are shown for four of the error sources. The central value measurement is shown for reference. Note that the color scales differ for each systematic error source. An explanation of each error is given in Section 6.4.7.

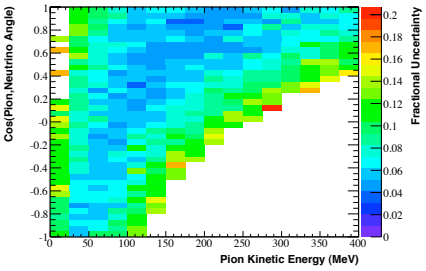

(a) The fractional systematic uncertainty from the "OM" error source.

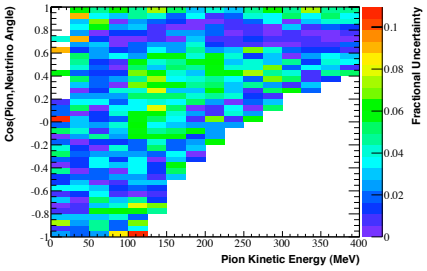

(b) The fractional systematic uncertainty from the "DISC" error source.

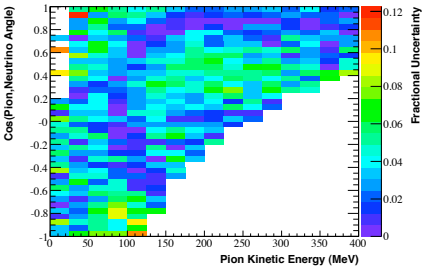

(c) The fractional systematic uncertainty from the "QTCORR" error source.

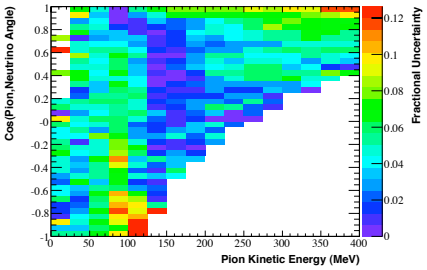

(d) The fractional systematic uncertainty from the "ITER" error source.

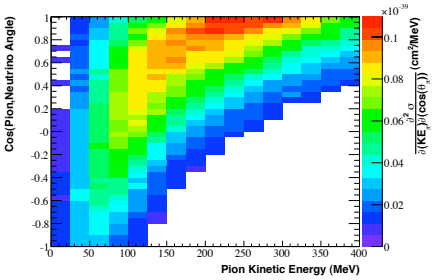

(e) Central value $\partial^2\sigma/\partial(cos(\theta_{\pi,\nu}))\partial(KE_\pi)$ Measurement

Figure 6.37: The fractional systematic uncertainties on the measured $\partial^2\sigma/\partial(cos(\theta_{\pi,\nu}))\partial(KE_\pi)$ values are shown for four of the error sources. The central value measurement is shown for reference. Note that the color scales differ for each systematic error source. An explanation of each error is given in Section 6.4.7.

Chapter 7

Conclusion

Results have been presented for the effective CCπ^+ cross section as a function of several fundamental kinematic variables. Of these results, the cross sections measured as a function of the neutrino energy are the least experiment dependent, since the predicted neutrino flux has been removed separately from each bin. Previous measurements of the neutrino energy cross section are shown in Figure 7.1. All comparable measurements below 2 GeV have uncertainties larger than 20%, upon which the present analysis provides a significant improvement. Each of these measurements has either been performed on, or extrapolated to, a single nucleon target, which has been explicitly avoided in this measurement. As discussed in Section 1.1.2.2, the current theoretical understanding of the vector and axial-vector nucleon form factors for both hydrogen and carbon, as well as nuclear effects such as the Fermi momentum distribution and nuclear screening, motivate measurements of model independent cross section quantities from which theoretical models can be derived.

To get a sense of how this measurement compares to previous measurements, the Nuance prediction in Figure 7.1 can be compared to the Monte Carlo prediction in Figure 6.11 after being convolved with the nuclear effects described in Section 1.2. The present measurement is on average about 20% higher than the Nuance prediction for the effective cross section. The Brookhaven experiment that provides the most proton and neutron data in the MiniBooNE neutrino energy range [72] is also roughly 20% higher

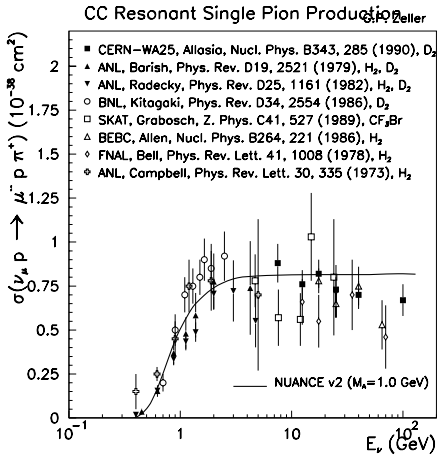

(a) Previous CCπ^+ measurements extrapolated to single proton targets.

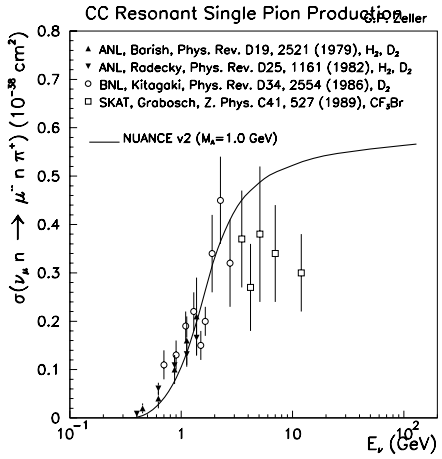

(b) Previous CCπ^+ measurements extrapolated to single proton targets.

Figure 7.1: Previous measurements of ν_μ induced CCπ^+ measurements are shown for proton and neutron targets [69, 70, 71, 72, 73, 74, 75, 76]. Those experiments not measured on H_2 have been extrapolated to single nucleon cross sections. The line indicating the Nuance prediction represents the Monte Carlo predicted cross section in Figure 6.11 prior to the modeling of nuclear effects.

than the Nuance prediction for the resonant Δ^{++} interactions (i.e. proton targets) that dominate the present result.[1]

The remaining kinematic CCπ^+ cross sections have never been measured before.[2] These measurements are also dependent on the flux shape prediction given in Figure 6.10. For this reason, each measurement of a final state kinematic quantity has also been measured in bins of neutrino energy. The one-dimensional have also been provided due to the familiarity of many in the field with flux-averaged results. Indeed, this is a commonly requested form for such measurements, as many theorists have been producing results according to the MiniBooNE flux for some time [77, 78, 79, 80].

[1] It should be mentioned that the Brookhaven experiment derived its flux prediction from the measured rate of CCQE interactions, effectively measuring a cross section ratio to CCQE.

[2] Although these differential cross sections have not been measured, previous experiments have performed fits to reconstructed Q^2 and π^+ angular distributions to extract values for parameters such as the axial mass.

The cross section measurements produced by this analysis provide a detailed description of the CCπ^+ interaction in terms of many of the interesting kinematic quantities. Hopefully these results will aid the effort to fully understand the properties of these interactions. In the immediate future, the cross sections provided by this analysis will help to constrain the largest charged current background in the next generation of neutrino oscillation experiments.

Bibliography

[1] C. Amsler et al. The Review of Particle Physics. Physics Letters, B667(1), 2008.

[2] D. Rein and L. H. Sehgal. Neutrino-Excitation of Baryon Resonances and Single Pion Production. Annals Physics, 133(79), 1981.

[3] M. Kislinger R. P. Feynman and F. Ravndal. Current Matrix Elements from a Relativistic Quark Model. Phys. Rev., D3(2706), 1971.

[4] F. Ravndal. Weak Production of Nuclear Resonances in Relativistic Quark Model. Nuovo Cimento, A18(385), 1973.

[5] E. T. Osypowski M. G. Olsson and E. H. Monsay. Electroproduction of Low Hadronic Masses. Phys. Rev., D17(2938), 1978.

[6] M. Hasegawa et al. Search for Coherent Charged Pion Production in Neutrino Carbon Interactions. Phys. Rev. Lett., 95(79), 1981.

[7] J. Nowak and W. Metcalf. MiniBooNE Technical Note. 260, 2008.

[8] V. V. Lynbushkin K. S. Kuzmin and V. A. Naumov. Lepton Polarization in Neutrino Nucleon Interactions. Mod. Phys. Lett., A19(2815), 2004.

[9] C. Berger and L. M. Sehgal. Lepton Mass Effects in Single Pion Production by Neutrinos. Phys. Rev., D76(113004), 2007.

[10] C. Berger and L. M. Sehgal. Erratum: Lepton Mass Effects in Single Pion Production by Neutrinos. Phys. Rev., D77(059901), 2007.

[11] K. M. Graczyk and J. T. Sobczyk. Lepton Mass Effects in Weak CC Single Pion Production. Phys. Rev., D77(053003), 2008.

[12] K. M. Graczyk and J. T. Sobczyk. Form Factors in the Quark Resonance Model. Phys. Rev., D77(053001), 2008.

[13] S. K. Singh L. Alvarez-Ruso and M. F. Vincente-Vascas. Charged Current Weak Electroproduction of the Δ Resonance. Phys. Rev., C57(2693), 1998.

[14] O. Lalakulich and E. A. Paschos. Resonance Production By Neutrinos: J=3/2 Resonances. Phys. Rev., D71(074003), 2005.

[15] A. Kartavtsev E. A. Paschos and G. J. Gounaris. Coherent pion Production by Neutrino Scattering Off Nuclei. Phys. Rev., D74(054007), 2006.

[16] S. Hirenzaki L. Alvarez-Ruso, L. S. Geng and M. J. Vicente Vacas. Charged Current Neutrino-Induced Coherent Pion Production. Phys. Rev., C75(055501), 2007.

[17] J. Nieves J. E. Amaro, E. Hernandez and M. Valverde. Theoretical Study of Neutrino-Induced Coherent Pion Production Off Nuclei at T2K and MiniBooNE Energies. Phys. Rev., D79(013002), 2009.

[18] K. Hiraide et al. Search for Charged Current Coherent Pion Production on Carbon in a Few-GeV Neutrino Beam. Phys. Rev., D78(112004), 2008.

[19] M. Hasegawa et al. Search for Coherent Charged Pion Production in Neutrino-Carbon Interactions. Phys. Rev. Lett., 95(252301), 2005.

[20] A. A. Aguilar-Arevalo et al. First observation of coherent π^0 production in neutrino-nucleus interactions with $E_\nu < 2$ GeV. Phys. Lett., B664(41), 2008.

[21] T2K Collaboration. Tokai-to-Kamioka (T2K) Long Baseline Neutrino Oscillation Experiment Proposal. http://j-parc.jp/NuclPart/pac_0606/pdf/p11-Nishikawa.pdf, 2006.

[22] NOνA Collaboration. NOνA Proposal to Build a 30 Kiloton Off-Axis Detector to Study Neutrino Oscillations in the Fermilab NuMI Beamline. arXiv:hep-ex/0503053, 2005.

[23] J. E. Amaro M. Valverde J. Nieves, M. J. Vicente-Vacas and E. Hernandez. Theoretical Update on Low Energy Neutrino-Nucleus Reactions. arXiv:0809.5219v2, 2008.

[24] T. Kobilarcik J. Monroe, D. Finley and H-O. Meyer. MiniBooNE Technical Note. 87, 2003.

[25] The BooNE Collaboration. Technical Design Report for the 8 GeV Beam, 2001.

[26] The BooNE Collaboration. Technical Design Report for the MiniBooNE Neutrino Beam, 2001.

[27] The BooNE Collaboration. The MiniBooNE Detector Technical Design Report, 2001.

[28] A. A. Aguilar-Arevalo et al. The MiniBooNE Detector. arXiv:0806.4201, 2008.

[29] S. Agostinelli et al. GEANT 4–A Simulation Toolkit. Nucl. Instrum. Meth., A506(250), 2003.

[30] H. A. Tanaka. MiniBooNE Technical Note. 186, 2006.

[31] R. J. Glauber. Lectures in Theoretical Physics, volume I. Interscience, New York, 1959.

[32] V. V. Gachurin et al. Measurement of Total Inelastic Cross-Sections of the Interaction of Protons and pi+ Mesons on Nuclei in the Momentum Range from 1.35-GeV/c to 3.75-GeV/c. ITEP-59-1985, 1985.

[33] B. M. Bobchenko et al. Measurement of Total Inelastic Cross-Sections from Proton Interactions with Nuclei in the Momentum Range from 5-GeV/c to 9-GeV/c and pi- Mesons with Nuclei in the Momentum Range from 1.75-GeV/c to 6.5-GeV/c. Sov. J. Nucl. Phys., 30(805), 1979.

[34] C. Ashery et al. True Absorption and Scattering of Pions on Nuclei. Phys. Rev., C23(2173), 1981.

[35] B. W. Allardyce et al. Pion Reaction Cross Sections and Nuclear Sizes. Nucl. Phys., A209(1), 1973.

[36] H. Tanaka and M. Wilking. MiniBooNE Technical Note. 206, 2006.

[37] A. A. Aguilar-Arevalo et al. Neutrino Flux Prediction at MiniBooNE. Phys. Rev., D79(072002), 2009.

[38] M. Tzanov. MiniBooNE Technical Note. 204, 2006.

[39] M. Shaevitz. MiniBooNE Technical Note. 209, 2006.

[40] J. R. Sanford and C. L. Wang. Emperical Formulas for Particle Production in p-Be Collision Between 10 and 35 BeV/c. BNL 11299, 1967.

[41] N. V. Mokhov et al. Recent Enhancements to the MARS15 Code. Radiat. Prot. Dosim., 116(99), 2005.

[42] M. G. Catanesi et al. Measurement of the Production Cross-Section of Positive Pions in the Collision of 8.9 GeV/c Protons on Beryllium. Eur. Phys. J., C52(29), 2007.

[43] F. Abe et al. Production of Neutral Strange Particles K_S^0 and Λ_0 by 12-GeV Protons on Nuclear Targets. Phys. Rev., D36(1302), 1987.

[44] M. Shaevitz. MiniBooNE Technical Note. 188, 2006.

[45] T. Abbott et al. Measurement of Particle Production in Proton-Induced Reactions at 14.6 GeV/c. Phys. Rev., D45(3906), 1992.

[46] J. V. Allaby et al. High-Energy Particle Spectra from Proton Interactions at 19.2-GeV/c. CERN 70-12, 1970.

[47] D. Dekkers et al. Experimental Study of Particle Production at Small Angles in Nucleon-Nucleon Collisions at 19 and 23 GeV/c. Phys. Rev., 137(B962), 1965.

[48] G. J. Marmer et al. Differential Production Cross Sections of Low-Momentum Particles from 12.3-BeV/c Protons on Beryllium and Copper. Phys. Rev., 179(1294), 1969.

[49] T. Eichten et al. Particle Production in Proton Interactions in Nuclei at 24 GeV/c. Nucl. Phys., B44(333), 1972.

[50] Aleshin et al. Production of K+- Mesons from Be Targets at 62-Mrad at 9.5-GeV/c Incident Proton Momenta. ITEP-80-1977, 1977.

[51] Vorontsov et al. A-Dependence Of Fragmentation Of 9.2-Gev Protons On Nuclei. ITEF-88-011, 1988.

[52] W.-M. Yao et al. The Review of Particle Physics. J. Phys., G33(1), 2006.

[53] S. Brice. MiniBooNE Technical Note. 257, 2008.

[54] D. Casper. The nuance Neutrino Simulation, and the Future. arXiv:hep-ph/0208030v1, 2001.

[55] C. H. Llewellyn Smith. Neutrino Reactions at Accelerator Energies. Phys. Rept., 3(261), 1972.

[56] R. A. Smith and E. J. Moniz. Neutrino Reactions on Nuclear Targets. Nucl. Phys, B43(605), 1972.

[57] E. J. Moniz. Nuclear Fermi Momenta from Quasielastic Electron Scattering. Phys. Rev. Lett., 26(445), 1971.

[58] R. Brun et al. GEANT3. CERN-DD/EE/84-1, 1987.

[59] R. B. Patterson. A Search for Muon Neutrino to Electron Neutrino Oscillations at $\Delta m^2 > 0.1$ eV^2. PhD thesis, Princeton University, 2007.

[60] D. F. Measday T. Suzuki and J. P. Roalsvig. Total Nuclear Capture Rates for Negative Muons. Phys. Rev., C35(2212), 1987.

[61] C. Zeitnitz and T. A. Gabriel. The GEANT-CALOR Interface and Benchmark Calculations of ZEUS test Calorimeters. Nucl. Instrum. Meth., A349(106), 1994.

[62] J. Birks. Theory and Practice of Scintillation Counting. Pergamon Press, 1964.

[63] I. Stancu. MiniBooNE Technical Note. 50, 2002.

[64] MINUIT. CERN Program Library entry D506. http://wwwasdoc.web.cern.ch/wwwasdoc/minuit/minmain.html, @copyright 1994-1998.

[65] M. O. Wascko. Charged Current Single Pion Cross Section Measurement at MiniBooNE. arXiv:hep-ex/0602050v1, 2006.

[66] G. D'Agostini. A Multidimensional Unfolding Method Based on Bayes' Theorem. Nucl. Instrum. Meth., A362(487), 1995.

[67] G. Cowen. A Survey of Unfolding Methods for Particle Physics. Conf. Proc. Advanced Statistical Techniques in Particle Physics, March 2002.

[68] http://www-boone.fnal.gov.

[69] D. Allasia et al. Investigation of Exclusive Channels in $\nu/\bar{\nu}$-Deuteron Charged Current Interactions. Nucl. Phys., B343(285), 1990.

[70] S. J. Barish et al. Study of Neutrino Interactions in Hydrogen and Deuterium. II. Inelastic Charged-Current Reactions. Phys. Rev, D19(2521), 1979.

[71] G. M. Radecky et al. Study of Single-Pion Production by Weak Charged Currents in Low-Energy νd Interactions. Phys. Rev., D25(1161), 1982.

[72] T. Kitagaki et al. Charged-Current Exclusive Pion Production in Neutrino-Deuterium Interactions. Phys. Rev., D34(2554), 1986.

[73] H.J. Grabosch et al. Cross-Section Measurements Of Single Pion Production In Charged Current Neutrino and Anti-Neutrino Interactions. Z. Phys., C41(527), 1989.

[74] P. Allen et al. A Study of Single-Meson Production in Neutrino and Antineutrino Charged-Current Interactions on Protons. Nucl. Phys., B264(221), 1986.

[75] J. Bell et al. Cross-Section Measurements for the Reactions $\nu p \rightarrow \mu^- \pi^+ p$ and $\nu p \rightarrow \mu^- K^+ p$ at High Energies. Phys Rev. Lett., 41(1008), 1978.

[76] J. Campbell. Study of the Reaction $\nu p \rightarrow \mu^- \pi^+ p$. Phys. Rev. Lett., 30(335), 1973.

[77] J. E. Amaro et al. Theoretical Study of Neutrino-Induced Coherent Pion Production Off Nuclei at T2K and MiniBooNE Energies. Advanced Statistical Techniques in Particle Physics.

[78] M. Sajjad Athar et al. Charged Current Anti-neutrino Reactions from ^{12}C at MiniBooNE Energies. Phys. Rev., D75(093003), 2007.

[79] S. K. Singh et al. Nuclear Effects in Neutrino Induced Coherent Pion Production at K2K and MiniBooNE. Phys. Rev. Lett., 96(241801), 2006.

[80] L. Alvarez-Ruso et al. Neutrino-Induced Coherent Pion Production. arXiv:0709.3019, AIP Conf. Proc., 967(201), 2007.

Appendix A

Event Displays

In the following sections, geometric representations of several aspects of the CCπ^+ fitter are presented. Each event display shows the X versus Z view in the left column and the Y versus Z view in the right column. The top plots show the emission point of every Cherenkov and scintillation photon in the event, and the bottom plots show the vertices where one of the following took place:

(1) event creation

(2) hadronic interaction

(3) particle decay

(4) a particle created in (1)-(3) came to rest

The particles that connect the vertices are shown as straight lines.

Each display is cumulative over the entire event time window. Particles produced in the decays of stopped particles occur in later subevents (i.e. PMT hit time groupings; see Section 6.3) and are not included in the CCπ^+ fits. In particular, Michel electrons produced by stopped muon decays or $\pi \rightarrow \mu \rightarrow e$ decay chains occur in every event due to the three subevent requirement, but they do not contribute to the charge or time likelihoods of the fit.

The graphical representations of the fitter show most of the fit parameters. The muon track (red line) and the kinked pion track (magenta line) give the vertex and all

of the directions. The remaining energy parameters for both the true and fit tracks are listed on each display, along with the goodness of fit, $-\log(\mathcal{L})$. The curved black line present in some of the displays represents the location of the front faces of the PMTs in the plane that contains the interaction, and the green stars give the locations of the reconstructed Michel electrons.

A.1 Truth Seeds

To verify that a maximum in the likelihood surface exists for the correct set of reconstructed track parameters, studies have been performed where the fitter has been seeded with the true Monte Carlo variables. In this section, event displays from true seeded fits are shown for a few different event types. The initial energy of each track segment is extracted from the Monte Carlo, so E_μ, E_π, and the energy of the downstream pion track all are set to their generated values. The kink location and the energy lost in the kink are more difficult to obtain, so these values are approximated by adding the energies for all GEANT-recorded particles created in the kink and extrapolating upstream from the energy of the pion that exits the interaction. As we will see in at least one example, this does not always account for all energy lost in the interaction (e.g. nuclear recoil is excluded).

The following types of seed / event relationships are displayed in this section:

(1) A CCπ^+ event with a high energy pion and a good seed (seed: Figure A.1, fit: Figure A.2);

(2) A low energy pion with a Cherenkov ring that overlaps with a high energy muon ring (seed: Figure A.3, fit: Figure A.4);

(3) An event with multiple hadronic interactions (seed: Figure A.5, fit: Figure A.6);

(4) A pion track where most of its energy is lost in the hadronic interaction (seed: Figure A.7, fit: Figure A.8);

(5) A slightly incorrect "true" seed (seed: Figure A.9, fit: Figure A.10);

(6) A pion that does not experience a hadronic interaction (seed: Figure A.11, fit: Figure A.12);

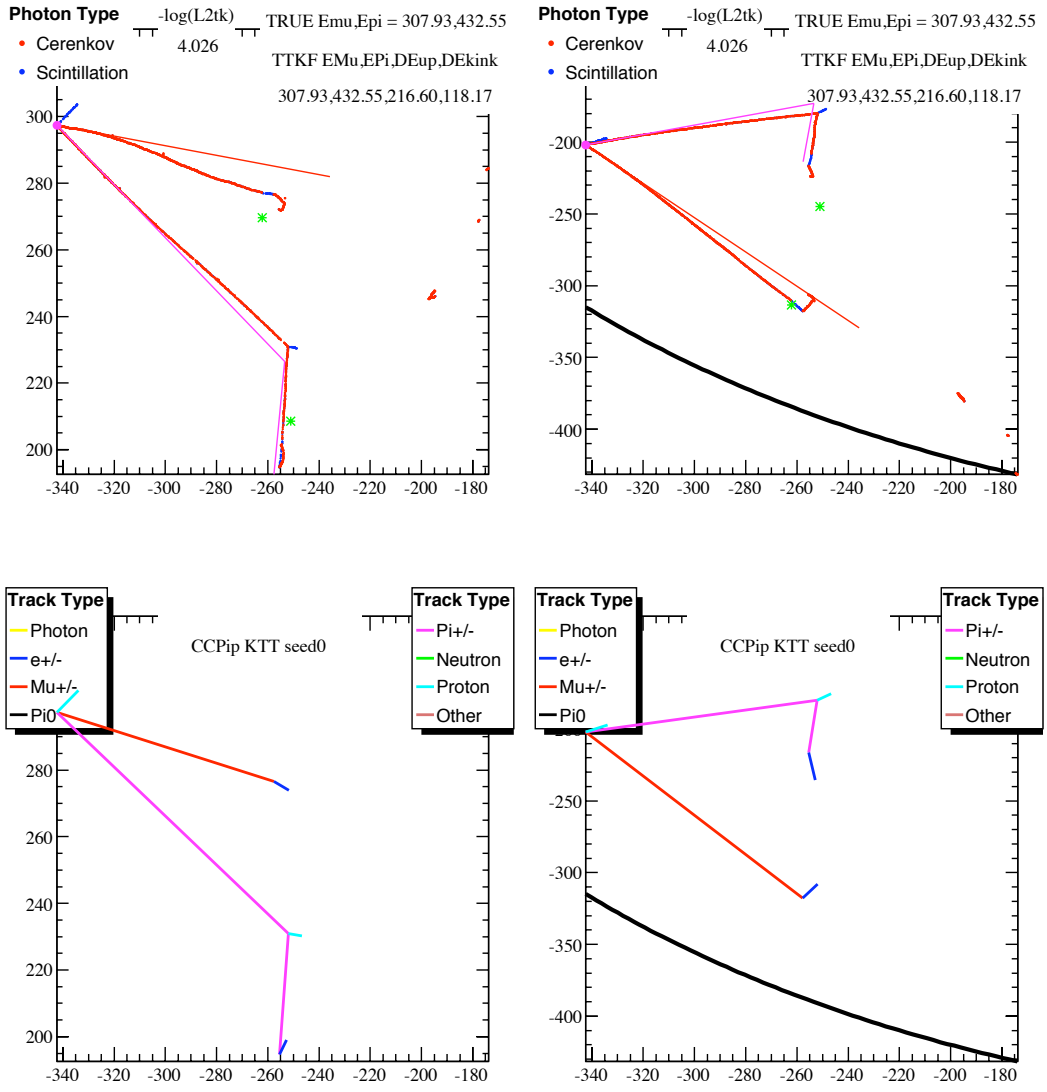

Figure A.1: The true seed for an event with a large pion energy. About half of the pion energy is lost in the upstream track segment, with about a quarter of the energy lost in both the kink and the downstream segment. The downstream segment is well above Cherenkov threshold.

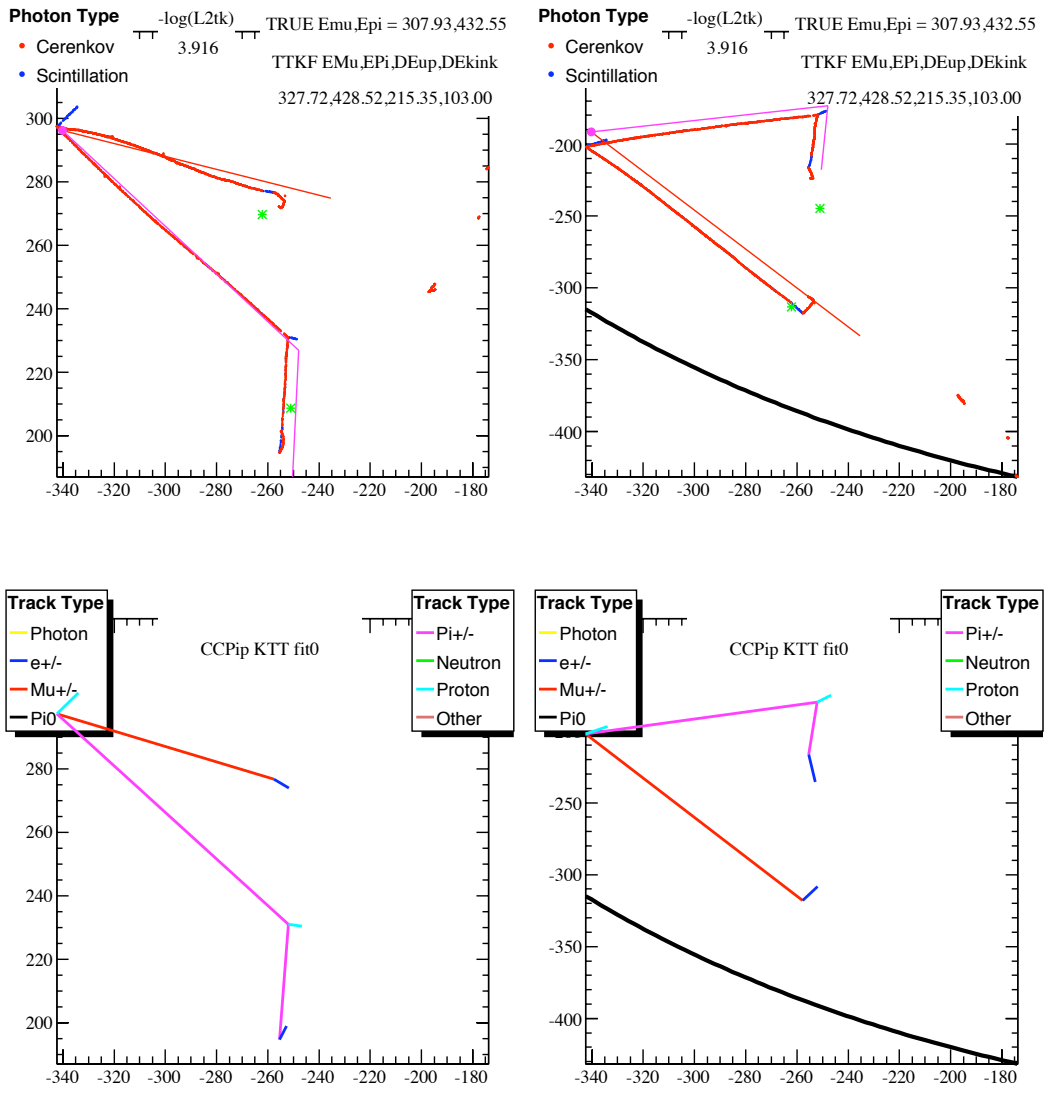

Figure A.2: A likelihood maximum clearly exists for this event. Almost no change has occurred in the track directions. A small amount of energy from the pion track (mostly the energy lost in the hadronic interaction) has been transferred to the muon track.

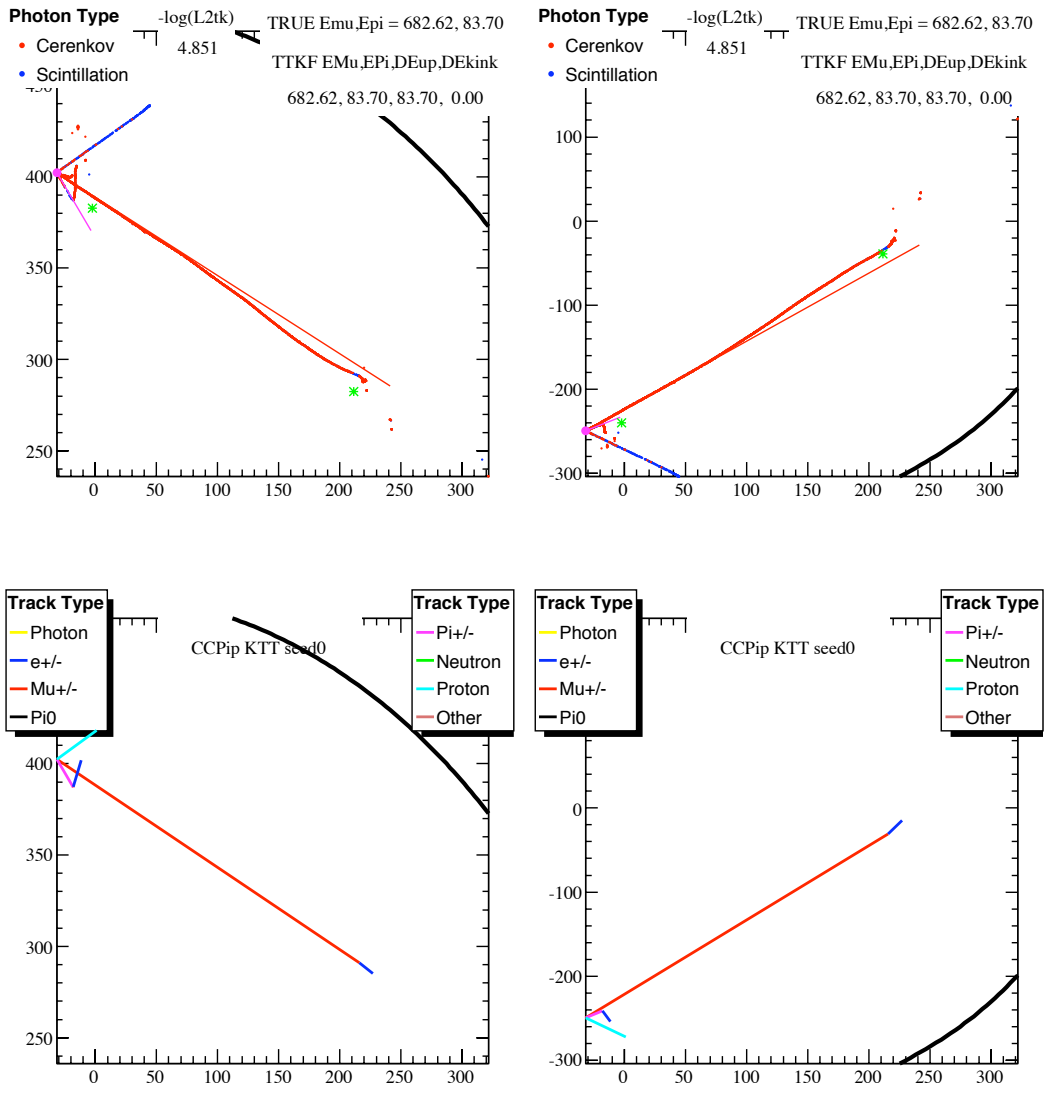

Figure A.3: A fit seed for a low energy, unkinked pion track that creates a Cherenkov ring that overlaps with the ring from a high energy muon track is shown. The Cherenkov emission angle at the upstream portion of the muon track is ∼50 degrees, and the angle between the two tracks is ∼15 degrees.

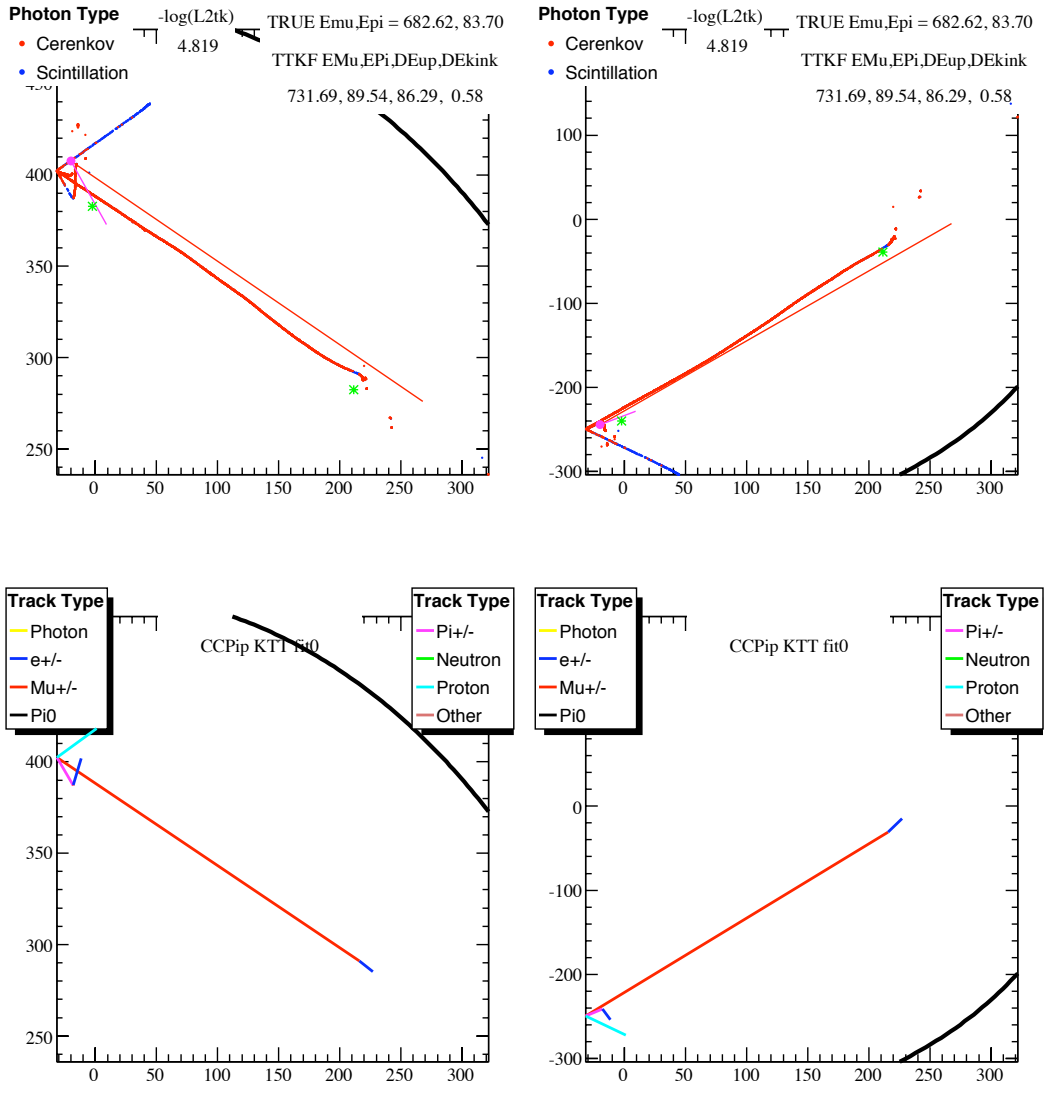

Figure A.4: Despite overlapping rings, there is still a likelihood maximum where both tracks are properly reconstructed.

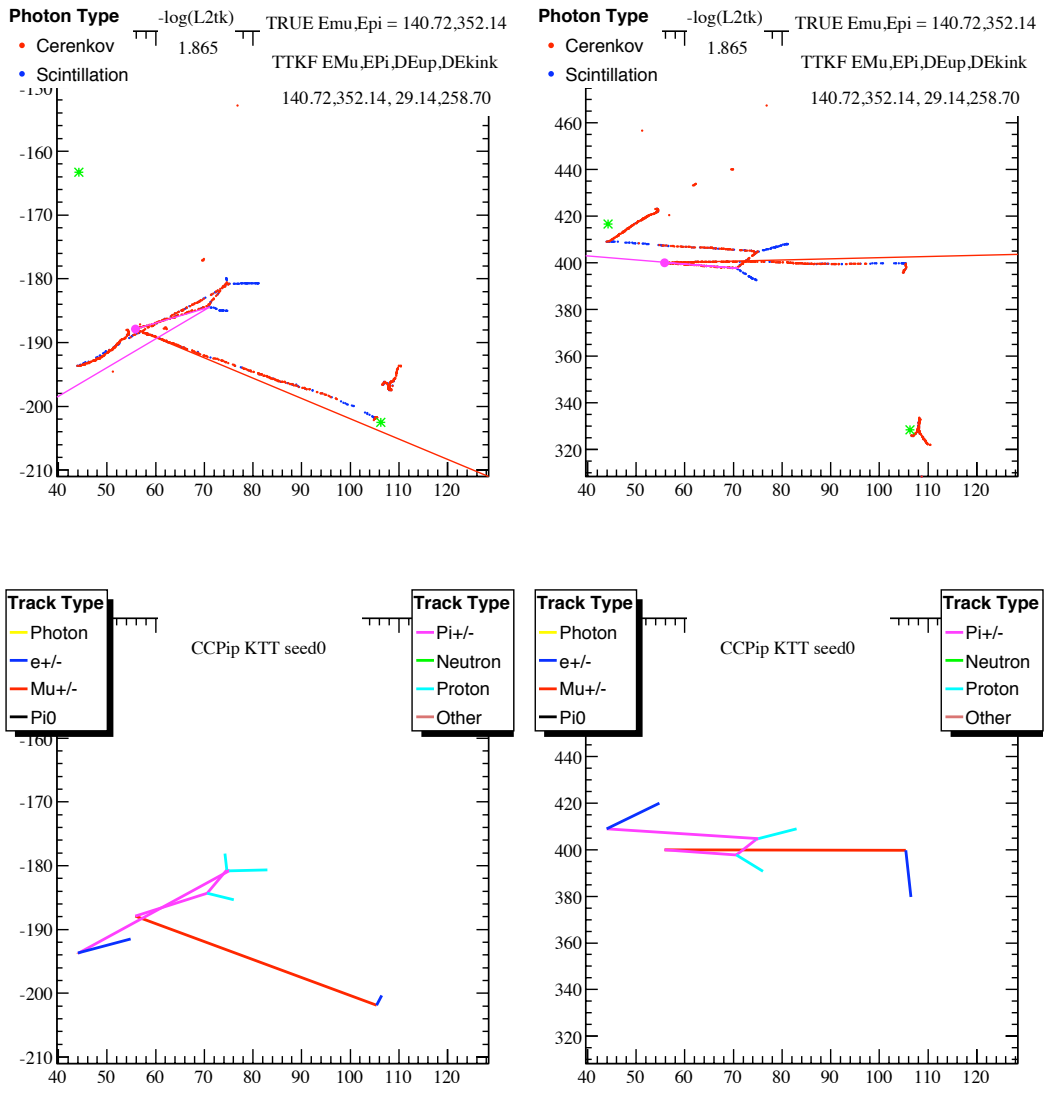

Figure A.5: A seed for an event with multiple hadronic interactions is shown. The "true" seed algorithm chooses the two longest tracks segments. The middle segment has been treated as part of the kink, which is why the "true" energy lost in the kink is so large.

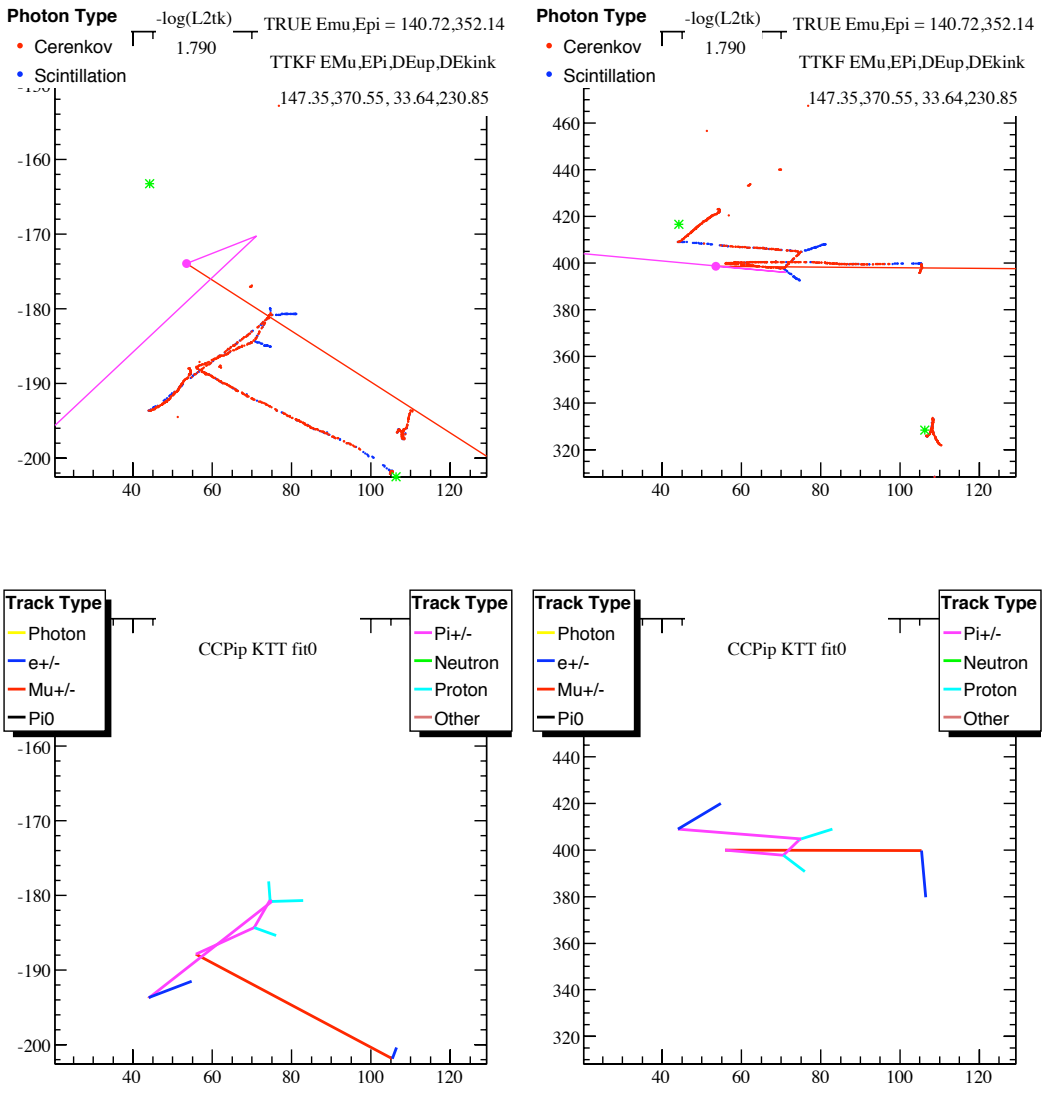

Figure A.6: The likelihood maximum was able to be properly reconstructed, in the sense that the physically interesting quantities are the initial energies and directions of each track. (Note: the reconstruction is less sensitive to the event vertex location.)

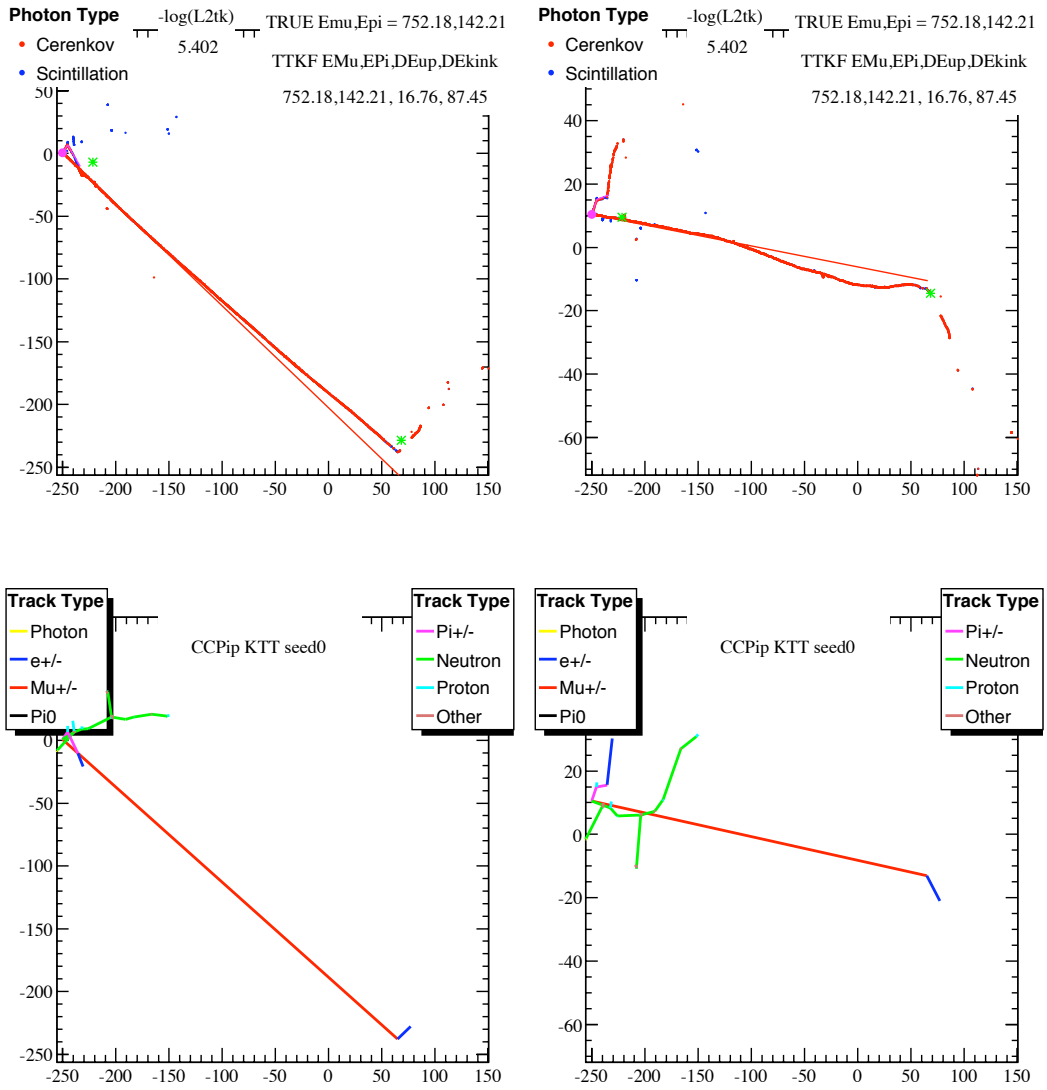

Figure A.7: More than half of the initial pion energy is lost in the hadronic interaction in this event, and the downstream segment emerges from the interaction below Cherenkov threshold.

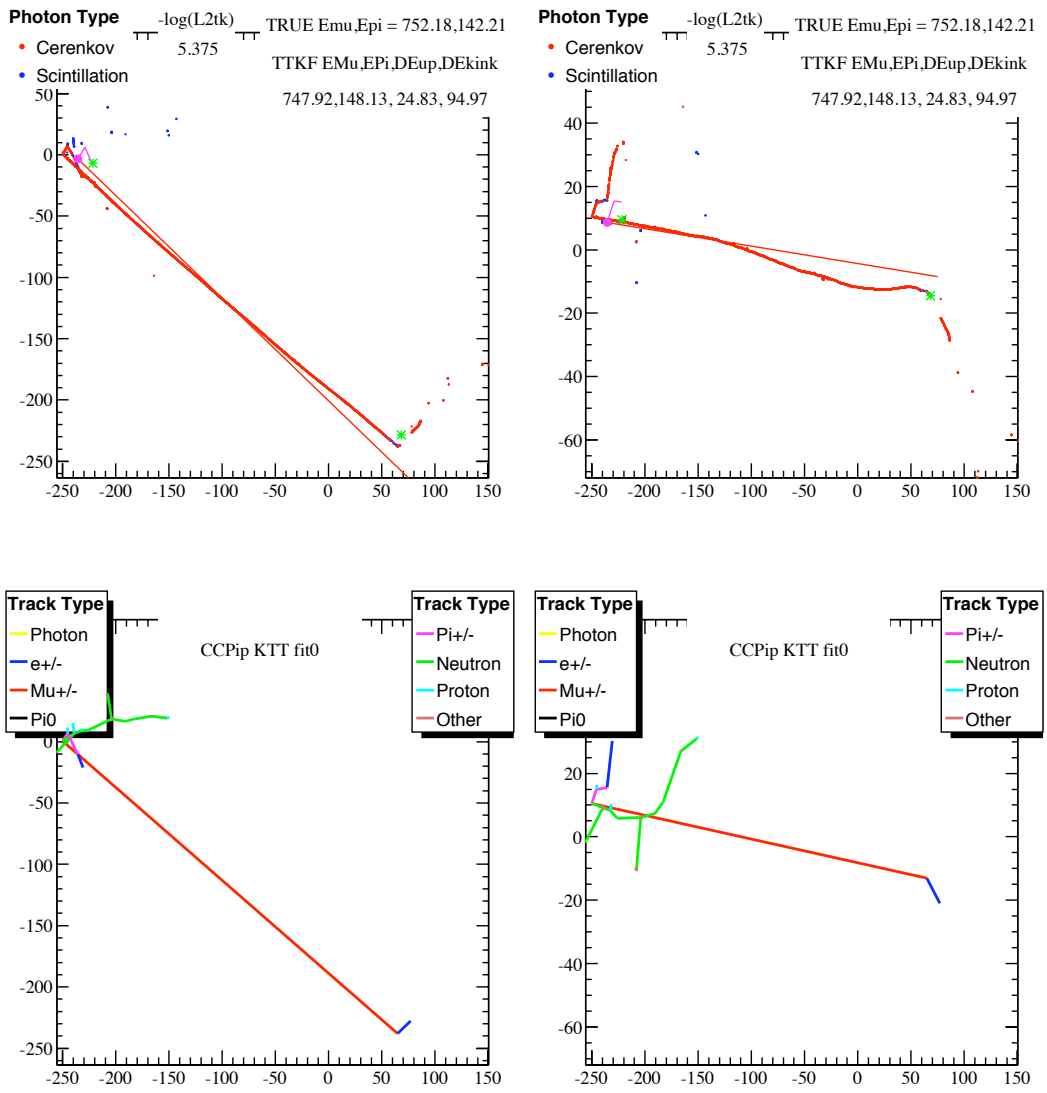

Figure A.8: The upstream pion segment is lengthened slightly, and the energy lost in the kink is increased somewhat, but the energy separation between the pion and the muon remains mostly unchanged.

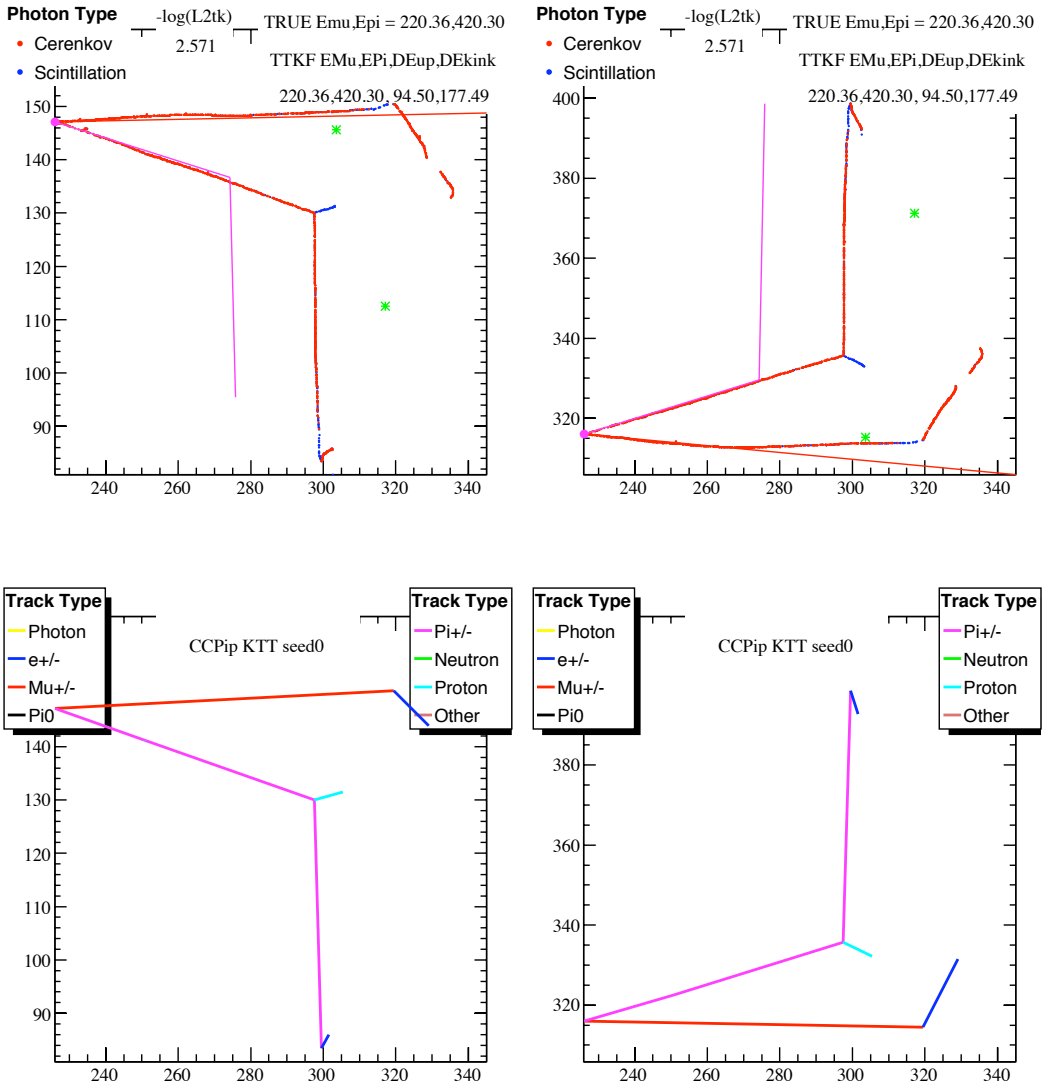

Figure A.9: This seed underestimates the energy lost in the upstream pion segment, and instead puts all of the excess energy into the hadronic interaction.

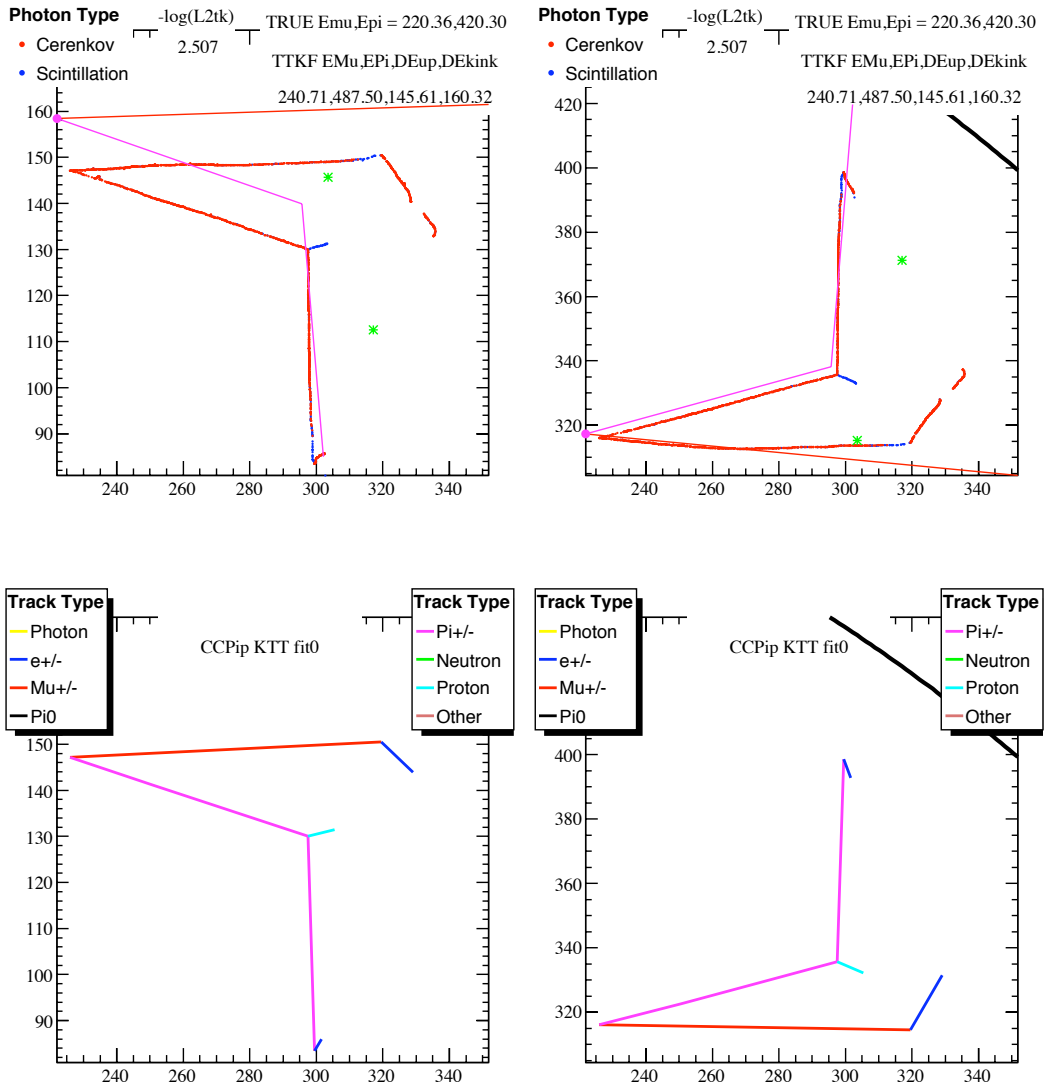

Figure A.10: The fitter has added the extra 50 MeV required for the upstream track segment, but only 17 MeV of that total has been taken from the hadronic energy loss. The downstream segment has also increased, largely due to a lack of constraints due to the close proximity of the tank wall, which then forces the total pion energy to be increased.

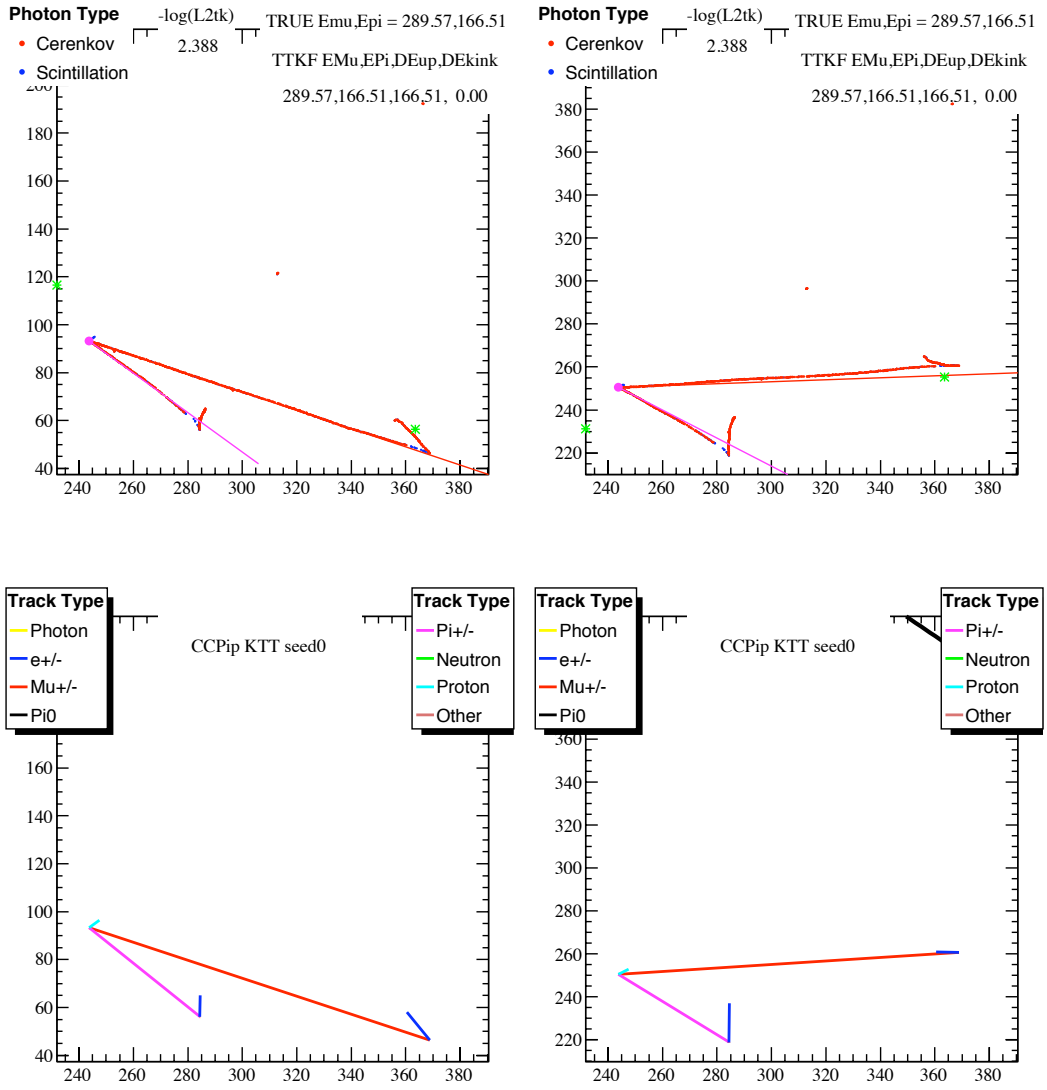

Figure A.11: This seed is for an event in which the pion does not experience a hadronic interaction.

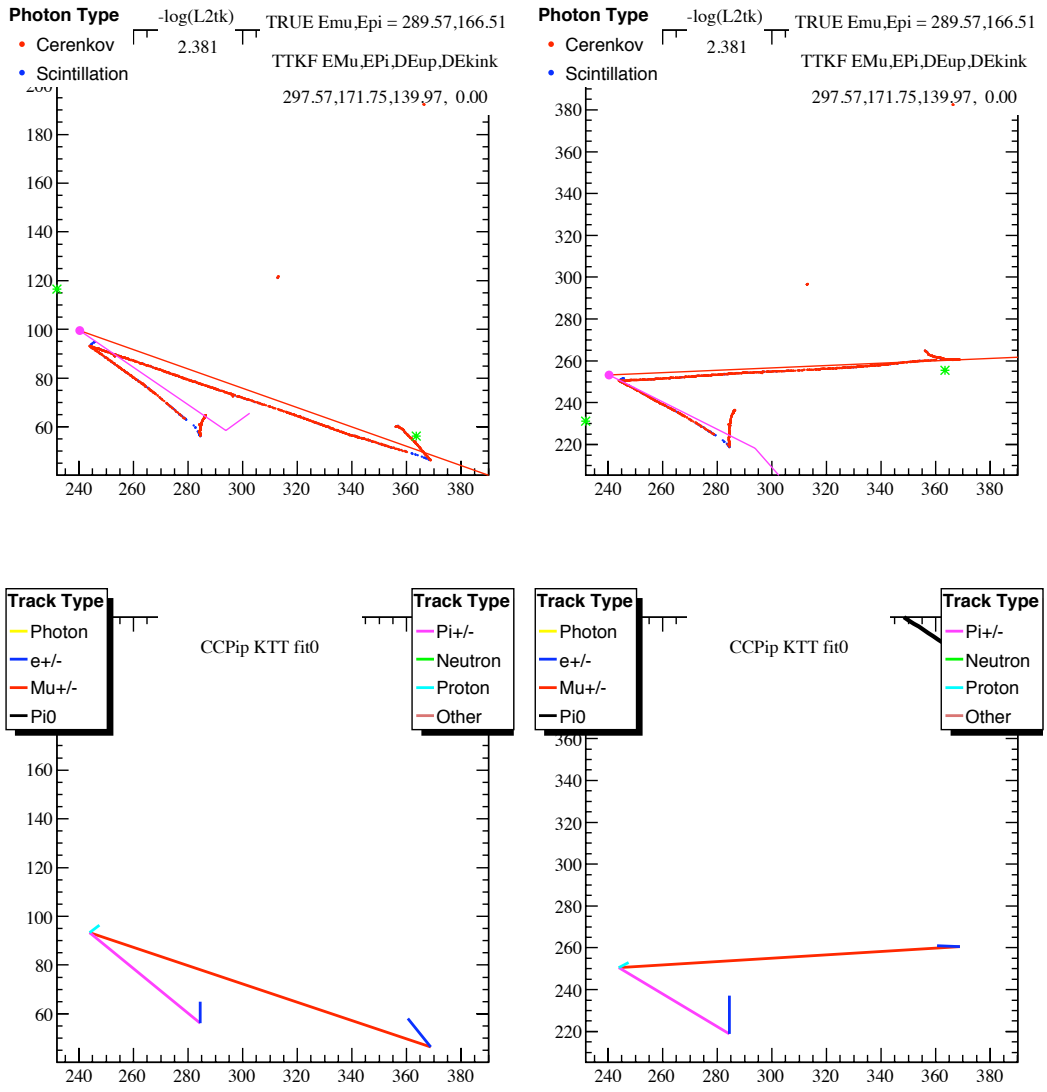

Figure A.12: A kink has been introduced to the pion trajectory, but it occurs after the track has crossed below Cherenkov threshold where there are no constraints on the track direction.

A.2 A CCπ^+ Fit Example

A series of event displays highlighting the CCπ^+ seeding and fitting process are presented in this section. A description and justification for the following sequence of events is given in Section 5.3.1. A summary of the steps and corresponding figures is given below.

(1) Figure A.13: one track fit.

(2) Figure A.14: two track likelihood scan.

(3) Figure A.15: two track fit.

(4) Figure A.16: three track likelihood scan.

(5) Figure A.17: three track fit.

(6) Figure A.18: CCπ^+ seed configuration #1

(7) Figure A.19: CCπ^+ fit #1 ($-\log(\mathcal{L}) = 3.112$; not accepted)

(8) Figure A.20: CCπ^+ seed configuration #2

(9) Figure A.21: CCπ^+ fit #2 ($-\log(\mathcal{L}) = 3.076$; not accepted)

(10) Figure A.22: CCπ^+ seed configuration #3

(11) Figure A.23: CCπ^+ fit #3 ($-\log(\mathcal{L}) = 2.982$; accepted)

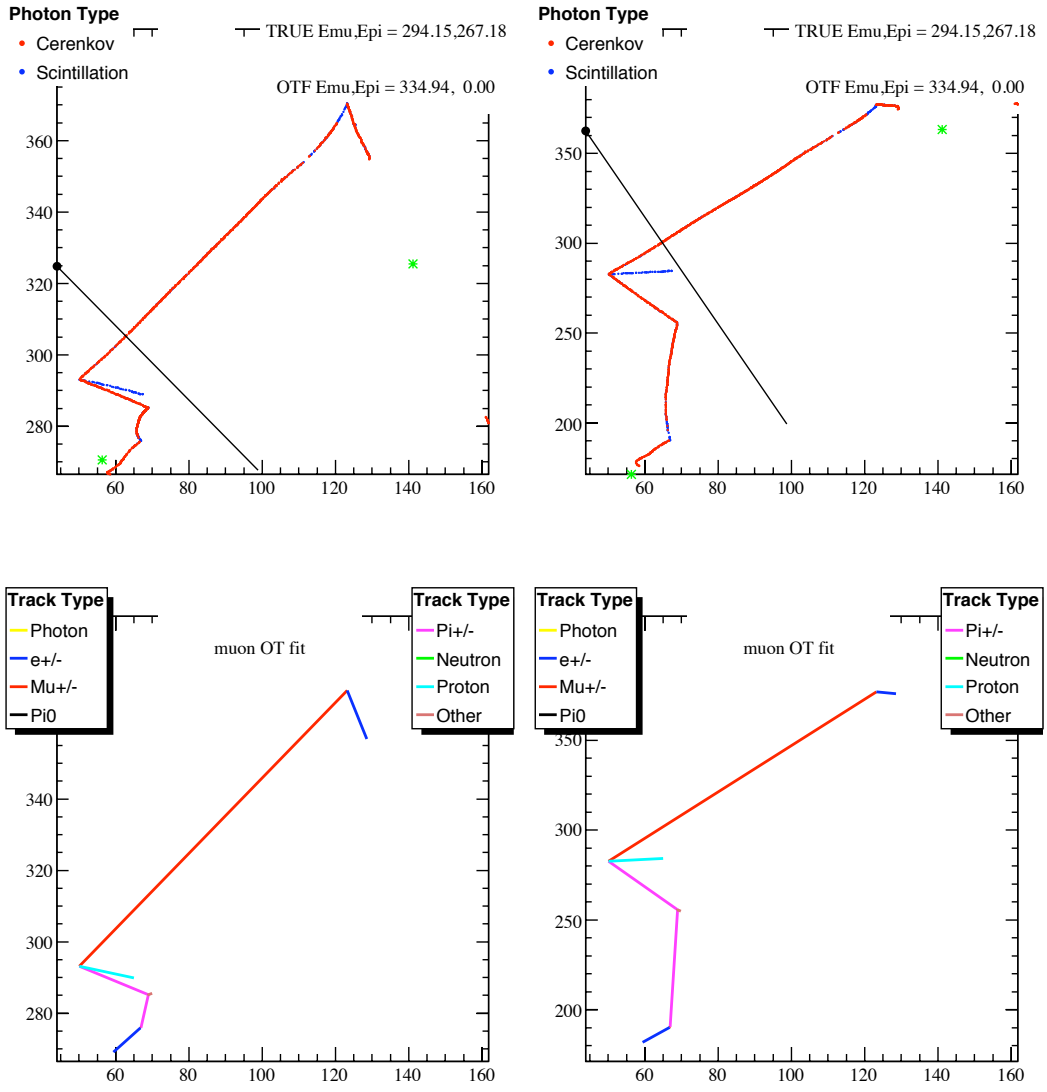

Figure A.13: CCπ^+ fit/seeding step 1: the one track fitter has found the ring belonging to the upstream segment of the kinked pion track. The fit energy overestimates the pion energy in an attempt to account for the additional light created by the other two tracks in the event.

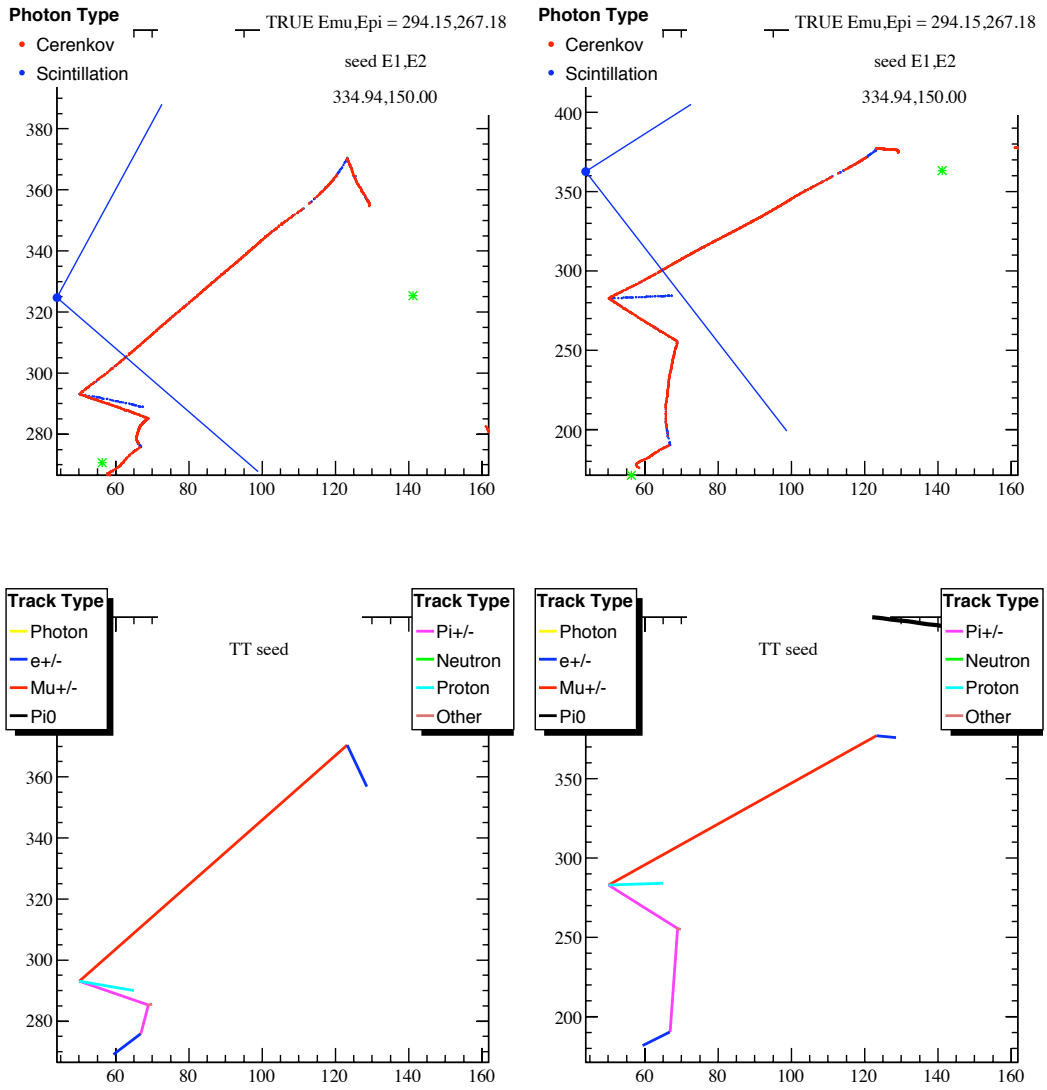

Figure A.14: CCπ^+ fit/seeding step 2: the likelihood scan for the second track (keeping the result of the one track fit fixed) has found the muon. The scan was performed with a track energy of 150 MeV, although 200 MeV is used in the final version of the fitter. Although the scan found a ring, the track direction isn't perfect. The underestimate for the track energy means that the predicted ring diameter is smaller than the actual ring diameter, so the scan has some freedom in choosing the actual track direction.

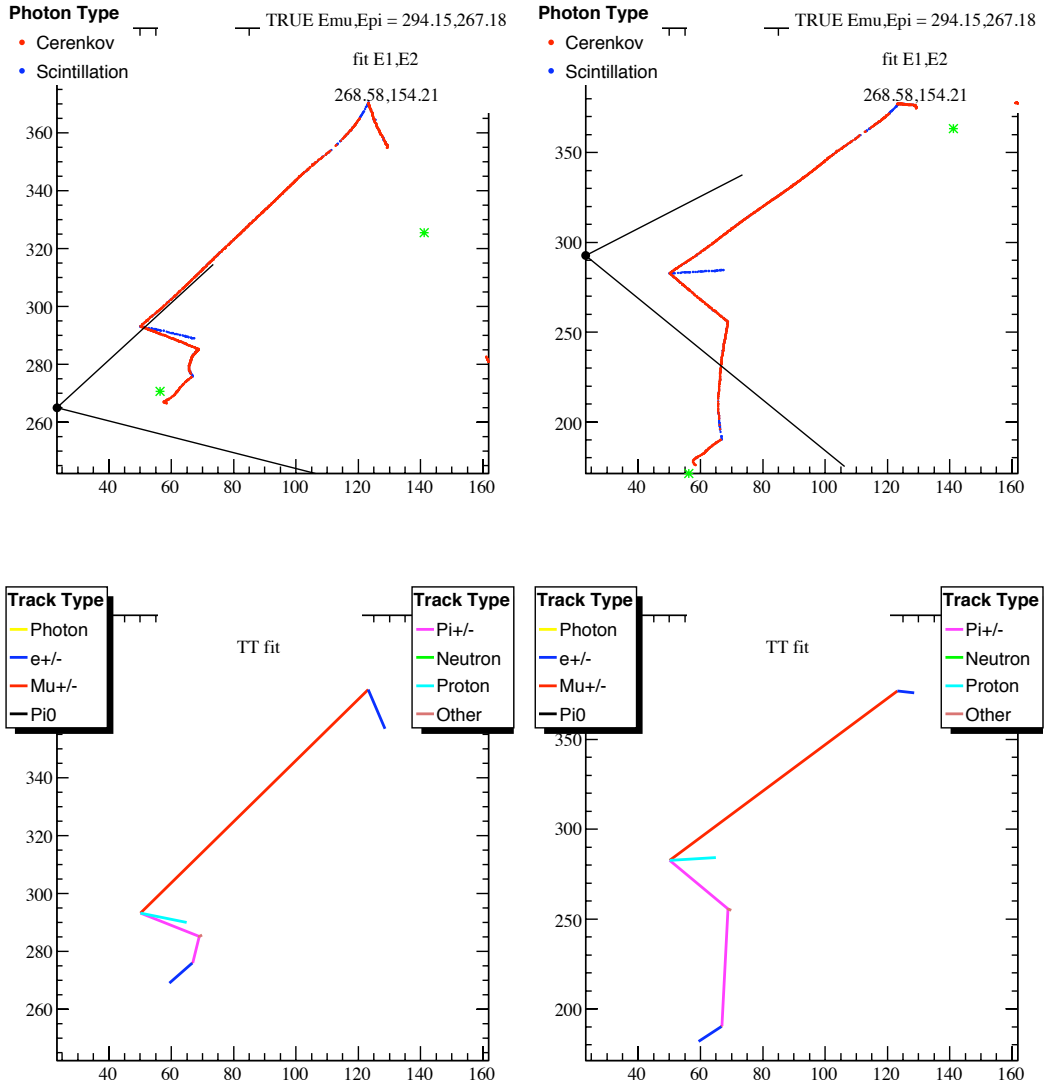

Figure A.15: CCπ^+ fit/seeding step 3: the two track fit has corrected the directions of both tracks to point at the center of their respective rings. The energy overestimate from the one track fit has been greatly reduced, although the second track energy has only been slightly increased so far.

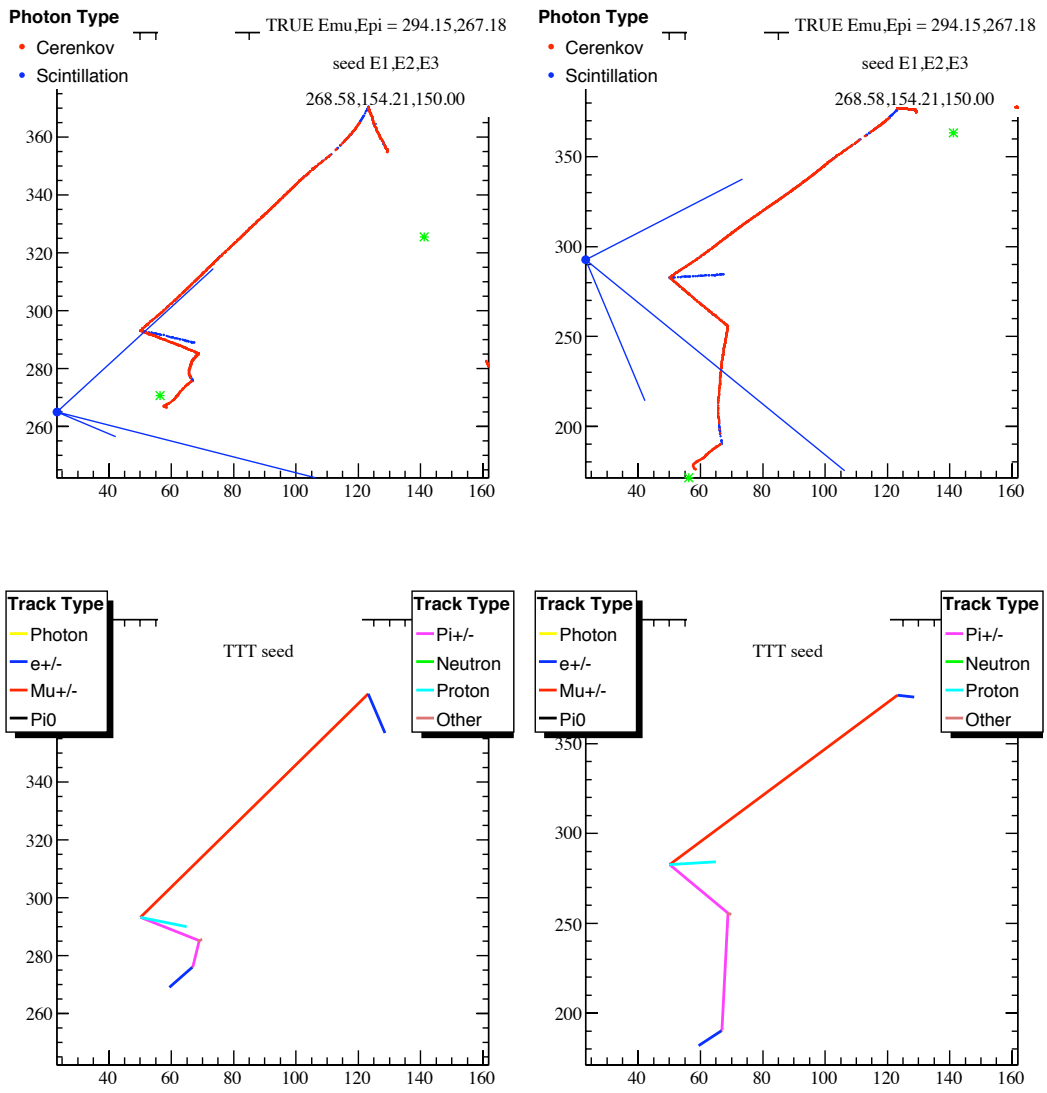

Figure A.16: CCπ^+ fit/seeding step 4: the three track likelihood scan has landed near the most downstream portion of the downstream pion track. Some portion of the upstream pion ring may have pulled the scan slightly toward the upstream pion track.

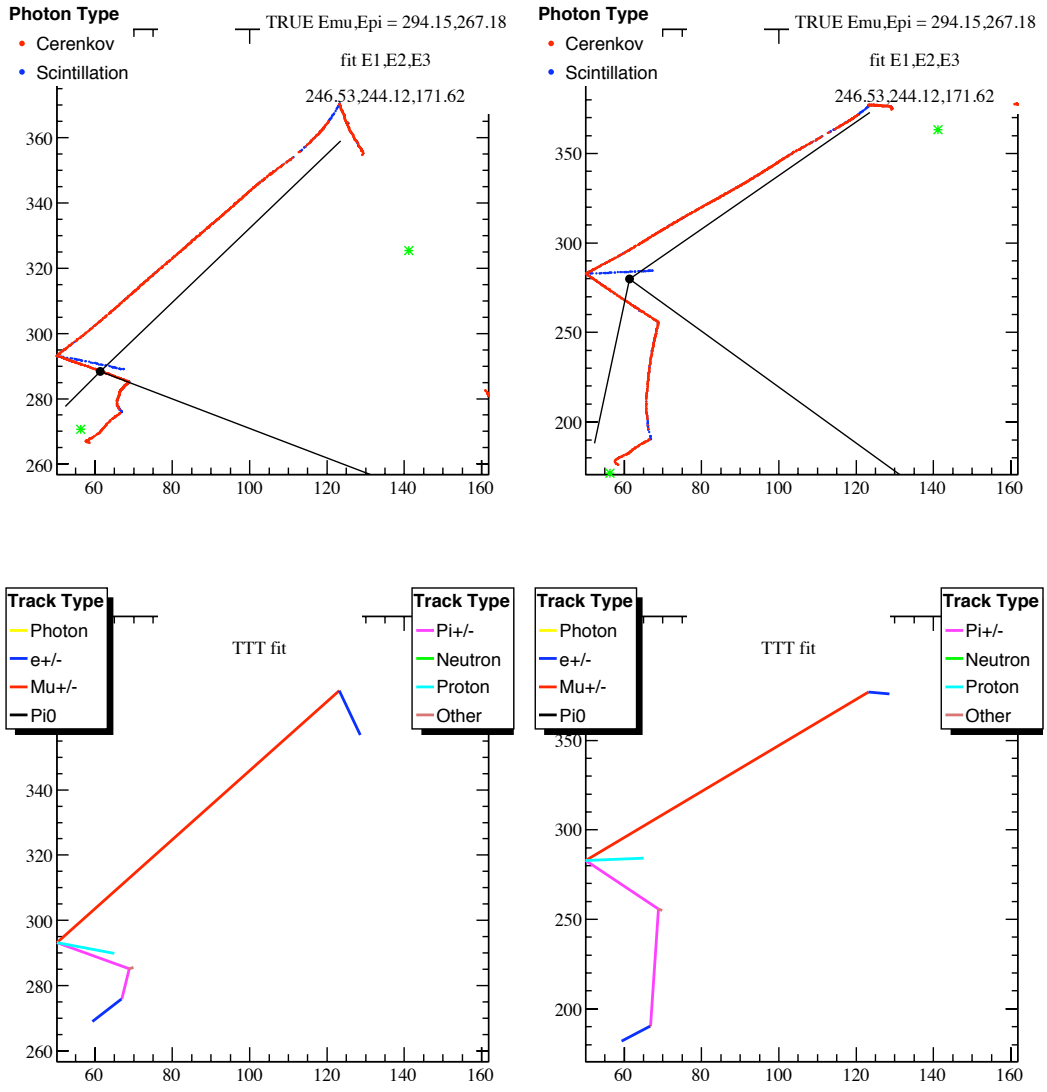

Figure A.17: CCπ^+ fit/seeding step 5: the three track fit has corrected the final scan track to point in the initial direction of the downstream pion segment. The energy has also been redistributed among the three tracks to more accurately represent the size of the Cherenkov rings. The first two tracks now only slightly underestimate the true muon and pion energies.

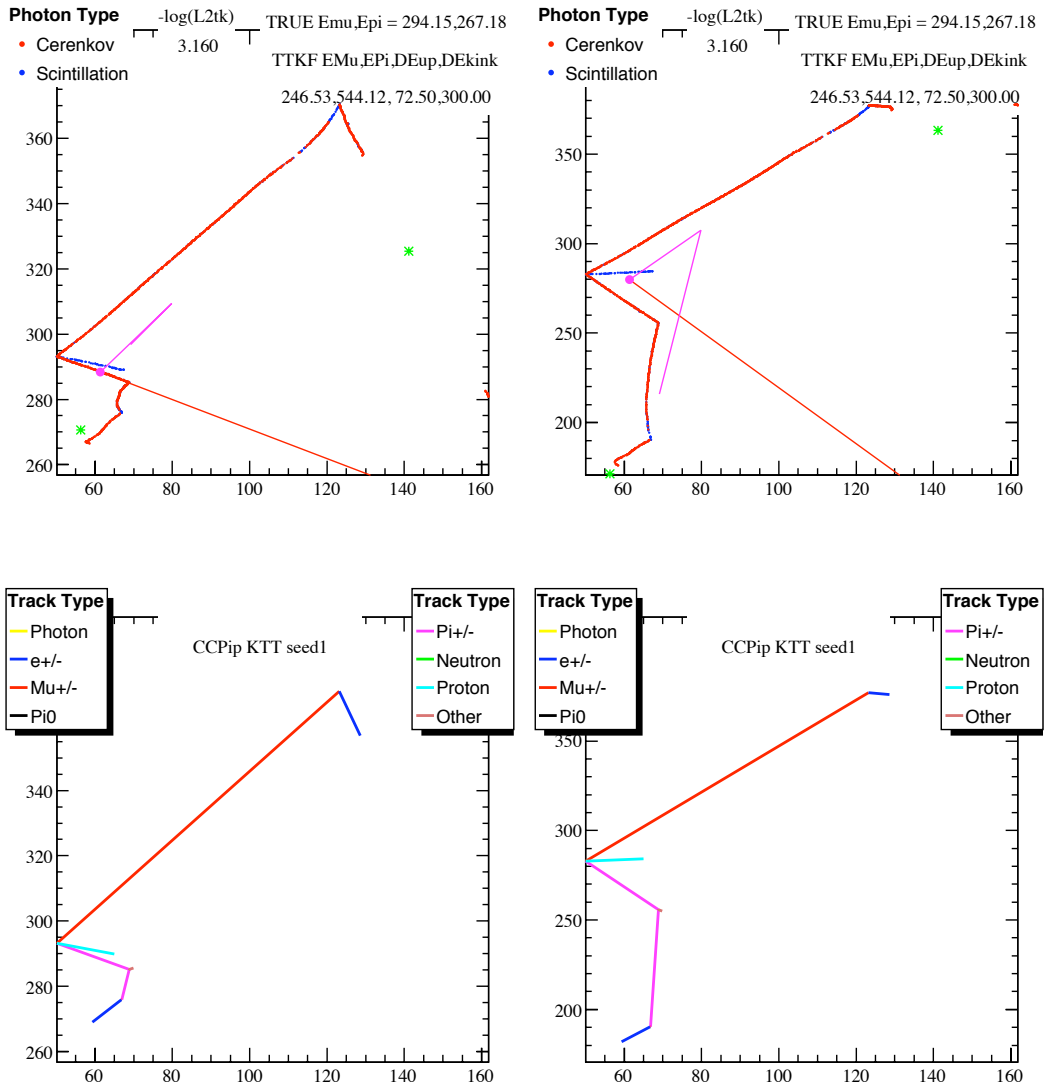

Figure A.18: CCπ^+ fit/seeding step 6: the first of the three seed configurations has picked the incorrect tracks for the muon and upstream pion segments. Since the upstream pion segment does not actually point at a pion track segment, the simultaneous $\Delta E_{up}/\Delta E_{kink}$ scan has incorrectly placed the energy lost in the kink at 300 MeV.

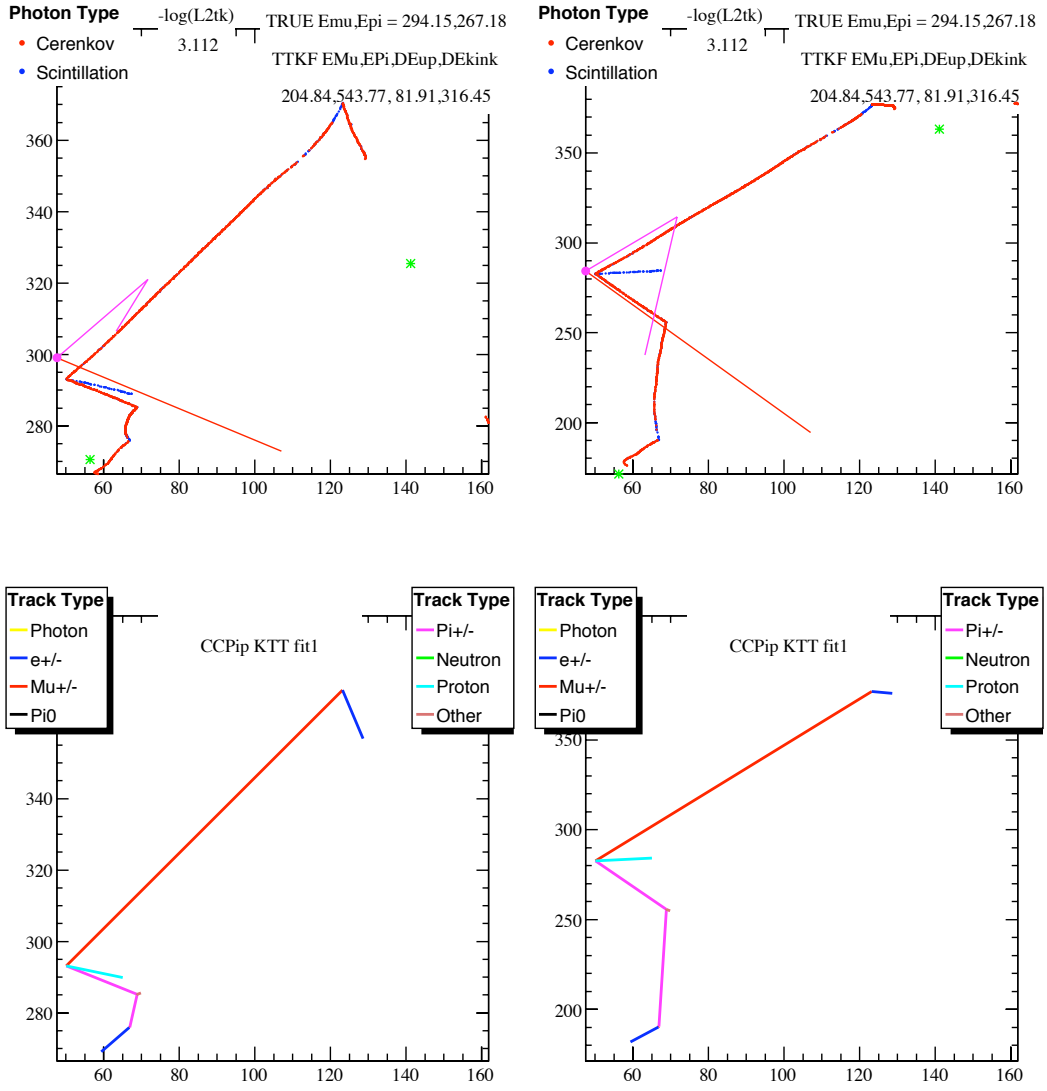

Figure A.19: CCπ^+ fit/seeding step 7: the fit result for the incorrect seed in Figure A.18 is still incorrect, as expected. The fit minimum is: $-\log(\mathcal{L}) = 3.112$.

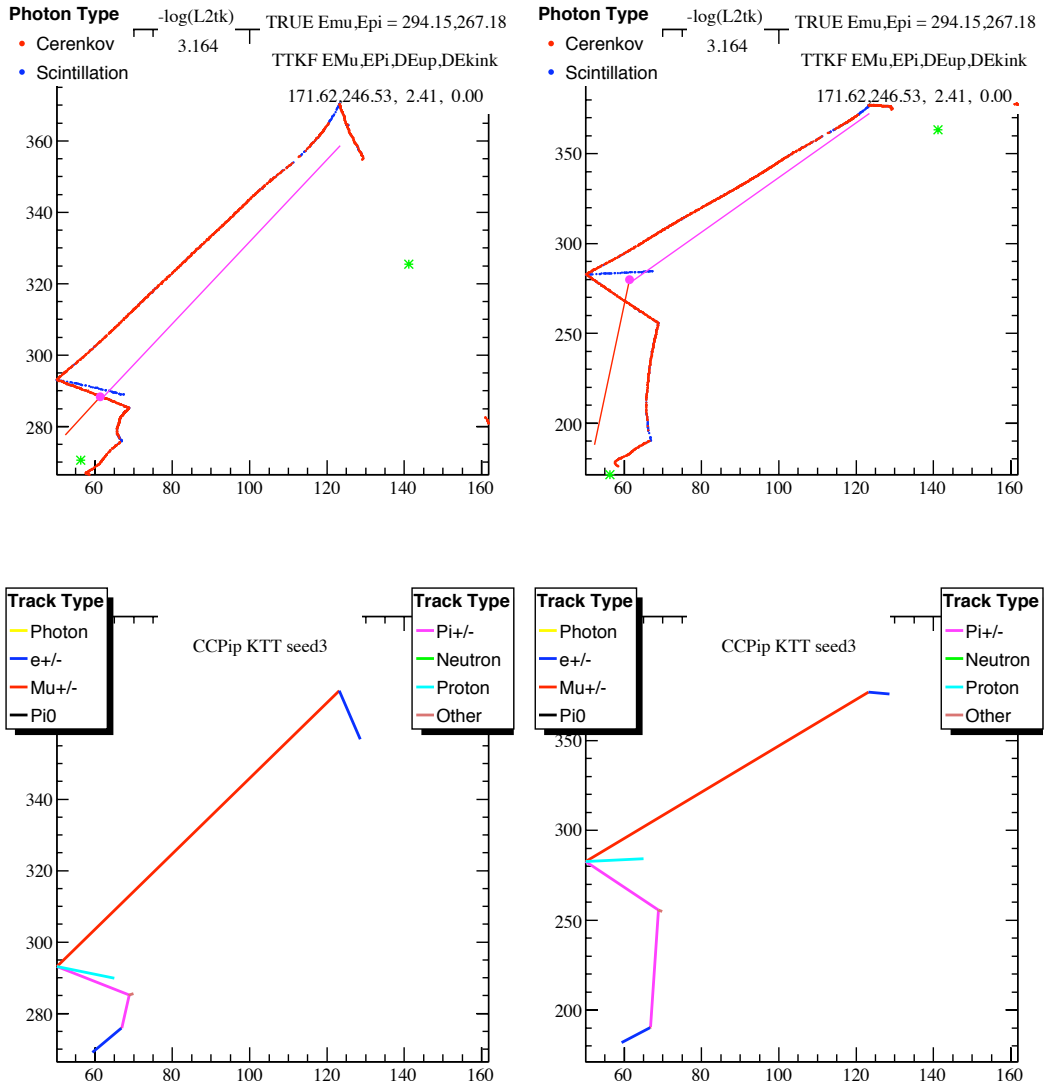

Figure A.20: CCπ^+ fit/seeding step 8: the second of the three seed configurations has picked the incorrect tracks for the muon and downstream pion segments.

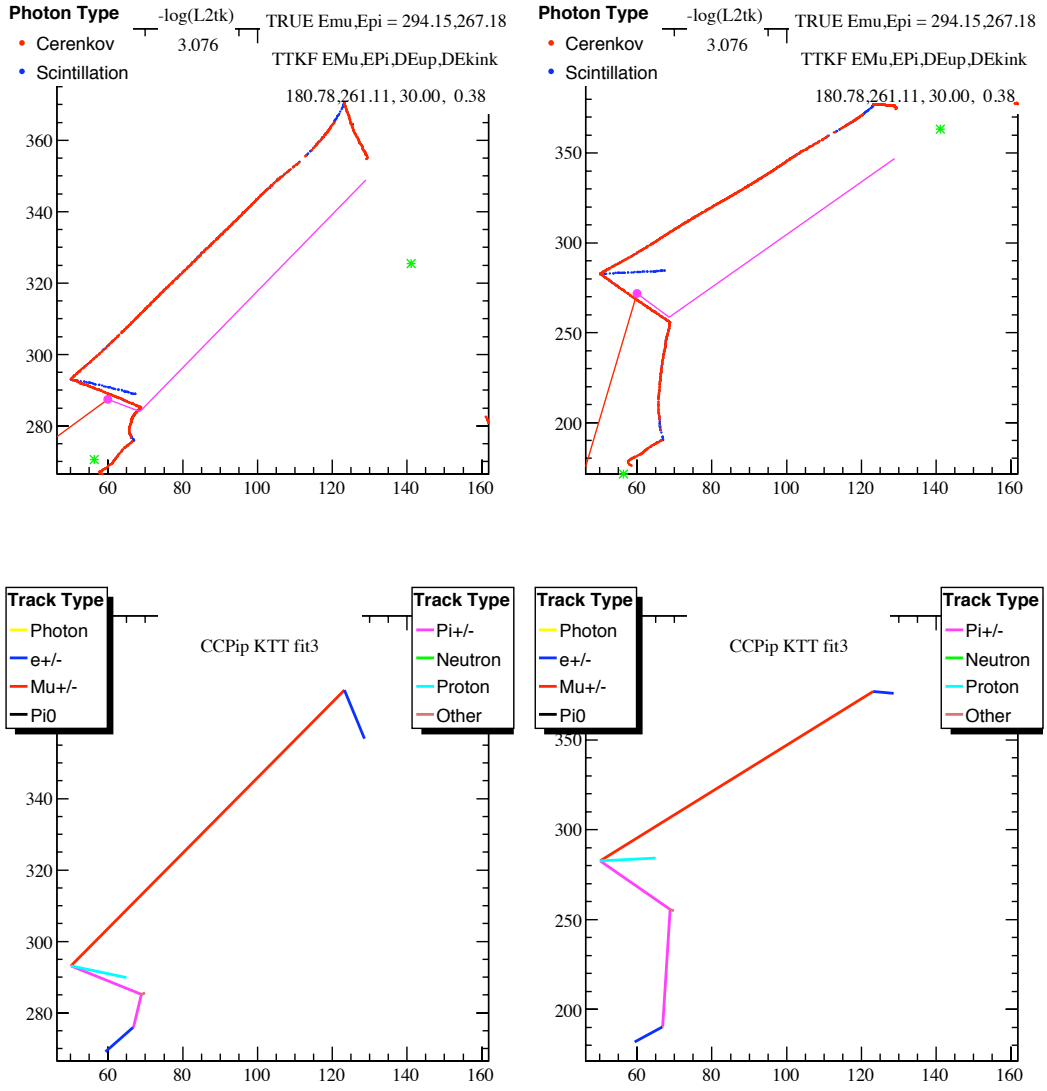

Figure A.21: CCπ^+ fit/seeding step 9: the fit result for the incorrect seed in Figure A.20 is still incorrect, as expected. The fit minimum is: $-\log(\mathcal{L}) = 3.076$

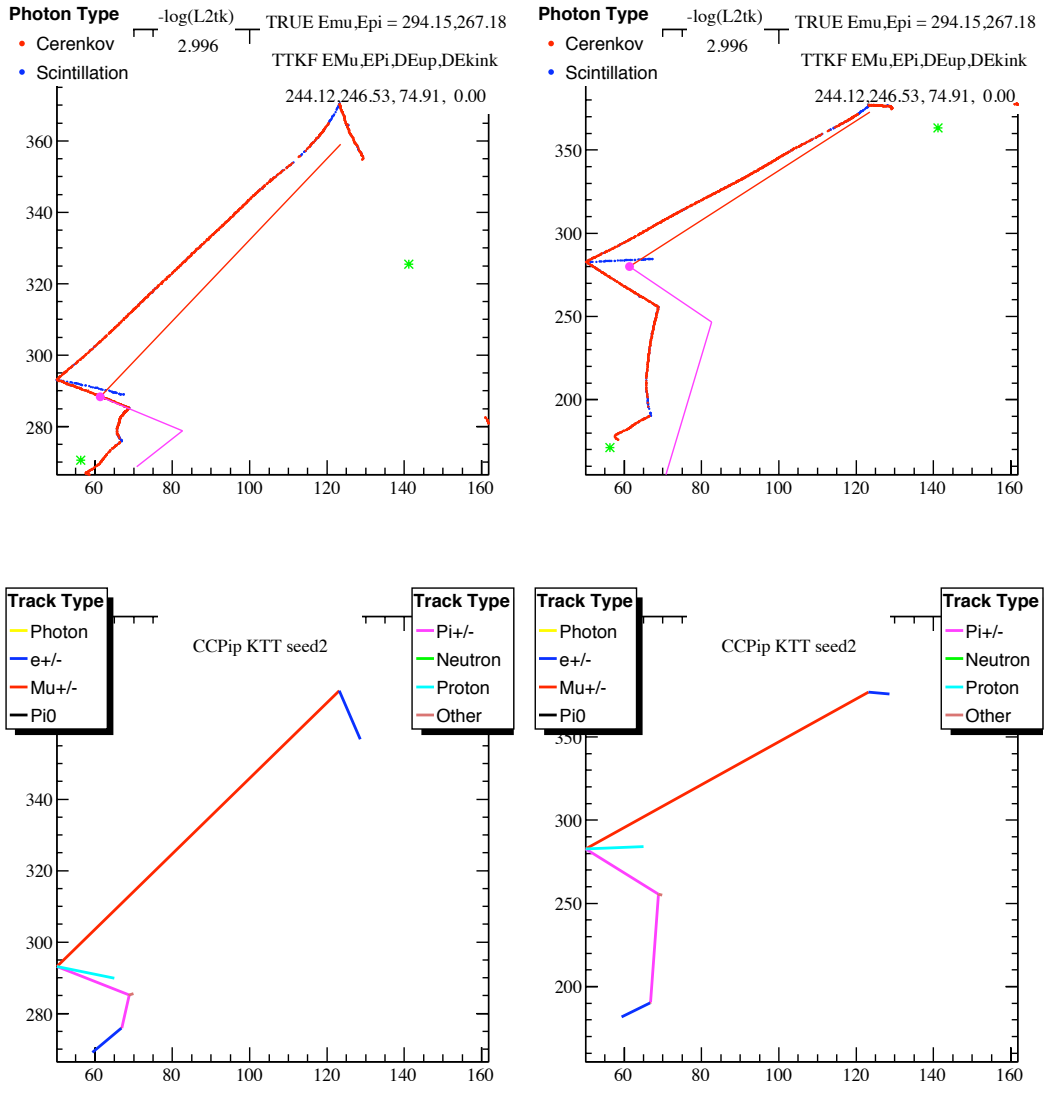

Figure A.22: CCπ^+ fit/seeding step 10: the last CCπ^+ seed configuration correctly assigns all three tracks.

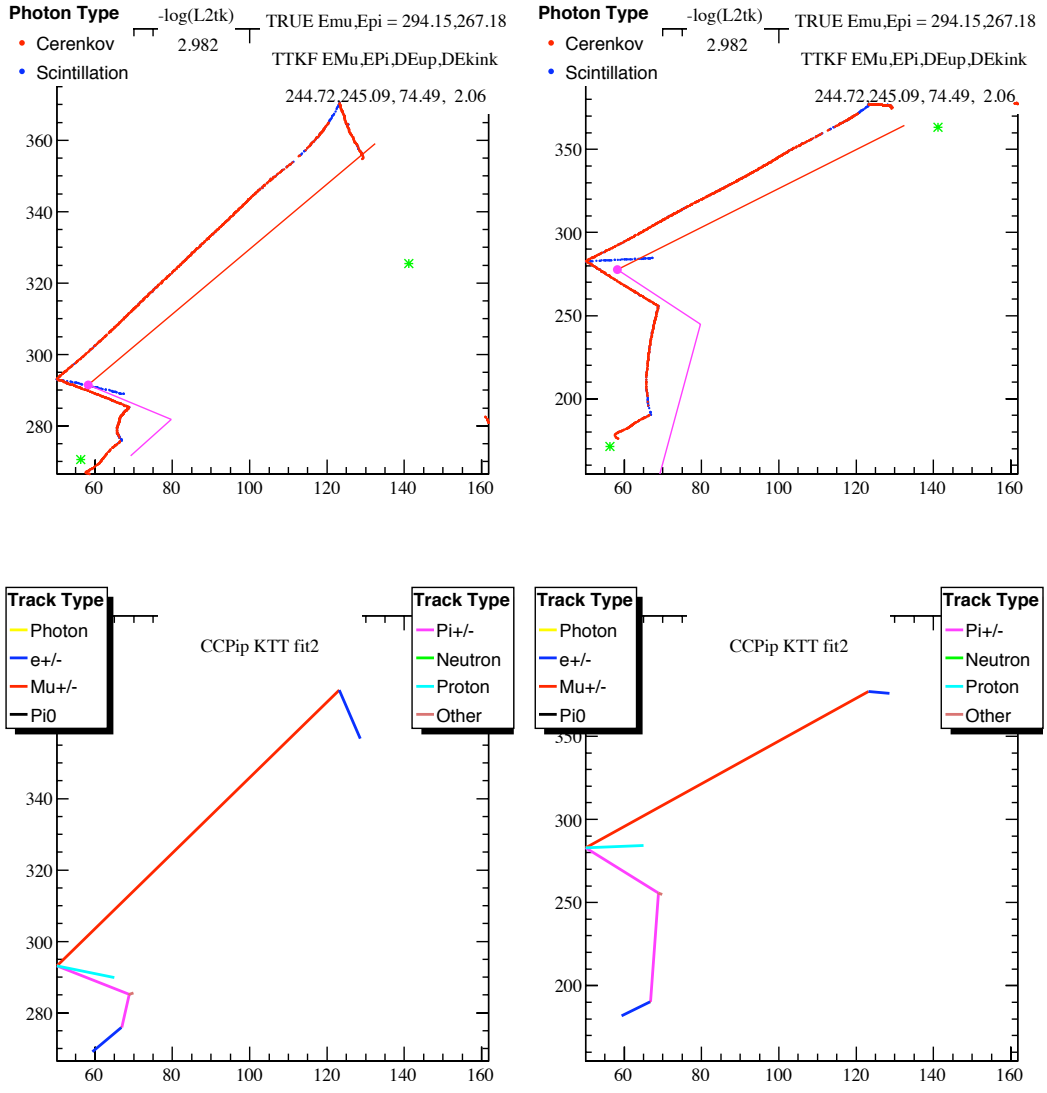

Figure A.23: CCπ^+ fit/seeding step 10: the CCπ^+ fit from the correct seed gives the best fit, $-\log(\mathcal{L}) = 2.982$.

Appendix B

Measurement Details

Further details of the cross section measurements present in Section 6.4.8 are given in this appendix. For each measurement, signal efficiency, signal purity, and a comparison between the reconstructed data and Monte Carlo are given. For the one-dimensional measurements, the unfolding matrix is also shown. One additional data/Monte Carlo comparison, the reconstructed $\pi + N$ mass, is also presented.

Unlike the measured cross sections, the uncertainties in the reconstructed Monte Carlo are dominated by the optical model and cross section errors. The dominant effects in each of these error sources are pion absorption and charge exchange. Pion interactions in the nucleus have a very small effect on the measured cross sections because an event is only labeled as signal if a pion exits the nucleus. As described in Section 4.2.3, pion interactions that occur in the nucleus are (somewhat counter-intuitively) grouped with the optical model errors and all others are part of the cross section errors. In addition, the statistical uncertainty also contributes to the optical model errors, as described in Section 6.4.7.2.

B.1 Neutrino Energy

- Reconstructed Data/Monte Carlo comparison: Figure B.1
- Unfolding Matrix: Figure B.2(b)
- Signal efficiency: Figure B.3(a)
- Signal purity: Figure B.3(b)

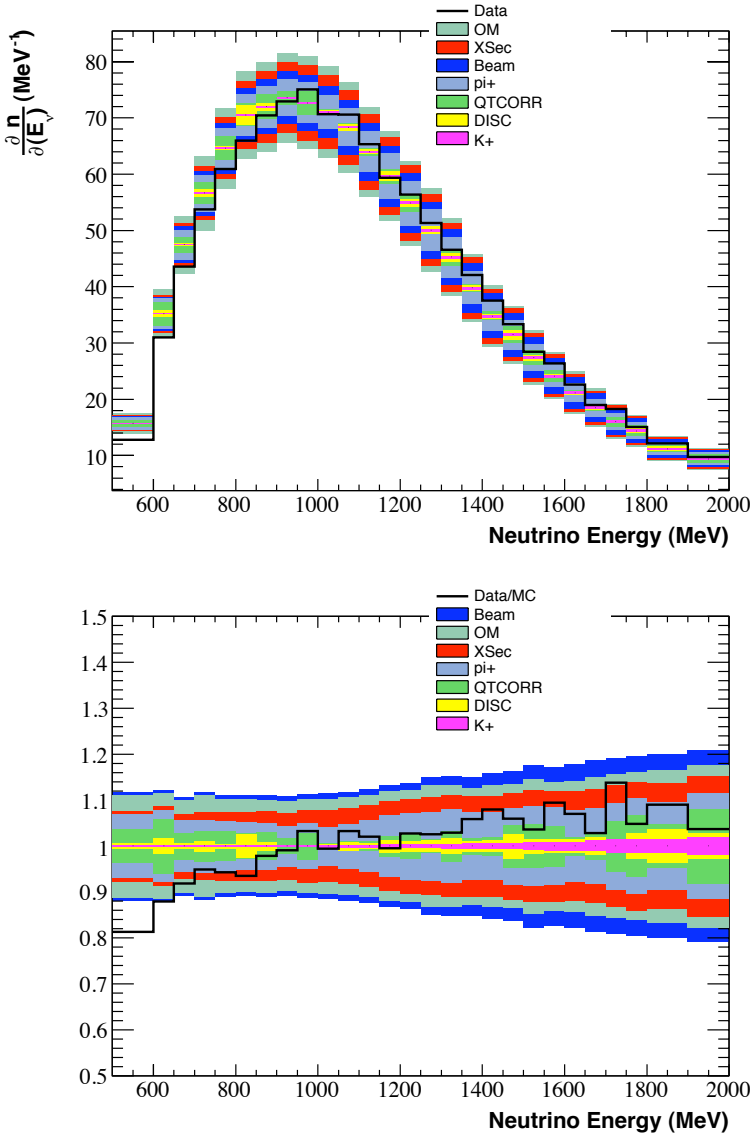

Figure B.1: A Data/Monte Carlo comparison of reconstructed neutrino energy is shown with cumulative systematic errors. The bottom plot shows the fractional errors compared with the Data/Monte Carlo ratio.

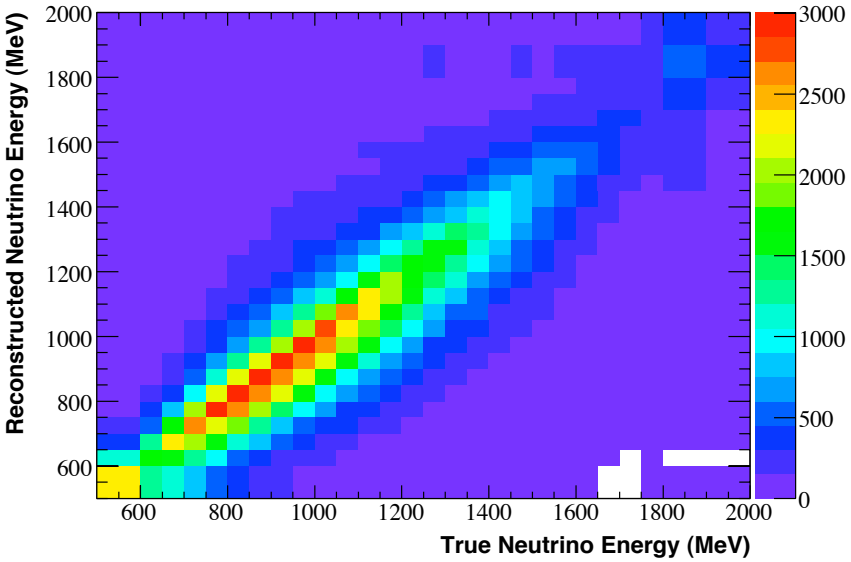

(a) Monte Carlo Event Distribution

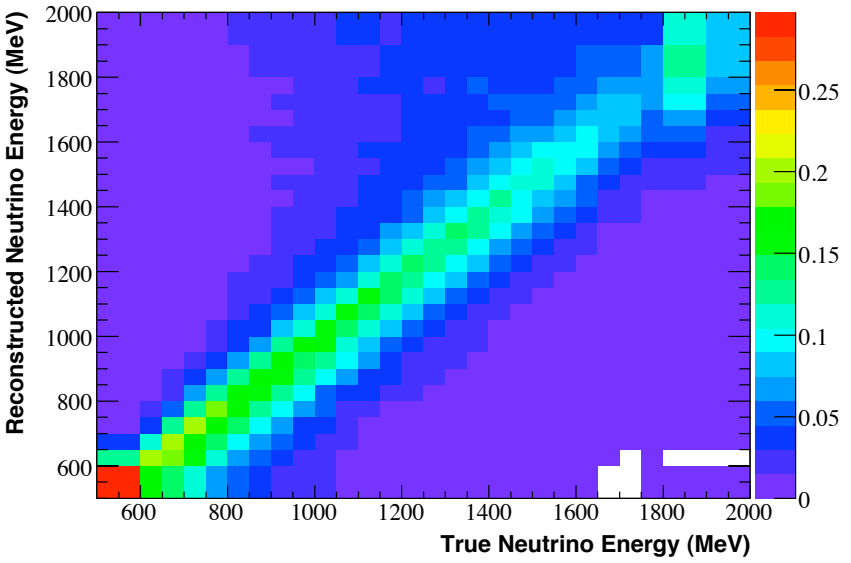

(b) Unfolding Matrix

Figure B.2: The reconstructed vs true distribution for neutrino energy is shown, along with the unfolding matrix used for the central value cross section measurement.

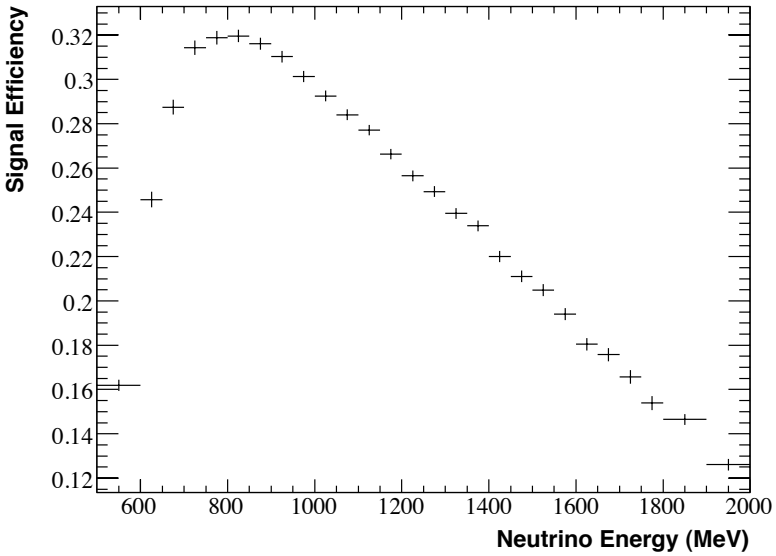

(a) Signal Efficiency

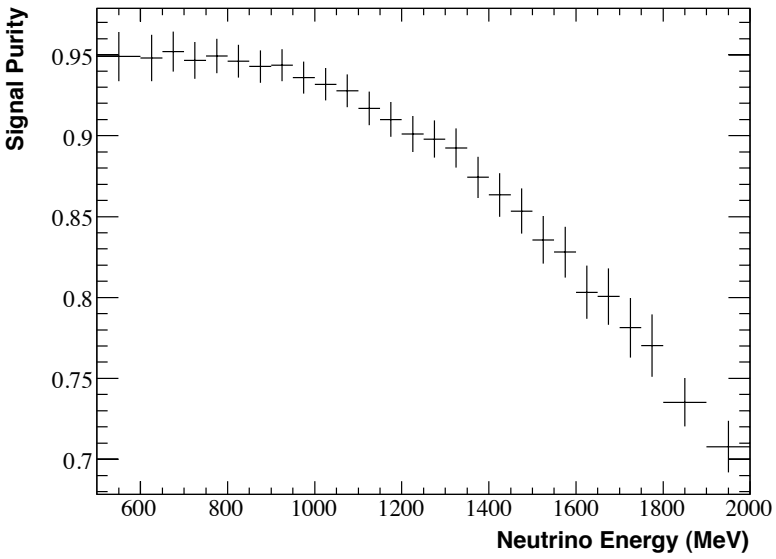

(b) Signal Purity

Figure B.3: The signal efficiency and purity is given in terms of neutrino energy. The error bars represent the Monte Carlo statistical uncertainty.

B.2 Q Squared

- Reconstructed Data/Monte Carlo comparison: Figure B.4
- Unfolding Matrix: Figure B.5(b)
- Signal efficiency: Figure B.6(a)
- Signal purity: Figure B.6(b)

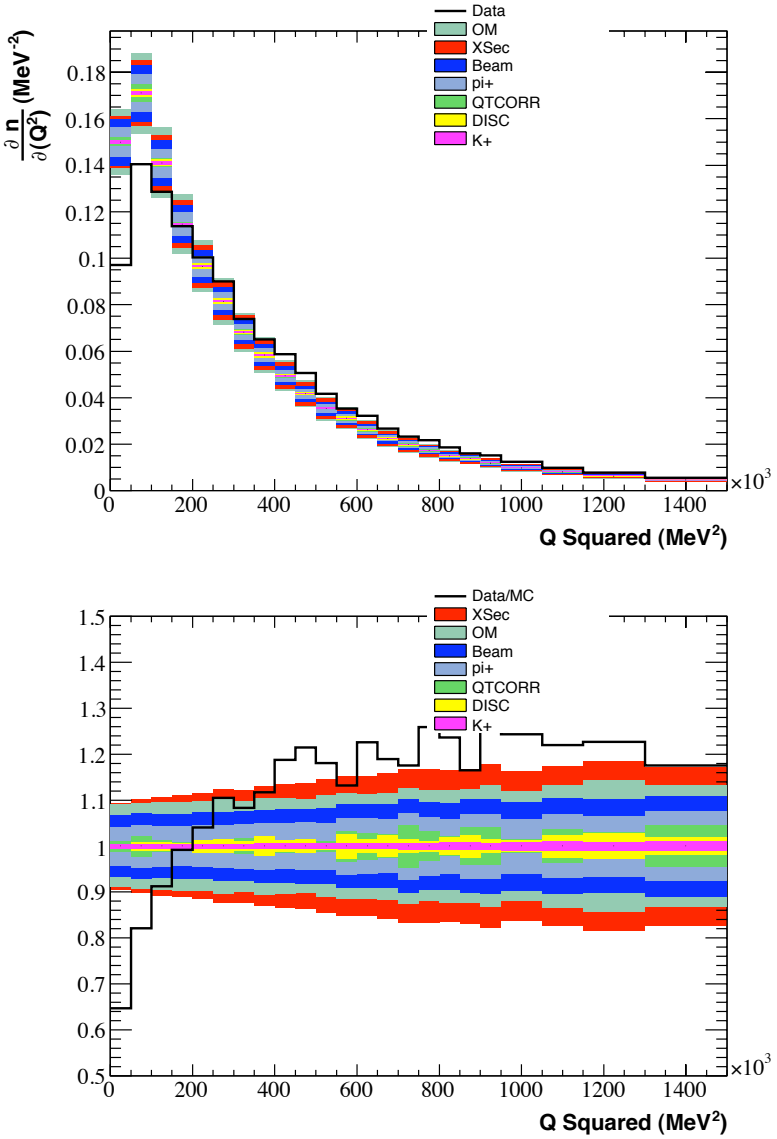

Figure B.4: A Data/Monte Carlo comparison of reconstructed Q^2 is shown with cumulative systematic errors. The bottom plot shows the fractional errors compared with the Data/Monte Carlo ratio.

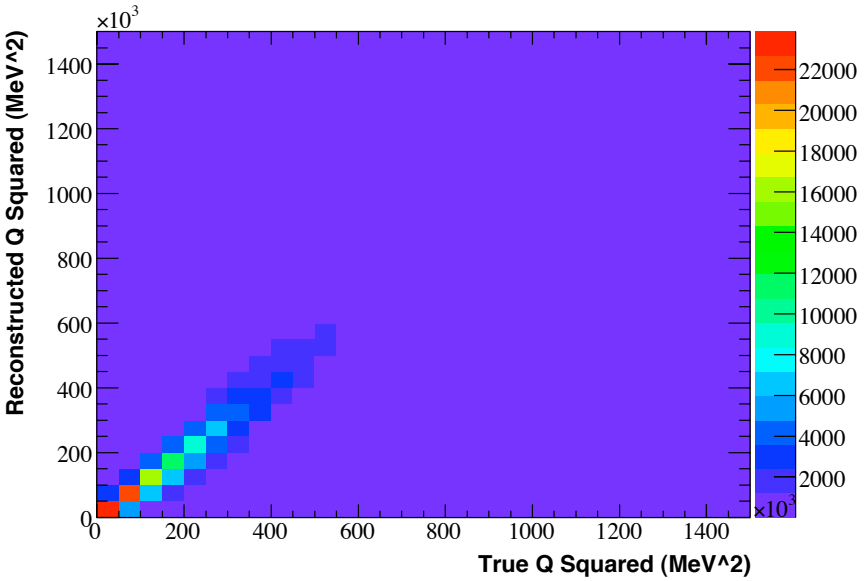

(a) Monte Carlo Event Distribution

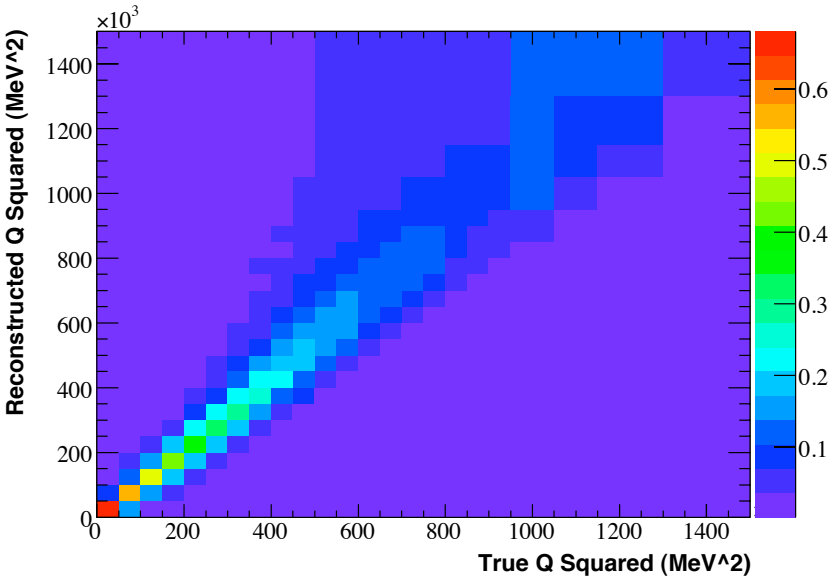

(b) Unfolding Matrix

Figure B.5: The reconstructed vs true distribution for Q^2 is shown, along with the unfolding matrix used for the central value cross section measurement.

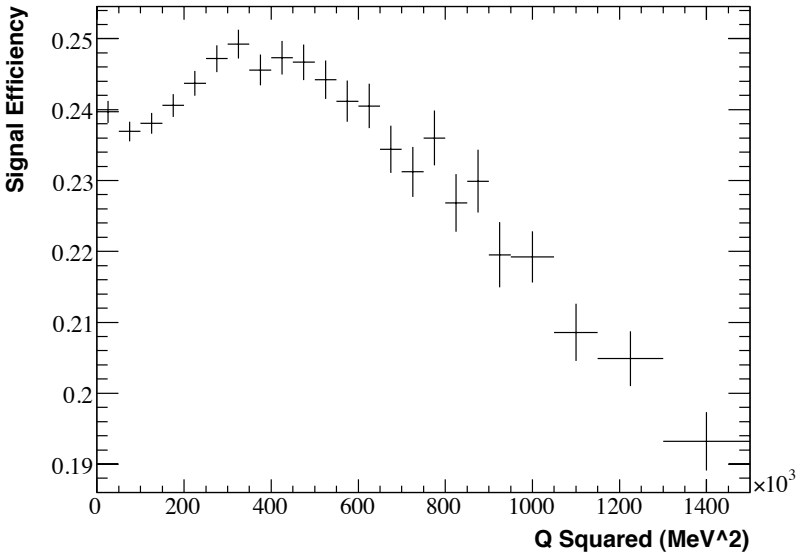

(a) Signal Efficiency

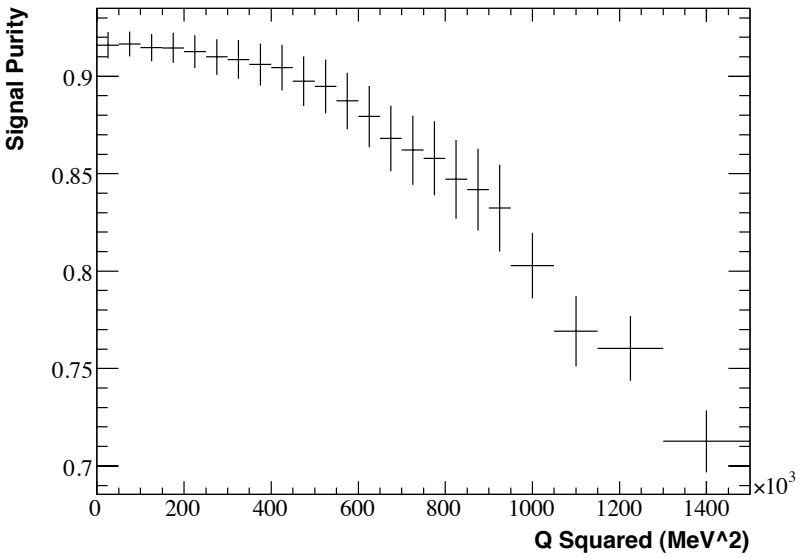

(b) Signal Purity

Figure B.6: The signal efficiency and purity is given in terms of Q^2. The error bars represent the Monte Carlo statistical uncertainty.

B.3 Muon Kinetic Energy

- Reconstructed Data/Monte Carlo comparison: Figure B.7
- Unfolding Matrix: Figure B.8(b)
- Signal efficiency: Figure B.9(a)
- Signal purity: Figure B.9(b)

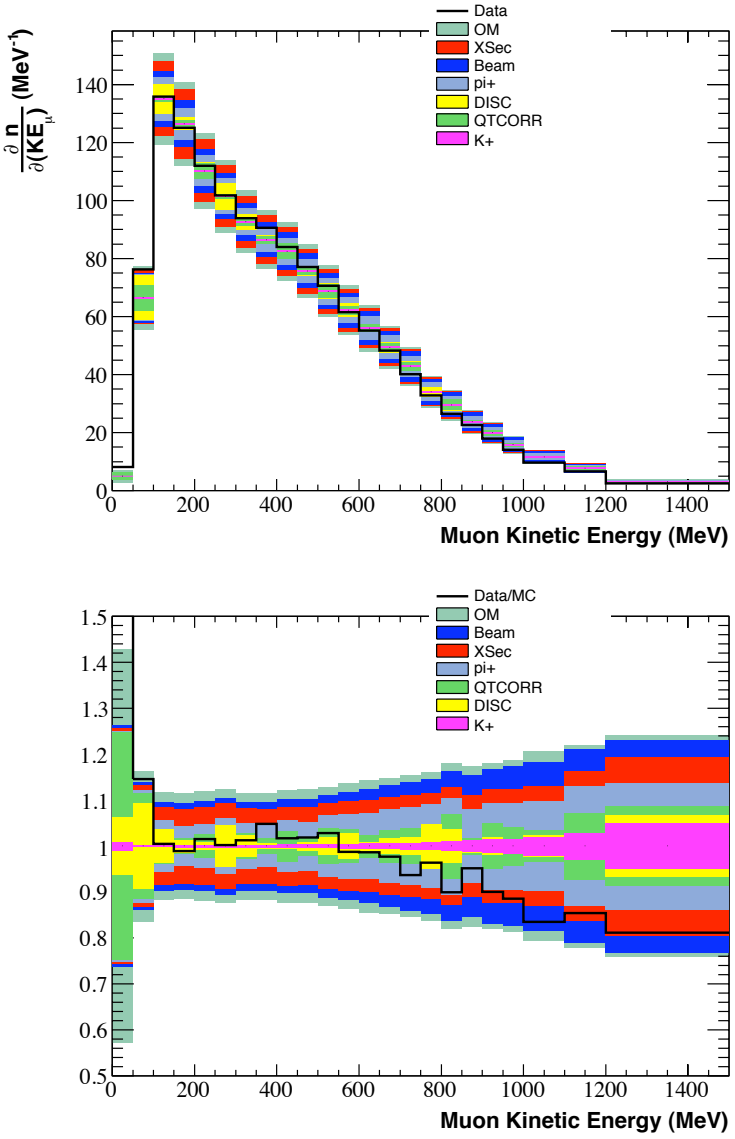

Figure B.7: A Data/Monte Carlo comparison of reconstructed muon kinetic energy is shown with cumulative systematic errors. The bottom plot shows the fractional errors compared with the Data/Monte Carlo ratio.

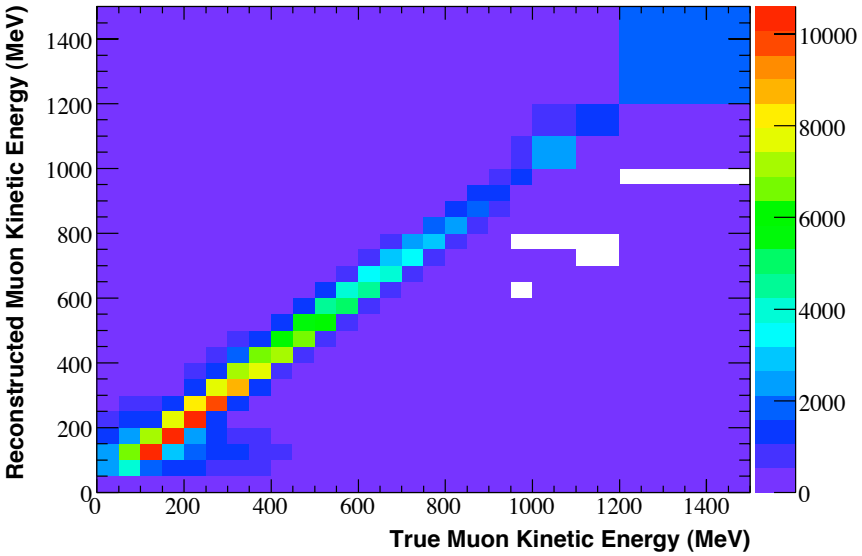

(a) Monte Carlo Event Distribution

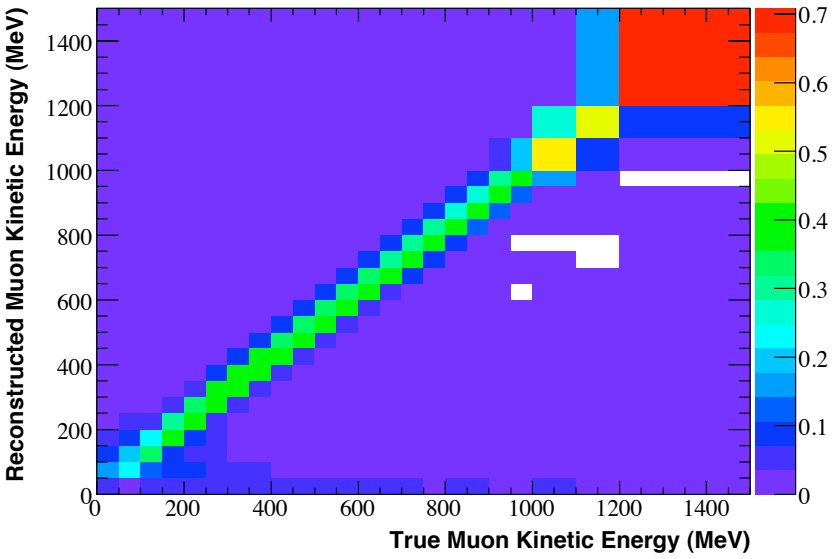

(b) Unfolding Matrix

Figure B.8: The reconstructed vs true distribution for muon kinetic energy is shown, along with the unfolding matrix used for the central value cross section measurement.

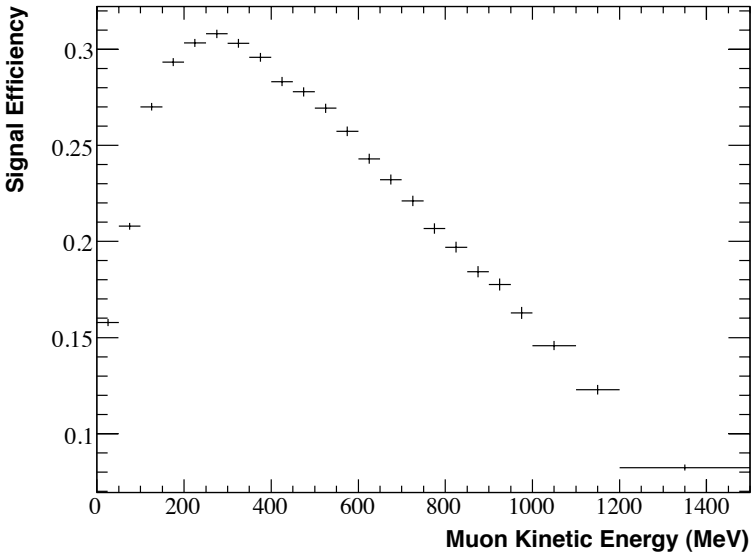

(a) Signal Efficiency

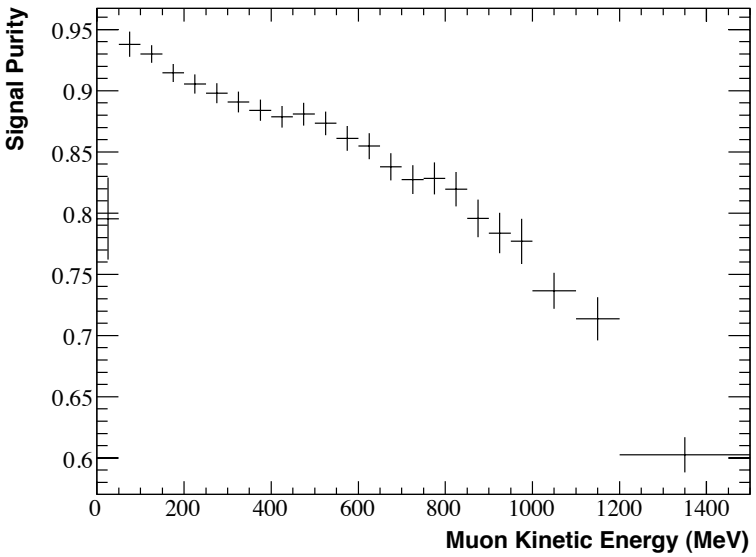

(b) Signal Purity

Figure B.9: The signal efficiency and purity is given in terms of muon kinetic energy. The error bars represent the Monte Carlo statistical uncertainty.

B.4 Muon Direction

- Reconstructed Data/Monte Carlo comparison: Figure B.10
- Unfolding Matrix: Figure B.11(b)
- Signal efficiency: Figure B.12(a)
- Signal purity: Figure B.12(b)

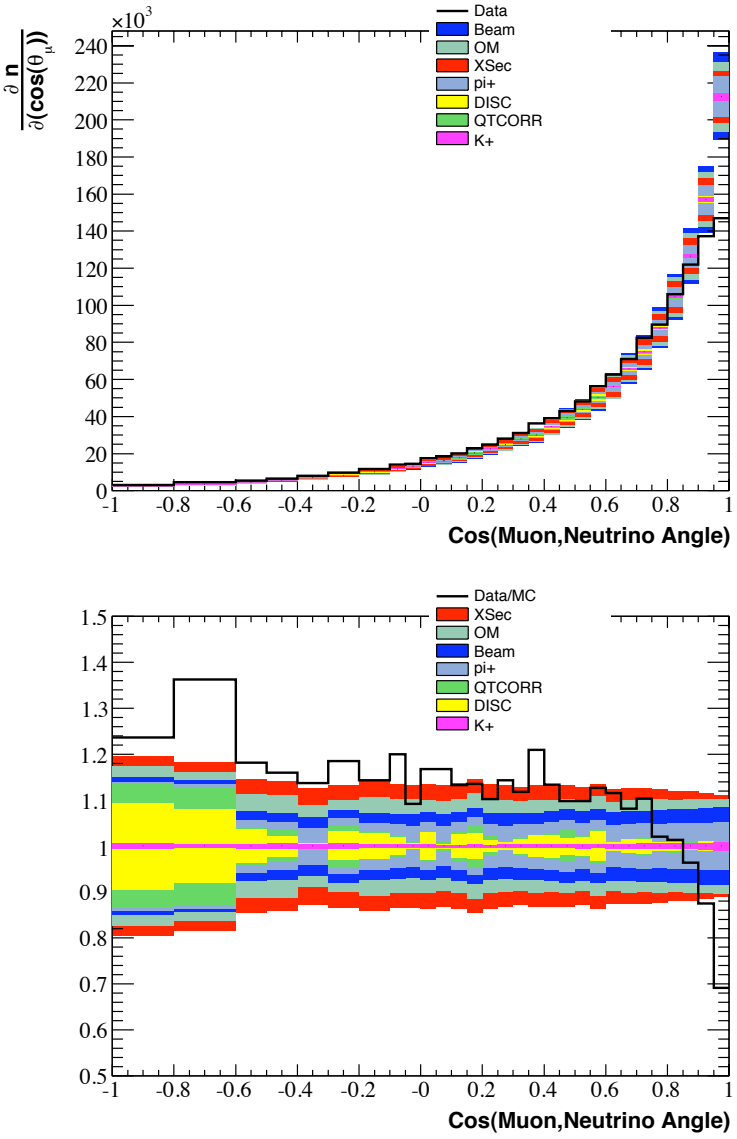

Figure B.10: A Data/Monte Carlo comparison of reconstructed cos(muon, neutrino angle) is shown with cumulative systematic errors. The bottom plot shows the fractional errors compared with the Data/Monte Carlo ratio.

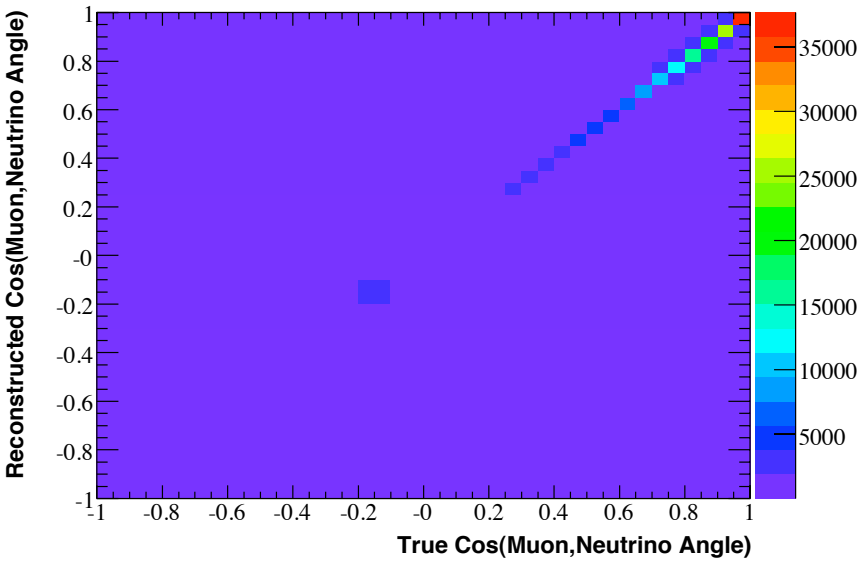

(a) Monte Carlo Event Distribution

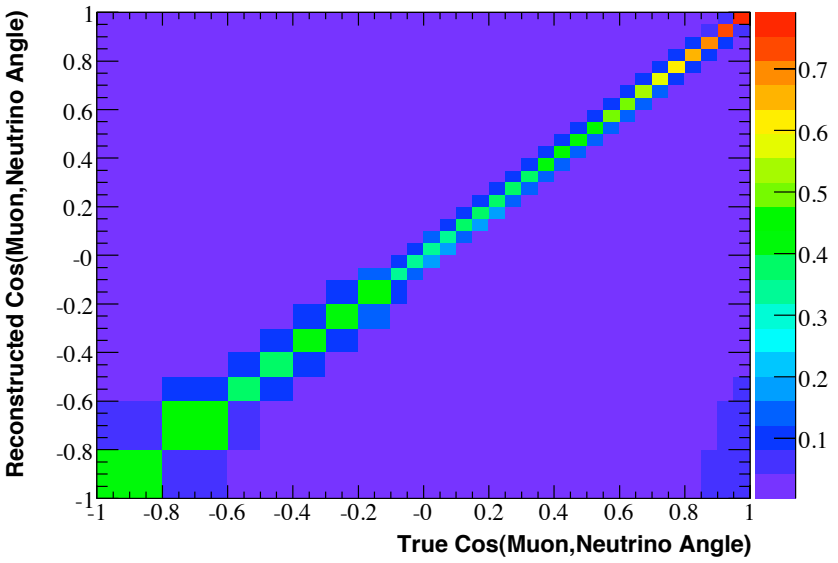

(b) Unfolding Matrix

Figure B.11: The reconstructed vs true distribution for cos(muon, neutrino angle) is shown, along with the unfolding matrix used for the central value cross section measurement.

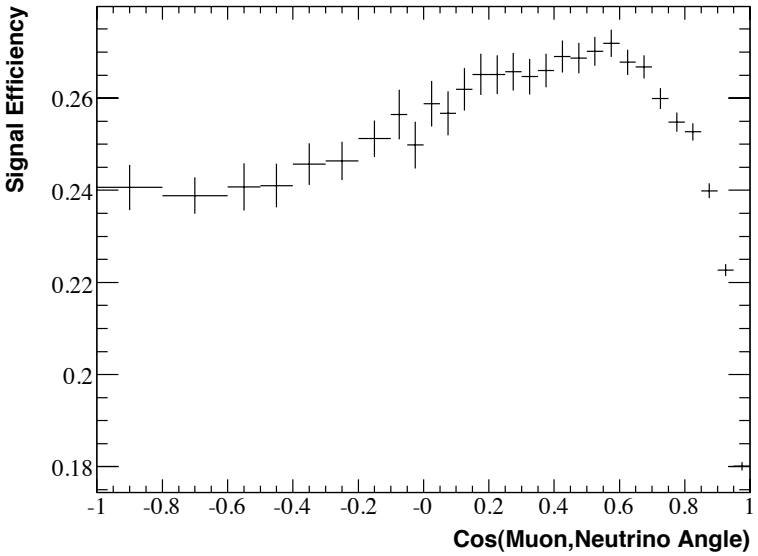

(a) Signal Efficiency

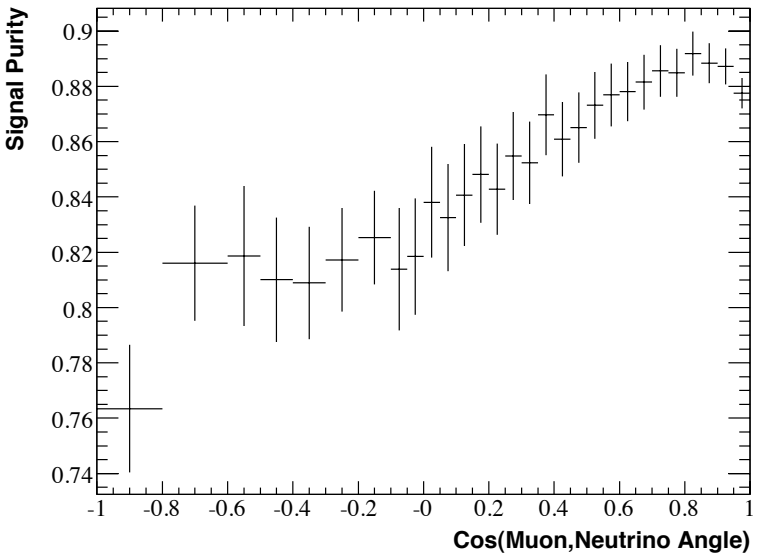

(b) Signal Purity

Figure B.12: The signal efficiency and purity is given in terms of cos(muon, neutrino angle). The error bars represent the Monte Carlo statistical uncertainty.

B.5 Pion Kinetic Energy

- Reconstructed Data/Monte Carlo comparison: Figure B.13
- Unfolding Matrix: Figure B.14(b)
- Signal efficiency: Figure B.15(a)
- Signal purity: Figure B.15(b)

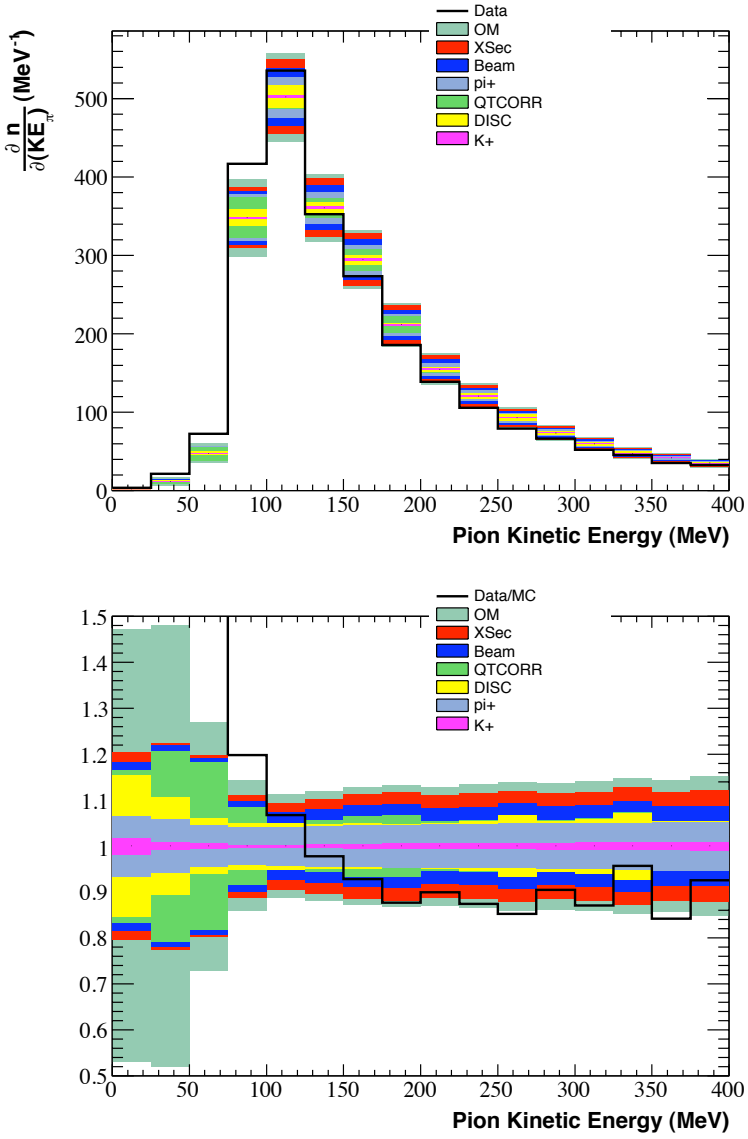

Figure B.13: A Data/Monte Carlo comparison of reconstructed pion kinetic energy is shown with cumulative systematic errors. The bottom plot shows the fractional errors compared with the Data/Monte Carlo ratio.

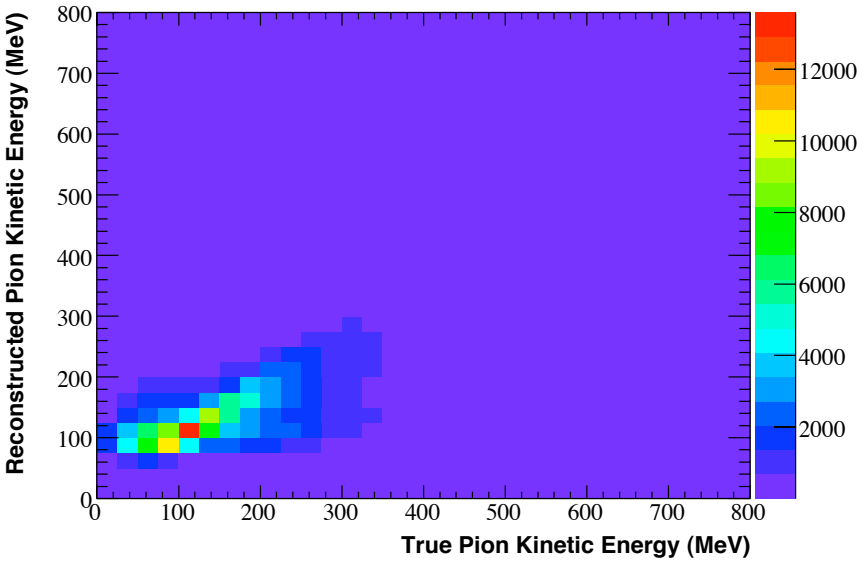

(a) Monte Carlo Event Distribution

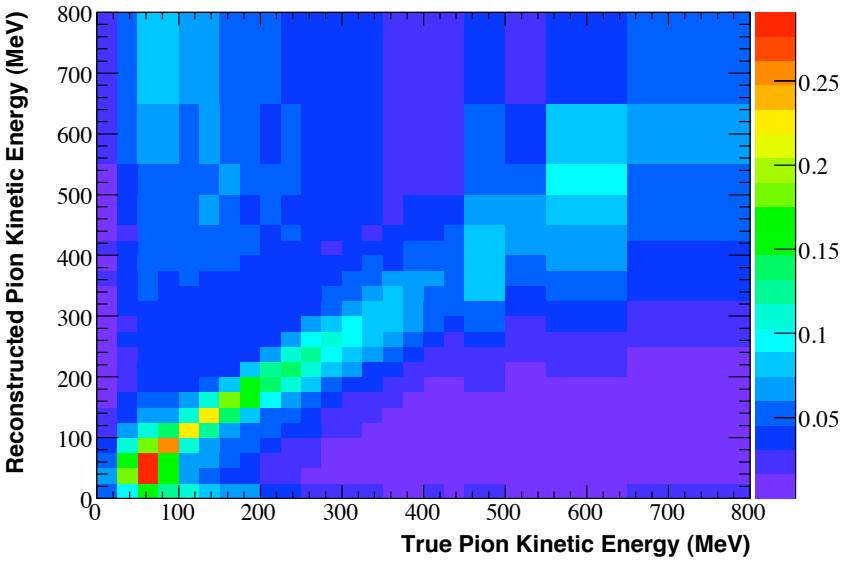

(b) Unfolding Matrix

Figure B.14: The reconstructed vs true distribution for pion kinetic energy is shown, along with the unfolding matrix used for the central value cross section measurement.

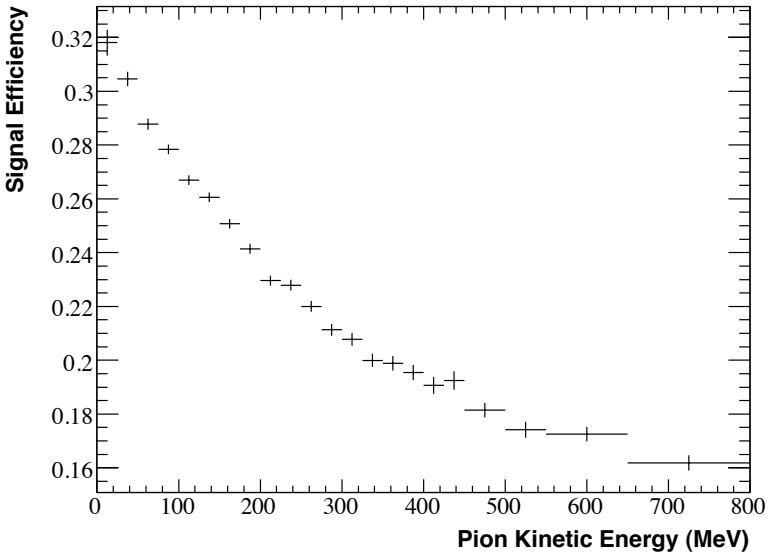

(a) Signal Efficiency

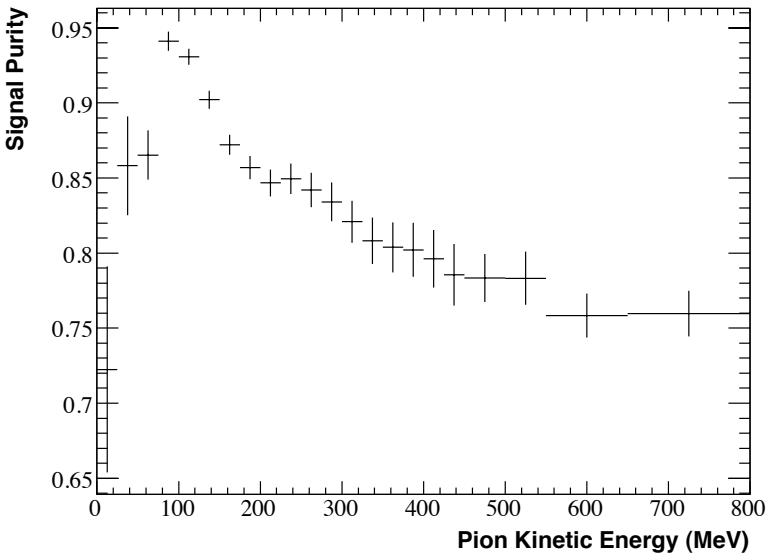

(b) Signal Purity

Figure B.15: The signal efficiency and purity is given in terms of pion kinetic energy. The error bars represent the Monte Carlo statistical uncertainty.

B.6 Pion Direction

- Reconstructed Data/Monte Carlo comparison: Figure B.16
- Unfolding Matrix: Figure B.17(b)
- Signal efficiency: Figure B.18(a)
- Signal purity: Figure B.18(b)

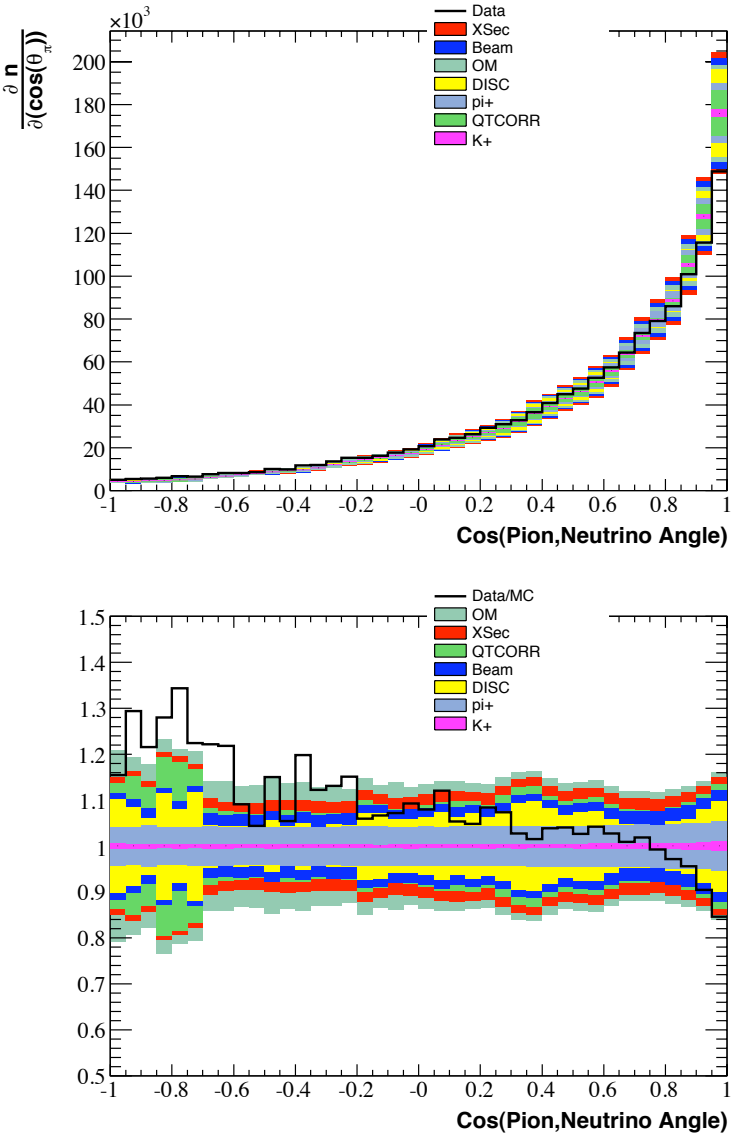

Figure B.16: A Data/Monte Carlo comparison of reconstructed cos(pion, neutrino angle) is shown with cumulative systematic errors. The bottom plot shows the fractional errors compared with the Data/Monte Carlo ratio.

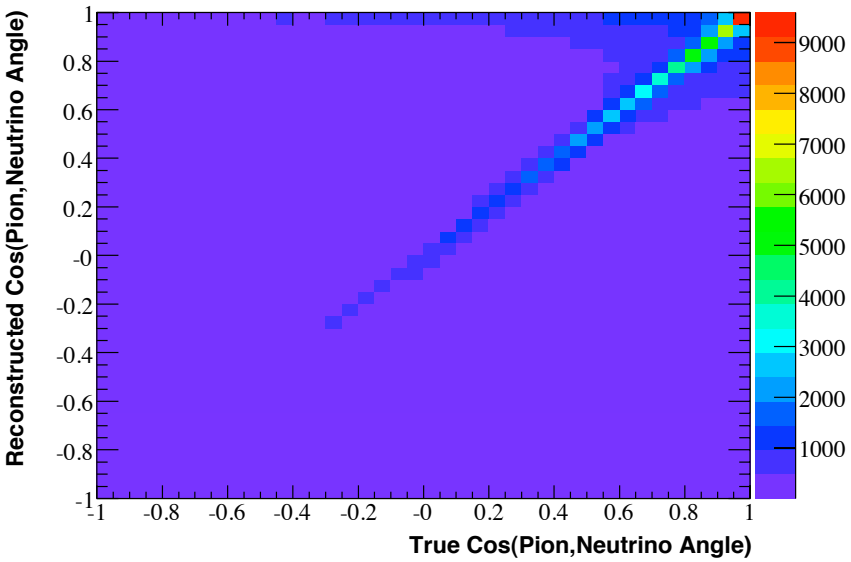

(a) Monte Carlo Event Distribution

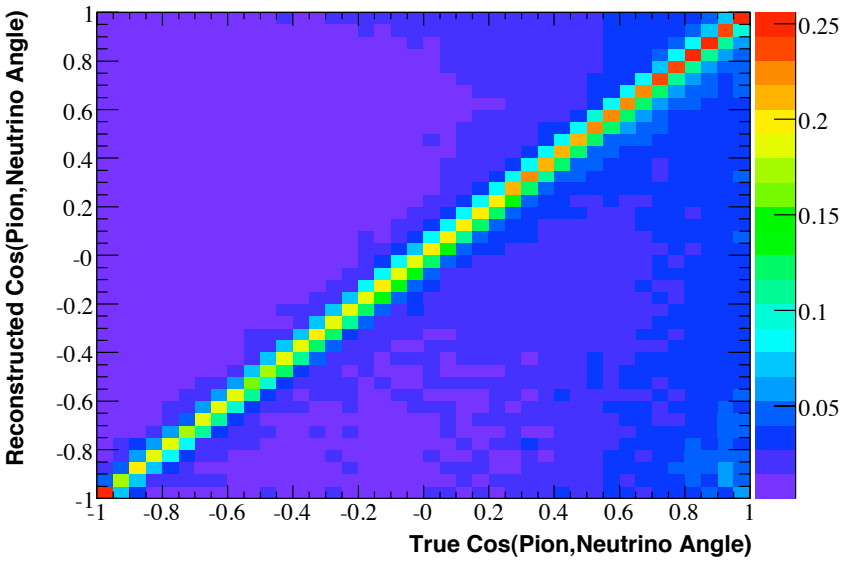

(b) Unfolding Matrix

Figure B.17: The reconstructed vs true distribution for cos(pion, neutrino angle) is shown, along with the unfolding matrix used for the central value cross section measurement.

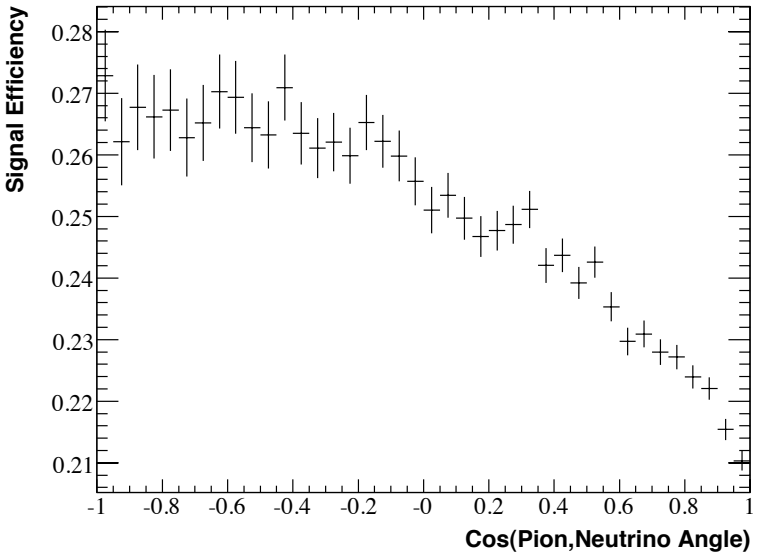

(a) Signal Efficiency

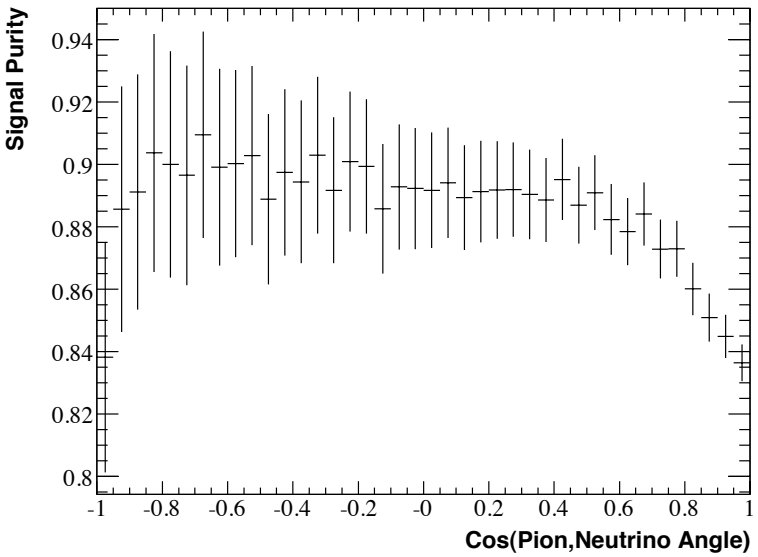

(b) Signal Purity

Figure B.18: The signal efficiency and purity is given in terms of cos(pion, neutrino angle). The error bars represent the Monte Carlo statistical uncertainty.

B.7 Pion/Nucleon Mass

- Reconstructed Data/Monte Carlo comparison: Figure B.19

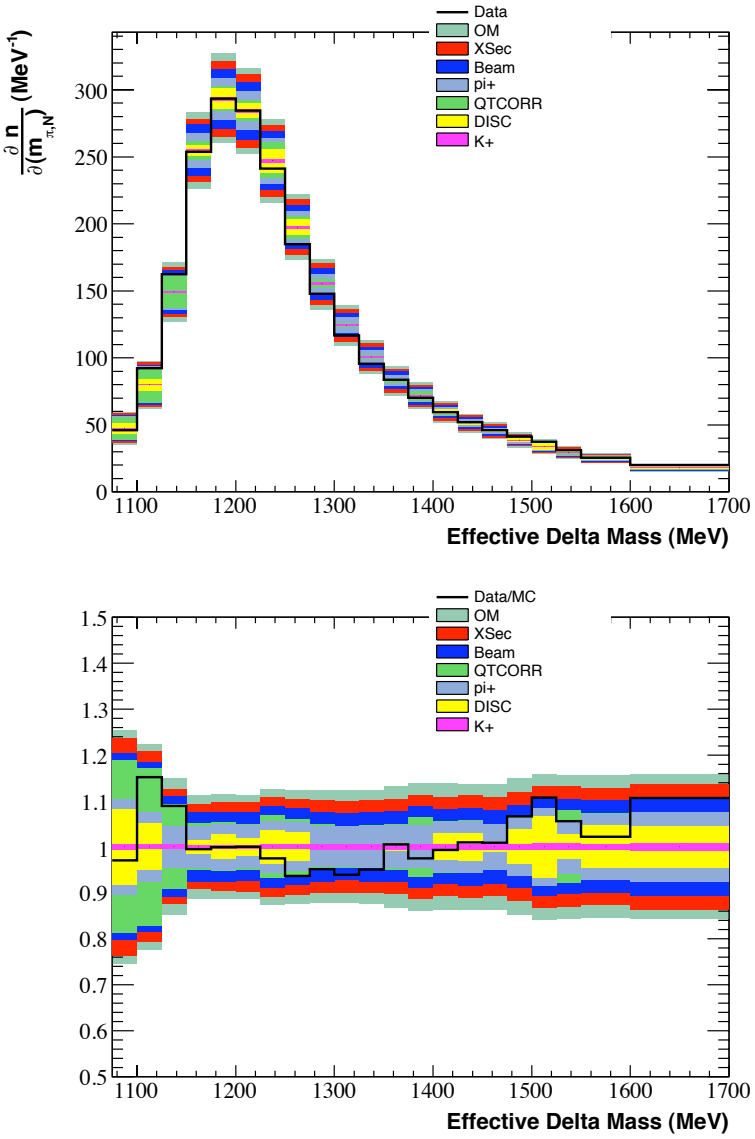

Figure B.19: A Data/Monte Carlo comparison of reconstructed $N+\pi^+$mass is shown with cumulative systematic errors. The bottom plot shows the fractional errors compared with the Data/Monte Carlo ratio.

B.8 Q Squared vs Neutrino Energy

- Reconstructed Data/Monte Carlo comparison: Figure B.20
- Reconstructed Monte Carlo Fractional Errors: Figures B.22 and B.23
- Signal efficiency: Figure B.24(a)
- Signal purity: Figure B.24(c)

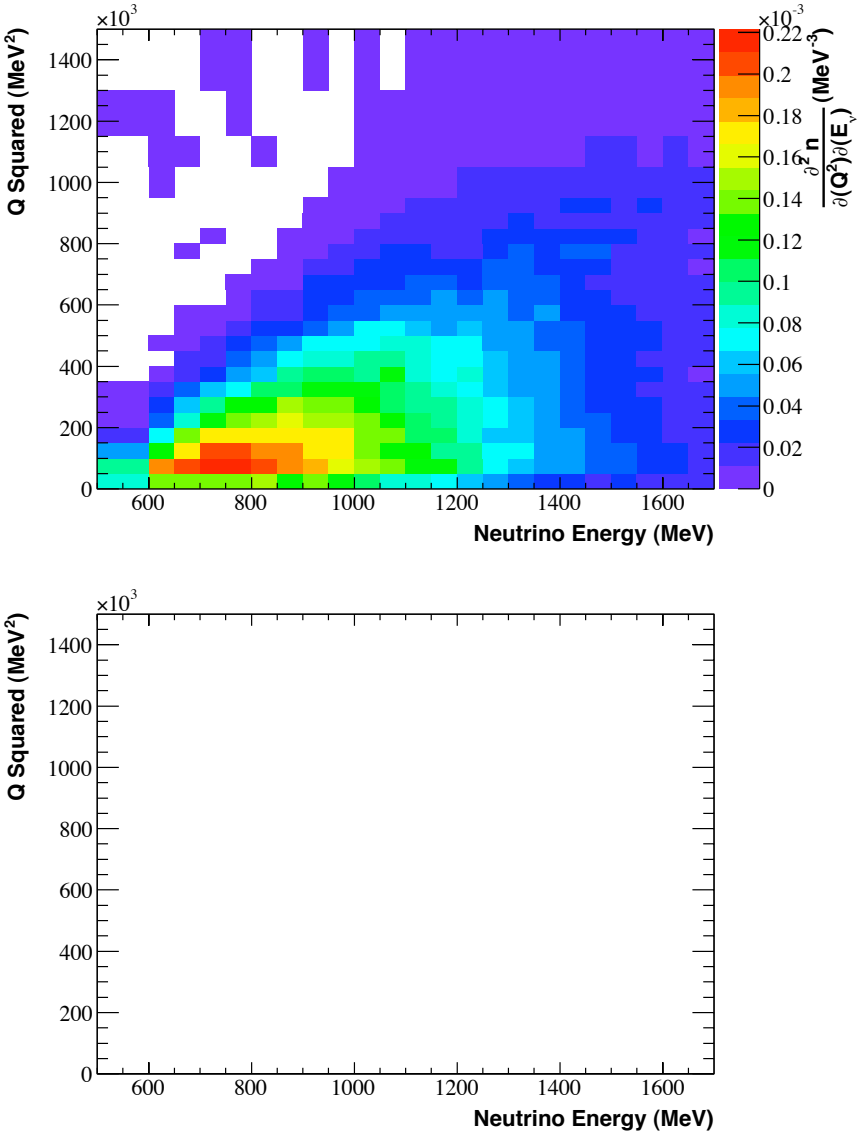

Figure B.20: The reconstructed Q^2 vs neutrino energy distribution is shown for both the data (top) and Monte Carlo (bottom).

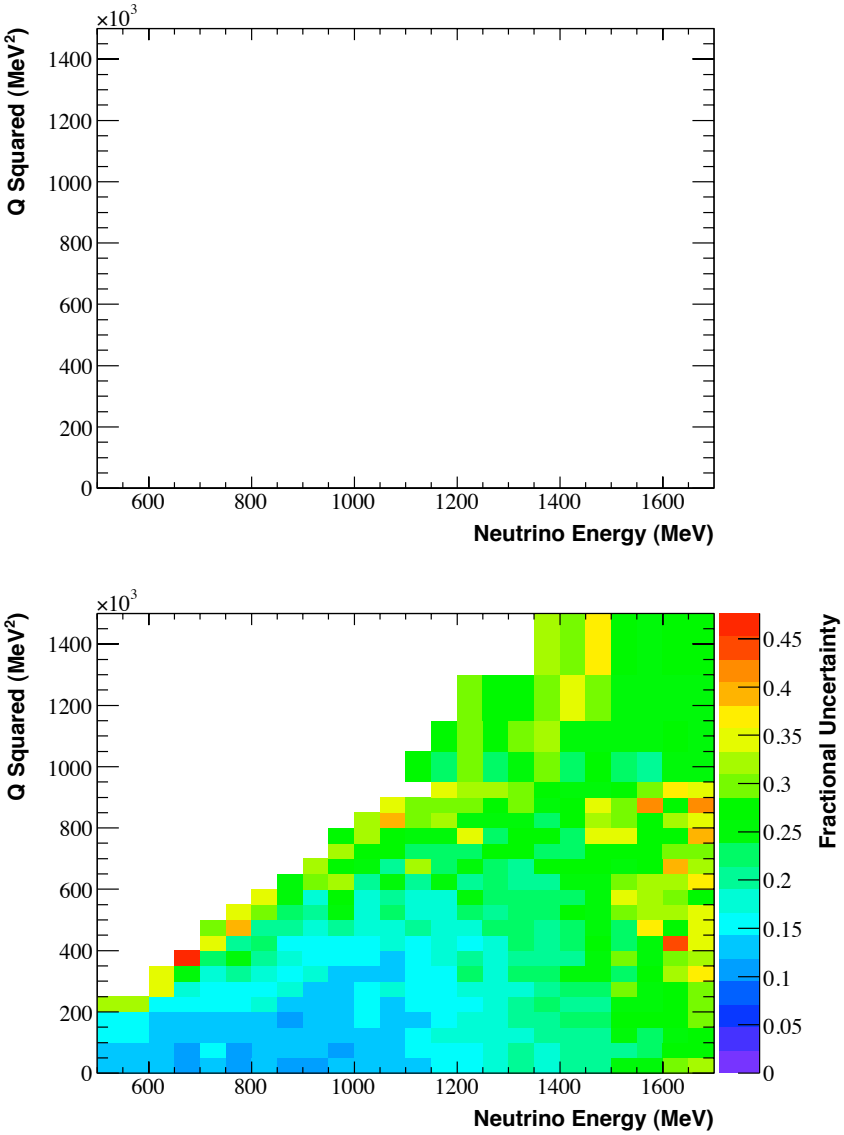

Figure B.21: The Monte Carlo reconstructed Q^2 vs energy distribution is shown (top) along with the total fractional uncertainties (bottom).

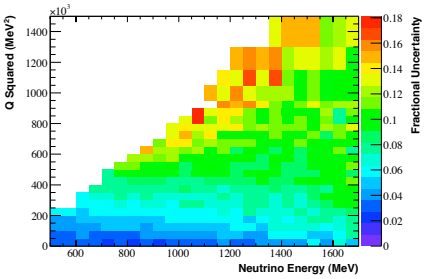

(a) The fractional systematic uncertainty from the "XSec" error source.

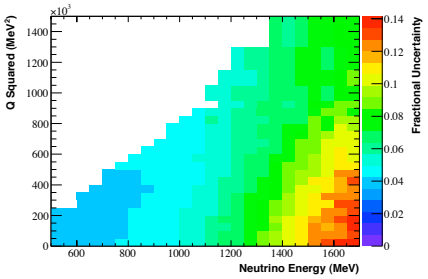

(b) The fractional systematic uncertainty from the "Beam" error source.

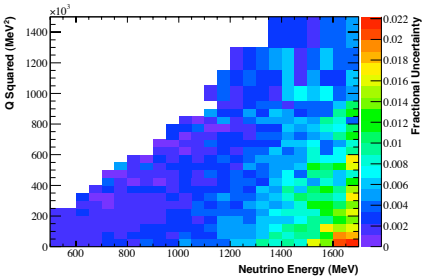

(c) The fractional systematic uncertainty from the "K^+" error source.

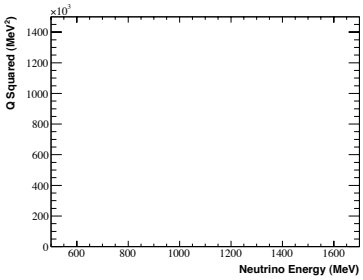

(d) Reconstructed Monte Carlo distribution

Figure B.22: The fractional systematic uncertainties on the reconstructed Monte Carlo distribution are shown for four of the error sources. The central value reconstructed Monte Carlo distribution is also shown for reference. Note that the color scales differ for each systematic error source. An explanation of each error is given in Section 6.4.7.

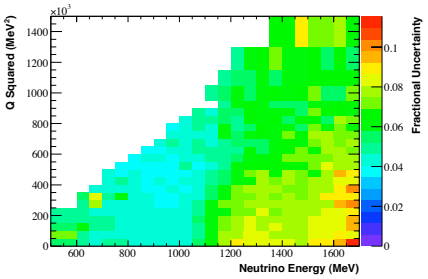

(a) The fractional systematic uncertainty from the "π^+" error source.

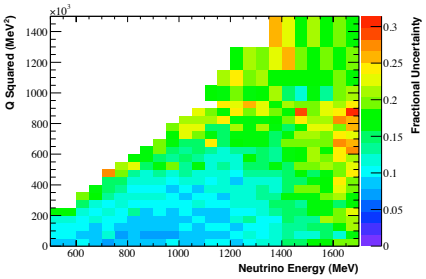

(b) The fractional systematic uncertainty from the "OM" error source.

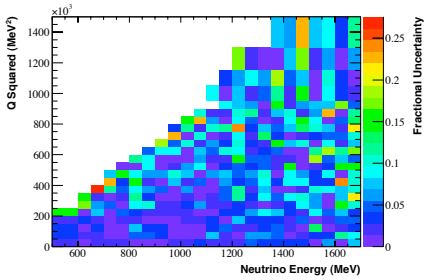

(c) The fractional systematic uncertainty from the "DISC" error source.

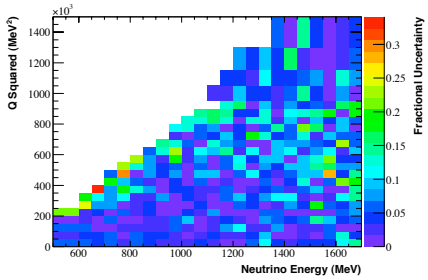

(d) The fractional systematic uncertainty from the "QTCORR" error source.

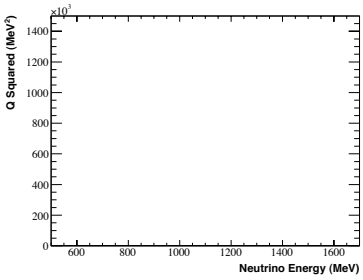

(e) Reconstructed Monte Carlo distribution

Figure B.23: The fractional systematic uncertainties on the reconstructed Monte Carlo distribution are shown for four of the error sources. The central value reconstructed Monte Carlo distribution is also shown for reference. Note that the color scales differ for each systematic error source. An explanation of each error is given in Section 6.4.7.

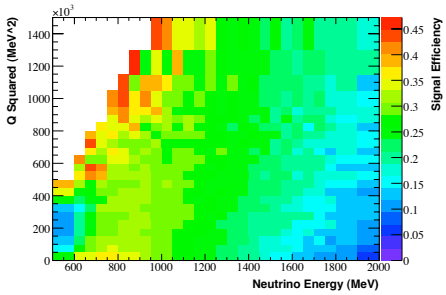

(a) Signal Efficiency

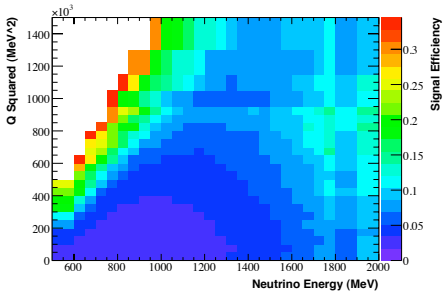

(b) Fractional Monte Carlo Statistical Error on the Signal Efficiency

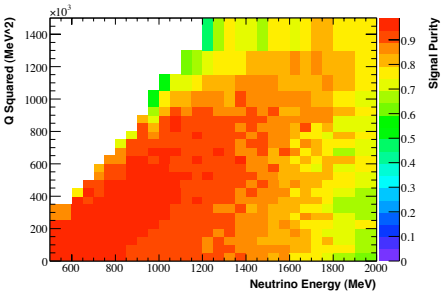

(c) Signal Purity

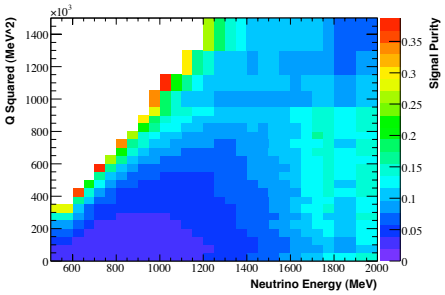

(d) Fractional Monte Carlo Statistical Error on the Signal Purity

Figure B.24: The signal efficiency and purity are shown for the Q^2 vs neutrino energy distribution. The fractional errors due to Monte Carlo statistics for each of these distributions is also given for all bins with at least 10 events in the numerator.

B.9 Muon Kinetic Energy vs Neutrino Energy

- Reconstructed Data/Monte Carlo comparison: Figure B.25
- Reconstructed Monte Carlo Fractional Errors: Figures B.27 and B.28
- Signal efficiency: Figure B.29(a)
- Signal purity: Figure B.29(c)

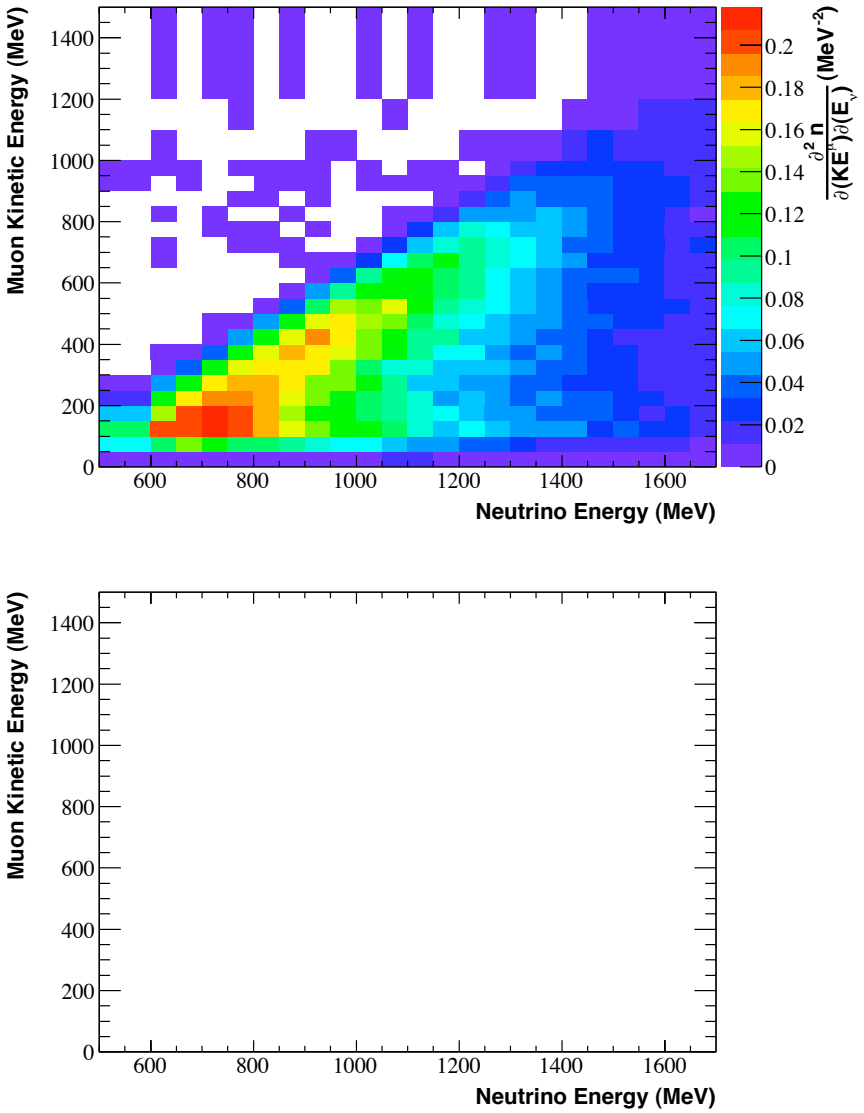

Figure B.25: The reconstructed muon kinetic energy vs neutrino energy distribution is shown for both the data (top) and Monte Carlo (bottom).

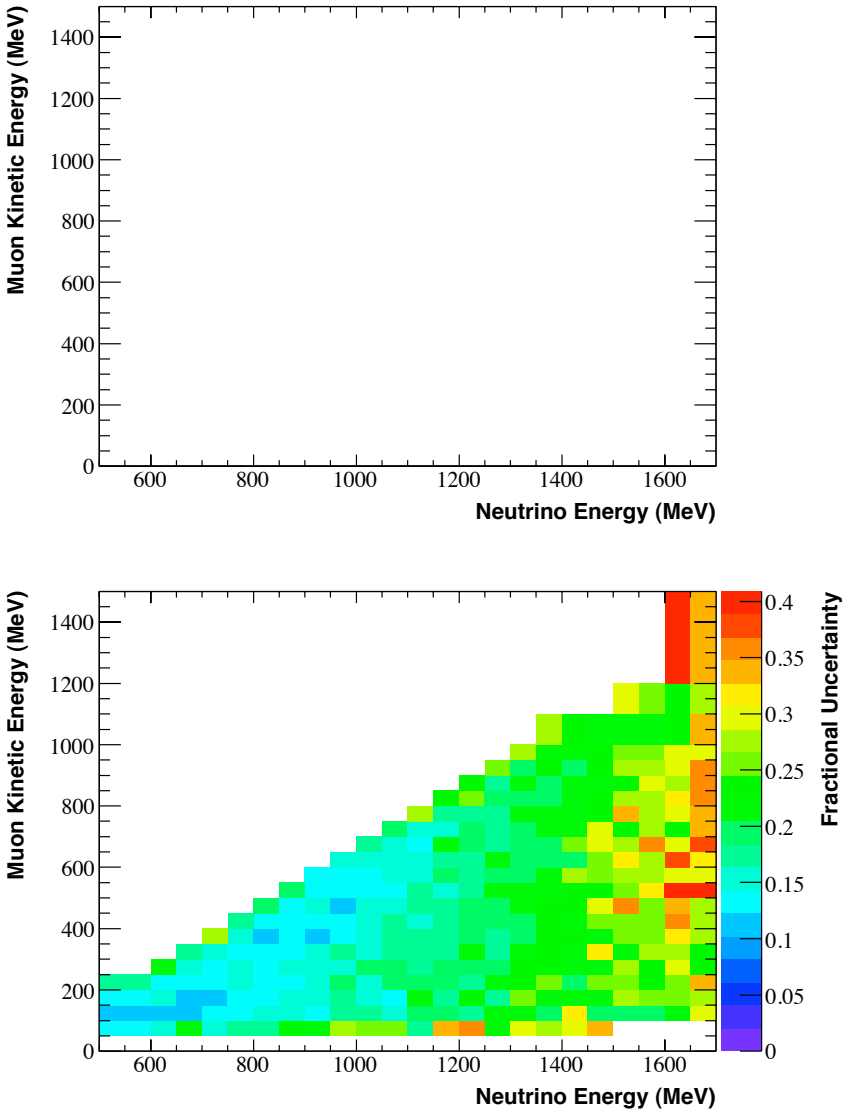

Figure B.26: The Monte Carlo reconstructed muon kinetic energy vs neutrino energy distribution is shown (top) along with the total fractional uncertainties (bottom).

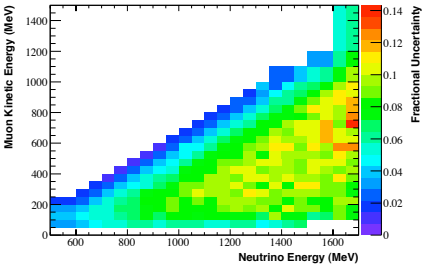

(a) The fractional systematic uncertainty from the "XSec" error source.

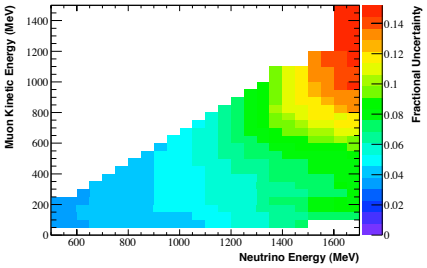

(b) The fractional systematic uncertainty from the "Beam" error source.

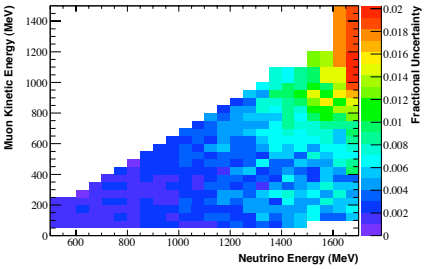

(c) The fractional systematic uncertainty from the "K^+" error source.

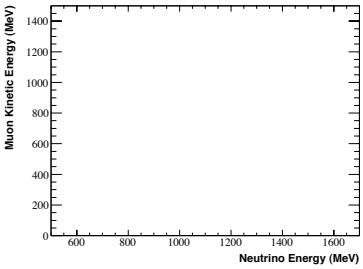

(d) Reconstructed Monte Carlo distribution

Figure B.27: The fractional systematic uncertainties on the reconstructed Monte Carlo distribution are shown for four of the error sources. The central value reconstructed Monte Carlo distribution is shown for reference. Note that the color scales differ for each systematic error source. An explanation of each error is given in Section 6.4.7.

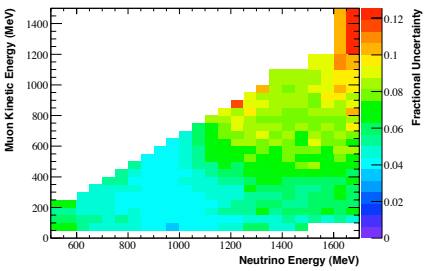

(a) The fractional systematic uncertainty from the "π^+" error source.

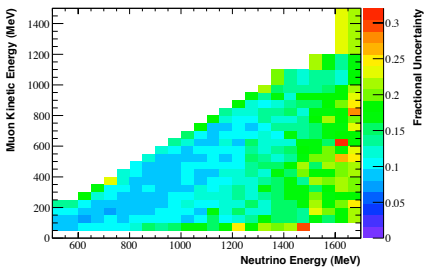

(b) The fractional systematic uncertainty from the "OM" error source.

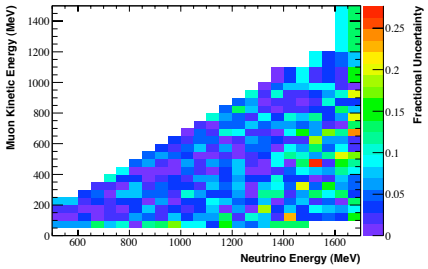

(c) The fractional systematic uncertainty from the "DISC" error source.

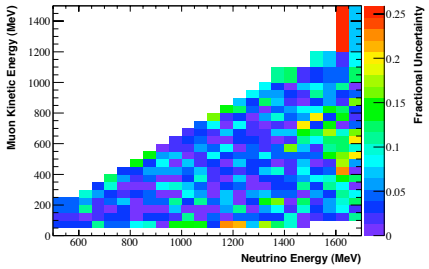

(d) The fractional systematic uncertainty from the "QTCORR" error source.

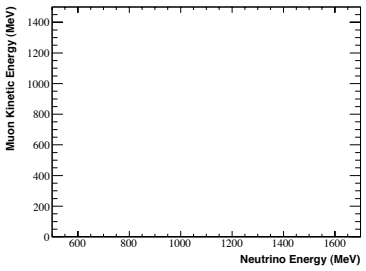

(e) Reconstructed Monte Carlo distribution

Figure B.28: The fractional systematic uncertainties on the reconstructed Monte Carlo distribution are shown for four of the error sources. The central value reconstructed Monte Carlo distribution is shown for reference. Note that the color scales differ for each systematic error source. An explanation of each error is given in Section 6.4.7.

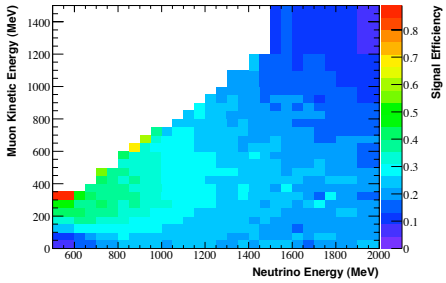

(a) Signal Efficiency

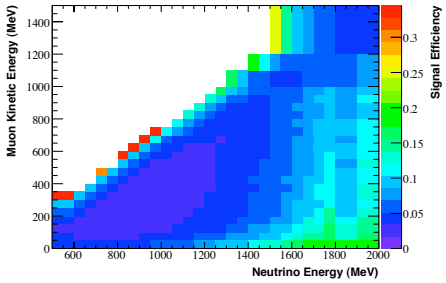

(b) Fractional Monte Carlo Statistical Error on the Signal Efficiency

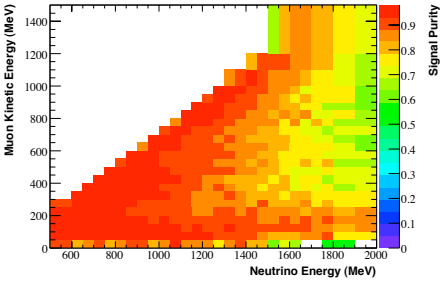

(c) Signal Purity

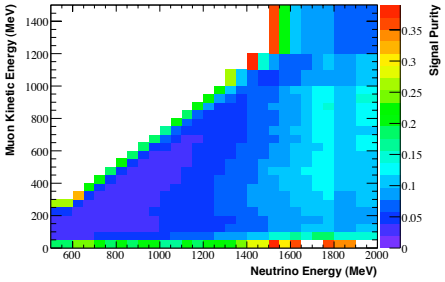

(d) Fractional Monte Carlo Statistical Error on the Signal Purity

Figure B.29: The signal efficiency and purity are shown for the muon kinetic energy vs neutrino energy distribution. The fractional errors due to Monte Carlo statistics for each of these distributions is also given for all bins with at least 10 events in the numerator.

B.10 Muon Direction vs Neutrino Energy

- Reconstructed Data/Monte Carlo comparison: Figure B.30
- Reconstructed Monte Carlo Fractional Errors: Figures B.32 and B.33
- Signal efficiency: Figure B.34(a)
- Signal purity: Figure B.34(c)

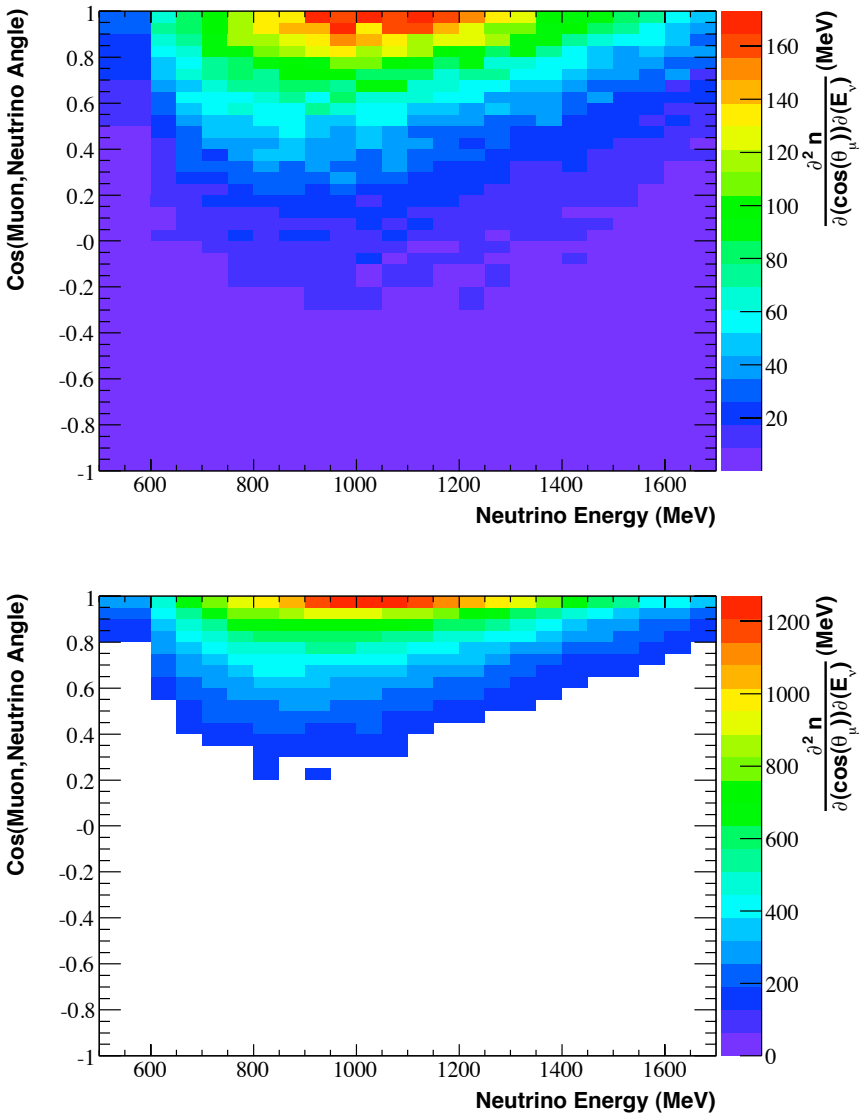

Figure B.30: The reconstructed cos(muon, neutrino angle) vs neutrino energy distribution is shown for both the data (top) and Monte Carlo (bottom).

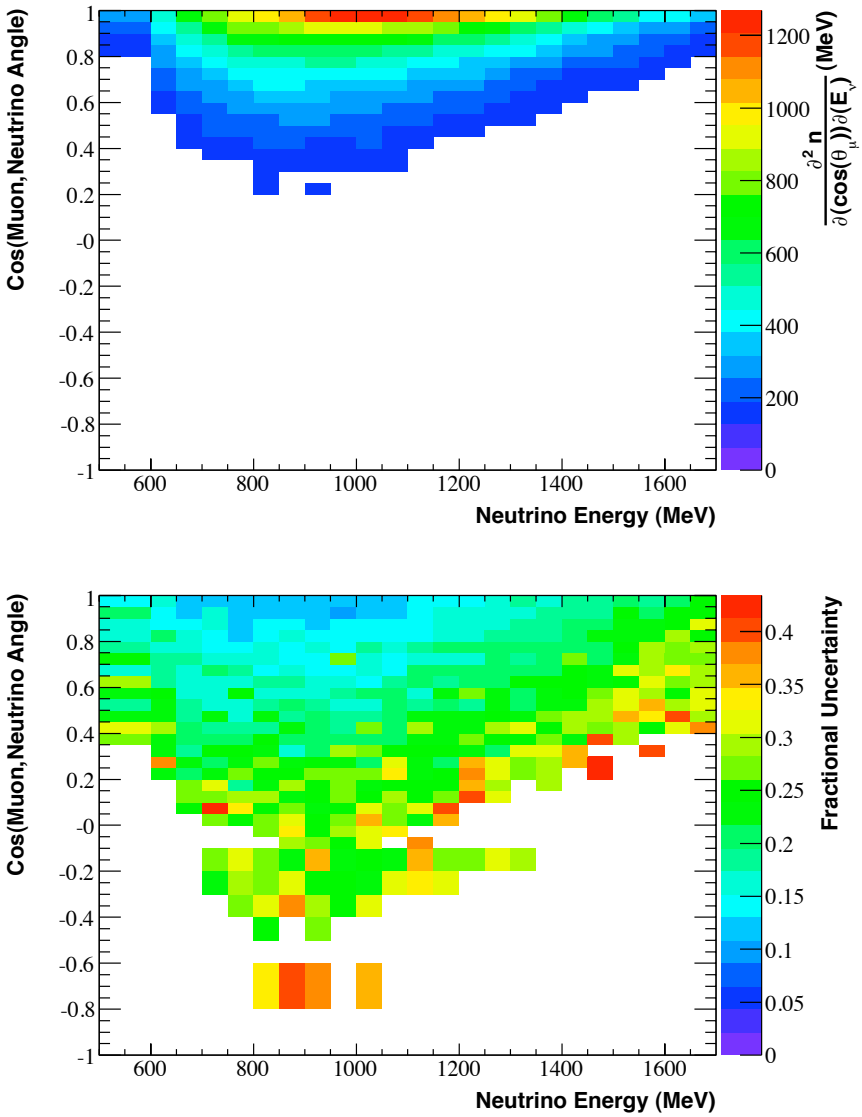

Figure B.31: The Monte Carlo reconstructed muon cos(muon, neutrino angle) vs neutrino energy distribution is shown (top) along with the total fractional uncertainties (bottom).

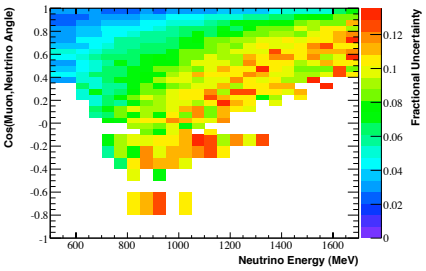

(a) The fractional systematic uncertainty from the "XSec" error source.

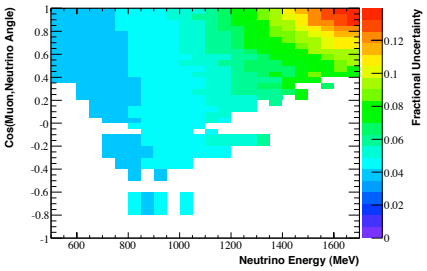

(b) The fractional systematic uncertainty from the "Beam" error source.

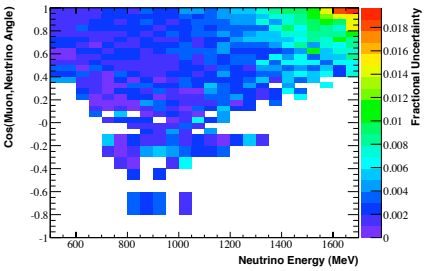

(c) The fractional systematic uncertainty from the "K^+" error source.

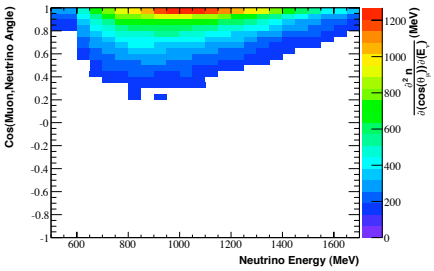

(d) Reconstructed Monte Carlo distribution

Figure B.32: The fractional systematic uncertainties on the reconstructed Monte Carlo distribution are shown for four of the error sources. The central value reconstructed Monte Carlo distribution is shown for reference. Note that the color scales differ for each systematic error source. An explanation of each error is given in Section 6.4.7.

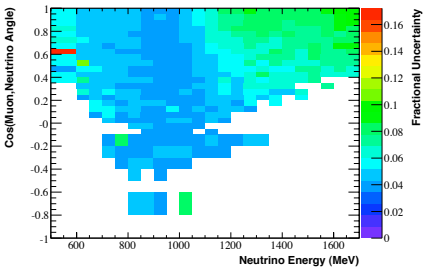

(a) The fractional systematic uncertainty from the "π^+" error source.

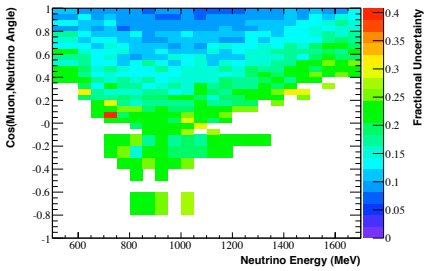

(b) The fractional systematic uncertainty from the "OM" error source.

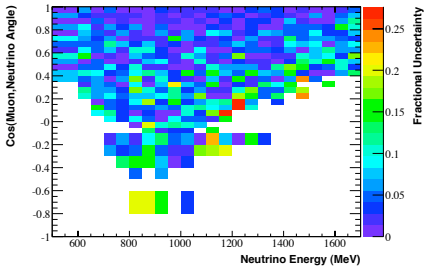

(c) The fractional systematic uncertainty from the "DISC" error source.

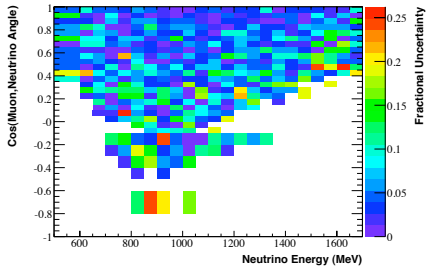

(d) The fractional systematic uncertainty from the "QTCORR" error source.

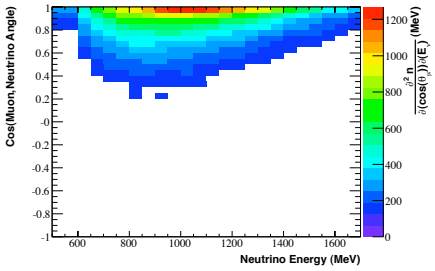

(e) Reconstructed Monte Carlo distribution

Figure B.33: The fractional systematic uncertainties on the reconstructed Monte Carlo distribution are shown for four of the error sources. The central value reconstructed Monte Carlo distribution is shown for reference. Note that the color scales differ for each systematic error source. An explanation of each error is given in Section 6.4.7.

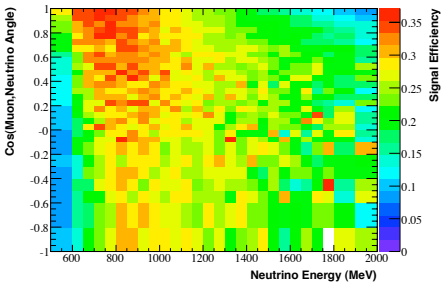

(a) Signal Efficiency

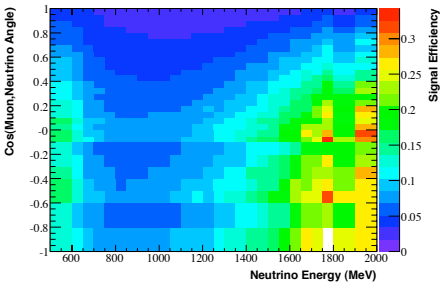

(b) Fractional Monte Carlo Statistical Error on the Signal Efficiency

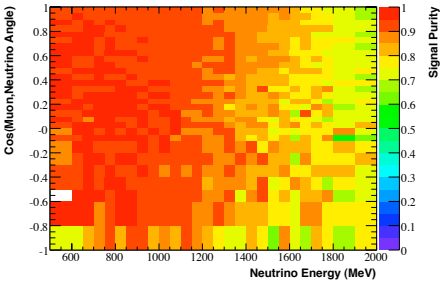

(c) Signal Purity

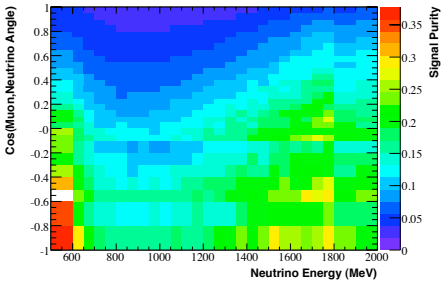

(d) Fractional Monte Carlo Statistical Error on the Signal Purity

Figure B.34: The signal efficiency and purity are shown for the muon cos(muon, neutrino angle) vs neutrino energy distribution. The fractional errors due to Monte Carlo statistics for each of these distributions is also given for all bins with at least 10 events in the numerator.

B.11 Pion Kinetic Energy vs Neutrino Energy

- Reconstructed Data/Monte Carlo comparison: Figure B.35
- Reconstructed Monte Carlo Fractional Errors: Figures B.37 and B.38
- Signal efficiency: Figure B.39(a)
- Signal purity: Figure B.39(c)

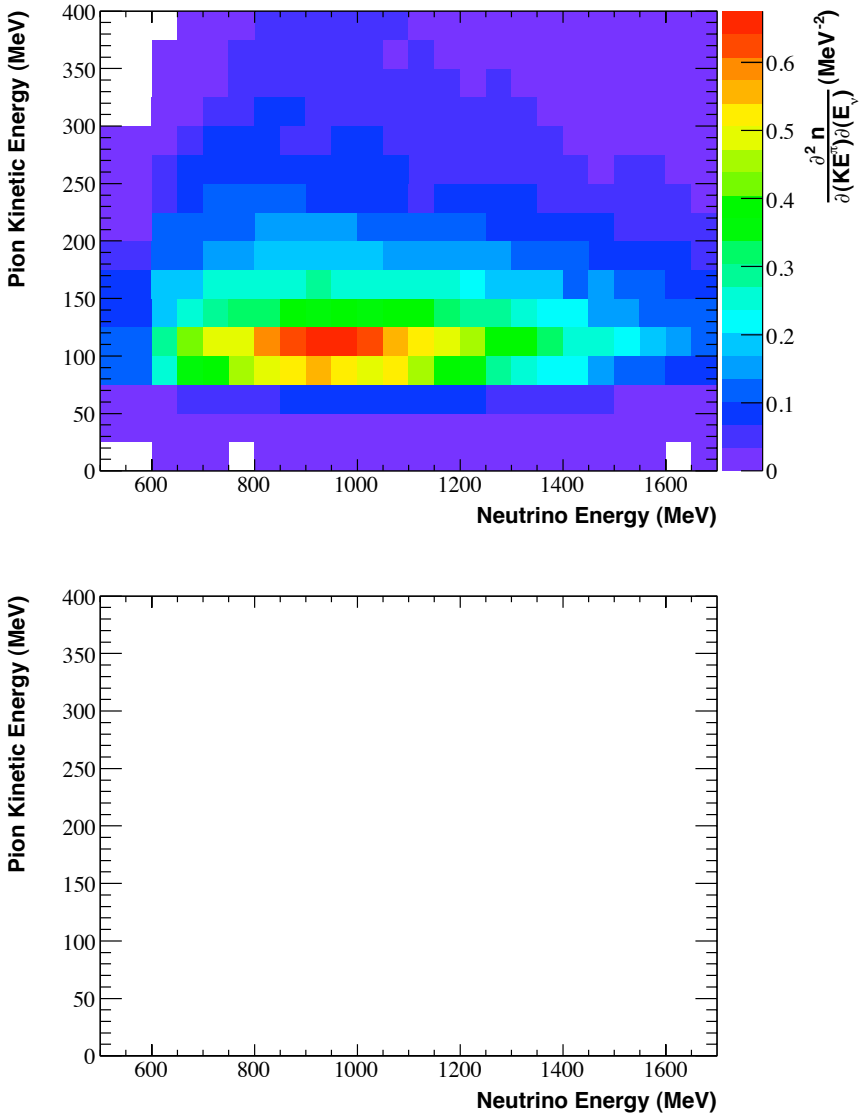

Figure B.35: The reconstructed pion kinetic energy vs neutrino energy distribution is shown for both the data (top) and Monte Carlo (bottom).

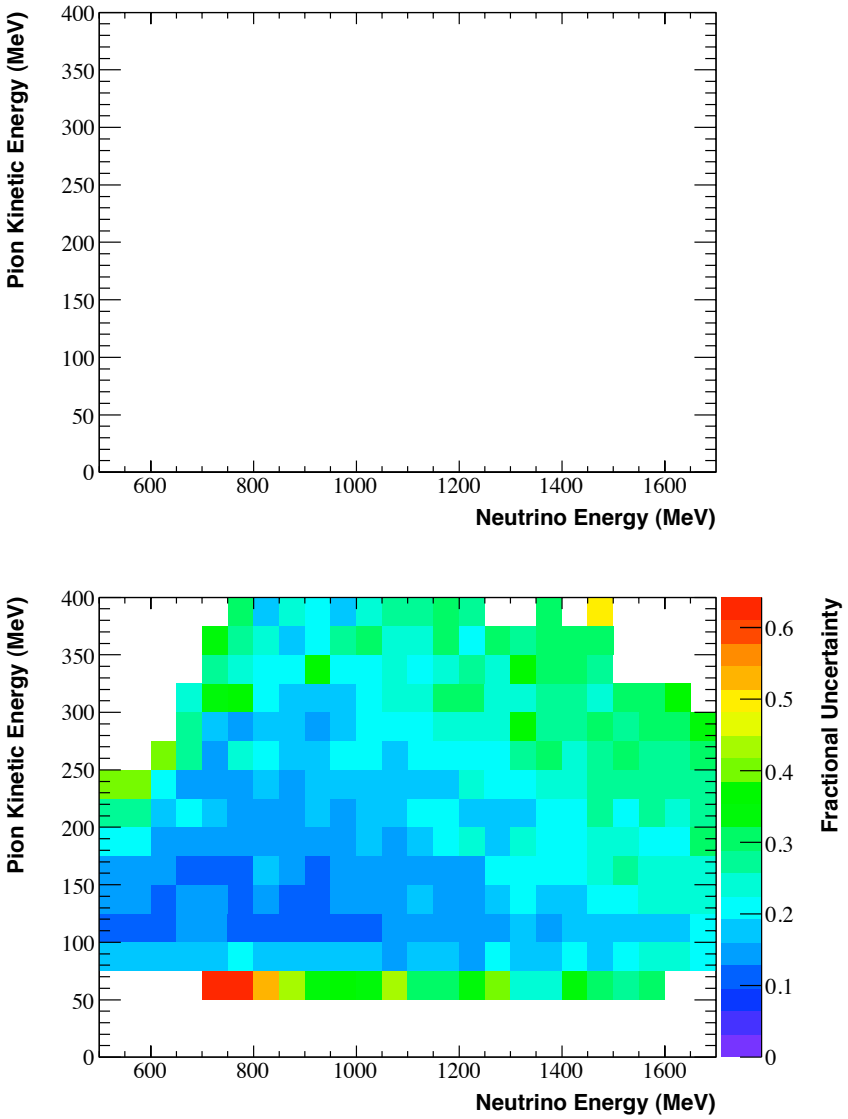

Figure B.36: The Monte Carlo reconstructed pion kinetic energy vs neutrino energy distribution is shown (top) along with the total fractional uncertainties (bottom).

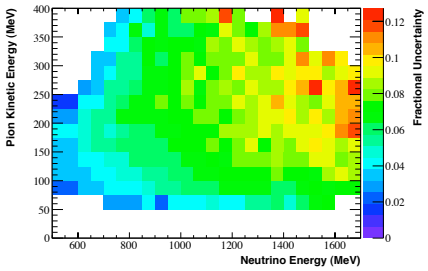

(a) The fractional systematic uncertainty from the "XSec" error source.

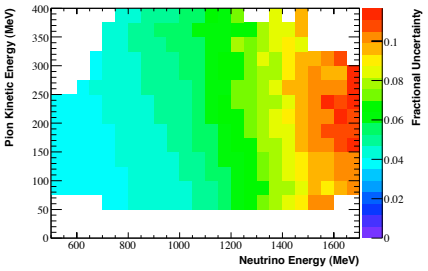

(b) The fractional systematic uncertainty from the "Beam" error source.

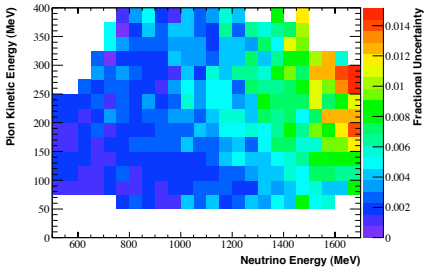

(c) The fractional systematic uncertainty from the "K^+" error source.

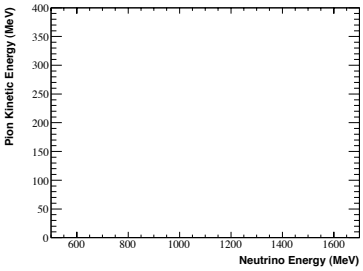

(d) Reconstructed Monte Carlo distribution

Figure B.37: The fractional systematic uncertainties on the reconstructed Monte Carlo distribution are shown for four of the error sources. The central value reconstructed Monte Carlo distribution is shown for reference. Note that the color scales differ for each systematic error source. An explanation of each error is given in Section 6.4.7.

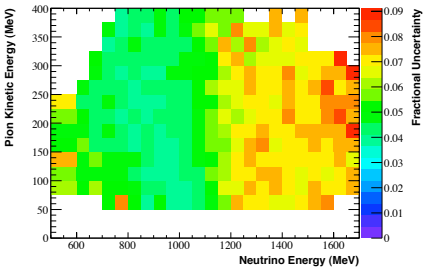

(a) The fractional systematic uncertainty from the "π^+" error source.

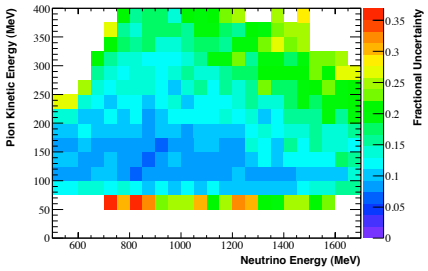

(b) The fractional systematic uncertainty from the "OM" error source.

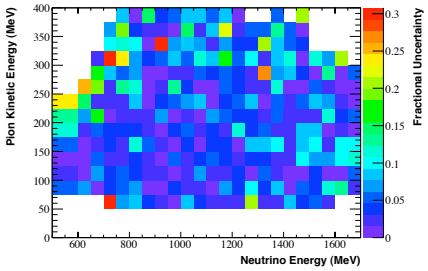

(c) The fractional systematic uncertainty from the "DISC" error source.

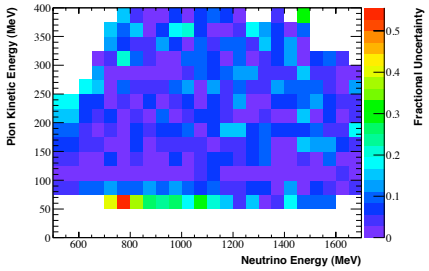

(d) The fractional systematic uncertainty from the "QTCORR" error source.

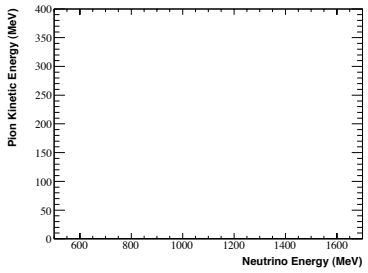

(e) Reconstructed Monte Carlo distribution

Figure B.38: The fractional systematic uncertainties on the reconstructed Monte Carlo distribution are shown for four of the error sources. The central value reconstructed Monte Carlo distribution is shown for reference. Note that the color scales differ for each systematic error source. An explanation of each error is given in Section 6.4.7.

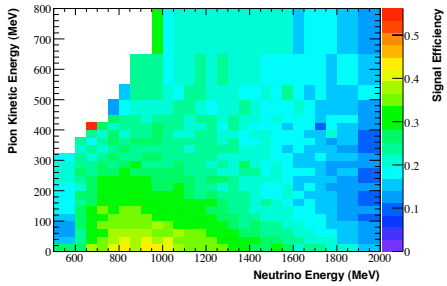

(a) Signal Efficiency

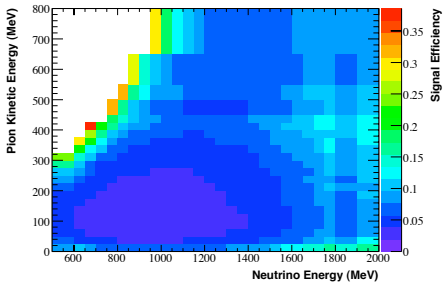

(b) Fractional Monte Carlo Statistical Error on the Signal Efficiency

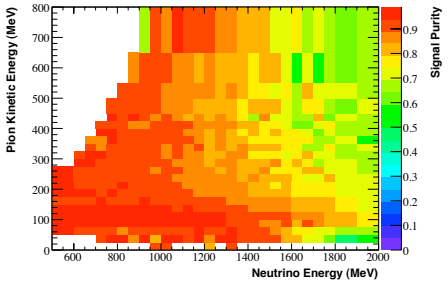

(c) Signal Purity

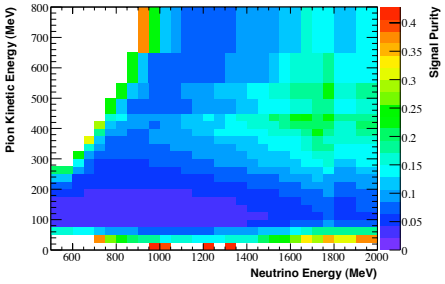

(d) Fractional Monte Carlo Statistical Error on the Signal Purity

Figure B.39: The signal efficiency and purity are shown for the pion kinetic energy vs neutrino energy distribution. The fractional errors due to Monte Carlo statistics for each of these distributions is also given for all bins with at least 10 events in the numerator.

B.12 Pion Direction vs Neutrino Energy

- Reconstructed Data/Monte Carlo comparison: Figure B.40
- Reconstructed Monte Carlo Fractional Errors: Figures B.42 and B.43
- Signal efficiency: Figure B.44(a)
- Signal purity: Figure B.44(c)

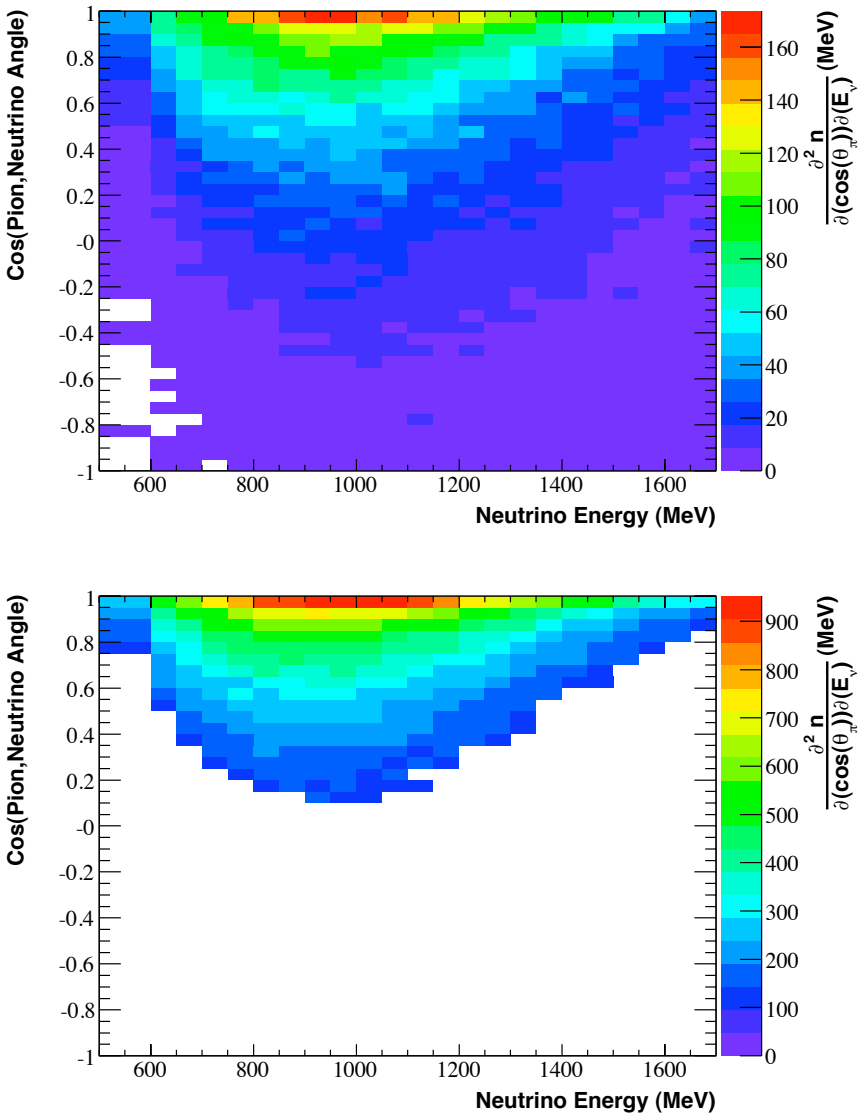

Figure B.40: The reconstructed cos(pion, neutrino angle) vs neutrino energy distribution is shown for both the data (top) and Monte Carlo (bottom).

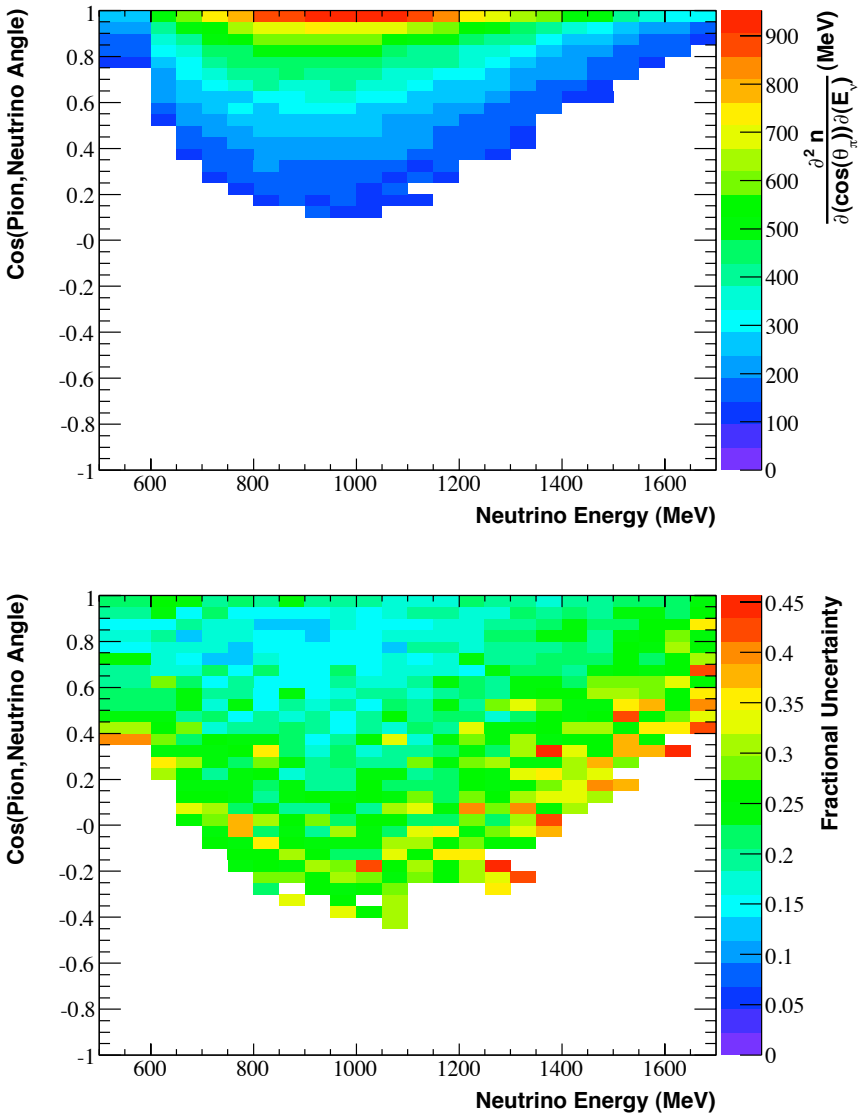

Figure B.41: The Monte Carlo reconstructed pion cos(pion, neutrino angle) vs neutrino energy distribution is shown (top) along with the total fractional uncertainties (bottom).

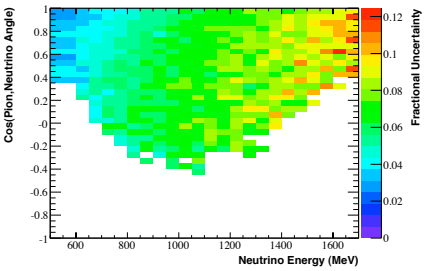

(a) The fractional systematic uncertainty from the "XSec" error source.

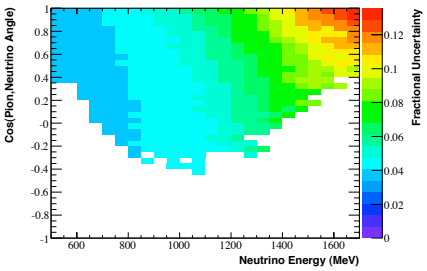

(b) The fractional systematic uncertainty from the "Beam" error source.

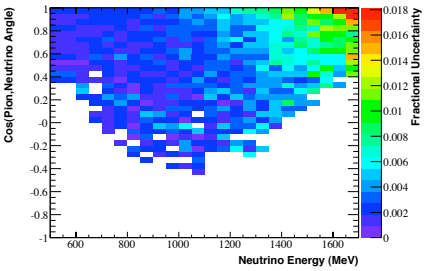

(c) The fractional systematic uncertainty from the "K^+" error source.

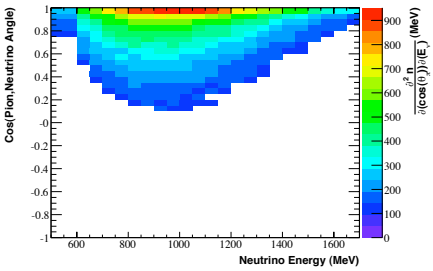

(d) Reconstructed Monte Carlo distribution

Figure B.42: The fractional systematic uncertainties on the reconstructed Monte Carlo distribution are shown for four of the error sources. The central value reconstructed Monte Carlo distribution is shown for reference. Note that the color scales differ for each systematic error source. An explanation of each error is given in Section 6.4.7.

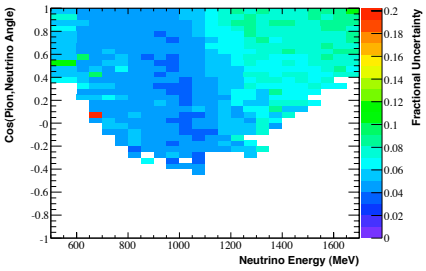

(a) The fractional systematic uncertainty from the "π^+" error source.

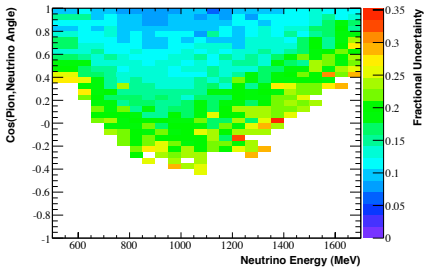

(b) The fractional systematic uncertainty from the "OM" error source.

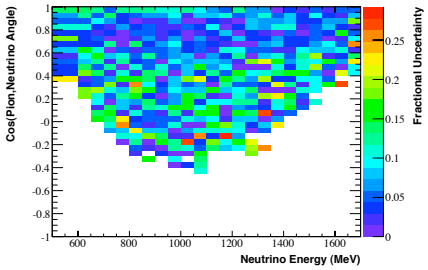

(c) The fractional systematic uncertainty from the "DISC" error source.

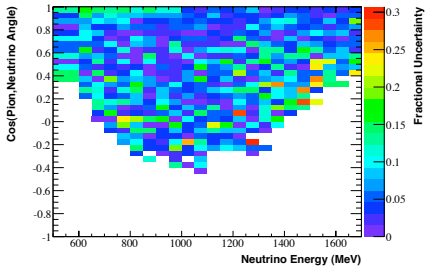

(d) The fractional systematic uncertainty from the "QTCORR" error source.

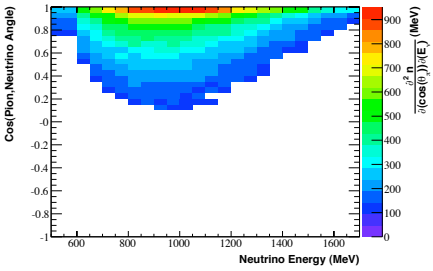

(e) Reconstructed Monte Carlo distribution

Figure B.43: The fractional systematic uncertainties on the reconstructed Monte Carlo distribution are shown for four of the error sources. The central value reconstructed Monte Carlo distribution is shown for reference. Note that the color scales differ for each systematic error source. An explanation of each error is given in Section 6.4.7.

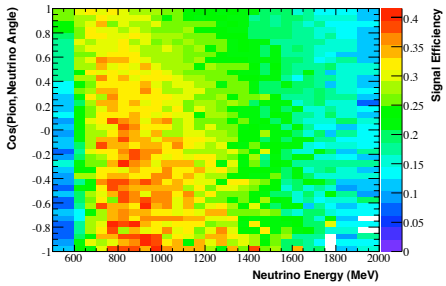

(a) Signal Efficiency

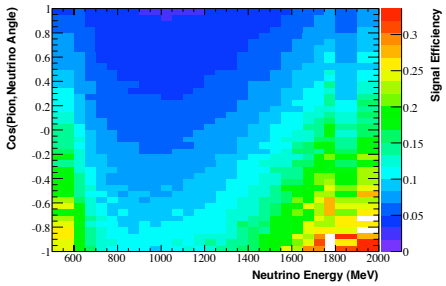

(b) Fractional Monte Carlo Statistical Error on the Signal Efficiency

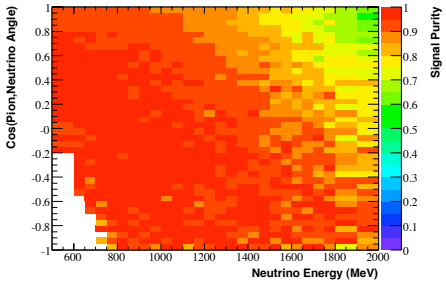

(c) Signal Purity

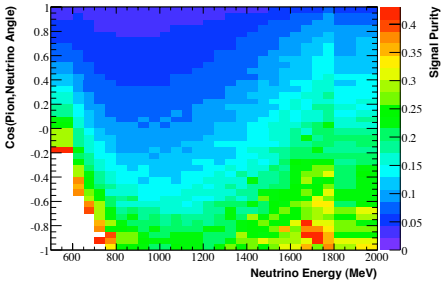

(d) Fractional Monte Carlo Statistical Error on the Signal Purity

Figure B.44: The signal efficiency and purity are shown for the pion cos(pion, neutrino angle) vs neutrino energy distribution. The fractional errors due to Monte Carlo statistics for each of these distributions is also given for all bins with at least 10 events in the numerator.

B.13 Muon Direction vs Kinetic Energy

- Reconstructed Data/Monte Carlo comparison: Figure B.45
- Reconstructed Monte Carlo Fractional Errors: Figures B.47 and B.48
- Signal efficiency: Figure B.49(a)
- Signal purity: Figure B.49(c)

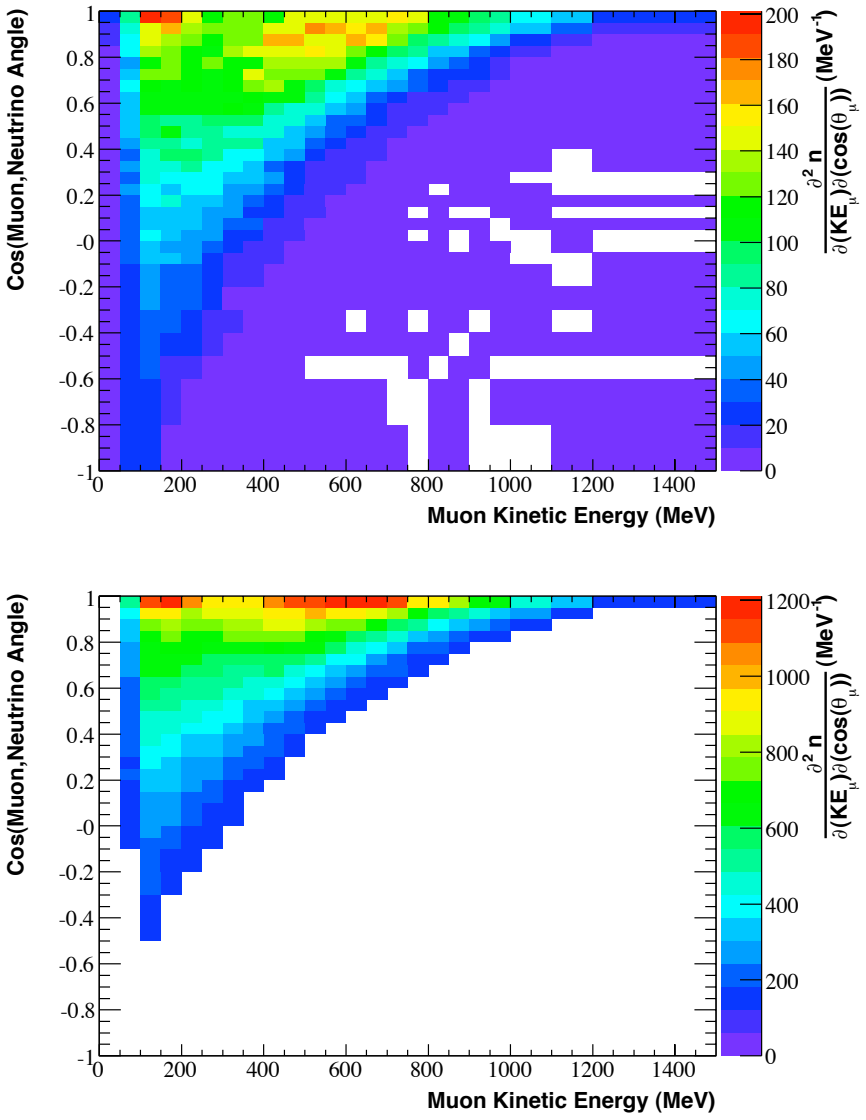

Figure B.45: The reconstructed cos(muon, neutrino angle) vs muon kinetic energy distribution is shown for both the data (top) and Monte Carlo (bottom).

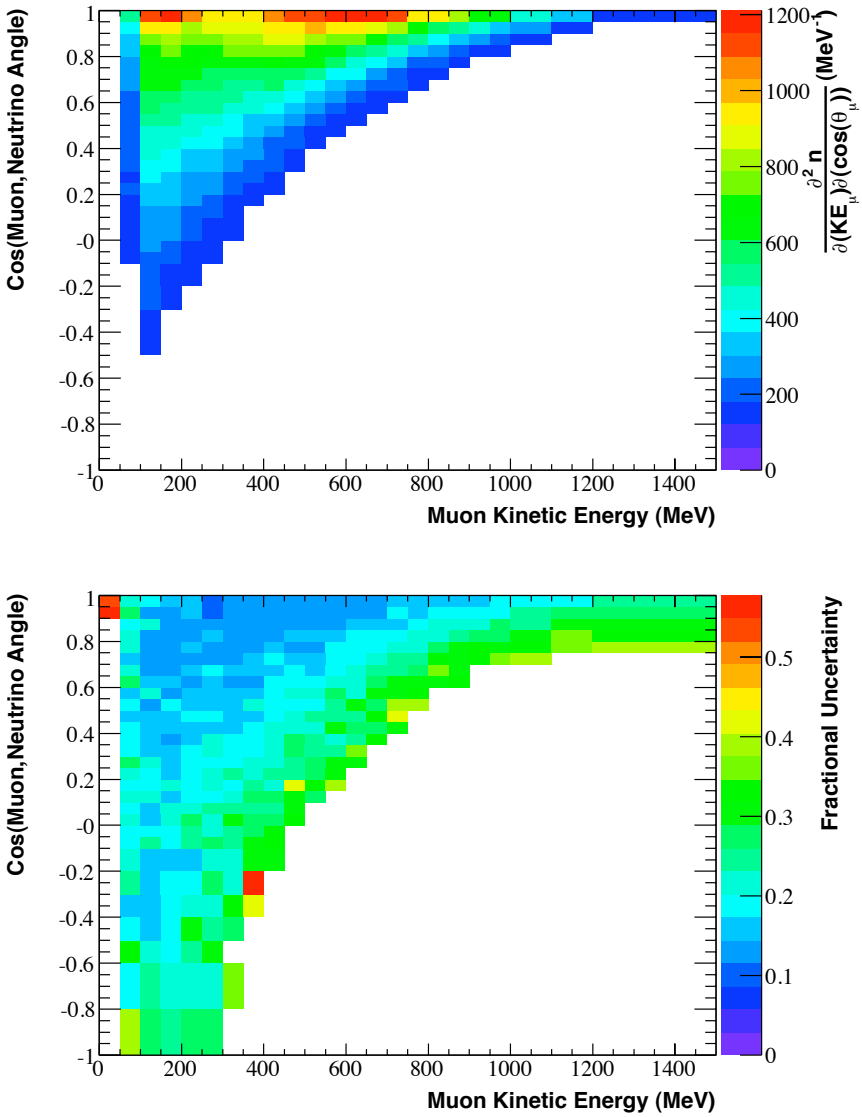

Figure B.46: The Monte Carlo reconstructed cos(muon, neutrino angle) vs muon kinetic energy distribution is shown (top) along with the total fractional uncertainties (bottom).

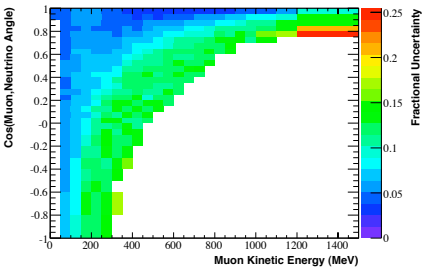

(a) The fractional systematic uncertainty from the "XSec" error source.

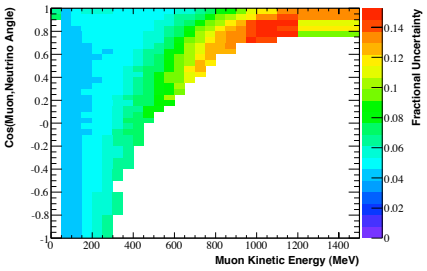

(b) The fractional systematic uncertainty from the "Beam" error source.

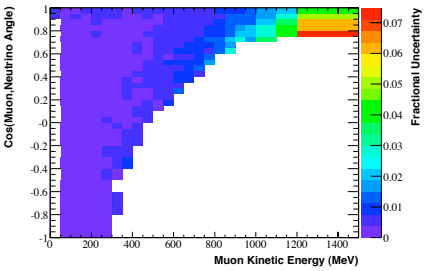

(c) The fractional systematic uncertainty from the "K^+" error source.

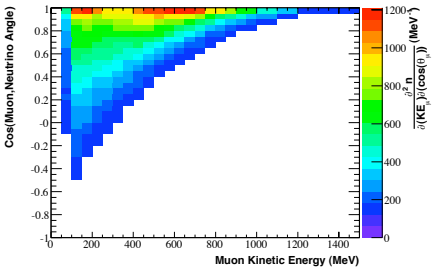

(d) Reconstructed Monte Carlo distribution

Figure B.47: The fractional systematic uncertainties on the reconstructed Monte Carlo distribution are shown for four of the error sources. The central value reconstructed Monte Carlo distribution is shown for reference. Note that the color scales differ for each systematic error source. An explanation of each error is given in Section 6.4.7.

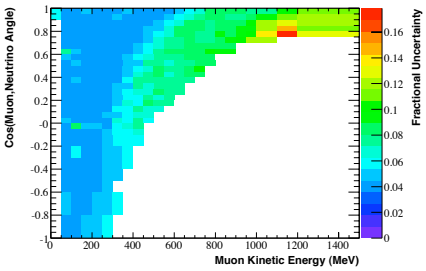

(a) The fractional systematic uncertainty from the "π^+" error source.

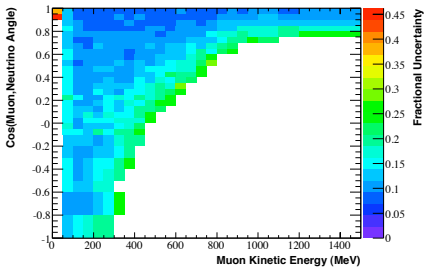

(b) The fractional systematic uncertainty from the "OM" error source.

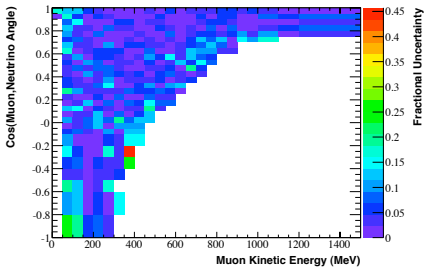

(c) The fractional systematic uncertainty from the "DISC" error source.

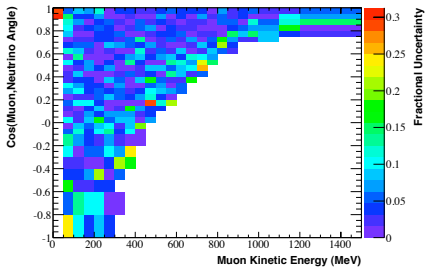

(d) The fractional systematic uncertainty from the "QTCORR" error source.

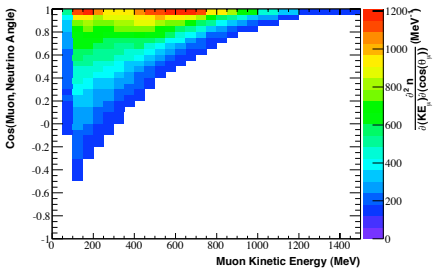

(e) Reconstructed Monte Carlo distribution

Figure B.48: The fractional systematic uncertainties on the reconstructed Monte Carlo distribution are shown for four of the error sources. The central value reconstructed Monte Carlo distribution is shown for reference. Note that the color scales differ for each systematic error source. An explanation of each error is given in Section 6.4.7.

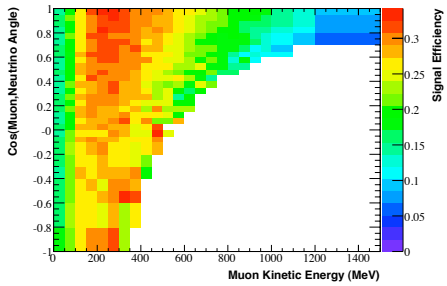

(a) Signal Efficiency

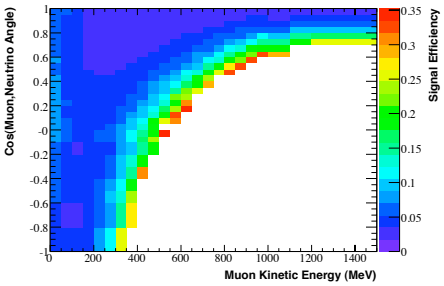

(b) Fractional Monte Carlo Statistical Error on the Signal Efficiency

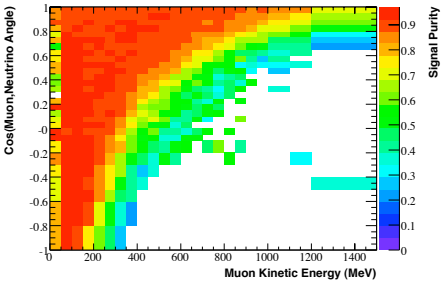

(c) Signal Purity

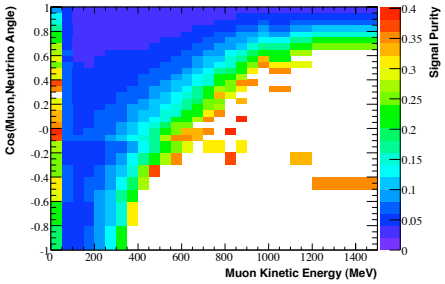

(d) Fractional Monte Carlo Statistical Error on the Signal Purity

Figure B.49: The signal efficiency and purity are shown for the cos(muon, neutrino angle) vs muon kinetic energy distribution. The fractional errors due to Monte Carlo statistics for each of these distributions is also given for all bins with at least 10 events in the numerator.

B.14 Pion Direction vs Kinetic Energy

- Reconstructed Data/Monte Carlo comparison: Figure B.50
- Reconstructed Monte Carlo Fractional Errors: Figures B.52 and B.53
- Signal efficiency: Figure B.54(a)
- Signal purity: Figure B.54(c)

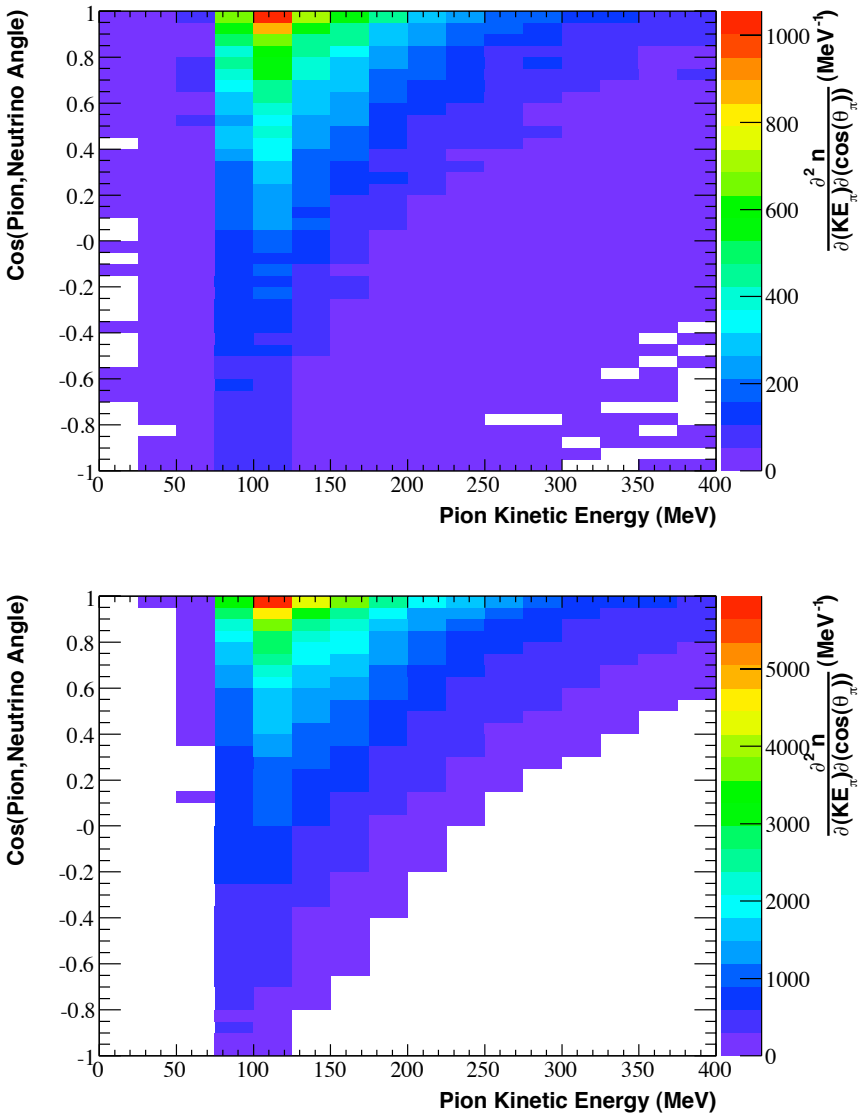

Figure B.50: The reconstructed cos(pion, neutrino angle) vs pion kinetic energy distribution is shown for both the data (top) and Monte Carlo (bottom).

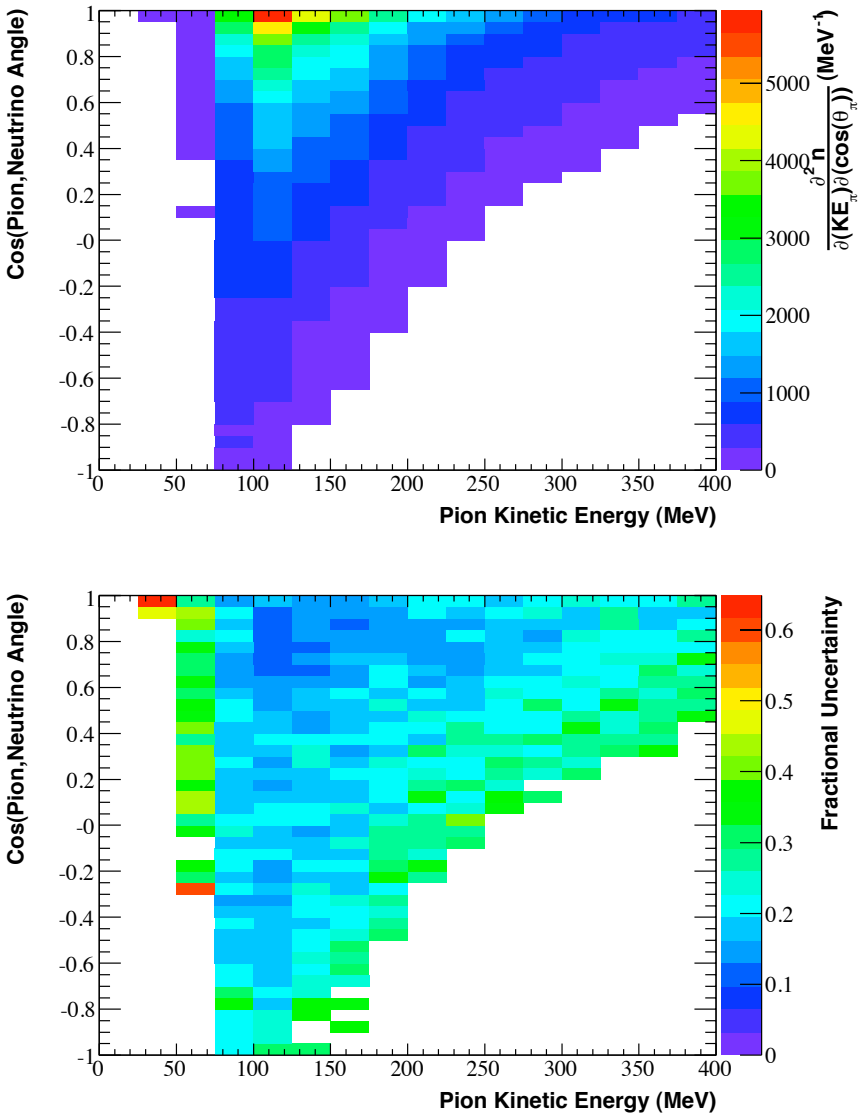

Figure B.51: The Monte Carlo reconstructed cos(pion, neutrino angle) vs pion kinetic energy distribution is shown (top) along with the total fractional uncertainties (bottom).

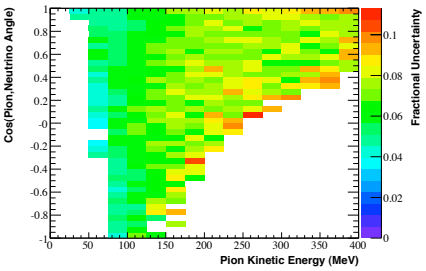

(a) The fractional systematic uncertainty from the "XSec" error source.

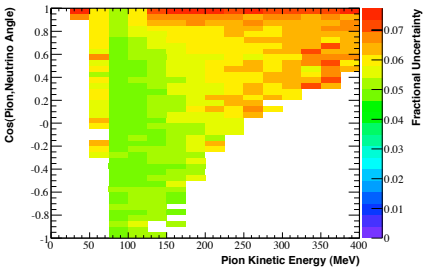

(b) The fractional systematic uncertainty from the "Beam" error source.

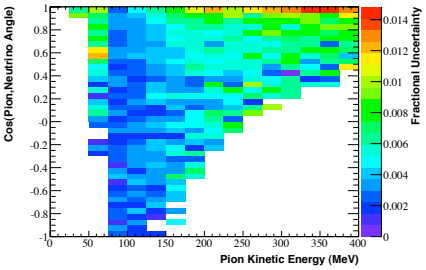

(c) The fractional systematic uncertainty from the "K^+" error source.

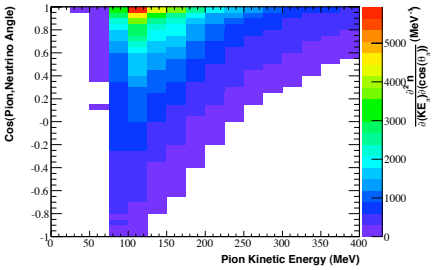

(d) Reconstructed Monte Carlo distribution

Figure B.52: The fractional systematic uncertainties on the reconstructed Monte Carlo distribution are shown for four of the error sources. The central value reconstructed Monte Carlo distribution is also shown for reference. Note that the color scales differ for each systematic error source. An explanation of each error is given in Section 6.4.7.

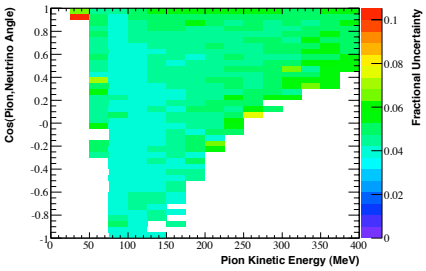

(a) The fractional systematic uncertainty from the "π^+" error source.

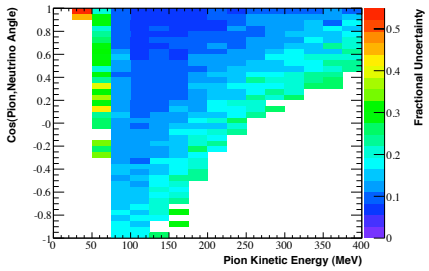

(b) The fractional systematic uncertainty from the "OM" error source.

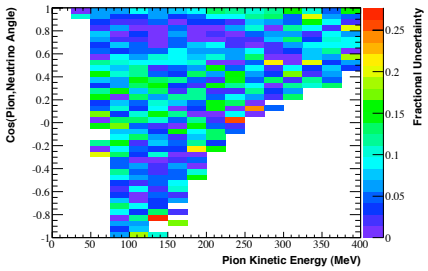

(c) The fractional systematic uncertainty from the "DISC" error source.

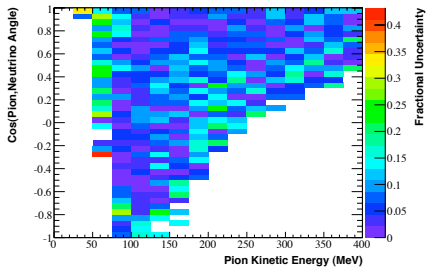

(d) The fractional systematic uncertainty from the "QTCORR" error source.

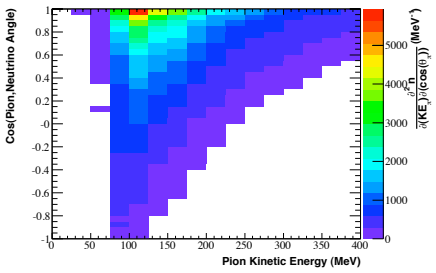

(e) Reconstructed Monte Carlo distribution

Figure B.53: The fractional systematic uncertainties on the reconstructed Monte Carlo distribution are shown for four of the error sources. The central value reconstructed Monte Carlo distribution is also shown for reference. Note that the color scales differ for each systematic error source. An explanation of each error is given in Section 6.4.7.

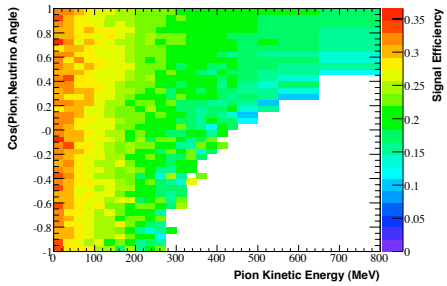

(a) Signal Efficiency

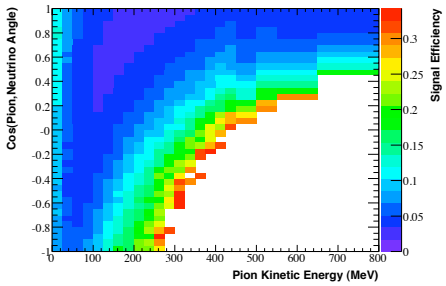

(b) Fractional Monte Carlo Statistical Error on the Signal Efficiency

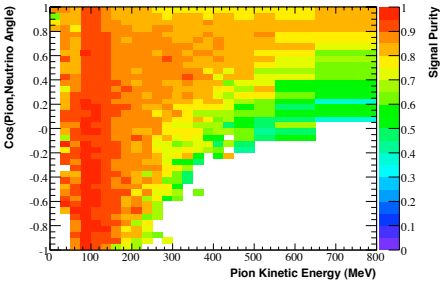

(c) Signal Purity

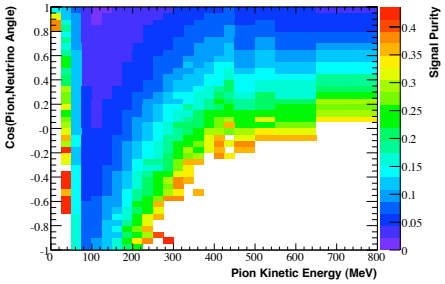

(d) Fractional Monte Carlo Statistical Error on the Signal Purity

Figure B.54: The signal efficiency and purity are shown for the pion cos(pion, neutrino angle) vs kinetic energy distribution. The fractional errors due to Monte Carlo statistics for each of these distributions is also given for all bins with at least 10 events in the numerator.

B.15 Cross Section Values

Table B.1: The $\sigma(E_\nu)$ results from Figure 6.11 are given with the total uncertainty.

bin low edge	central value ($/10^{-38}\text{cm}^2$)	% uncertainty
500	0.621	12.819
600	1.168	11.576
650	1.603	10.522
700	1.996	10.199
750	2.456	10.068
800	2.880	9.957
850	3.286	9.826
900	3.757	10.234
950	4.174	10.375
1000	4.661	10.740
1050	4.954	11.316
1100	5.266	11.520
1150	5.600	12.327
1200	5.875	12.810
1250	6.197	13.276
1300	6.630	13.853
1350	7.001	14.573
1400	7.232	15.191
1450	7.785	15.850
1500	8.139	16.480
1550	8.483	16.887
1600	8.831	17.334
1650	9.076	17.947
1700	9.619	18.224
1750	9.651	18.900
1800	10.272	19.574
1900	10.737	19.935

Table B.2: The $\partial\sigma/\partial(Q^2)$ results from Figure 6.12 are given with the total uncertainty.

bin low edge	central value ($/10^{-45}\mathrm{cm}^2/\mathrm{MeV}^2$)	% uncertainty
0.00e+00	38.519	20.002
5.00e+04	56.958	14.916
1.00e+05	56.837	13.491
1.50e+05	53.352	12.949
2.00e+05	47.265	13.088
2.50e+05	42.504	13.366
3.00e+05	38.038	13.421
3.50e+05	33.204	13.801
4.00e+05	29.188	14.073
4.50e+05	25.001	14.365
5.00e+05	21.881	14.531
5.50e+05	18.851	14.624
6.00e+05	16.538	15.101
6.50e+05	14.183	14.928
7.00e+05	12.277	15.414
7.50e+05	10.576	15.899
8.00e+05	8.895	15.799
8.50e+05	7.736	15.812
9.00e+05	6.549	16.477
9.50e+05	5.323	16.856
1.05e+06	3.994	16.637
1.15e+06	2.691	17.320
1.30e+06	1.676	18.252

Table B.3: The $\partial\sigma/\partial(KE_\mu)$ results from Figure 6.13 are given with the total uncertainty.

bin low edge	central value ($/10^{-42}$cm^2/MeV)	% uncertainty
0	24.794	15.043
50	36.949	14.622
100	41.325	14.145
150	42.464	13.866
200	41.572	13.825
250	39.211	13.749
300	37.265	13.803
350	34.602	13.555
400	31.720	13.610
450	28.758	13.325
500	26.119	13.673
550	23.114	13.862
600	20.615	13.995
650	18.515	14.334
700	15.970	14.355
750	14.209	14.902
800	12.372	15.381
850	10.601	15.888
900	9.219	16.522
950	7.713	17.328
1000	5.966	18.105
1100	4.328	19.844
1200	2.258	26.186

Table B.4: The $\partial\sigma/\partial(\cos(\theta_{\mu,\nu}))$ results from Figure 6.14 are given with the total uncertainty.

bin low edge	central value ($/10^{-39}$cm^2)	% uncertainty
-1.00	1.556	17.290
-0.80	2.496	16.926
-0.60	2.997	15.049
-0.50	3.446	14.588
-0.40	3.875	14.002
-0.30	4.496	14.317
-0.20	5.259	14.965
-0.10	5.802	14.494
-0.05	6.327	14.240
0.00	6.931	13.983
0.05	7.414	14.293
0.10	8.063	13.964
0.15	8.673	14.360
0.20	9.602	13.839
0.25	10.371	13.845
0.30	11.594	13.753
0.35	13.528	14.385
0.40	14.599	13.839
0.45	15.683	13.746
0.50	17.844	13.879
0.55	20.569	13.997
0.60	23.676	13.715
0.65	26.614	13.288
0.70	31.753	13.563
0.75	35.541	13.586
0.80	42.882	13.307
0.85	52.197	13.425
0.90	63.302	14.161
0.95	81.990	18.891

Table B.5: The $\partial\sigma/\partial(KE_\pi)$ results from Figure 6.15 are given with the total uncertainty.

bin low edge	central value ($/10^{-41}$cm^2/MeV)	% uncertainty
0	1.791	12.818
25	5.411	12.437
50	8.806	13.150
75	10.847	12.618
100	10.904	11.527
125	9.885	12.155
150	8.756	13.079
175	7.775	13.861
200	7.128	14.580
225	6.221	15.310
250	5.447	16.084
275	4.703	16.887
300	4.038	17.465
325	3.372	17.826
350	2.800	18.055
375	2.385	18.435

Table B.6: The $\partial\sigma/\partial(\cos(\theta_{\pi,\nu}))$ results from Figure 6.16 are given with the total uncertainty.

bin low edge	central value ($/10^{-39}$cm^2)	% uncertainty
-1.00	2.877	12.745
-0.95	3.127	12.921
-0.90	3.298	13.495
-0.85	3.586	12.982
-0.80	3.797	13.978
-0.75	3.946	13.038
-0.70	4.282	13.079
-0.65	4.570	11.915
-0.60	4.738	12.078
-0.55	5.077	11.500
-0.50	5.394	11.459
-0.45	5.558	12.247
-0.40	6.117	12.243
-0.35	6.684	11.946
-0.30	7.063	12.141
-0.25	7.534	12.069
-0.20	7.979	11.658
-0.15	8.539	11.872
-0.10	8.994	11.727
-0.05	9.974	11.907
0.00	10.756	11.946
0.05	11.431	12.032
0.10	12.303	12.405
0.15	13.454	12.540
0.20	14.364	12.744
0.25	15.264	12.582
0.30	16.399	13.136
0.35	17.446	13.589
0.40	18.867	13.182
0.45	20.586	13.484
0.50	22.492	13.566
0.55	23.890	14.028
0.60	26.112	13.870
0.65	28.189	14.008
0.70	30.226	14.102
0.75	32.520	14.367
0.80	34.819	14.822
0.85	37.354	15.108
0.90	39.415	16.496
0.95	42.948	18.497

Table B.7: The first of three tables detailing the $\partial\sigma(E_\nu)/\partial(Q^2)$ results from Figure 6.17 ($10^{-44}\text{cm}^2/\text{MeV}^2$).

bin low edge	500	600	650	700	750	800	850	900
7.00e+05								0.932
6.50e+05							0.806	1.517
6.00e+05						0.646	1.290	2.167
5.50e+05					0.459	1.158	1.803	2.327
5.00e+05				0.353	0.767	1.787	2.399	3.150
4.50e+05				0.683	1.543	2.353	3.072	3.886
4.00e+05			0.548	1.340	2.537	3.191	4.158	4.768
3.50e+05			1.150	2.046	3.198	4.011	4.777	5.582
3.00e+05		0.993	1.964	3.159	4.067	5.099	5.920	5.970
2.50e+05		1.882	3.081	4.116	5.271	5.917	6.591	6.694
2.00e+05	0.986	2.904	4.204	5.243	6.100	6.727	6.970	7.525
1.50e+05	1.917	4.096	5.480	6.357	7.188	7.488	7.603	8.328
1.00e+05	3.156	5.231	6.633	7.079	7.532	7.782	8.096	8.888
5.00e+04	4.375	6.040	6.601	7.093	7.429	7.614	7.789	8.185
0.00e+00	1.861	2.757	3.289	3.711	4.056	4.556	4.937	5.279

Table B.8: The second of three tables detailing the $\partial\sigma(E_\nu)/\partial(Q^2)$ results from Figure 6.17 ($10^{-44}\text{cm}^2/\text{MeV}^2$).

bin low edge	950	1000	1050	1100	1150	1200	1250	1300
1.15e+06						0.333	0.596	0.766
1.05e+06					0.595	0.834	1.046	1.159
9.50e+05			0.469	0.695	1.069	1.297	1.631	1.856
9.00e+05			0.820	1.229	1.449	1.879	1.875	2.260
8.50e+05		0.742	1.121	1.416	1.676	2.054	2.499	2.619
8.00e+05	0.636	1.031	1.480	1.905	2.370	2.677	2.892	3.274
7.50e+05	1.008	1.586	2.029	2.316	2.608	3.046	3.303	3.372
7.00e+05	1.499	2.057	2.407	2.789	3.142	3.392	3.724	3.813
6.50e+05	2.064	2.496	2.876	3.018	3.844	3.597	4.008	4.439
6.00e+05	2.386	3.200	3.585	4.018	4.074	4.363	4.993	5.196
5.50e+05	2.994	3.669	4.008	4.406	4.548	5.049	4.862	5.385
5.00e+05	3.602	4.339	4.688	5.169	5.374	5.540	5.462	6.302
4.50e+05	4.602	5.047	5.526	5.256	5.798	6.214	6.092	6.214
4.00e+05	4.994	5.880	6.231	6.436	6.426	6.832	6.815	6.990
3.50e+05	6.262	6.569	6.563	6.818	7.139	7.488	7.278	7.870
3.00e+05	7.234	7.151	7.173	7.826	7.725	7.768	8.157	8.602
2.50e+05	7.425	7.544	8.027	7.951	7.791	8.131	8.616	8.677
2.00e+05	7.850	8.582	8.326	8.630	8.484	9.038	8.943	9.329
1.50e+05	8.696	9.166	8.978	9.307	9.107	9.353	9.215	9.497
1.00e+05	8.397	9.308	9.311	9.425	9.666	9.245	9.329	9.848
5.00e+04	8.117	8.280	8.509	8.845	9.052	8.684	9.115	8.676
0.00e+00	5.781	6.062	6.058	5.843	6.484	6.555	6.622	6.939

Table B.9: The third of three tables detailing the $\partial\sigma(E_\nu)/\partial(Q^2)$ results from Figure 6.17 ($10^{-44}\text{cm}^2/\text{MeV}^2$).

bin low edge	1350	1400	1450	1500	1550	1600	1650
1.30e+06	0.438	0.606	0.746	0.984	1.022	1.199	1.171
1.15e+06	1.058	1.050	1.264	1.502	1.553	1.882	1.805
1.05e+06	1.375	1.793	1.899	2.252	2.496	2.274	2.592
9.50e+05	2.111	2.194	2.326	2.604	3.160	3.146	3.031
9.00e+05	2.345	2.721	3.381	2.946	3.485		
8.50e+05	2.813	3.055	3.464	4.094	3.578	3.745	
8.00e+05	3.305	3.280	3.758	3.571	4.125	4.249	
7.50e+05	3.760	4.486	4.092	4.525	3.957	4.384	
7.00e+05	4.129	4.350	5.271	4.625	5.042	4.644	
6.50e+05	4.527	4.931	4.894	5.365	5.191	4.878	5.262
6.00e+05	5.074	4.805	5.616	5.856	5.345	5.990	5.815
5.50e+05	5.215	5.770	5.588	6.548	6.928	7.009	6.828
5.00e+05	6.082	6.269	6.604	5.908	6.977	7.043	6.844
4.50e+05	6.506	7.303	6.800	7.075	6.239	7.311	7.508
4.00e+05	7.189	6.774	7.877	7.358	8.101	7.682	8.538
3.50e+05	7.642	7.517	8.022	8.483	8.091	8.253	8.469
3.00e+05	8.659	8.488	8.425	8.523	8.910	8.678	9.805
2.50e+05	9.662	9.219	9.449	8.803	9.665	10.011	10.328
2.00e+05	9.463	9.367	9.811	10.191	10.055	11.370	11.142
1.50e+05	9.779	9.953	10.354	11.403	10.905	11.464	10.531
1.00e+05	9.600	10.109	10.819	9.854	10.978	10.876	10.345
5.00e+04	9.032	8.598	9.618	10.206	10.193	10.347	10.747
0.00e+00	7.489	7.162	7.385	7.918	8.393	8.392	8.842

Table B.10: The first of three tables detailing the percent uncertainty of the $\partial\sigma(E_\nu)/\partial(Q^2)$ results from Figure 6.17.

bin low edge	500	600	650	700	750	800	850	900
7.00e+05								17.076
6.50e+05							18.670	19.730
6.00e+05						24.816	22.389	20.757
5.50e+05					21.930	17.187	15.991	17.035
5.00e+05				24.148	17.522	18.547	15.262	13.727
4.50e+05				19.273	16.476	14.636	12.762	12.697
4.00e+05			18.832	15.072	15.785	11.566	11.957	13.192
3.50e+05			17.857	13.842	11.961	12.696	11.782	12.899
3.00e+05		15.731	12.518	11.060	12.504	12.242	11.840	12.274
2.50e+05		13.159	12.030	12.520	11.531	11.475	11.645	11.519
2.00e+05	14.390	13.563	11.254	11.258	11.347	10.819	10.680	10.892
1.50e+05	10.705	10.617	11.069	10.712	10.692	10.860	10.610	11.520
1.00e+05	10.406	11.120	10.751	10.731	10.842	11.431	11.396	11.233
5.00e+04	12.380	12.798	12.516	13.953	13.894	13.658	13.626	13.295
0.00e+00	20.463	19.097	19.683	19.353	18.618	18.143	17.532	16.648

Table B.11: The second of three tables detailing the percent uncertainty of the $\partial\sigma(E_\nu)/\partial(Q^2)$ results from Figure 6.17.

bin low edge	950	1000	1050	1100	1150	1200	1250	1300
1.15e+06						22.806	26.379	23.959
1.05e+06					24.119	23.494	28.685	23.828
9.50e+05			24.824	21.910	21.837	20.730	19.260	20.610
9.00e+05			21.933	22.214	20.136	23.845	20.378	19.112
8.50e+05		28.602	21.824	18.064	20.220	18.063	21.357	20.409
8.00e+05	24.182	21.858	20.610	20.631	19.266	18.015	17.698	19.275
7.50e+05	23.584	19.887	21.405	18.313	16.142	18.153	17.168	18.095
7.00e+05	19.911	17.155	18.005	16.981	16.758	15.598	15.741	17.691
6.50e+05	18.157	18.974	16.808	14.970	15.230	16.686	16.235	17.935
6.00e+05	16.799	16.266	14.710	14.406	16.380	14.913	16.357	17.656
5.50e+05	15.227	14.775	13.565	14.282	15.224	16.326	16.013	16.106
5.00e+05	14.386	13.306	14.459	15.244	15.118	14.451	15.340	16.202
4.50e+05	13.325	13.188	13.852	13.855	14.579	17.523	15.894	16.627
4.00e+05	13.237	14.047	14.476	14.730	15.223	14.493	15.574	14.841
3.50e+05	12.533	13.321	13.810	13.504	14.768	14.422	15.065	15.249
3.00e+05	12.265	12.670	12.609	12.686	12.808	14.653	15.004	14.665
2.50e+05	11.473	11.760	11.862	12.518	13.350	13.379	13.779	14.920
2.00e+05	11.139	12.265	12.174	12.568	13.296	13.889	14.272	14.562
1.50e+05	11.480	11.847	12.139	12.084	13.661	13.882	15.069	14.888
1.00e+05	12.123	12.007	12.688	12.663	13.709	14.514	14.808	15.552
5.00e+04	13.277	13.305	13.971	14.023	15.061	15.477	17.314	19.337
0.00e+00	16.382	16.446	18.496	18.757	19.266	18.693	19.873	21.585

Table B.12: The third of three tables detailing the percent uncertainty of the $\partial\sigma(E_\nu)/\partial(Q^2)$ results from Figure 6.17.

bin low edge	1350	1400	1450	1500	1550	1600	1650
1.30e+06	21.978	26.894	23.020	27.855	30.377	27.739	25.605
1.15e+06	22.942	22.018	25.809	21.762	23.289	22.462	25.960
1.05e+06	20.985	20.616	26.295	24.242	20.202	25.326	25.508
9.50e+05	21.590	20.685	20.954	24.246	20.556	20.645	21.885
9.00e+05	19.837	19.542	22.352	22.159	28.156		
8.50e+05	18.876	20.632	21.641	22.364	27.700	22.379	
8.00e+05	19.213	20.695	20.639	21.638	25.241	23.963	
7.50e+05	19.857	20.739	20.365	23.444	22.171	23.923	
7.00e+05	17.793	21.951	18.702	22.167	21.538	24.283	
6.50e+05	19.073	20.071	19.505	18.770	21.473	21.802	25.285
6.00e+05	17.246	17.348	19.626	20.669	23.532	19.290	24.587
5.50e+05	16.426	17.900	17.785	21.241	20.952	21.020	24.467
5.00e+05	17.020	19.260	19.344	21.050	21.323	22.179	23.441
4.50e+05	16.975	18.650	17.855	19.759	20.903	28.385	24.200
4.00e+05	16.848	18.124	17.646	18.577	19.367	21.174	22.363
3.50e+05	17.583	15.941	17.705	19.010	20.218	20.207	24.460
3.00e+05	15.657	17.321	17.602	18.753	18.601	20.352	21.525
2.50e+05	16.481	16.327	17.509	17.685	18.049	20.139	21.546
2.00e+05	15.144	16.927	18.037	17.820	19.912	20.318	23.828
1.50e+05	16.305	16.223	18.273	17.819	18.631	20.850	22.687
1.00e+05	16.308	16.789	17.662	18.513	18.823	20.548	21.797
5.00e+04	19.387	21.157	20.099	20.615	20.543	22.107	23.944
0.00e+00	24.105	24.796	25.610	25.867	24.793	27.592	26.247

Table B.13: The first of three tables detailing the $\partial\sigma(E_\nu)/\partial(KE_\mu)$ results from Figure 6.20 ($10^{-41}\text{cm}^2/\text{MeV}$).

bin low edge	500	600	650	700	750	800	850	900
550							0.509	1.250
500						0.517	1.291	2.650
450					0.411	1.173	2.431	4.633
400				0.361	1.046	2.293	4.376	7.084
350				1.082	2.116	4.401	6.895	8.378
300		0.330	1.026	2.187	4.395	6.299	7.930	9.218
250	0.174	0.960	2.031	4.007	6.264	7.921	8.586	9.411
200	0.541	1.864	4.109	6.129	7.794	8.542	9.231	9.298
150	1.293	3.705	5.805	7.722	8.623	9.272	9.255	8.877
100	2.298	5.533	7.364	8.330	8.824	8.741	8.129	7.634
50	4.049	6.906	7.837	7.581	7.371	6.575	5.902	5.402
0	4.619	5.036	4.818	4.079	3.733	3.364	2.913	2.761

Table B.14: The second of three tables detailing the $\partial\sigma(E_\nu)/\partial(KE_\mu)$ results from Figure 6.20 ($10^{-41}\text{cm}^2/\text{MeV}$).

bin low edge	950	1000	1050	1100	1150	1200	1250	1300
950								1.545
900								2.694
850						1.330	2.732	4.500
800					1.272	2.607	5.073	7.500
750				1.441	2.788	4.941	7.215	8.726
700			1.218	2.563	5.080	7.222	8.260	9.030
650		1.256	2.622	4.816	7.083	8.532	9.787	9.571
600	1.226	2.639	4.966	7.181	8.828	9.129	9.004	8.972
550	2.461	4.787	6.840	8.450	9.137	9.345	8.836	9.658
500	4.606	7.248	8.544	9.405	9.185	9.172	8.911	8.836
450	7.255	8.379	9.101	9.771	9.578	8.856	8.489	8.406
400	8.753	9.596	9.791	9.262	8.707	8.870	8.711	8.088
350	9.746	10.209	9.561	9.194	8.758	7.945	8.486	7.953
300	9.406	9.917	9.884	8.718	9.002	8.040	7.970	7.719
250	9.574	9.186	9.134	8.617	8.197	7.918	7.195	7.412
200	9.346	9.078	8.572	7.958	7.738	7.196	6.500	6.229
150	8.383	8.046	7.265	7.074	6.563	6.468	5.919	5.490
100	6.699	6.737	6.181	5.702	5.471	4.836	4.446	4.143
50	4.783	4.475	4.034	3.801	3.604	3.289	3.097	2.990
0	2.583	2.554	2.463	2.220	1.955	1.932	1.848	1.837

Table B.15: The third of three tables detailing the $\partial\sigma(E_\nu)/\partial(KE_\mu)$ results from Figure 6.20 ($10^{-41}\text{cm}^2/\text{MeV}$).

bin low edge	1350	1400	1450	1500	1550	1600	1650
1200							2.123
1100				2.294	4.436	6.776	8.775
1000	0.952	2.068	4.056	6.528	8.514	9.483	9.233
950	3.048	5.045	7.303	8.862	9.693	9.839	9.499
900	5.182	7.333	9.137	9.661	10.080	9.209	9.378
850	7.152	8.763	9.344	10.488	9.668	9.052	8.868
800	8.234	9.698	9.481	9.661	9.464	8.217	9.136
750	9.600	9.546	9.525	8.046	8.281	8.905	9.057
700	8.871	9.071	9.011	8.417	8.519	8.313	7.389
650	9.798	9.033	8.721	7.838	7.828	7.155	7.110
600	9.102	9.086	8.170	8.208	7.413	7.640	6.511
550	8.592	7.388	8.586	7.598	7.937	6.935	7.209
500	8.800	7.821	8.014	7.816	7.031	7.276	6.270
450	7.895	8.599	7.281	7.636	7.417	6.176	5.680
400	7.689	7.307	7.624	7.142	6.270	6.195	6.025
350	7.203	6.738	6.856	7.277	5.849	6.655	5.821
300	7.002	6.712	6.856	6.437	6.339	5.866	5.647
250	6.645	6.334	6.419	6.054	5.484	5.113	5.040
200	6.578	5.695	5.545	5.643	4.899	4.793	4.489
150	5.209	4.716	4.924	4.515	4.238	4.407	
100	4.064	3.549	3.783	3.413	3.148		
50	3.066	2.686	2.750	2.733			
0	1.811						

Table B.16: The first of three tables detailing the percent uncertainty of the $\partial\sigma(E_\nu)/\partial(KE_\mu)$ results from Figure 6.20.

bin low edge	500	600	650	700	750	800	850	900
550							21.814	14.167
500						20.471	14.496	11.495
450					20.470	16.346	12.777	11.316
400				23.378	17.554	15.004	12.382	11.226
350				19.259	16.071	13.198	11.046	10.570
300		20.445	16.453	14.631	12.951	11.563	10.791	10.700
250	22.921	16.256	13.362	11.856	11.207	10.957	9.708	10.744
200	17.893	13.677	11.238	10.209	10.245	10.589	10.118	11.333
150	14.647	12.615	10.944	10.701	10.553	10.626	10.715	11.606
100	15.183	12.344	11.092	11.047	10.779	11.465	11.805	12.699
50	14.288	13.429	12.204	12.529	13.221	12.716	13.826	14.785
0	14.015	13.168	13.519	14.866	15.020	15.465	17.773	18.029

Table B.17: The second of three tables detailing the percent uncertainty of the $\partial\sigma(E_\nu)/\partial(KE_\mu)$ results from Figure 6.20.

bin low edge	950	1000	1050	1100	1150	1200	1250	1300
950								25.088
900								18.354
850						23.249	18.368	17.970
800					20.305	18.445	18.196	16.102
750				17.463	15.616	14.687	15.020	15.347
700			18.359	16.167	14.382	14.381	15.708	15.824
650		19.331	16.827	14.576	14.231	14.214	14.881	16.170
600	14.755	14.052	12.347	12.453	13.675	15.146	14.693	15.492
550	13.964	13.497	12.701	13.237	13.651	15.008	15.235	16.645
500	11.700	12.100	11.422	12.936	14.048	14.256	15.214	16.311
450	11.083	10.784	11.427	12.443	13.474	14.240	14.475	15.080
400	11.250	11.523	12.037	12.359	13.630	13.395	15.744	16.348
350	10.856	11.818	12.294	13.085	13.309	13.773	14.766	16.341
300	10.871	11.929	13.380	13.666	14.683	14.669	14.621	17.747
250	10.916	12.299	12.621	13.547	13.837	15.218	15.646	16.479
200	11.437	12.094	13.075	13.433	14.634	15.236	16.122	17.624
150	12.224	12.712	13.813	13.378	15.318	15.656	16.746	17.341
100	12.731	13.334	14.528	15.463	15.623	17.357	16.446	20.274
50	14.085	16.201	16.396	17.926	18.306	18.851	20.213	19.264
0	16.935	18.468	21.206	18.833	24.038	22.265	22.611	25.563

Table B.18: The third of three tables detailing the percent uncertainty of the $\partial\sigma(E_\nu)/\partial(KE_\mu)$ results from Figure 6.20.

bin low edge	1350	1400	1450	1500	1550	1600	1650
1200							24.634
1100				23.074	20.985	21.298	21.646
1000	23.891	19.533	20.394	17.988	19.658	21.897	23.351
950	19.403	18.425	19.058	20.047	20.771	21.509	26.089
900	18.676	18.665	18.778	19.799	21.205	22.769	24.365
850	16.558	17.440	18.099	19.501	23.183	22.018	25.582
800	16.233	17.253	19.369	20.555	20.766	26.124	24.908
750	16.171	18.548	18.976	20.266	20.640	25.908	28.601
700	16.548	18.139	18.668	21.089	21.155	23.280	26.921
650	18.164	18.392	19.941	20.630	22.547	21.834	25.720
600	17.235	18.404	20.070	20.500	22.442	25.160	23.165
550	17.264	19.325	20.613	21.459	23.129	21.487	24.649
500	17.485	17.718	20.167	24.692	23.273	24.402	24.598
450	16.319	18.992	18.969	21.795	21.075	21.391	21.341
400	16.514	18.135	19.914	19.832	22.522	21.994	24.511
350	18.192	17.801	17.739	20.870	20.240	22.989	24.870
300	18.205	19.205	19.962	20.205	21.778	21.352	24.541
250	17.029	19.622	20.661	19.821	22.183	24.656	28.373
200	17.466	16.664	18.785	21.373	23.937	23.150	21.099
150	20.342	20.105	19.694	22.805	23.250	23.892	
100	20.105	22.192	23.041	25.924	25.396		
50	22.852	23.824	26.277	25.495			
0	24.089						

Table B.19: The first of three tables detailing the $\partial\sigma(E_\nu)/\partial(\cos(\theta_{\mu,\nu}))$ results from Figure 6.23 (10^{-38}cm^2).

bin low edge	500	600	650	700	750	800	850	900
0.95	0.736	1.353	1.983	2.548	3.204	4.194	5.314	6.289
0.90	0.868	1.607	2.116	2.811	3.732	4.442	5.307	6.508
0.85	0.811	1.491	2.058	2.720	3.315	4.246	4.925	6.217
0.80	0.743	1.429	1.927	2.652	3.157	3.591	4.365	5.319
0.75	0.694	1.266	1.857	2.131	2.628	3.401	3.797	4.794
0.70	0.684	1.173	1.703	2.260	2.739	3.324	3.766	4.499
0.65	0.591	1.124	1.676	2.031	2.639	2.861	3.264	3.853
0.60	0.563	1.207	1.448	1.912	2.346	2.702	3.021	3.391
0.55	0.560	1.095	1.439	1.743	2.245	2.506	2.836	3.059
0.50		0.913	1.379	1.696	1.859	2.200	2.515	2.783
0.45		0.900	1.206	1.578	1.728	1.911	2.337	2.461
0.40		0.810	1.036	1.490	1.722	1.983	1.943	2.409
0.35		0.720	1.030	1.273	1.620	1.986	2.199	2.294
0.30		0.706	0.989	1.049	1.480	1.690	1.976	1.850
0.25			0.890	1.165	1.308	1.421	1.802	1.868
0.20			0.838	1.024	1.202	1.389	1.449	1.612
0.15			0.748	0.927	1.123	1.248	1.584	1.449
0.10			0.772	0.846	1.130	1.286	1.361	1.420
0.05			0.724	0.752	1.056	1.112	1.253	1.120
0.00			0.592	0.768	0.984	1.143	1.207	1.282
-0.05			0.640	0.840	0.880	1.050	1.033	1.146
-0.10				0.723	0.813	0.856	1.008	1.030
-0.20		0.459	0.527	0.643	0.822	0.837	0.857	0.942
-0.30			0.469	0.505	0.664	0.807	0.780	0.873
-0.40			0.432	0.489	0.589	0.653	0.649	0.744
-0.50			0.421	0.452	0.493	0.581	0.619	0.669
-0.60			0.370	0.429	0.488	0.553	0.537	0.526
-0.80		0.226	0.324	0.349	0.385	0.427	0.466	0.463
-1.00			0.195	0.226	0.246	0.246	0.287	0.273

Table B.20: The second of three tables detailing the $\partial\sigma(E_\nu)/\partial(\cos(\theta_{\mu,\nu}))$ results from Figure 6.23 (10^{-38}cm^2).

bin low edge	950	1000	1050	1100	1150	1200	1250	1300
0.95	7.893	9.056	10.407	11.558	13.791	14.901	16.715	18.160
0.90	7.139	8.579	9.616	10.855	12.143	12.843	14.171	15.972
0.85	6.542	7.825	8.589	9.913	10.571	11.646	12.665	13.455
0.80	6.071	7.375	7.663	8.248	8.470	9.627	10.068	11.830
0.75	5.424	6.022	6.636	7.272	7.572	8.445	8.597	9.785
0.70	4.939	5.775	5.868	6.498	6.764	7.267	7.695	7.761
0.65	4.630	4.642	4.922	5.483	5.598	5.919	6.307	6.455
0.60	3.914	4.263	4.942	5.215	5.098	5.559	5.142	5.512
0.55	3.543	3.959	3.993	4.097	4.236	4.221	4.243	4.728
0.50	3.200	3.633	3.842	3.521	3.841	3.304	4.141	4.037
0.45	2.836	2.647	3.202	3.173	3.088	3.708	3.290	3.196
0.40	2.912	2.894	3.075	2.824	3.047	3.363	2.964	3.045
0.35	2.417	2.519	2.786	2.691	2.791	2.727	2.907	2.788
0.30	2.070	2.325	2.357	2.159	2.447	2.359	2.497	2.398
0.25	1.864	1.910	2.047	2.154	2.286	1.791	2.176	1.873
0.20	1.884	1.689	1.881	1.935	1.889	2.087	2.120	1.932
0.15	1.524	1.696	1.640	1.894	1.641	1.551	1.620	1.830
0.10	1.392	1.634	1.587	1.726	1.468	1.486	1.507	1.710
0.05	1.343	1.522	1.405	1.507	1.513	1.487	1.390	
0.00	1.170	1.532	1.299	1.201	1.282	1.156		
-0.05	1.251	1.175	1.155	1.190	1.132	1.059		
-0.10	1.052	1.139	1.184	1.123	1.003	1.066		
-0.20	0.881	1.032	0.978	0.996	0.956	0.913	0.938	0.869
-0.30	0.838	0.912	0.830	0.824	0.838	0.714	0.708	0.714
-0.40	0.709	0.759	0.679	0.680	0.689	0.679	0.647	
-0.50	0.639	0.609	0.593	0.529	0.727	0.591		
-0.60	0.558	0.561	0.536	0.514				
-0.80	0.454	0.435	0.460	0.420	0.423	0.397	0.361	0.314
-1.00	0.293	0.267	0.247	0.196	0.235	0.303		

Table B.21: The third of three tables detailing the $\partial\sigma(E_\nu)/\partial(\cos(\theta_{\mu,\nu}))$ results from Figure 6.23 (10^{-38}cm^2).

bin low edge	1350	1400	1450	1500	1550	1600	1650
0.95	20.684	21.727	24.874	27.900	31.365	32.930	36.202
0.90	17.304	18.903	21.093	23.509	23.495	25.895	27.000
0.85	15.393	15.876	16.993	16.632	18.979	19.791	21.329
0.80	11.925	12.528	13.173	13.017	13.954	14.749	15.485
0.75	9.697	9.733	10.479	10.183	11.242	11.294	10.970
0.70	8.028	8.217	9.028	9.402	9.414	8.335	8.933
0.65	6.212	6.331	6.684	7.701	6.721	7.342	6.973
0.60	5.415	5.754	5.936	5.993	5.825	5.454	6.109
0.55	4.859	5.092	4.840	4.856	4.868	5.345	4.412
0.50	4.056	3.626	3.769	3.990	3.997	4.298	
0.45	3.277	3.377	3.202	3.795	3.165		
0.40	2.978	2.799	3.113	3.034			
0.35	2.542	2.827	2.875		2.426		
0.30	2.307	2.336	1.943				
0.25	2.055	2.145					
0.20	1.936	1.989					
0.15	1.589	1.619					
0.10	1.618						
-0.20	0.851						
-0.30	0.800						

Table B.22: The first of three tables detailing the percent uncertainty of the $\partial\sigma(E_\nu)/\partial(\cos(\theta_{\mu,\nu}))$ results from Figure 6.23.

bin low edge	500	600	650	700	750	800	850	900
0.95	25.918	24.595	23.772	22.510	20.909	19.174	17.633	16.622
0.90	20.028	18.144	16.955	17.502	15.846	14.587	13.832	12.658
0.85	20.724	17.406	16.195	15.000	14.145	13.873	13.503	12.095
0.80	16.526	15.737	13.479	13.992	13.157	12.737	11.731	11.277
0.75	15.493	14.457	13.962	14.648	12.581	11.951	11.730	11.177
0.70	15.000	14.375	13.747	11.900	11.734	11.556	11.737	12.771
0.65	15.428	14.222	12.964	11.217	11.603	10.743	10.680	11.698
0.60	16.290	12.769	14.419	12.337	12.624	12.046	12.306	12.066
0.55	15.096	13.321	13.311	12.530	13.254	11.485	13.023	13.288
0.50		14.472	14.179	12.973	12.772	11.894	11.679	13.217
0.45		15.042	12.974	12.288	12.266	14.173	12.273	13.262
0.40		15.994	13.105	12.615	11.601	13.314	12.892	14.020
0.35		13.434	14.185	13.755	14.299	14.556	14.079	14.013
0.30		17.402	15.385	15.110	12.340	13.916	14.510	16.109
0.25			14.910	14.206	15.436	13.686	13.393	15.617
0.20			14.546	13.870	13.136	13.496	14.772	15.788
0.15			15.747	17.038	14.020	13.226	14.449	14.484
0.10			17.541	14.732	15.404	15.532	13.716	16.141
0.05			16.348	15.625	13.203	16.113	15.176	18.602
0.00			17.401	15.764	18.178	17.372	17.761	16.177
-0.05			18.963	20.048	16.777	14.657	19.936	18.417
-0.10				16.265	16.682	16.384	16.413	21.818
-0.20		24.322	15.189	17.270	19.201	14.380	14.799	17.317
-0.30			14.663	15.247	15.777	16.183	14.677	14.772
-0.40			15.754	18.690	16.912	17.134	13.787	19.794
-0.50			21.168	24.121	18.505	15.894	16.832	17.872
-0.60			20.260	20.817	16.002	18.148	21.341	16.970
-0.80		19.884	19.082	21.025	19.029	20.291	21.595	16.548
-1.00			19.708	27.104	17.329	20.127	22.905	19.328

Table B.23: The second of three tables detailing the percent uncertainty of the $\partial\sigma(E_\nu)/\partial(\cos(\theta_{\mu,\nu}))$ results from Figure 6.23.

bin low edge	950	1000	1050	1100	1150	1200	1250	1300
0.95	16.151	16.118	16.761	16.191	16.607	16.269	17.229	18.398
0.90	12.330	12.351	12.531	12.329	13.470	13.655	14.619	14.799
0.85	11.898	11.807	11.847	12.414	13.103	13.768	14.035	14.280
0.80	12.070	11.682	12.610	12.245	13.067	13.798	14.483	15.111
0.75	11.472	11.658	11.980	12.395	13.370	14.210	15.528	15.365
0.70	12.120	12.861	12.728	12.782	13.619	14.668	15.921	15.090
0.65	11.201	12.963	13.057	13.547	13.663	14.461	15.400	16.387
0.60	12.354	12.782	13.336	13.656	15.294	15.665	15.958	15.678
0.55	13.597	12.983	13.715	14.394	15.552	15.352	15.512	17.001
0.50	13.023	12.945	14.235	14.260	14.829	16.121	17.476	18.045
0.45	12.313	13.657	14.201	13.209	15.860	15.351	16.510	17.583
0.40	13.329	14.329	15.497	15.108	15.754	18.836	16.681	17.570
0.35	14.119	15.303	16.760	15.957	19.043	18.453	18.170	19.584
0.30	14.704	16.658	15.273	15.096	16.958	17.653	16.499	18.858
0.25	14.207	15.130	17.120	17.583	16.668	20.766	17.763	21.763
0.20	16.555	16.921	16.521	18.155	18.713	19.442	21.198	24.138
0.15	16.182	18.681	18.421	16.923	18.137	19.027	20.468	25.423
0.10	14.540	21.048	16.547	21.392	21.825	25.132	21.684	21.836
0.05	16.397	16.876	17.583	17.486	18.642	23.977	20.916	
0.00	17.931	18.538	16.133	17.559	18.340	22.732		
-0.05	18.162	18.799	19.726	19.414	21.007	21.290		
-0.10	17.657	18.646	18.793	20.442	21.021	22.285		
-0.20	16.112	15.326	17.271	17.015	18.034	19.033	21.209	28.795
-0.30	16.215	15.725	17.593	17.784	19.288	18.615	19.384	22.032
-0.40	17.383	16.331	17.754	18.212	19.571	24.366	20.528	
-0.50	17.457	17.995	19.044	18.385	21.251	24.468		
-0.60	16.640	16.978	24.731	25.479				
-0.80	17.783	18.270	19.468	18.319	22.779	20.362	23.645	23.026
-1.00	19.871	21.797	22.559	20.772	23.566	27.009		

Table B.24: The third of three tables detailing the percent uncertainty of the $\partial\sigma(E_\nu)/\partial(\cos(\theta_{\mu,\nu}))$ results from Figure 6.23.

bin low edge	1350	1400	1450	1500	1550	1600	1650
0.95	19.333	20.564	20.338	19.925	19.862	21.926	22.661
0.90	15.559	15.451	17.304	17.489	18.974	19.863	20.450
0.85	15.626	16.435	17.565	18.054	18.514	20.024	21.840
0.80	16.049	16.564	17.124	18.058	19.092	20.099	21.960
0.75	16.446	18.260	18.028	19.434	19.198	19.792	24.192
0.70	17.590	17.251	18.085	19.922	20.007	20.413	22.092
0.65	15.889	19.634	18.991	19.574	20.619	20.264	21.735
0.60	17.968	18.925	19.325	20.983	20.704	22.228	23.519
0.55	17.130	18.841	21.573	20.753	25.525	22.817	27.837
0.50	20.370	20.596	20.545	22.374	21.545	22.379	
0.45	17.699	18.284	20.715	28.177	28.857		
0.40	19.524	25.766	20.831	24.689			
0.35	19.442	20.856	22.003		25.084		
0.30	20.626	18.132	20.453				
0.25	20.937	20.960					
0.20	27.180	25.640					
0.15	22.366	23.950					
0.10	24.535						
-0.20	27.136						
-0.30	23.038						

Table B.25: The first of three tables detailing the $\partial\sigma(E_\nu)/\partial(KE_\pi)$ results from Figure 6.26 ($10^{-41}\text{cm}^2/\text{MeV}$).

bin low edge	500	600	650	700	750	800	850	900
375						1.590	1.962	2.439
350					1.319	1.922	2.351	3.098
325					1.965	2.726	3.398	4.219
300				1.691	2.708	3.807	4.305	5.023
275			1.616	2.784	3.700	4.608	5.459	6.779
250		1.374	2.413	3.431	4.741	5.595	6.621	7.504
225	0.693	2.392	3.364	4.435	5.612	6.670	7.855	8.666
200	1.398	3.189	4.311	5.755	7.110	8.558	9.519	10.259
175	1.928	3.840	5.241	6.365	8.374	9.788	10.226	11.431
150	2.616	5.295	6.952	8.032	8.973	10.084	11.637	12.902
125	3.382	5.741	7.277	8.761	10.635	11.282	12.445	14.847
100	3.832	6.600	8.977	10.614	11.758	12.835	14.452	15.746
75	4.272	7.083	9.075	10.580	12.336	13.625	14.848	16.074
50	3.764	5.923	7.517	8.597	9.819	11.032	12.080	13.418
25	2.216	3.533	4.422	5.079	5.821	6.681	7.401	8.001
0	0.672	1.038	1.332	1.683	1.712	2.144	2.529	2.588

Table B.26: The second of three tables detailing the $\partial\sigma(E_\nu)/\partial(KE_\pi)$ results from Figure 6.26 (10^{-41}cm^2/MeV).

bin low edge	950	1000	1050	1100	1150	1200	1250	1300
375	2.807	3.729	4.613	5.119	5.474	5.555	6.216	6.772
350	3.719	4.562	5.560	5.699	6.404	7.169	6.933	7.490
325	5.355	5.579	6.245	7.181	7.165	7.881	8.053	9.008
300	5.931	6.991	7.613	8.511	8.474	9.033	10.227	11.246
275	7.644	8.140	8.691	9.044	9.578	10.836	10.854	12.039
250	8.433	9.887	10.313	11.450	11.928	11.503	12.015	13.169
225	9.765	11.208	11.442	12.435	13.175	12.978	13.662	14.545
200	11.602	12.413	12.135	13.247	14.967	14.207	15.192	15.918
175	12.424	13.333	13.171	14.999	15.461	15.540	15.948	16.968
150	13.762	15.290	16.294	15.760	16.357	16.095	17.667	18.248
125	15.868	17.410	17.552	17.974	18.422	19.646	19.715	21.049
100	17.015	18.403	19.043	20.238	20.261	21.091	22.012	22.330
75	16.622	18.101	19.469	19.059	19.003	20.611	20.774	21.976
50	13.832	15.150	14.467	15.177	16.017	16.623	17.784	16.778
25	8.898	8.988	9.980	9.527	10.241	10.187	10.257	11.478
0	2.544	3.034	3.141	3.626	3.476	3.352	3.603	3.953

Table B.27: The third of three tables detailing the $\partial\sigma(E_\nu)/\partial(KE_\pi)$ results from Figure 6.26 (10^{-41}cm^2/MeV).

bin low edge	1350	1400	1450	1500	1550	1600	1650
375	7.382	7.715	8.186	8.737	9.026	10.002	
350	8.476	8.050	9.688	9.862	10.554	9.662	11.594
325	9.576	10.368	11.344	11.416	12.168	11.746	12.591
300	11.119	11.076	11.951	12.491	14.079	13.195	15.057
275	11.293	12.349	14.624	13.722	14.552	15.562	13.816
250	13.083	13.815	14.339	15.168	17.079	16.521	17.585
225	15.674	16.244	15.628	16.630	18.085	17.916	17.969
200	16.539	17.021	18.070	18.233	18.278	20.475	19.120
175	18.105	17.403	20.113	20.715	19.250	20.015	22.985
150	18.693	20.371	19.131	20.486	22.697	23.181	20.613
125	20.671	22.141	21.384	22.833	24.818	24.999	25.691
100	22.771	23.218	25.310	25.909	25.920	27.105	27.879
75	22.844	21.720	23.506	25.308	24.698	22.489	25.582
50	17.516	17.741	18.878	19.239	18.985	19.411	18.558
25	12.342	11.186	11.262	11.725	11.914	13.108	12.585
0	3.958	4.244	4.552	4.126			

Table B.28: The first of three tables detailing the percent uncertainty of the $\partial\sigma(E_\nu)/\partial(KE_\pi)$ results from Figure 6.26.

bin low edge	500	600	650	700	750	800	850	900
375						21.601	19.008	19.524
350					22.864	19.517	18.002	18.422
325					19.170	18.575	18.088	17.753
300				18.722	17.018	18.050	17.500	17.131
275			19.825	17.251	17.059	16.780	15.712	16.843
250		19.728	18.022	17.248	15.496	15.066	14.467	15.569
225	19.683	17.080	16.679	16.090	15.162	14.447	14.349	14.075
200	17.621	16.495	15.726	15.102	13.683	13.654	14.153	13.596
175	16.787	17.523	15.966	14.121	12.494	12.451	12.050	12.174
150	15.848	15.065	13.712	12.793	12.761	11.722	11.167	11.748
125	16.587	14.906	11.554	10.881	11.366	10.926	10.460	10.707
100	14.389	12.125	10.495	9.437	9.654	9.601	8.720	9.399
75	11.841	12.041	10.078	10.264	10.170	11.338	10.498	11.757
50	13.317	11.947	11.163	12.061	12.380	11.530	12.725	12.421
25	12.117	13.586	11.881	12.028	14.278	12.744	13.053	13.268
0	14.695	20.311	18.489	16.527	14.231	17.868	17.317	19.245

Table B.29: The second of three tables detailing the percent uncertainty of the $\partial\sigma(E_\nu)/\partial(KE_\pi)$ results from Figure 6.26.

bin low edge	950	1000	1050	1100	1150	1200	1250	1300
375	17.763	19.581	18.866	19.561	20.294	19.485	20.811	21.421
350	17.920	17.461	19.500	18.672	19.920	19.296	18.635	20.020
325	17.508	17.171	16.985	18.162	19.657	19.289	19.797	18.987
300	16.228	16.292	16.877	16.942	19.185	20.000	18.574	19.463
275	15.317	16.145	17.553	17.207	19.082	17.663	17.233	18.093
250	16.009	15.866	15.822	15.914	16.356	16.887	17.759	16.956
225	14.344	14.882	14.690	14.110	15.508	15.640	17.081	16.021
200	13.569	13.426	13.915	13.953	15.477	15.014	15.333	15.713
175	11.794	12.682	13.373	13.562	13.815	13.590	14.258	16.099
150	11.623	11.587	12.861	12.578	12.943	13.706	14.328	14.092
125	10.290	10.706	11.859	11.581	13.003	12.963	13.704	14.079
100	9.530	11.541	11.070	11.088	12.035	13.095	13.364	14.574
75	12.201	12.083	13.504	13.193	13.315	13.710	14.452	13.813
50	11.915	13.339	13.237	13.192	15.072	14.092	13.383	14.324
25	11.858	13.529	13.486	14.041	13.686	13.168	13.524	14.882
0	12.760	16.133	15.361	15.523	17.562	16.628	16.376	18.358

Table B.30: The third of three tables detailing the percent uncertainty of the $\partial\sigma(E_\nu)/\partial(KE_\pi)$ results from Figure 6.26.

bin low edge	1350	1400	1450	1500	1550	1600	1650
375	21.273	22.409	22.806	25.214	25.510	25.306	
350	23.113	23.409	21.402	24.047	26.875	28.068	26.796
325	21.422	21.154	21.428	21.699	21.482	25.873	24.632
300	19.168	22.221	23.184	20.896	21.083	22.785	26.674
275	18.455	18.962	19.311	22.834	20.254	23.084	23.972
250	17.151	18.556	21.664	19.989	22.348	20.635	23.055
225	16.377	17.409	20.733	21.791	17.779	20.748	21.429
200	17.793	17.073	17.002	18.785	20.846	20.642	20.019
175	16.065	16.038	16.825	18.009	18.383	21.121	22.375
150	16.040	17.421	17.366	18.586	18.324	19.809	19.038
125	15.370	17.486	16.676	17.071	18.508	17.853	21.032
100	15.257	15.204	16.480	16.700	18.098	19.483	19.061
75	14.922	15.815	15.817	17.967	18.163	18.160	21.134
50	15.942	15.953	15.389	17.699	17.418	17.527	20.487
25	14.569	14.991	16.091	17.293	17.104	20.353	19.313
0	17.480	22.051	19.049	27.068			

Table B.31: The first of three tables detailing the $\partial\sigma(E_\nu)/\partial(\cos(\theta_{\pi,\nu}))$ results from Figure 6.29 (10^{-38}cm^2).

bin low edge	500	600	650	700	750	800	850	900
0.95	0.887	1.328	1.840	2.327	2.865	3.606	4.251	4.971
0.90	0.685	1.406	1.842	2.239	2.824	3.469	3.755	4.610
0.85	0.650	1.342	1.742	2.206	3.070	3.492	3.968	4.723
0.80	0.587	1.113	1.546	2.008	2.734	3.300	3.492	4.364
0.75	0.570	1.197	1.534	2.001	2.591	3.075	3.411	3.924
0.70	0.563	1.077	1.503	1.937	2.584	3.056	3.737	3.849
0.65	0.559	1.073	1.474	1.905	2.286	2.892	3.269	3.762
0.60	0.530	1.033	1.431	1.801	2.105	2.631	2.951	3.449
0.55	0.488	0.921	1.288	1.655	1.946	2.393	2.659	3.131
0.50	0.479	0.914	1.336	1.630	2.050	2.237	2.665	2.997
0.45	0.470	0.819	1.049	1.639	1.832	2.068	2.356	2.716
0.40	0.418	0.812	1.238	1.285	1.578	1.935	2.432	2.414
0.35		0.782	1.037	1.299	1.545	1.819	1.993	2.347
0.30		0.673	0.988	1.109	1.489	1.873	2.027	2.039
0.25		0.735	0.960	1.166	1.330	1.591	1.848	2.088
0.20		0.773	0.936	1.074	1.351	1.461	1.726	2.018
0.15		0.612	0.822	1.071	1.178	1.500	1.749	1.860
0.10		0.577	0.883	0.972	1.204	1.368	1.474	1.687
0.05			0.784	0.899	1.066	1.291	1.354	1.675
0.00			0.708	0.912	1.097	1.149	1.258	1.555
-0.05			0.595	0.849	1.029	1.059	1.249	1.491
-0.10			0.645	0.776	0.884	0.989	1.139	1.319
-0.15			0.620	0.640	0.833	0.975	1.100	1.203
-0.20			0.602	0.667	0.803	0.902	0.981	1.174
-0.25			0.567	0.681	0.777	0.843	0.988	0.994
-0.30			0.579	0.642	0.786	0.704	0.807	1.079
-0.35				0.555	0.676	0.739	0.935	0.901
-0.40				0.530	0.627	0.725	0.747	0.866
-0.45				0.391	0.601	0.617	0.717	0.769
-0.50				0.480	0.474	0.610	0.788	0.776
-0.55					0.506	0.594	0.609	0.759
-0.60				0.462		0.470	0.553	0.663
-0.65					0.476	0.544	0.609	0.621
-0.70					0.477	0.418	0.506	0.580
-0.75						0.497	0.542	0.594
-0.80					0.364	0.439	0.483	0.500
-0.85							0.495	
-0.90						0.421	0.428	0.436
-0.95								0.426

Table B.32: The second of three tables detailing the $\partial\sigma(E_\nu)/\partial(\cos(\theta_{\pi,\nu}))$ results from Figure 6.29 (10^{-38}cm^2).

bin low edge	950	1000	1050	1100	1150	1200	1250	1300
0.95	5.386	6.335	6.708	7.464	7.978	8.578	9.153	9.487
0.90	5.426	6.273	6.528	7.083	7.901	8.474	8.418	9.656
0.85	5.090	5.915	6.304	7.016	7.422	7.741	8.185	8.960
0.80	5.013	5.745	6.324	6.441	6.840	7.710	8.240	7.999
0.75	4.877	5.369	5.767	6.171	6.378	7.059	6.978	7.638
0.70	4.496	4.854	5.188	5.520	5.852	6.023	6.599	7.369
0.65	4.190	4.252	4.996	5.142	5.454	5.796	5.928	6.908
0.60	3.786	4.431	4.431	5.036	5.165	5.245	5.424	6.334
0.55	3.479	3.844	4.161	4.388	4.442	5.027	5.406	5.637
0.50	3.222	3.829	3.726	4.164	4.308	4.343	4.816	5.179
0.45	2.849	3.465	3.645	3.954	4.067	4.169	4.270	4.720
0.40	2.905	2.953	3.308	3.287	3.654	3.732	3.894	4.173
0.35	2.550	2.914	3.138	2.990	3.455	3.515	3.997	4.018
0.30	2.644	2.742	3.015	3.126	3.029	3.321	3.532	3.832
0.25	2.160	2.672	2.705	2.752	3.094	3.001	3.124	3.237
0.20	2.164	2.400	2.597	2.782	2.743	2.541	2.915	2.967
0.15	1.838	2.225	2.262	2.484	2.434	2.519	2.974	3.031
0.10	1.787	1.929	2.051	2.178	2.510	2.350	2.464	2.650
0.05	1.785	1.606	1.975	1.982	2.255	2.259	2.310	2.667
0.00	1.547	1.670	1.848	1.777	2.241	2.065	2.257	2.344
-0.05	1.448	1.734	1.679	1.818	1.795	2.091	2.002	2.121
-0.10	1.389	1.467	1.533	1.586	1.527	1.680	1.660	1.756
-0.15	1.378	1.428	1.336	1.650	1.510	1.764	1.662	1.942
-0.20	1.138	1.430	1.394	1.350	1.485	1.623	1.525	1.715
-0.25	1.171	1.368	1.274	1.430	1.284	1.455	1.432	1.652
-0.30	1.194	1.181	1.196	1.178	1.575	1.315	1.670	1.141
-0.35	1.122	1.098	1.108	1.153	1.260	1.165	1.346	1.423
-0.40	0.946	0.919	1.069	1.078	1.130	1.154	1.232	1.394
-0.45	0.843	0.977	0.958	0.951	1.165	1.056	1.286	1.034
-0.50	0.847	0.796	0.857	1.097	0.934	1.113	1.029	
-0.55	0.759	0.783	0.818	0.873	0.947	0.895		
-0.60	0.679	0.679	0.874	0.784	0.828			
-0.65	0.668	0.764	0.825	0.746	0.958			
-0.70	0.617	0.720	0.690	0.831	0.829			
-0.75	0.578	0.635	0.616	0.629				
-0.80	0.562	0.642	0.613					
-0.85	0.528	0.520						
-1.00	0.462							

Table B.33: The third of three tables detailing the $\partial\sigma(E_\nu)/\partial(\cos(\theta_{\pi,\nu}))$ results from Figure 6.29 (10^{-38}cm^2).

bin low edge	1350	1400	1450	1500	1550	1600	1650
0.95	10.482	11.259	11.522	12.819	12.595	13.816	13.895
0.90	10.167	11.365	11.442	12.033	11.685	12.689	12.633
0.85	9.614	9.773	10.377	11.595	11.068	11.429	12.468
0.80	9.134	9.412	9.506	11.218	10.101	10.871	10.456
0.75	8.179	8.147	9.430	9.529	9.380	10.333	10.111
0.70	7.656	7.505	7.840	8.673	9.594	8.746	9.294
0.65	6.818	7.049	7.470	7.691	8.962	8.560	8.748
0.60	5.970	6.602	7.414	7.036	7.782	7.775	8.290
0.55	5.976	5.618	6.734	6.765	6.719	7.502	7.634
0.50	5.087	4.861	6.266	6.126	6.675	6.769	6.964
0.45	4.893	5.238	5.389	5.575	6.382	5.899	5.697
0.40	4.480	4.566	4.902	4.818	6.151	6.020	5.357
0.35	3.919	3.830	5.127	4.610	4.608	5.057	5.049
0.30	3.767	4.030	4.136	4.823	4.269	4.318	
0.25	3.738	3.586	3.391	3.801	4.567	4.856	
0.20	3.223	3.424	3.374	3.804	3.803		
0.15	3.319	3.359	3.535	3.549	3.656	3.947	
0.10	3.149	3.007	3.016	2.795			
0.05	2.756	2.699	2.667	3.169			
0.00	2.461	2.472	2.801				
-0.05	2.214	2.363	2.151				
-0.10	1.912	2.200	2.429				
-0.15	1.829	1.809					
-0.20	1.790	1.848	1.694				
-0.25	1.637	1.571					
-0.45	1.180						

Table B.34: The first of three tables detailing the percent uncertainty of the $\partial\sigma(E_\nu)/\partial(\cos(\theta_{\pi,\nu}))$ results from Figure 6.29.

bin low edge	500	600	650	700	750	800	850	900
0.95	20.800	21.207	19.474	19.201	18.895	18.122	16.699	16.917
0.90	18.967	18.988	16.236	17.222	16.654	16.545	15.227	15.027
0.85	19.489	16.300	15.433	14.651	13.409	14.128	14.058	13.898
0.80	16.290	16.580	15.040	13.471	13.525	13.348	12.640	13.502
0.75	18.086	14.676	13.157	13.043	13.151	12.602	12.690	12.223
0.70	17.478	14.420	13.150	13.853	11.450	13.207	12.237	12.106
0.65	16.210	15.517	13.913	14.038	12.978	12.215	12.977	13.077
0.60	17.359	16.770	13.955	13.918	12.847	12.259	12.652	12.939
0.55	17.660	14.355	14.581	14.988	13.483	11.948	13.246	14.258
0.50	16.180	19.315	15.304	15.303	12.986	12.177	11.917	12.947
0.45	16.298	17.041	13.759	13.166	14.087	13.851	12.895	14.462
0.40	16.384	16.523	14.726	14.938	14.346	13.936	12.477	12.441
0.35		15.984	16.993	14.887	14.696	14.388	12.559	13.042
0.30		18.035	13.963	14.068	14.125	14.897	13.739	13.116
0.25		14.755	14.470	18.782	14.232	14.024	11.309	13.558
0.20		16.824	15.679	13.807	13.371	12.336	13.718	12.535
0.15		15.882	14.697	13.824	12.867	12.684	11.958	13.124
0.10		17.732	16.090	13.997	14.247	14.467	11.671	13.540
0.05			14.677	16.455	13.869	11.261	12.437	13.194
0.00			14.587	12.530	15.142	14.072	12.761	13.906
-0.05			17.156	13.852	14.964	12.781	13.815	12.738
-0.10			16.273	14.778	13.884	13.875	14.524	14.786
-0.15			17.051	14.128	13.320	18.161	12.101	13.920
-0.20			15.636	15.881	14.497	15.319	12.027	14.941
-0.25			17.653	15.577	13.628	14.670	14.420	15.747
-0.30			17.725	14.969	15.136	14.855	13.553	18.395
-0.35				16.769	14.895	13.224	17.218	13.834
-0.40				18.577	15.322	13.683	14.038	13.010
-0.45				17.709	15.700	18.373	13.347	13.392
-0.50				18.763	14.369	16.229	16.960	15.573
-0.55					14.330	15.524	16.303	16.908
-0.60				16.402		19.220	16.240	14.162
-0.65					16.512	14.449	16.737	15.484
-0.70					17.846	15.541	14.645	17.339
-0.75						18.444	15.351	17.676
-0.80					16.701	20.162	16.938	18.860
-0.85							17.819	
-0.90						20.697	20.327	19.404
-0.95								21.636

Table B.35: The second of three tables detailing the percent uncertainty of the $\partial\sigma(E_\nu)/\partial(\cos(\theta_{\pi,\nu}))$ results from Figure 6.29.

bin low edge	950	1000	1050	1100	1150	1200	1250	1300
0.95	16.708	16.332	16.857	16.282	16.860	18.255	19.049	19.484
0.90	14.562	15.800	15.481	15.824	15.989	17.203	16.919	17.619
0.85	13.181	13.528	14.148	14.607	15.282	15.273	15.891	16.903
0.80	12.614	13.820	14.173	14.063	15.363	15.481	16.689	16.648
0.75	12.995	13.384	13.331	13.425	15.449	15.760	15.831	16.972
0.70	12.674	13.654	13.664	13.292	14.814	15.127	15.741	16.867
0.65	12.728	12.958	13.413	14.498	14.998	15.428	16.220	15.801
0.60	12.471	13.096	13.992	13.686	15.680	15.814	16.033	17.309
0.55	12.930	13.163	14.563	14.060	14.792	15.766	15.561	17.585
0.50	13.136	12.517	13.769	13.052	14.162	16.276	15.750	16.611
0.45	13.590	11.135	13.097	14.075	15.425	15.383	15.358	16.141
0.40	12.836	13.331	13.686	15.040	15.398	15.589	15.712	16.498
0.35	13.257	13.460	14.270	15.470	15.359	16.076	15.815	19.169
0.30	15.411	13.411	13.128	13.719	13.742	15.095	19.068	16.496
0.25	12.943	12.821	13.778	13.467	15.147	16.463	14.505	15.669
0.20	12.811	13.807	13.920	13.908	13.594	16.702	16.864	16.411
0.15	15.168	13.892	13.516	13.479	13.714	14.988	16.018	16.652
0.10	14.084	13.284	13.033	14.087	14.767	15.174	15.536	16.255
0.05	14.049	11.838	13.075	13.315	14.339	15.961	17.466	17.845
0.00	13.379	13.650	13.555	13.650	13.833	16.616	16.785	14.872
-0.05	12.969	13.273	13.724	14.026	14.510	14.720	17.025	17.504
-0.10	13.266	12.765	16.012	13.431	14.936	16.789	17.301	19.092
-0.15	12.327	13.651	14.994	15.040	15.394	15.891	15.679	19.681
-0.20	14.157	13.334	14.936	14.348	14.537	16.398	17.113	20.666
-0.25	15.576	13.688	14.851	13.932	13.563	15.138	16.701	16.304
-0.30	16.067	15.975	14.777	17.564	15.004	16.726	16.445	17.771
-0.35	14.161	16.166	14.137	16.895	17.659	16.146	18.010	20.461
-0.40	11.845	14.154	15.560	16.499	16.390	17.905	17.652	20.326
-0.45	14.068	14.059	14.144	17.359	22.326	17.681	16.023	17.035
-0.50	14.436	12.985	18.857	16.799	16.876	19.008	16.386	
-0.55	15.921	12.507	16.482	16.593	17.645	17.183		
-0.60	15.674	16.074	16.322	17.028	16.049			
-0.65	16.079	16.669	15.592	17.085	19.528			
-0.70	16.237	17.996	17.720	22.815	17.828			
-0.75	16.446	19.365	20.507	21.066				
-0.80	17.192	19.459	17.447					
-0.85	15.541	17.766						
-1.00	17.241							

Table B.36: The third of three tables detailing the percent uncertainty of the $\partial\sigma(E_\nu)/\partial(\cos(\theta_{\pi,\nu}))$ results from Figure 6.29.

bin low edge	1350	1400	1450	1500	1550	1600	1650
0.95	19.449	20.675	21.308	21.664	22.230	23.430	25.874
0.90	18.559	19.564	19.746	22.340	22.613	22.553	23.706
0.85	19.008	19.622	21.905	21.038	20.992	22.018	23.051
0.80	18.125	18.817	19.750	20.603	25.084	22.420	22.866
0.75	17.784	18.147	19.768	20.886	20.991	24.650	23.766
0.70	17.518	19.779	20.218	19.324	20.030	22.252	24.979
0.65	17.321	21.941	20.042	20.113	23.068	23.215	21.524
0.60	18.602	18.469	19.924	21.135	21.544	21.800	24.294
0.55	17.460	19.398	19.921	22.913	21.784	23.513	25.287
0.50	18.136	18.823	18.259	22.780	19.299	23.524	21.837
0.45	17.172	17.751	17.528	19.788	21.499	23.964	26.177
0.40	17.589	18.312	22.105	19.757	19.927	21.450	22.239
0.35	16.883	20.483	19.305	20.840	20.111	22.505	24.765
0.30	17.900	18.689	22.360	21.113	21.235	23.656	
0.25	17.219	19.800	20.124	18.919	20.543	25.707	
0.20	17.490	21.987	19.504	21.279	26.401		
0.15	17.851	20.238	19.969	20.539	25.499	22.012	
0.10	17.117	18.646	22.870	25.153			
0.05	18.483	17.855	19.875	23.918			
0.00	17.578	18.781	20.371				
-0.05	17.337	19.203	24.658				
-0.10	20.673	20.830	21.920				
-0.15	16.747	18.932					
-0.20	19.300	18.760	21.198				
-0.25	18.081	19.458					
-0.45	24.848						

Table B.37: The first of three tables detailing the $\partial^2\sigma/\partial(KE_\mu)\partial(\cos(\theta_{\mu,\nu}))$ results from Figure 6.32 (10^{-42}cm^2/MeV).

bin low edge	0	50	100	150	200	250	300	350
0.95	17.798	13.968	21.164	26.281	29.365	34.319	41.483	45.205
0.90	21.830	26.129	27.996	33.186	38.107	42.214	46.595	54.308
0.85	21.220	24.725	30.728	34.559	37.591	44.224	50.632	56.669
0.80	20.377	22.825	31.709	34.175	40.208	43.944	52.822	60.313
0.75	16.694	25.800	28.230	35.465	40.796	45.277	52.258	55.306
0.70	17.112	24.686	30.457	38.413	40.914	47.241	56.130	54.599
0.65	16.139	24.829	28.792	37.334	41.482	44.970	48.849	53.554
0.60	16.262	24.244	28.947	34.278	43.032	46.044	45.632	48.215
0.55	16.129	23.788	29.173	34.932	40.749	44.844	46.791	40.094
0.50	14.631	22.535	28.472	32.532	36.968	42.072	41.463	37.040
0.45	14.071	22.583	28.346	32.322	36.053	36.238	36.535	30.855
0.40	14.659	23.428	26.388	32.346	35.412	38.663	34.981	28.355
0.35	13.849	21.561	27.477	36.228	38.156	34.769	30.227	27.358
0.30	12.928	21.878	26.134	30.057	33.307	28.934	27.886	20.222
0.25	13.518	20.991	25.281	29.108	30.216	29.203	21.700	17.033
0.20	12.219	20.135	24.673	26.648	29.887	26.547	21.025	13.138
0.15	12.216	21.049	25.488	26.397	27.735	23.911	17.709	9.145
0.10	11.960	21.099	23.756	26.227	26.181	21.093	14.890	8.043
0.05	12.450	17.837	23.766	25.152	25.688	19.400	12.751	6.365
0.00	12.674	20.846	23.373	23.765	22.053	16.153	9.795	5.099
-0.05	12.150	19.586	23.252	24.252	19.009	13.294	7.181	
-0.10	11.633	19.000	22.931	21.054	17.137	11.106	5.894	
-0.20	11.676	18.404	20.568	20.001	16.109	9.864	4.876	2.448
-0.30	10.063	17.423	19.414	17.697	12.493	6.093	2.864	
-0.40	10.411	17.217	16.879	14.862	9.498	5.523	1.950	
-0.50	10.055	16.290	16.299	12.453	7.791	3.328		
-0.60	9.228	14.794	14.556	10.602	5.742	2.508		
-0.80	8.357	13.809	12.347	7.914	3.377	1.486		
-1.00	5.975	9.696	7.910	4.108	1.504			

Table B.38: The second of three tables detailing the $\partial^2\sigma/\partial(KE_\mu)\partial(\cos(\theta_{\mu,\nu}))$ results from Figure 6.32 (10^{-42}cm^2/MeV).

bin low edge	400	450	500	550	600	650	700	750
0.95	50.062	57.570	60.914	63.030	65.862	68.693	70.577	73.235
0.90	58.905	64.431	71.462	70.470	71.978	72.455	65.354	64.490
0.85	66.737	66.021	67.521	69.549	69.693	67.506	54.151	50.242
0.80	59.280	62.355	64.548	58.949	54.518	53.013	44.318	36.734
0.75	57.055	56.394	57.130	50.728	43.139	35.489	32.112	25.552
0.70	56.319	52.308	50.791	41.468	34.152	27.743	21.773	14.918
0.65	47.087	43.503	37.563	29.397	23.620	17.033	14.444	9.865
0.60	49.090	39.284	29.860	23.715	16.107	11.381	7.825	
0.55	35.430	32.490	23.624	16.098	10.471	6.228		
0.50	32.347	25.587	15.477	11.626	7.179			
0.45	25.079	17.896	12.601	8.098				
0.40	21.937	14.788	8.701	5.265				
0.35	17.001	11.995	6.821					
0.30	12.226	8.108						
0.25	10.323	6.184						
0.20	8.416							
0.15	5.710							

Table B.39: The third of three tables detailing the $\partial^2\sigma/\partial(KE_\mu)\partial(\cos(\theta_{\mu,\nu}))$ results from Figure 6.32 (10^{-42}cm^2/MeV).

bin low edge	800	850	900	950	1000	1100	1200
0.95	69.351	60.842	59.787	56.517	48.687	43.415	26.724
0.90	58.081	56.950	49.551	44.935	37.239	25.639	11.287
0.85	46.050	38.861	33.634	25.846	18.525	11.770	5.132
0.80	32.725	23.404	18.083	14.240	8.540		
0.75	18.242	13.005	9.033				
0.70	11.700	8.753					

Table B.40: The first of three tables detailing the percent uncertainty of the $\partial^2\sigma/\partial(KE_\mu)\partial(\cos(\theta_{\mu,\nu}))$ results from Figure 6.32.

bin low edge	0	50	100	150	200	250	300	350
0.95	17.996	18.718	19.846	23.435	25.199	24.280	21.122	20.058
0.90	18.488	17.231	19.710	19.034	18.817	18.467	18.316	17.124
0.85	17.909	16.867	18.360	18.534	18.457	17.230	17.381	16.388
0.80	17.482	16.954	16.877	17.489	16.912	16.223	14.718	14.893
0.75	18.243	16.243	16.988	16.308	16.394	14.959	14.807	13.831
0.70	16.620	16.900	15.300	15.669	16.043	14.986	15.124	16.306
0.65	18.683	15.481	16.708	15.857	14.306	14.161	14.676	15.051
0.60	18.118	16.341	17.159	15.934	13.888	14.057	15.072	15.161
0.55	16.072	16.340	17.222	15.037	15.169	15.348	14.933	15.037
0.50	18.106	16.595	16.371	16.427	15.400	14.519	16.506	15.705
0.45	18.800	15.690	14.765	14.591	15.711	14.661	15.370	14.925
0.40	17.134	15.441	15.397	15.260	14.997	15.660	16.777	16.408
0.35	17.005	16.049	14.855	16.377	17.671	16.213	16.496	19.219
0.30	17.577	15.581	15.303	15.215	16.631	15.852	15.645	16.652
0.25	17.583	16.122	14.761	14.611	15.382	16.261	17.325	19.068
0.20	17.995	15.677	16.306	14.944	15.732	16.648	17.434	19.007
0.15	17.236	16.454	15.170	15.345	15.748	17.824	19.641	19.267
0.10	18.402	17.394	14.911	15.140	17.172	18.373	19.498	19.637
0.05	20.004	16.405	13.268	17.333	19.057	19.094	21.752	21.587
0.00	17.251	16.275	16.144	16.010	19.025	19.172	19.469	31.547
-0.05	19.753	16.242	15.625	17.924	17.680	19.560	24.469	
-0.10	17.281	15.144	16.982	20.840	18.041	21.548	22.819	
-0.20	17.714	16.511	15.865	16.871	18.802	22.646	25.537	36.101
-0.30	16.755	15.373	15.790	17.424	17.918	20.049	24.975	
-0.40	16.064	16.165	15.451	18.329	18.248	23.338	31.433	
-0.50	18.915	17.256	15.380	19.157	20.566	22.999		
-0.60	16.343	17.269	17.120	20.896	20.283	34.666		
-0.80	14.380	17.883	20.755	19.489	20.374	24.729		
-1.00	15.156	22.598	23.703	20.256	24.138			

Table B.41: The second of three tables detailing the percent uncertainty of the $\partial^2\sigma/\partial(KE_\mu)\partial(\cos(\theta_{\mu,\nu}))$ results from Figure 6.32.

bin low edge	400	450	500	550	600	650	700	750
0.95	19.882	16.437	17.526	18.597	17.636	17.591	15.786	15.183
0.90	15.448	14.136	14.351	14.296	14.714	14.560	15.561	15.501
0.85	14.792	13.538	14.274	13.779	15.396	15.095	14.269	14.631
0.80	15.267	14.036	14.685	13.572	14.364	14.656	15.530	16.083
0.75	14.331	14.227	14.451	15.039	16.380	16.548	16.328	17.562
0.70	15.497	14.859	15.699	16.212	15.190	15.952	20.110	19.761
0.65	14.746	15.333	14.723	15.059	16.197	15.733	19.057	23.664
0.60	17.033	15.933	15.841	16.233	21.435	20.490	21.892	
0.55	14.612	17.874	19.083	17.791	23.763	27.331		
0.50	16.970	18.656	18.758	25.079	22.939			
0.45	17.546	17.822	17.585	25.201				
0.40	17.285	17.618	24.370	35.067				
0.35	21.757	23.340	25.452					
0.30	21.514	25.719						
0.25	22.044	28.761						
0.20	24.499							
0.15	22.600							

Table B.42: The third of three tables detailing the percent uncertainty of the $\partial^2\sigma/\partial(KE_\mu)\partial(\cos(\theta_{\mu,\nu}))$ results from Figure 6.32.

bin low edge	800	850	900	950	1000	1100	1200
0.95	16.621	19.487	19.344	18.284	17.675	16.207	19.763
0.90	14.620	14.986	14.215	16.774	17.411	18.902	25.094
0.85	15.476	17.286	18.232	18.897	19.718	23.582	30.520
0.80	16.468	17.215	21.763	24.733	30.434		
0.75	17.413	21.381	29.104				
0.70	23.359	30.077					

Table B.43: The first of three tables detailing the $\partial^2\sigma/\partial(KE_\pi)\partial(\cos(\theta_{\pi,\nu}))$ results from Figure 6.35 (10^{-41}cm^2/MeV).

bin low edge	0	25	50	75	100	125
0.95		1.536	2.674	3.991	5.145	6.514
0.90		1.391	2.628	4.475	5.647	6.998
0.85		1.432	3.036	4.636	6.605	7.993
0.80		1.776	3.112	4.554	6.541	8.347
0.75		1.612	3.346	5.047	7.108	9.074
0.70	0.690	1.645	3.533	5.612	7.701	9.054
0.65		1.900	3.657	6.028	8.414	9.315
0.60	0.720	1.878	3.759	6.333	8.312	9.268
0.55		1.956	3.657	6.214	8.690	9.210
0.50		2.206	4.427	7.080	8.725	8.654
0.45		2.053	4.133	6.806	8.691	9.177
0.40	0.841	2.360	4.392	7.041	8.296	8.352
0.35		2.122	4.779	6.840	8.312	8.430
0.30		2.398	4.648	7.179	8.574	7.465
0.25		2.310	4.851	7.509	8.578	7.581
0.20		2.599	4.971	7.391	8.732	7.080
0.15	0.809	2.860	5.417	7.522	8.113	7.444
0.10	0.855	2.810	5.120	7.578	7.414	6.424
0.05	0.711	2.737	5.236	7.009	7.826	6.160
0.00	0.922	2.865	5.300	7.061	7.160	5.515
-0.05	0.987	2.932	5.200	7.159	6.782	5.139
-0.10	0.848	3.072	5.029	6.855	5.902	4.461
-0.15	0.809	3.124	5.539	6.947	5.885	3.681
-0.20	0.961	3.168	5.059	6.525	5.556	3.741
-0.25	0.998	3.169	5.223	6.351	5.064	3.385
-0.30	0.969	3.275	5.133	6.223	4.800	2.857
-0.35	0.995	3.202	5.300	5.909	4.276	2.672
-0.40	1.115	3.242	5.000	5.522	3.763	2.173
-0.45	1.179	3.202	4.786	4.800	3.110	1.887
-0.50	1.097	3.285	4.944	4.517	3.340	1.769
-0.55	1.152	3.377	4.595	4.451	2.580	1.645
-0.60	1.064	3.319	4.720	3.845	2.427	1.402
-0.65	1.117	3.281	4.418	3.731	2.261	1.144
-0.70	1.166	3.178	4.177	3.312	2.213	1.128
-0.75	1.094	3.243	3.789	3.039	1.688	1.036
-0.80	1.156	3.076	3.784	2.973	1.527	1.058
-0.85	1.269	3.056	3.562	2.654	1.469	
-0.90	1.208	3.061	3.481	2.382	1.300	
-0.95	1.139	3.031	2.981	1.940	1.458	
-1.00	1.201	3.216	2.955	1.702	1.211	

Table B.44: The second of three tables detailing the $\partial^2\sigma/\partial(KE_\pi)\partial(\cos(\theta_{\pi,\nu}))$ results from Figure 6.35 ($10^{-41}\text{cm}^2/\text{MeV}$).

bin low edge	150	175	200	225	250
0.95	7.873	8.947	10.435	10.970	10.258
0.90	8.427	9.631	10.198	10.106	10.145
0.85	9.578	9.997	10.829	10.153	9.420
0.80	9.110	9.862	9.642	9.255	8.550
0.75	9.630	9.100	9.152	8.695	7.986
0.70	9.139	9.666	8.991	8.316	7.557
0.65	9.265	8.669	8.360	7.760	6.636
0.60	9.342	8.517	8.478	7.164	6.061
0.55	9.048	7.832	7.404	6.215	5.565
0.50	8.497	7.549	6.449	5.747	5.148
0.45	7.545	6.876	6.034	5.091	4.216
0.40	7.629	6.347	5.511	4.586	3.638
0.35	7.070	6.014	5.020	3.847	3.217
0.30	7.013	5.715	4.516	3.491	2.722
0.25	6.425	5.398	3.837	2.759	2.467
0.20	6.001	4.467	3.635	2.828	2.081
0.15	5.323	3.899	2.921	2.065	1.721
0.10	4.606	3.653	2.363	1.813	1.703
0.05	4.384	2.955	2.333	1.681	1.432
0.00	3.872	2.585	2.069	1.834	1.163
-0.05	3.243	2.258	1.729	1.428	
-0.10	3.021	1.879	1.582		
-0.15	2.439	1.699	1.489		
-0.20	2.233	1.540	1.239		
-0.25	2.105	1.417			
-0.30	1.605	1.246			
-0.35	1.499	1.061			
-0.40	1.530				
-0.45	1.325				
-0.50	1.156				

Table B.45: The third of three tables detailing the $\partial^2\sigma/\partial(KE_\pi)\partial(\cos(\theta_{\pi,\nu}))$ results from Figure 6.35 (10^{-41}cm^2/MeV).

bin low edge	275	300	325	350	375
0.95	10.643	9.606	8.276	6.901	6.195
0.90	9.364	8.854	7.767	6.488	5.541
0.85	8.728	7.743	6.851	5.644	4.855
0.80	7.750	7.112	6.113	5.512	4.484
0.75	7.385	6.491	5.446	4.412	4.318
0.70	6.421	5.607	4.306	4.003	3.426
0.65	6.026	4.908	4.296	3.306	3.052
0.60	5.115	4.134	3.565	3.198	2.594
0.55	4.760	3.630	3.169	2.454	2.237
0.50	3.867	3.354	2.741	2.113	2.098
0.45	3.390	2.727	2.384	2.053	1.726
0.40	2.633	2.288	2.013	1.665	1.442
0.35	2.636	1.993	1.702	1.543	
0.30	2.053	2.203	1.537		
0.25	1.943	1.479	1.227		
0.20	1.610				
0.15	1.590				
0.10	1.488				

Table B.46: The first of three tables detailing the percent uncertainty of the $\partial^2\sigma/\partial(KE_\pi)\partial(\cos(\theta_{\pi,\nu}))$ results from Figure 6.35.

bin low edge	0	25	50	75	100	125
0.95		19.098	17.068	15.740	15.130	17.074
0.90		23.775	15.252	15.324	14.774	15.101
0.85		16.540	17.527	11.069	13.621	13.889
0.80		17.630	17.426	12.517	12.406	12.805
0.75		20.075	14.402	13.476	11.649	12.912
0.70	20.544	17.261	13.509	12.711	12.829	12.698
0.65		16.149	16.057	13.835	13.657	13.241
0.60	27.079	16.051	15.458	14.096	12.146	13.542
0.55		22.156	14.021	15.206	12.799	15.013
0.50		15.424	13.524	13.637	13.791	14.396
0.45		17.041	15.275	14.221	13.649	13.636
0.40	24.671	15.936	13.865	13.091	14.465	14.668
0.35		16.360	14.020	13.460	13.940	15.743
0.30		14.984	12.993	13.613	15.030	15.627
0.25		13.195	11.814	13.845	13.921	15.423
0.20		14.152	13.914	13.527	14.739	14.422
0.15	16.979	14.294	14.212	13.375	14.238	14.125
0.10	20.960	14.935	14.337	12.754	14.253	16.484
0.05	13.604	13.263	12.816	13.765	15.346	15.649
0.00	24.008	14.995	14.962	13.238	14.414	14.677
-0.05	19.241	14.070	13.665	12.845	14.334	14.704
-0.10	17.709	15.715	11.476	13.680	13.484	16.292
-0.15	18.348	14.764	15.253	13.727	15.685	15.813
-0.20	16.851	12.429	12.587	14.212	14.450	15.123
-0.25	18.077	14.919	13.117	14.574	18.040	16.290
-0.30	19.836	13.843	13.346	16.043	15.038	14.457
-0.35	16.966	13.812	14.814	17.566	14.352	15.343
-0.40	17.018	13.196	13.549	15.165	14.898	17.673
-0.45	18.866	13.810	13.966	14.493	18.684	16.323
-0.50	14.809	13.065	13.832	13.469	14.146	16.727
-0.55	16.436	15.309	12.889	13.770	13.580	17.198
-0.60	19.470	13.306	14.508	14.770	16.957	17.436
-0.65	18.176	12.493	15.286	16.694	16.714	16.433
-0.70	15.156	12.263	15.037	17.161	20.494	20.825
-0.75	14.807	11.543	14.148	18.383	19.990	19.919
-0.80	14.759	12.400	16.590	21.048	19.793	25.052
-0.85	14.483	12.227	14.396	19.111	20.196	
-0.90	20.409	13.433	15.263	18.445	25.167	
-0.95	15.132	12.751	14.961	17.030	23.027	
-1.00	17.440	14.483	17.662	20.686	26.851	

Table B.47: The second of three tables detailing the percent uncertainty of the $\partial^2\sigma/\partial(KE_\pi)\partial(\cos(\theta_{\pi,\nu}))$ results from Figure 6.35.

bin low edge	150	175	200	225	250
0.95	17.142	16.913	16.948	17.222	18.863
0.90	14.987	16.047	15.782	17.239	17.868
0.85	13.209	13.734	15.297	16.067	17.078
0.80	14.042	14.426	15.217	15.776	17.222
0.75	13.339	14.984	16.180	16.071	17.043
0.70	14.544	15.454	15.102	16.910	16.928
0.65	13.572	15.483	14.624	15.725	16.093
0.60	13.465	15.547	15.609	16.401	18.917
0.55	14.691	16.061	18.573	17.768	18.322
0.50	15.156	16.907	18.377	16.456	17.692
0.45	16.064	16.744	17.545	17.288	19.448
0.40	15.240	15.066	17.947	19.210	20.513
0.35	15.303	15.274	18.283	17.978	19.382
0.30	16.283	16.798	18.020	17.422	19.188
0.25	14.909	16.540	19.075	18.775	18.791
0.20	14.982	17.111	18.247	19.524	18.904
0.15	15.864	16.394	18.031	17.435	21.418
0.10	16.098	15.449	17.980	19.061	20.913
0.05	16.433	15.871	15.697	20.920	19.639
0.00	15.331	15.604	19.690	21.116	21.897
-0.05	15.297	16.087	18.882	20.257	
-0.10	17.375	18.762	19.650		
-0.15	19.895	17.441	20.828		
-0.20	16.283	18.443	21.728		
-0.25	16.943	19.278			
-0.30	20.128	19.211			
-0.35	21.054	20.422			
-0.40	22.146				
-0.45	20.188				
-0.50	19.318				

Table B.48: The third of three tables detailing the percent uncertainty of the $\partial^2\sigma/\partial(KE_\pi)\partial(\cos(\theta_{\pi,\nu}))$ results from Figure 6.35.

bin low edge	275	300	325	350	375
0.95	20.074	20.251	21.692	21.603	22.148
0.90	19.192	19.092	19.178	20.799	21.193
0.85	17.830	19.321	18.438	18.793	19.840
0.80	19.749	18.857	19.279	19.347	19.160
0.75	17.063	18.930	18.546	20.084	19.059
0.70	17.220	19.128	18.398	18.636	19.801
0.65	16.810	17.379	21.202	19.197	21.029
0.60	18.157	19.912	19.231	20.101	21.455
0.55	17.878	19.300	19.778	20.640	21.644
0.50	18.308	19.868	21.849	21.849	19.619
0.45	20.392	19.711	21.216	20.511	21.486
0.40	19.679	19.490	21.785	24.972	25.029
0.35	21.338	22.529	20.548	24.372	
0.30	20.324	21.019	23.361		
0.25	23.067	21.823	25.748		
0.20	21.936				
0.15	20.165				
0.10	27.356				